Internal waves and slope mixing in the Faroe-Shetland Channel

Thesis submitted in accordance with the requirements of
the University of Liverpool for the degree of Doctor in Philosophy
by
Robert Alan Hall

December 2008

Abstract

Internal waves play an important role in supporting turbulent mixing on continental shelf slopes worldwide. In this thesis the energy transported by internal waves onto the West Shetland slope, the eastern bank of the Faroe-Shetland Channel, is measured and related to estimates of turbulent mixing. A numerical model is used to assess how much internal wave energy is reflected and how much is dissipated on the slope.

A semi-diurnal internal tide and trains of near-bed, non-linear internal waves are observed on the slope. The across-slope energy flux of the internal tide is 155 W m^{-1}, the majority ($\sim$ 100 W m^{-1}) contained within the main pycnocline. Where the pycnocline intersects the shelf slope the topography is supercritical to the internal tide and model simulations suggest up to 68% of the incident energy is reflected. The internal tide maintains its modal structure upon reflection and so the reflective behaviour cannot be explained simply by critical slope theory. The energy flux of the non-linear internal waves is intermittent in time, up to 200 W m^{-1}, but typically of the order 10 W m^{-1} up the slope. These waves are bottom trapped and so must dissipate or break in the local area because the near-bed buoyancy frequency further up the slope is less than the angular frequency of the waves. Up-slope of the intersection with the pycnocline, model simulations show the horizontal group velocity is too small for the wave energy to make significant progress onto the shelf, so the energy is dissipated locally.

The rate of turbulent kinetic energy dissipation in the pycnocline is of the order 5×10^{-8} W kg^{-1}, inferred from Thorpe scale analysis of density overturns and using a finescale parameterisation of vertical shear and strain. This dissipation rate is equivalent to a diapycnal eddy diffusivity of the order 2×10^{-4} m^2 s^{-1}, an order of magnitude larger than typical values for the interior of the open ocean. The high turbulent kinetic energy dissipation rate can be sustained by the energy fluxes associated with the internal tide and non-linear internal waves if it is assumed that the whole up-slope energy flux in the pycnocline is dissipated in the region between the location of the energy flux estimate and the shelf slope.

Acknowledgements

Many thanks to my supervisors, John Huthnance from Proudman Oceanographic Laboratory, and Ric Williams from the Department of Earth and Ocean Science at the University of Liverpool. John provided me with endless expert advice and guidance when I (frequently) lost the plot. Meanwhile, Ric reeled me back in when my research drifted a too far off course by reminding me to write work up and get it published (I'll get there eventually).

Although I did not participate, this thesis relies heavily on data collected during a research cruise to the Faroe-Shetland Channel. I would therefore like to thank to the Master and crew of the *F. S. Poseidon* (IFM-GEOMAR) , Proudman Oceanographic Laboratory and National Marine Facilities staff for support with the measurements, Mark Inall (Scottish Association of Marine Science) and Hans van Haren (Netherlands Institute of Sea Research) for scientific input into the cruise, and Bogi Hansen (Faroese Fisheries Laboratory) for supplying the lowered ADCP. Thanks also to Jiuxing Xing for help and advice with the numerical modelling, Alan Davies, and Chris Hughes (all from POL).

Finally a big thanks to my girlfriend Sarah for putting up me for the past few months while I've been stressed out, my long-running flatmate Dave for the craic and infuriating me with his inability to get hangovers, Eleanor for keeping me organised and making her fair share of tea, Craig, VJ, Mark, John, Eddie, Max, and all the usual Cambridge suspects.

This Ph.D. was funded by the Natural Environment Research Council studentship no. NER/S/A/2005/13812.

Contents

Chapter 1

Introduction

1.1 Motivation

Mixing of water masses in the abyssal ocean is required to allow upwelling of deep water that closes the Meridional Overturning Circulation. Presently, there is a discrepancy between direct measurements of the level of mixing in the interior of the open ocean, from the dispersion of chemical tracer (Ledwell et al., 1993) and measurements of small-scale turbulence (Toole et al., 1994), and indirect estimates from the balance of deep convection and global upwelling against the strength of abyssal stratification (Munk, 1966). One explanation for the inconsistency between direct and indirect estimates is that much of the mixing occurs at the ocean boundaries and mixed water is transported into the interior along density surfaces (Munk and Wunsch, 1998). Areas of enhanced mixing over rough topography have been identified, linked to interactions with tidal flows or strong currents (e.g. Polzin et al. 1997; Naveira Garabato et al. 2004b), but further work is required to close the global deep ocean mixing budget.

For the North Atlantic, formation of deep water masses occurs primarily in the Labrador Sea but also in the Nordic Seas. The transport of deep water from the Nordic seas into the North Atlantic is constrained by the Greenland-Scotland Ridge, a series of submarine ridges between Greenland, Iceland, and Scotland. Deep water overflows the ridge primarily through two passageways, the Denmark Strait and the Faroe-Shetland Channel/Faroe Bank Channel. In doing so it entrains ambient North Atlantic Water and becomes a component of North Atlantic Deep Water, thereby contributing to the Meridional Overturning Circulation. The level of mixing in these passageways is of interest because there is potential for large-scale ocean circulation to be affected through the modification of deep water masses entering the North Atlantic. This thesis is about mixing

processes that occur on the continental shelf slope that forms the eastern bank of the Faroe-Shetland Channel.

Mixing on the shelf slope may be enhanced above background levels by the interaction of internal waves with the sloping topography. Internal waves transport energy from wind and tidal forcing through the ocean interior. The internal waves reflect with sloping topography leading to increases in the energy density of waves and eventually causing internal wave breaking and turbulent mixing. This is especially likely where the topographic slope is critical to the slope of the internal wave characteristic. By cascading energy from large-scale motions to the small-scale mixing, internal waves are important in determining local water mass properties and may also be important in supplying the mixing energy required to support the Meridional Overturning Circulation.

1.2 Internal waves

Internal waves are displacements of density surfaces (isopycnals) that propagate through the interior of the ocean. Like swell waves at the surface, internal waves are restored by gravity and so can only exist where the ocean is stably stratified (density of the water increasing with depth). They are generated by mechanical forcing at the surface or by barotropic currents vertically displacing isopycnals when flowing over steep topography.

Near ocean boundaries internal wave variability often peaks at tidal frequencies. These internal tides are generated most efficiently by barotropic tidal currents flowing across steep topographic slopes and as such are often generated at seamounts and deep ocean ridges (Holloway and Merrifield, 1999; Rudnick et al., 2003). A schematic of internal tide generation at a deep ocean ridge is shown in Figure 1.1. Internal tides may also be generated on continental shelf slopes if across-slope tidal currents are large (Pingree and New, 1991; Green et al., 2008) or if slope is fractured by submarine canyons (Garcia Lafuente et al., 1999; Kunze et al., 2002). Most of the tidal energy dissipated in the ocean is thought to occur in shelf seas, where tidal currents are amplified, but it has been shown that 25-30% of tidal energy loss occurs in the deep ocean, probably by the generation of internal tides (Egbert and Ray, 2000, 2001).

Wind stress at the surface tends to generate internal oscillations near the inertial frequency, related to the rotation of the Earth. These so called near-inertial internal waves propagate downwards, into the ocean interior, and towards the equator (Alford, 2003a). They are often generated at high latitudes by winter

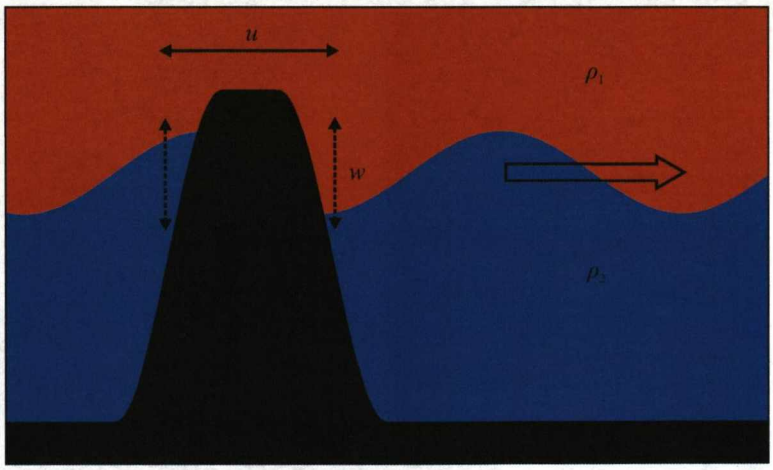

Figure 1.1: Schematic of internal tide generation at a deep ocean ridge for an idealised two-layer watercolumn with a low density upper layer (ρ_1) and higher density lower layer (ρ_2). Across-slope barotropic tidal currents over the ridge (u) induce vertical motions on the slope (w) which displace the pycnocline and form internal waves that propagate away from the ridge in both directions.

storm events (Alford, 2003b) and can have very long horizontal wavelengths, of the order 1000 km, but negligible vertical displacements (Thomson and Huggett, 1981). Internal waves have been shown to transport up to 50% of semi-diurnal and near-inertial energy away from their generation regions (Alford, 2003b).

For an idealised two-layer watercolumn with a low density upper layer (ρ_1) and higher density lower layer (ρ_2), internal waves on the interface are analogous to swell waves at the surface. The restoring force acting on vertical displacements of the interface is reduced gravity, $g' = g(\rho_2 - \rho_1)/\rho_2$, proportional to the density difference between the two layers. The smaller restoring force means internal waves typically have slower phase speeds and higher amplitudes than surface waves. The two-layer approximation is a good approximation for the base of the surface mixed layer and for poorly mixed estuaries, where saltwater intrudes under the inflowing freshwater, separated by a sharp halocline.

If stratification varies in a continuous manner, as it is in the majority of the ocean, internal waves propagate vertically as well as horizontally (Fig. 1.2). The angle of the of the wavenumber vector ($\mathbf{k}$) and by definition the phase velocity vector ($\mathbf{c}$) with the vertical, θ, and also the ratio of horizontal to vertical wavenumber, $\tan\theta = k_h/k_z$, is given by the internal wave dispersion relation,

$$\omega^2 = f^2 \cos^2\theta + N^2 \sin^2\theta, \tag{1.1}$$

where ω is the angular frequency of the wave (Phillips, 1977); $f = 2\Omega \sin \phi$ is the inertial (or Coriolis) frequency, where Ω the angular rotational frequency of the Earth and ϕ is latitude; and $N = [-(g/\rho_0)(d\rho/dz)]^{1/2}$ is the buoyancy (or Brunt-Väisälä) frequency, where ρ_0 is a reference density, and $d\rho/dz$ is the vertical potential density gradient. The form of the dispersion relation implies that internal waves can only exist at frequencies between the inertial frequency and the buoyancy frequency, i.e. $f < \omega < N$. This has two implications: firstly, because inertial frequency is a function of latitude, low-frequency oscillations can only exist as free internal waves below a critical latitude. Secondly, high-frequency internal waves can only exist where stratification is strong enough to support them and so may become trapped within a pycnocline.

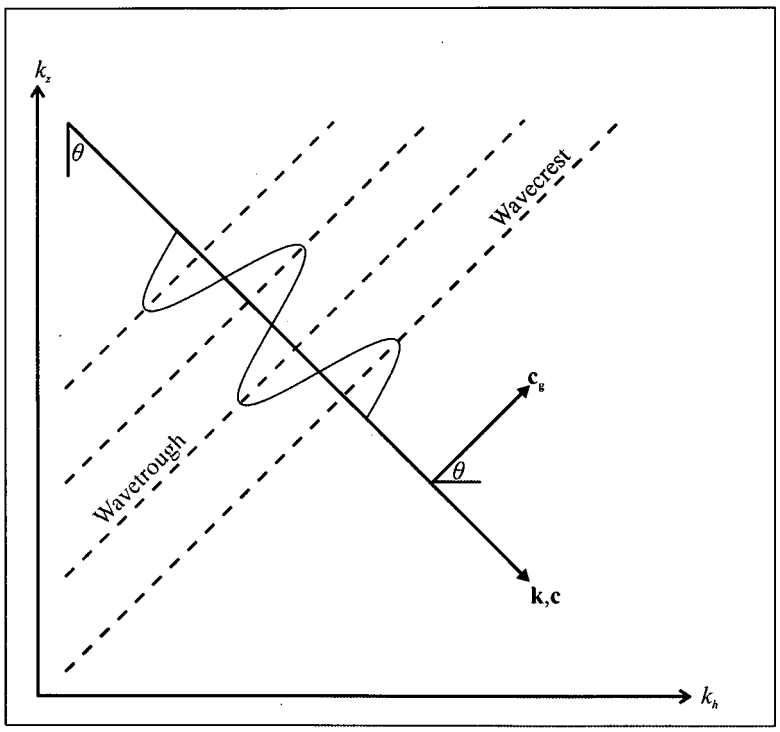

Figure 1.2: Schematic of internal wave propagation in a continuously stratified watercolumn. k_h is horizontal wavenumber; k_z is the vertical wavenumber; $\mathbf{k}$ is the wavenumber vector; $\mathbf{c}$ is the phase velocity vector; $\mathbf{c_g}$ is the group velocity vector.

Internal waves in continuous stratification are transverse waves and so water parcels move along the wave crests and troughs, perpendicular to the wavenumber vector. This means that for low frequency waves (close to f) water parcels move nearly horizontally while for high frequency waves (close to N) water parcels move nearly vertically. Another peculiarity of internal waves in continuous stratification is that the group velocity vector ($\mathbf{c_g}$) is normal to the phase velocity vector, directed towards the horizontal wavenumber; the angle of the group velocity vector with the horizontal is therefore θ. As for surface waves, the group velocity is the velocity of internal wave energy propagation; the direction of the group velocity vector is referred to as the internal wave characteristic and has a slope $s_{\text{wave}} = \tan\theta$. By rearranging the internal wave dispersion relation (1.1),

$$s_{\text{wave}} = \tan\theta = \frac{k_h}{k_z} = \left(\frac{\omega^2 - f^2}{N^2 - \omega^2}\right)^{1/2}, \tag{1.2}$$

the horizontal and vertical distribution of s_{wave} can be calculated for a specific angular frequency if the distributions of N and f are known, i.e. if $\omega \rightarrow f$, $s_{\text{wave}} \rightarrow 0$ and if $\omega \rightarrow N$, $s_{\text{wave}} \rightarrow \infty$. The ray path of internal wave characteristics from any point can then be plotted.

The angle of the characteristic with the vertical is conserved upon reflection with the surface or a horizontal bottom, so an internal wave approaching the surface at an angle i_1 with the vertical leaves the surface at an angle $r_1 = -i_1$. The behaviour of the characteristic upon reflection with topography is determined by the ratio of topographic slope ($s_{\text{topog}} = dh/dx$, where h is the position of the bottom) to the internal wave characteristic slope, $\alpha = s_{\text{topog}}/s_{\text{wave}}$. If $\alpha < 1$ the topography is subcritical and the angle of the characteristic with the vertical is again conserved, as with the surface or a horizontal bottom. The internal wave is therefore reflected up the slope (Fig. 1.3 upper panel). However, if $\alpha > 1$ the topography is supercritical and the angle of the characteristic with the *horizontal* is conserved, so an internal wave approaching the slope at an angle i_2 with the horizontal leaves the slope at an angle $r_2 = -i_2$. In this case the internal wave is reflected back into deeper water (Fig. 1.3 lower panel). In both cases the energy density of the reflected wave increases because the separation between two adjacent characteristics (called an internal wave ray tube) becomes narrower upon reflection, concentrating the energy into a smaller region. If $\alpha = 1$ the topography is critical and internal waves tend to dissipate because the vertical wavenumber and amplitude of the reflected waves goes to infinity (Wunsch, 1969). In this case the internal wave ray tube become infinitesimally narrow, trapping

internal wave energy at the boundary, and leading to shear instabilities, internal wave breaking, and turbulent mixing (Eriksen, 1982, 1985).

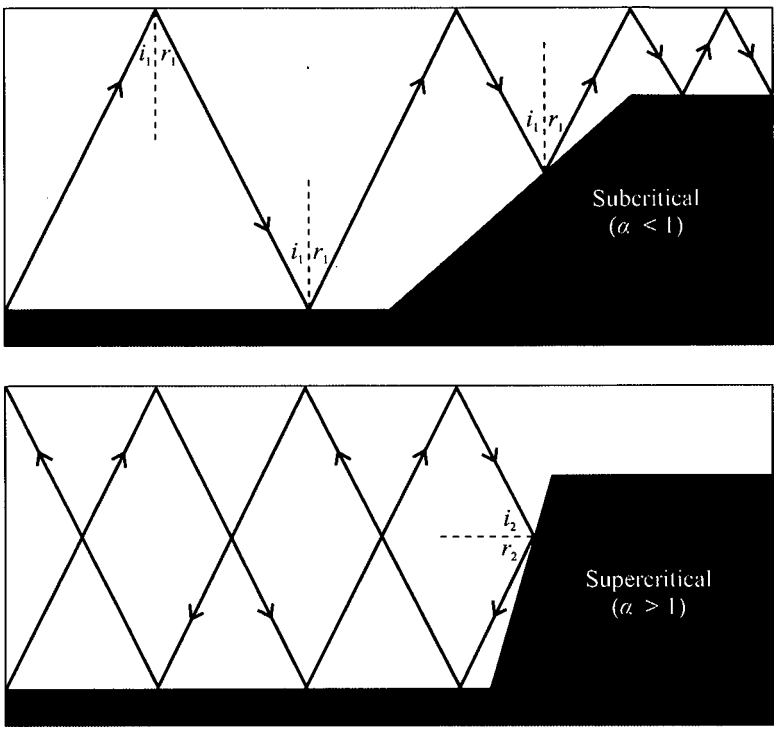

Figure 1.3: Schematic of internal wave reflection with subcritical and supercritical topography for uniform stratification (uniform N). θ_i is the angle of the incident internal wave characteristic; θ_r is the angle of the reflected internal wave characteristic.

Internal tides are thought to be preferentially generated over near-critical topography (Prinsenberg and Rattray, 1975; Baines, 1982) and may even help determine the gradient of continental slopes by inhibiting deposition of sediment where topography is near-critical (Cacchione et al., 2002).

1.2.1 Slope mixing processes

On continental shelf slopes, water masses with different properties (such as temperature, salinity, and nutrient concentration) may be mixed by turbulence caused by the interaction of internal waves with the sloping topography. Mixing is en-

hanced near the bottom where remotely generated internal tides undergo critical reflection with the slope (Nash et al., 2004), while locally generated internal tides can enhance mixing near the shelf break (New, 1988; New and Pingree, 1990) and several hundred metres above the slope (Lien and Gregg, 2001). Where the tidal currents are primarily along the shelf slope, mixing hotspots can be generated by flow over small-scale topographic features (Nash et al., 2007).

Turbulent mixing may also be caused by the interaction of large-scale flows and barotropic tidal currents with sloping topography. Close to the seabed mixing by convective instabilities results from the asymmetric response of the bottom boundary layer to along-slope flows (MacCready and Rhines, 1993; Hosegood and van Haren, 2003). In the northern hemisphere, with a shelf slope to the east, a northwards flow induces a down-slope Ekman transport in the bottom boundary layer. This Ekman transport advects low density water beneath higher density water, downwelling isopycnals against the slope and creating static instabilities that result in convective overturning. Conversely, a southwards flow induces an up-slope Ekman transport in the the bottom boundary layer that advects high density water beneath lower density water and so enhances stratification.

The level of mixing on shelf slopes is an important control on horizontal exchange across the shelf edge (with shelf seas) and vertical exchange between overlying water masses adjacent to the slope. Water mixed on the slope is transported into the ocean interior along isopycnal surfaces, for example in intermediate nepheloid layers (Moum et al., 2002), and so may also contribute to abyssal mixing.

1.3 The Faroe-Shetland Channel

This thesis focuses on internal waves and their induced mixing on the West Shetland slope, the continental shelf slope north of Scotland, which forms the eastern bank of the Faroe-Shetland Channel. This semi-enclosed channel, located between 60°N and 62°N, 1°W and 6°W, is orientated southwest to northeast and separates the Shetland and Faroe shelves (Fig. 1.4). To the northeast the channel is open to the Norwegian Sea, while the southwest end is partially closed by the Wyville Thomson Ridge and connected to the Iceland Basin by the Faroe Bank Channel. The Faroe-Shetland Channel shoals from more than 1500 m at the open end to around 1000 m at a sill (60°30′N, 5°W) then deepens to around 1200 m at the base of the Wyville Thomson Ridge. The West Shetland slope is gentle compared to typical continental shelf slopes. The slope gradient is around 1.2°

and relatively uniform along the shelf between the Wyville Thomson Ridge and 1°W.

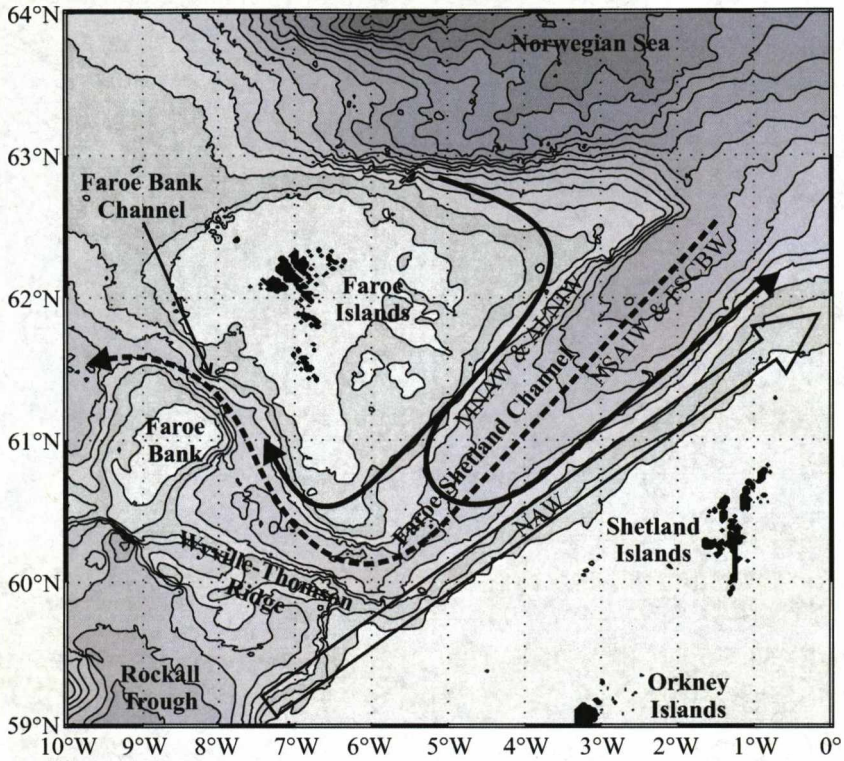

Figure 1.4: Bathymetry of the Faroe-Shetland Channel and the circulation of the water masses, adapted from Turrell et al. (1999). All maps in this thesis use satellite geodesy derived bathymetry from Scripps Institution of Oceanography (Smith and Sandwell, 1997).

The Faroe-Shetland Channel is an important passageway for the exchange of water masses between the North Atlantic and the Nordic Seas. Near the surface, warm, saline North Atlantic Water flows northeast along the edge of the Shetland shelf into the Norwegian Sea. Below the main pycnocline, cold, fresher Norwegian Sea Deep Water flows southwest along the axis of the channel then either overflows the Wyville Thompson Ridge (where the sill depth is around 600 m) into the Rockall Trough (Sherwin and Turrell, 2005) or flows through the

Faroe Bank Channel (where the sill is deeper, around 850 m) into the Iceland Basin (Borenäs and Lundberg, 2004).

1.3.1 Water mass circulation

The circulation of water masses through the Faroe-Shetland Channel is shown in Figure 1.4, adapted from Turrell et al. (1999). North Atlantic Water (NAW) forms a high salinity core at the top of the West Shetland slope and flows northeast, along the shelf edge, in a barotropic slope current. Slightly cooler and fresher Modified North Atlantic Water (MNAW) enters the channel from the northeast and flows southwest, near the surface, along the Faroe slope (Becker and Hansen, 1988). The MNAW then recirculates in the channel, flowing into the Norwegian Sea along the West Shetland slope with the NAW (van Aken and Eisma, 1987; van Aken, 1988). Slightly denser Arctic Intermediate/North Iceland Water (AI/NIW) lies underneath the surface waters and enters the channel from the northeast, primarily along the Faroe slope (Meincke, 1978). The AI/NIW also recirculates in the channel, flowing into to the Norwegian Sea below the NAW and MNAW (Becker and Hansen, 1988). Norwegian Sea Arctic Intermediate Water (NSAIW) is the freshest water in the channel and flows southwest, primarily along the Faroe slope, below the AI/NIW (Blindheim, 1990; Martin, 1993; Blindheim et al., 1996). The densest water in the channel is Faroe-Shetland Channel Bottom Water (FSCBW), composed of NSAIW and Norwegian Sea Deep Water (NSDW), and flows southwest along the axis of the channel (Turrell et al., 1999).

1.3.2 Exchange across the Greenland-Scotland Ridge

The Faroe-Shetland Channel and Faroe Bank Channel together form one of two main passageways through which deep water overflows the Greenland-Scotland Ridge (Fig. 1.5). Warm, saline water masses near the surface (NAW and MNAW) flow into the Nordic Seas from the North Atlantic along the edge of the Shetland shelf; over the Iceland-Faroe Ridge; and through the Denmark Strait (between Greenland and Iceland) along the edge of the Iceland shelf (Østerhus et al., 2005). Cold, fresher deep water is formed north of the Greenland-Scotland Ridge by the cooling and sinking of these near-surface waters and returns to the North Atlantic, primarily through the Denmark Strait (where the sill depth is around 600 m) and the Faroe-Shetland Channel/Faroe Bank Channel (Dickson and Brown, 1994), but also over the Faroe-Iceland Ridge and the Wyville Thomson Ridge (see Hansen and Østerhus 2000 for a review). There is also a southwards flow of

near-surface Polar Water through the Denmark Strait, along the edge of the Greenland shelf (Foldvik et al., 1988).

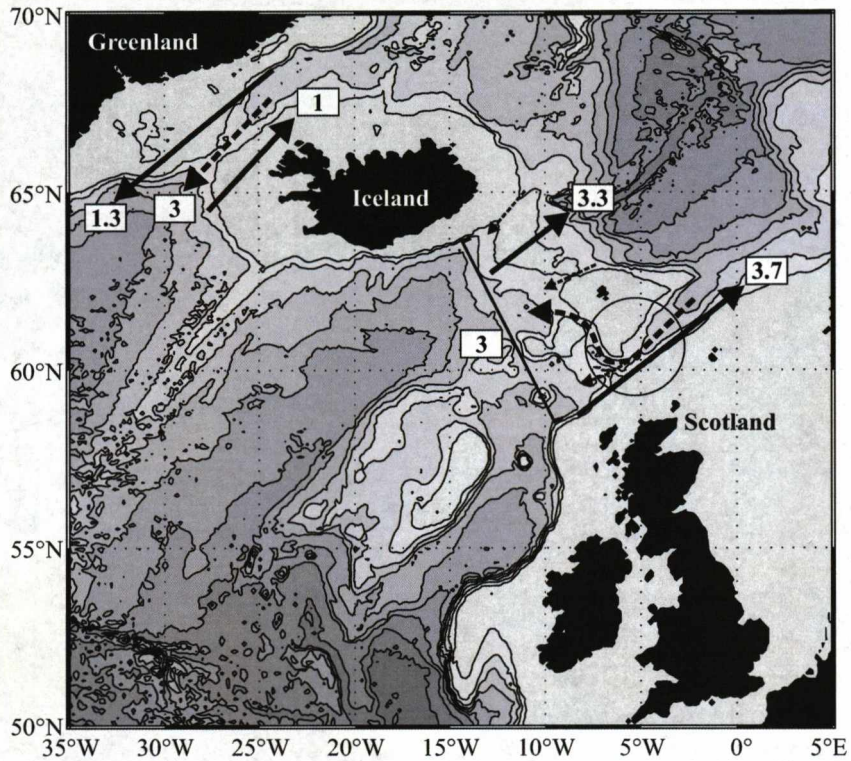

Figure 1.5: Exchange across the Greenland-Scotland Ridge. Solid arrows are surface transports; dashed arrows are deep transports; all transports are in Sv ($1\ \mathrm{Sv} = 10^6\ \mathrm{m^3\ s^{-1}}$). The circle marks the Faroe-Shetland Channel.

Estimates of the volume transports across the Greenland-Scotland Ridge from Hansen and Østerhus (2000) are shown in Figure 1.5. The deep overflow through the Faroe Bank Channel has been measured regularly since the late 1950s and has a yearly-average volume transport of around 2 Sv (see Borenäs and Lundberg 2004 for a review). Recently, Hansen et al. (2001) identified a 20% decrease in the volume transport of the overflow since 1950 that has been linked to widspread freshening on the deep North Alantic (Dickson et al., 2002).

The overflow of deep water across the Wyville Thomson Ridge is typically smaller, between 0.1 and 0.3 Sv, but intermittent in time (Hansen and Østerhus,

2000). Sherwin and Turrell (2005) observed a large overflowing event in which 0.5 to 0.8 Sv of NSDW cascaded down the southern side of the ridge, entraining 0.9 to 1.3 Sv of ambient NAW.

The deep overflow through the Denmark Strait was previously regarded to be stable (2.7 to 2.9 Sv) on time-scales longer than weeks (Dickson et al., 1990; Dickson and Brown, 1994). However, significant warming and slowing of the overflow during the winter of 1996-1997 was measured by Dickson et al. (1999). More recently, Macrander et al. (2005) identified a 20% decrease in the volume transport and a 5°C increase in the temperature of the overflow between 1999 and 2003. Köhl et al. (2007) suggest the strength of the deep overflow may be controlled by the volume of dense water north of the sill and the barotropic flow through the Denmark Strait, determined by wind stress curl around Iceland. They find a relation between the volume of dense water and sea surface height north of the sill and use it to predict the variability of the overflow from satellite altimeter measurements.

1.4 This thesis

The aim of this thesis is to measure the energy transported onto the West Shetland slope by internal waves and relate this energy flux to estimates of turbulent mixing on the slope. It is a joint observational and modelling study using hydrographic data collected during a slope mixing experiment on the West Shetland slope and from a historic hydrographic section across the Faroe-Shetland Channel. Numerical model simulations are conducted to investigate internal wave behaviour that cannot be determined from observations. Six questions are posed:

1. On what time-scales do changes in the large-scale water mass structure of the Faroe-Shetland Channel occur?

2. Were the hydrographic conditions during the slope mixing experiment extreme compared to the variability observed in the historic dataset?

3. How much turbulent mixing occurs on the West Shetland slope?

4. How much energy is transported onto the slope by internal waves?

5. Can internal wave energy fluxes account for the measured mixing?

6. What factors effect how much internal wave energy is reflected and how much is dissipated on the slope?

This thesis contains six main chapters. The first five chapters are an analysis of the hydrographic data from the West Shetland slope and Faroe-Shetland Channel. In Chapter 2, a 32-year time series of temperature and salinity data from the historic section is collated and analysed to identify the time-scales on which changes in the large-scale water mass structure occur. The next four chapters are concerned with results of the slope mixing experiment. Chapter 3 contains summaries of the instruments deployed during the experiment and initial analysis of the data collected, including observations of internal waves. Independent estimates of turbulent mixing on the slope are made in Chapter 4 and the energy fluxes associated with the observed internal waves calculated in Chapter 5. The dissipation of internal wave energy on the slope is discussed in Chapter 6 and reconciled with the independent estimates of mixing. Chapter 7 is a numerical model investigation of internal wave reflection and energy dissipation on continental shelf slopes. The results of the model are used to help answer questions left open after the observational study. Key results from the six main chapters are summarised in Chapter 8 and combined in a synthesis of this work.

Chapter 2

Historic data: The Fair Isle-Munken line

2.1 Introduction

Before investigating the internal wave field and small-scale mixing processes on the West Shetland slope, it is of interest to look at the large-scale water mass structure of the Faroe-Shetland Channel and identify the time-scales on which changes occur. For this purpose, a 32-year time series of temperature and salinity data from a historic section across the channel is collated and analysed.

The Fair Isle-Munken hydrographic section has been regularly occupied by the Fisheries Research Services (FRS) and the Faroese Fisheries Laboratory (FFL) since 1893. It consists of fifteen stations running down the West Shetland slope, North of the Orkney Islands, across the Faroe-Shetland Channel and onto the Faroe shelf south of the Faroe Islands (Fig. 2.1, Table A.1). Historically the section is occupied once or twice a year although since the 1970s the frequency has varied significantly. During the International Council for the Exploration of the Sea (ICES) Overflow '73 project the section was occupied eight times with a further five occupations in 1974. Between 1994 and 2005, ADCPs were deployed at five locations along the section, initially as part of the Nordic-WOCE project, and sustained by the VEINS, MAIA, and ROAME AE1190 projects. As the instruments required frequent redeployment, the frequency of occupations was increased to between four and eight per year.

In this chapter, temperature and salinity data from the Fair Isle-Munken line between 1973 and 2005 are used to investigate the time-scales of variability in the structure and position of the main pycnocline, the water masses in the channel, and the heat and salt content. The origin of the data and temporal biases in the dataset are identified in Section 2.2. The distribution of temperature and

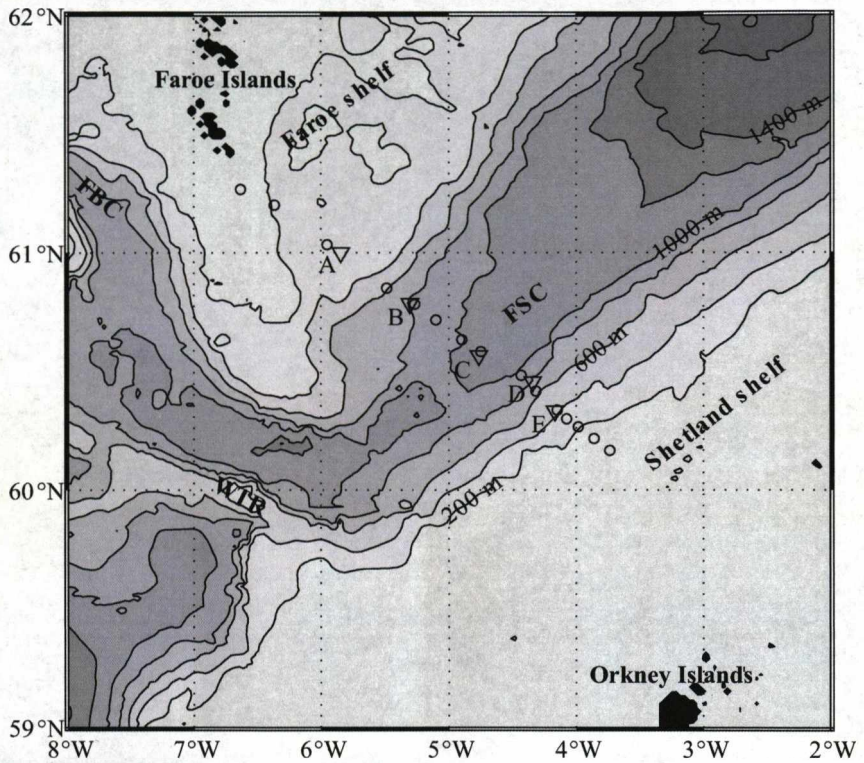

Figure 2.1: Location of the CTD stations (circles) and ADCP moorings (triangles) along the Fair Isle-Munken line. FSC is the Faroe-Shetland Channel; FBC is the Faroe Bank Channel; and WTR is the Wyville Thomson Ridge.

salinity in the channel and modes of variability are shown is Section 2.3. Timescales of pycnocline variability from temperature sections and moored thermistors are estimated in Section 2.4 and correlated with changes in sea surface height. Changes in water mass properties are identified in Section 2.5 and changes in the heat and salt content of the waters in the channel are calculated in Section 2.6. The results are summarised in Section 2.7.

2.2 Data sources

CTD data from 71 occupations during the period September 1994 to May 2005 were acquired from FRS, sub-sampled at 25 m depth intervals, along with ADCP data and temperature time series data from thermistors attached to four of the ADCP moorings. Temperature and salinity data from 46 occupations during the period August 1973 to May 1994 were acquired from the ICES online database. The vertical resolution of the archived data varied between approximately 5 m and 200 m and so were interpolated onto the same 25 m depth levels as the data from FRS. In total the data from 117 occupations of the section were collated.

As well as the frequency of occupations varying year-by-year, the dates of occupation are not uniformly distributed throughout the year (Fig. 2.2). Occupations are most frequent in September, May, and June but there are no occupations in January and few in March and April. Not all the stations are sampled during each cruise because FRS and FFL occupy a slightly different set of stations and extra stations have been added over time. Other stations are missed due to bad weather or instrument failure. The stations sampled during each occupation are shown in Table A.2.

2.3 Temperature and salinity distribution

The temperature and salinity structure of the Faroe-Shetland Channel is dominated by the main pycnocline between 300 and 700 m that slopes down towards the southeast (Fig. 2.3). This pycnocline separates cold ($\theta < 0°C$), low salinity (< 34.95 psu) bottom water from warm, high salinity surface water. In the surface layer there is a horizontal temperature and salinity gradient (both increase to the southeast) and a core of high salinity (> 35.35 psu) NAW near the shelf break at the top of the West Shetland slope. The horizontal temperature gradient can be clearly observed in satellite sea surface temperature (SST) images and occurs all along the shelf edge (not shown). Seawater density in the channel is primarily

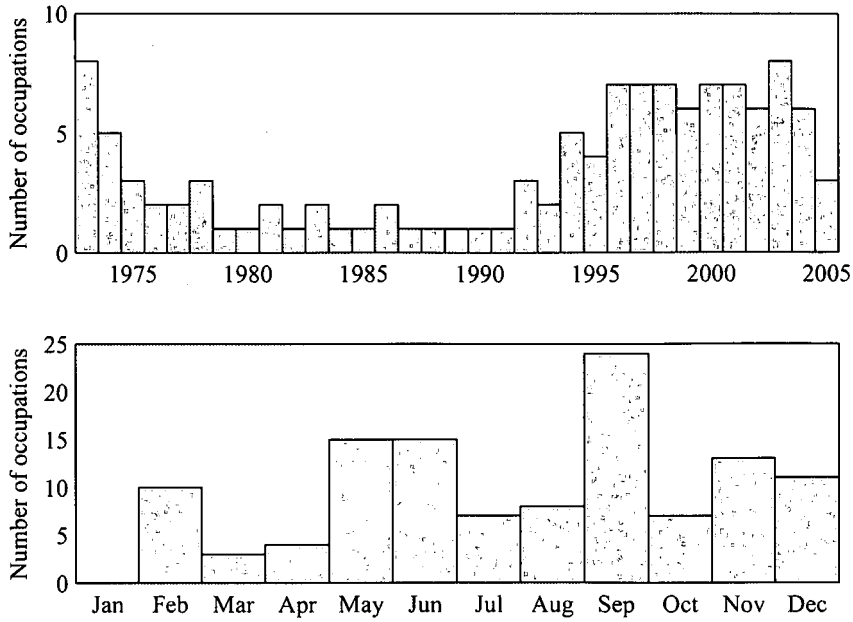

Figure 2.2: Distribution of section occupations by year and month.

determined by temperature, with salinity partially compensating. The isotherms and isohalines run parallel to the isopycnals in and below the pycnocline. In the surface layer the isohalines become steeper over the West Shetland slope and cross the isopycnals.

Most of the seasonal variability in temperature and salinity occurs in the surface layer. Surface heating in spring and summer leads to the formation of a seasonal thermocline in the upper 200 m during the summer months, that partially obscures the surface signature of the horizontal temperature gradient. The seasonal thermocline is eroded by increased wind mixing and surface convection in autumn and winter, with the maximum surface mixed layer depth around 400 m. The horizontal salinity gradient at the surface is present throughout the year, but retreats to the southeast during the summer months. This results in a subsurface salinity maximum at around 100 m, attached to the high salinity core of NAW. The vertical temperature and salinity gradients through the main pycnocline are larger in winter than summer, due to a deeper surface mixed layer, but below 500 m there is little seasonal variability.

The five water masses present in the channel can be identified in the time-average potential temperature-salinity (θ-S) diagram (Fig. 2.4). The θ-S properties of the water masses are summarised in Table 2.1.

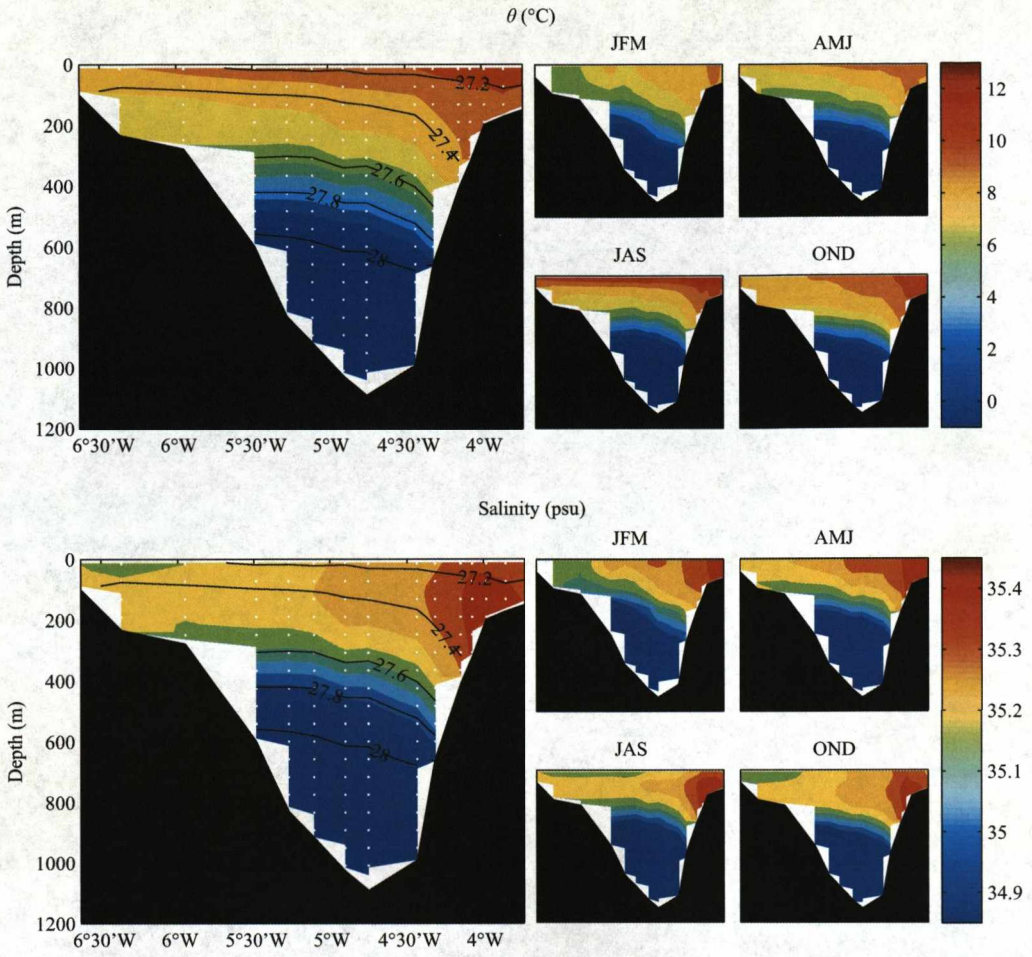

Figure 2.3: Time-averaged distribution of potential temperature and salinity in the Faroe-Shetland Channel and seasonal variability. The black lines are contours of σ_θ.

Water mass	Acronym	θ (°C)	S (psu)
North Atlantic Water	NAW	> 9.5	> 35.3
Modified North Atlantic Water	MNAW	6.5-8.5	35.15-35.28
Arctic Intermediate/North Iceland Water	AI/NIW	2-5	34.93-35.03
Norwegian Sea Arctic Intermediate Water	NSAIW	0	34.89
Faroe-Shetland Channel Bottom Water	FSCBW	< -0.5	34.91-34.92

Table 2.1: Water mass potential temperature and salinity in the Faroe-Shetland Channel after Hosegood (2005).

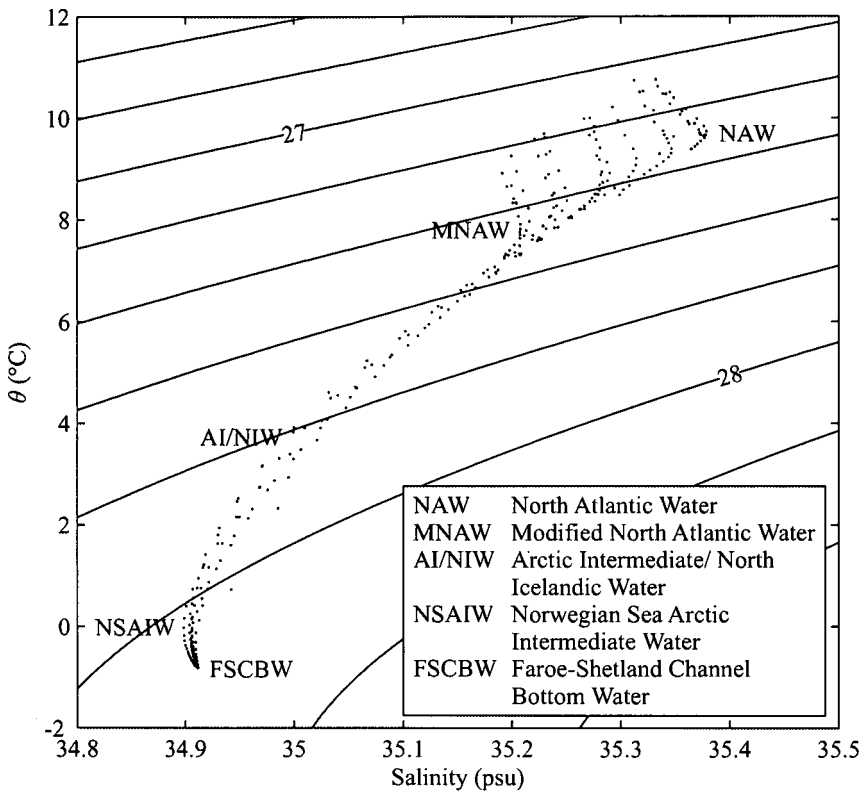

Figure 2.4: Location of the water masses present in the Faro-Shetland Channel in θ-S space.

2.3.1 Modes of variability

Modes of temperature and salinity variability are identified by calculating empirical orthogonal functions (EOFs) of the temperature and salinity datasets from FRS (1994 to 2005). EOF analysis is a method of dimension reduction that displays the 3-dimensional dataset as a series of 2-dimensional spatial fields and and corresponding time series (see Emery and Thomson 2001) and has been used to identify fluctuations in the the Norwegian Atlantic slope current (Skagseth and Orvik, 2002).

For both temperature and salinity, the first EOF accounts for nearly 50% of the variability, with most of this variability occuring around the main pycnocline (Fig. 2.5 and 2.6). This relates to horizontally uniform vertical displacement, or thickening/thinning, of the pycnocline. The corrisponding time series is noisy, but with a definite variability minimum around 2000. The second EOF of temperature accounts for nearly 20% of the remaining variability, primarily in the upper 200 m, and represents the seasonal cycle of surface heating and cooling. As expected the corresponding time series is highly seasonal, increasing in spring and summer then decreasing in autumn and winter. The second EOF of salinity accounts for 13% of the remaining variability and has a bipolar distribution, low in the pycnocline over the axis of the channel and positive over the West Shetland slope. This may be related to variability in the strength or position of the slope current.

2.4 Pycnocline variability

The structure and position of the main pycnocline can vary dramatically from the time-average shown in Figure 2.3. As an example, the distribution of potential temperature and potential density across the section on 26th March 1997 and 23th May 1997 are shown in Figure 2.7. In the first case the pycnocline is almost 200 m deeper than average against the West Shetland slope, the across-channel isopycnal slope is steeper, and the vertical density gradient through the pycnocline is larger than average. In the second case the pycnocline is shallower over the West Shetland slope than the Faroe slope.

The time-scales on which changes in pycnocline structure and position occur are hard to quantify from the CTD data alone because of irregular temporal sampling. From the eight occupations within a month during the Overflow '73 project, however, it is apparent that large changes can occur on time-scales shorter than a week. The maximum observed temperature change at a constant depth

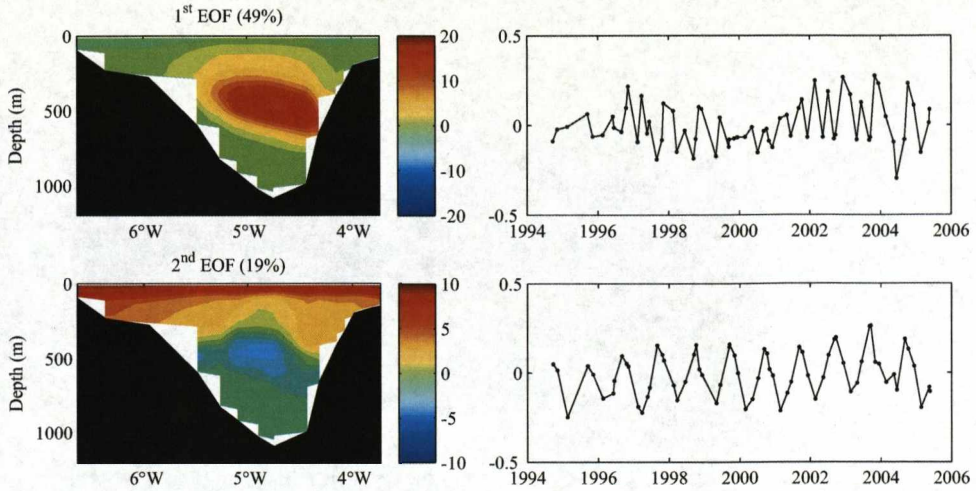

Figure 2.5: First two empirical orthogonal functions of potential temperature. The panels on the left show the spatial variability; the panels on the right show the temporal variability.

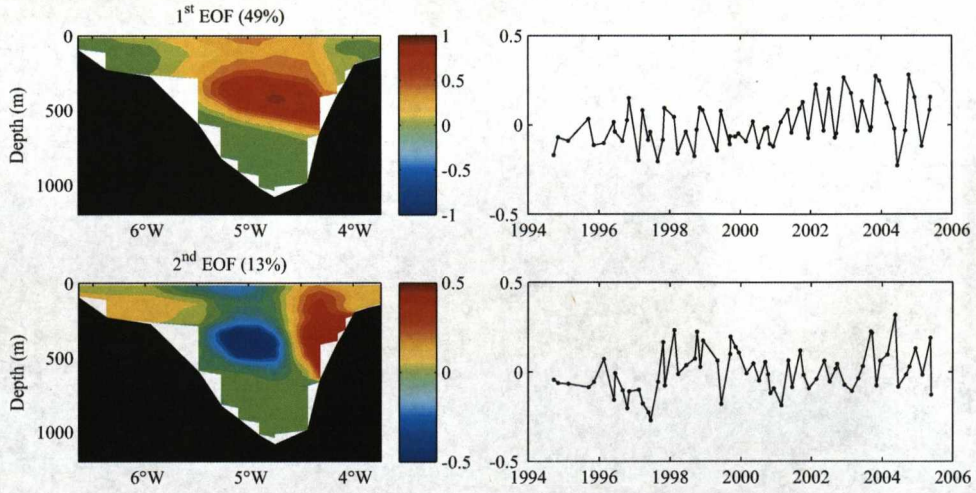

Figure 2.6: First two empirical orthogonal functions of salinity. The panels on the left show the spatial variability; the panels on the right show the temporal variability.

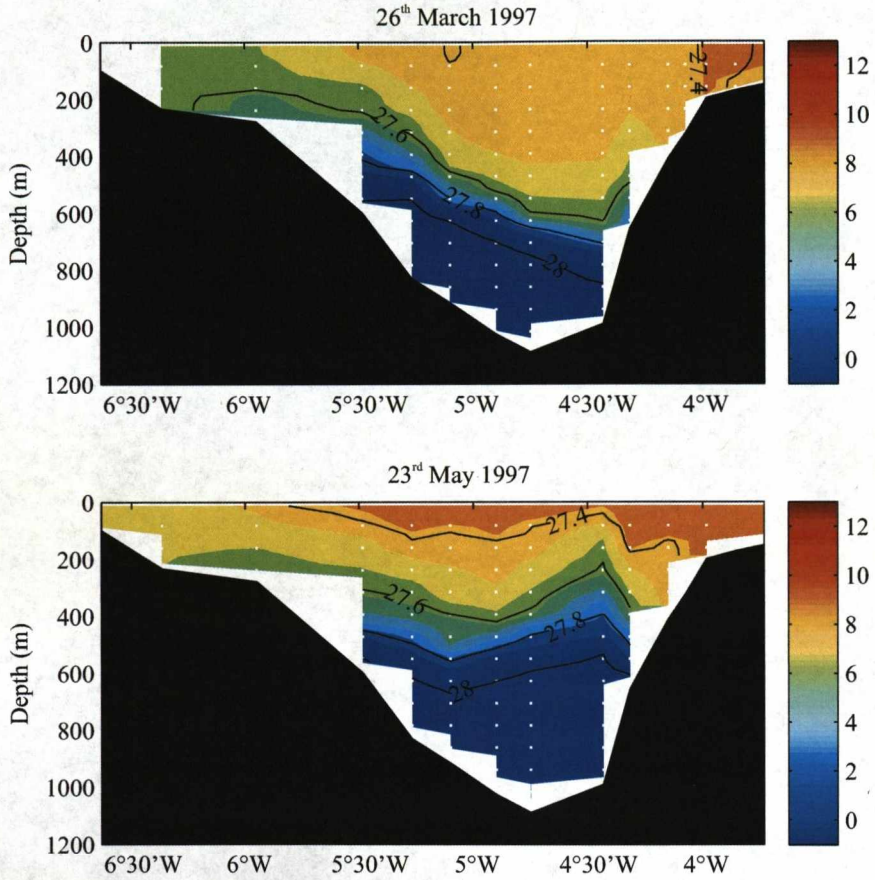

Figure 2.7: Examples of the variable distribution of potential temperature (°C) in the Faroe-Shetland Channel. The black lines are contours of σ_θ.

between two successive occupations of the same station is 5°C, occurring when the occupations are only two days apart.

2.4.1 Thermistor moorings

A better estimate of the time-scale of pycnocline variability comes from the four thermistors fixed to the ADCP moorings. They provide hourly temperature time series for the period September 1994 to May 2005, although there are gaps in the time series during mooring redeployment and due to instrument failure. Thermistor B is located at $\sim$ 675 m over the lower Faroe slope, below the pycnocline. Thermistor C is located at $\sim$ 655 m over the axis of channel, typically at the base of the pycnocline. Thermistor D is moored at a variety of depths between 630 and 820 m over the lower West Shetland slope. For the majority of the time series it is located at $\sim$ 790 m, below the the pycnocline; however, for the first four years it is moored in the pycnocline, $\sim$ 640 m. Thermistor E is located at $\sim$ 440 m on the upper West Shetland slope, at the top of the pycnocline.

The thermistors are uncalibrated, so where possible the thermistor temperatures are compared to CTD temperatures to validate the time series. For each thermistor and section occupation, CTD temperature from the nearest cast is linearly interpolated onto the depth of the thermistor and correlated with the thermistor temperature at the time of the occupation. Of the four time series, thermistor C best matches the CTD temperatures with a root mean square (rms) random error of < 0.3°C over a range of 4°C (Fig. 2.8). Thermistors D and E have larger random errors of 0.9 and 0.6°C respectively. Thermistor B is the only time series with a systematic error, recording temperature on average 0.3°C cooler than CTD temperature. As it is the temperature variability, not the absolute temperate, that is of concern here, the systematic error is not an issue.

The vertical displacement of isotherms (ξ) is related to the temperature change (ΔT) by $\xi = -\Delta T(dT/dz)^{-1}$, where dT/dz is the background vertical temperature gradient. As the vertical gradient cannot be inferred from single thermistors, it must be calculated from CTD casts. The most rapid temperature changes are likely to occur when a thermistor is located near the temperature gradient maximum in the centre of the pycnocline. This may be by design (i.e. the first four years of the time series from thermistor D), or because the pycnocline is temporarily displaced vertically so that thermistors typically located at the base or the top of the thermocline are actually in the centre (i.e. thermistors C and E). Therefore, the relevant vertical temperature gradient for the assessment of maximum isotherm displacement from these thermistors is the gradient at the centre

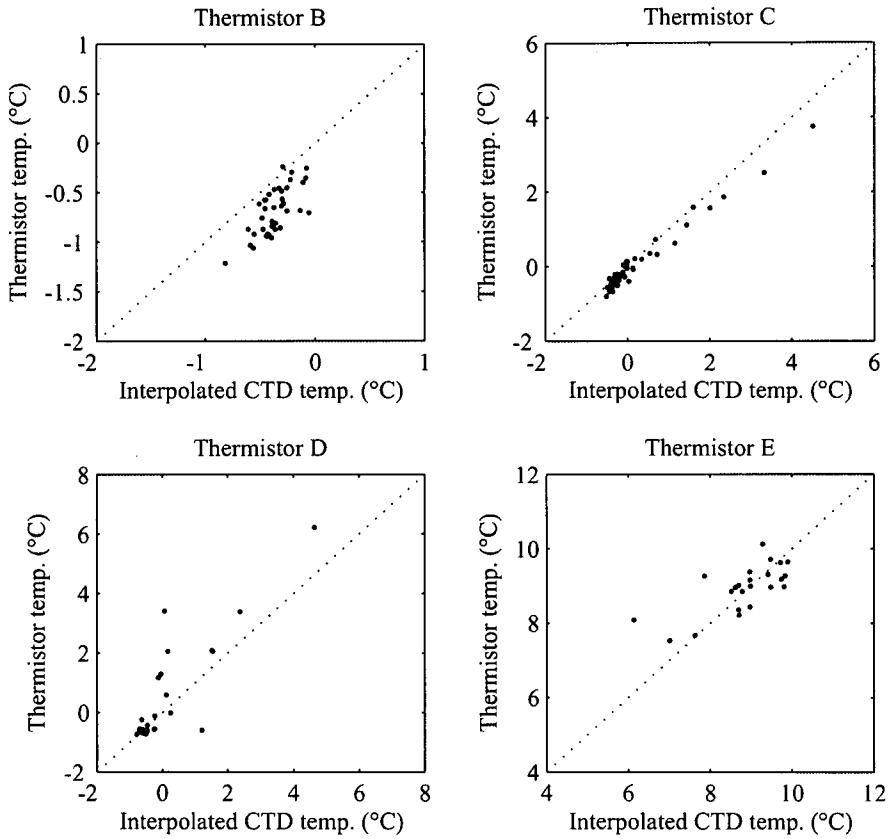

Figure 2.8: Correlations between thermistor temperature and interpolated CTD temperature.

of the pycnocline, $\sim 0.025°C\ m^{-1}$. For thermistors permanently below the pycnocline (i.e. thermistor B and the majority of the time series from thermistor D), the vertical temperature gradient is lower, $\sim 0.01°C\ m^{-1}$.

High frequency variability was removed from the time series by FRS with 72-hour low-pass filter, but the variability at lower frequencies contains rates of temperature change comparable to those observed between the Overflow '73 occupations (Fig. 2.9). The most complete time series is from thermistor C and contains temperature changes up to 5°C, equivalent to a 200 m vertical isotherm displacement, occurring within a week. The time series from thermistor D contains faster rates of temperature change (up to 7°C or 280 m within a week) although the magnitude of the temperature variability depends on the depth at which it is moored. The most rapid temperature changes occur when moored at a depth of ~ 640 m, although for the majority of time series it is located at ~ 790 m, where rates of temperature change are typically of the order of 1°C (100 m) within three or four days.

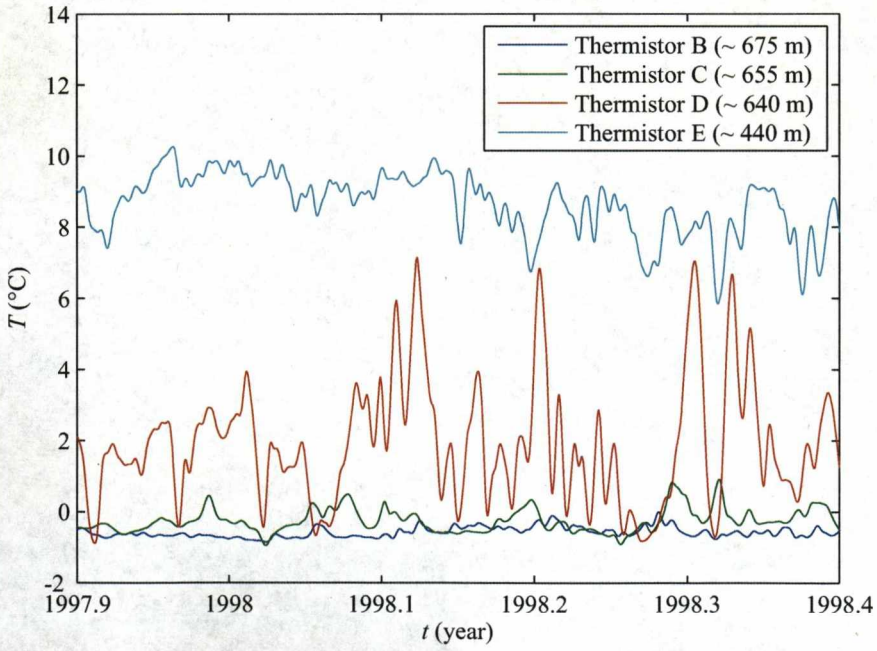

Figure 2.9: A six month example of temperature from the four thermistors time series.

To investigate the variability at different frequencies in more detail, the power spectra[1] of each thermistor time series is calculated using Welch's periodogram (see Chapter 3 for details) with a 2-year Hanning window and 1-year overlap; this method resolves frequencies ≥ 0.5 cycles per year. The power spectral density (PSD) from each thermistor is then normalised by the PSD integrated through all frequencies (Fig. 2.10). All four time series contain contain strong annual cycles (0.003 cpd) and other variance maxima with periods longer than one month (< 0.033 cpd) although there are no other coherent signals between all four time series. The is a reasonably coherent peak at approximately 0.015 cpd (2 month period) in the time series from thermistors C and D. Time series C also contains a variance maximum at 0.006 cpd (6 month period) that is of a comparable magnitude to the annual cycle; time series B contains a variance peak at at 0.008 cpd (4 month period).

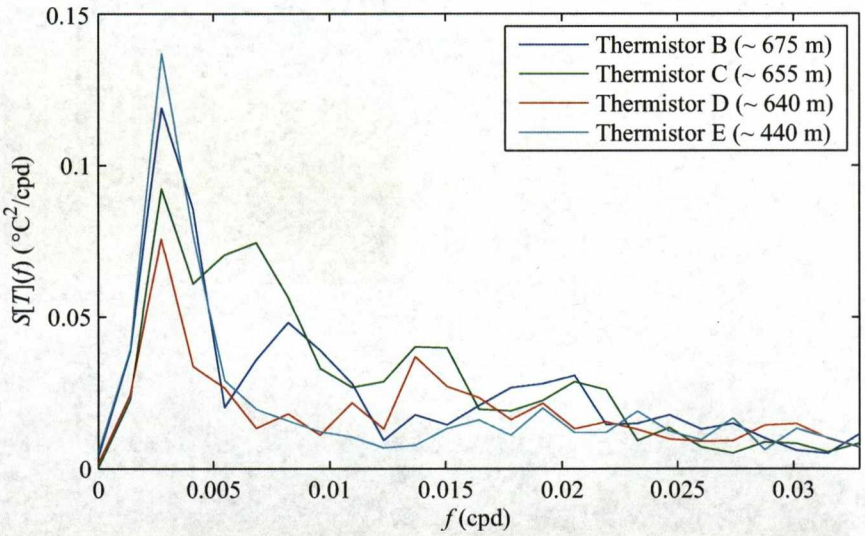

Figure 2.10: Normalised power spectra of temperature from the four thermistors time series.

There is little correlation between the four thermistor time series suggesting the temperature changes are not simply the result of horizontally uniform

[1]Throughout this thesis the notation $S[y](x)$ denotes the power spectra of y as a function of x.

isotherm displacement but also reflect changes in the slope of the pycnocline and the distance between isotherms.

2.4.2 Pycnocline parameters

To assess changes in the structure and position of the pycnocline on time-scales longer than a year, three pycnocline parameters were calculated from each CTD section for the whole 1973 to 2005 period:

1. Pycnocline depth: the mean depth of the 6°C isotherm.
2. Pycnocline slope: the slope of the 6°C isotherm from linear least-squares regression.
3. Pycnocline thickness: the mean vertical distance between the 6°C and 2°C isotherms.

The temporal sampling is sparse when compared to the frequency of the variability previously observed so there is a lot of noise in the parameter time series from undersampling. Some of the noise is the result of random sampling of the seasonal cycle and is removed by fitting sinusoids with 1-year periods to each time series using the model

$$x(t) = \overline{x} + A\cos(2\pi t) + B\sin(2\pi t) + x_r(t), \tag{2.1}$$

where $x(t)$ is the variable, t is the year day of the section occupation as a decimal between 0 and 1, $\overline{x}$ is the time-average constant, and $x_r(t)$ is the residual with zero time-mean. The constants $\overline{x}$, A, and B are found by linear least-squares regression and if the fit is statistically significant at the 95% confidence limit the sinusoids are removed from the time series so that $x(t) = \overline{x} + x_r(t)$. Equation (2.1) can be rewritten

$$x(t) = \overline{x} + x_0\cos(2\pi t - \phi) + x_r(t), \tag{2.2}$$

where $x_0 = (A^2 + B^2)^{1/2}$ is the amplitude of the fitted cycle and $\phi = \tan^{-1}(B/A)$ is the phase lag. To determine if there are any decadal time-scale changes in the pycnocline parameters, a trend is fit to each time series using a linear least-squares regression and is considered real if statistically significant at the 95% confidence limit.

Both pycnocline depth and thickness contain a seasonal cycle although the spread of values about the fitted sinusoid is large in both cases. Pycnocline depth has an amplitude of 40.6 m and is deepest in January (Fig. 2.11 upper

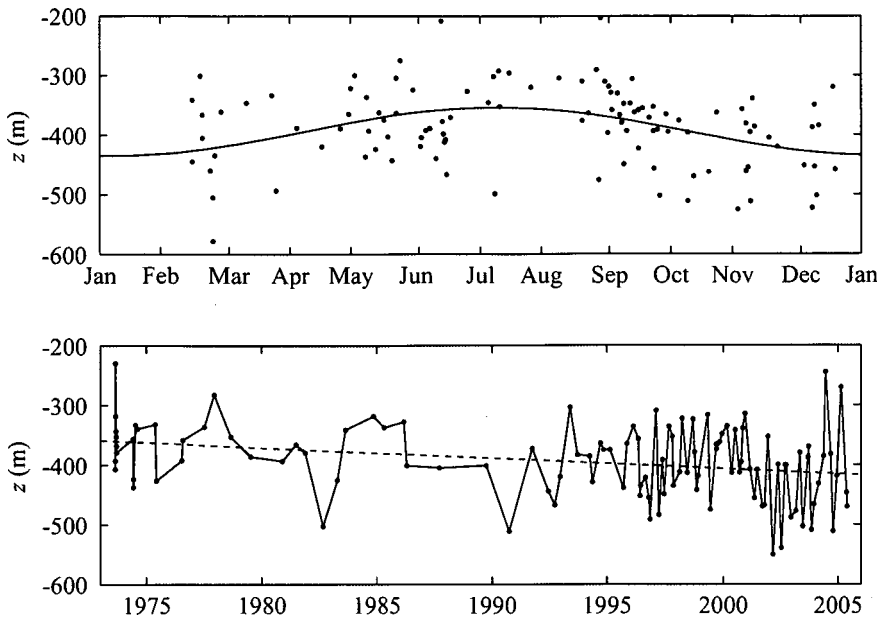

Figure 2.11: Depth of the 6°C isotherm by month and by year. The solid line in the upper panel is the seasonal cycle; the dashed line in the lower panel is the trend.

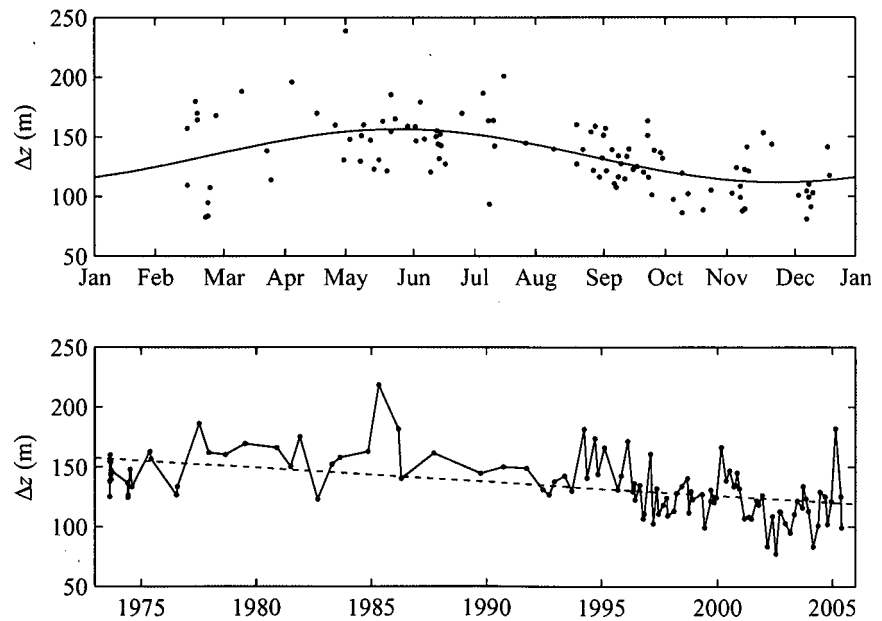

Figure 2.12: Vertical distance between the 6°C and 2°C isotherms by month and by year. The solid line in the upper panel is the seasonal cycle; the dashed line in the lower panel is the trend.

panel). Pycnocline thickness has a amplitude of 22.3 m and is thickest in May (Fig. 2.12 upper panel). There is no significant seasonal cycle in the time series of pycnocline slope (not shown).

Between 1997 and 2005, pycnocline depth and thickness contain shallowing and thickening trends separated by a period of deepening and thinning in 2000/2001. This suggests a decadal period oscillation, but occupations before 1995 are too infrequent to allow an oscillation of this period to be resolved. The pycnocline is consistently thicker than the time-average ($\sim$ 135 m) between 1977 and 1992. However, due to the infrequency of occupations during this 15-year period, and a bias towards summer and autumn occupation, there may still be some aliasing with the seasonal cycle.

The pycnocline depth time series contains a deepening trend of 17.7 m per decade for the 1973 to 2005 period (Fig. 2.11 lower panel) while the pycnocline thickness time series contains a thinning trend of 11.7 m per decade (Fig. 2.12 lower panel). There is no significant trend in the time series of pycnocline slope (not shown). A summary of the seasonal cycles and decadal time-scale trends is shown in Table 2.2.

Parameter	Seasonal cycle		Decadal change
	Amplitude	Maximum	
Pycnocline depth	40.6 m	January	-17.7 m
Pycnocline slope	-	-	-
Pycnocline thickness	22.3 m	May	-11.7 m

Table 2.2: Summary of the seasonal cycles and trends of pycnocline parameters.

2.4.3 Pycnocline slope and sea surface height

To investigate a potential cause of the pycnocline slope variability, the slope of the pycnocline is compared with the slope of the sea surface. Approximating the watercolumn as two layers of uniform density, a relationship between the slope of the sea surface ($d\eta/dx$) and the slope of the interface (dh/dx where h is the position of the interface) can be made by equating the barotropic and baroclinic

geostrophic equations and assuming the lower layer is at rest,

$$v = \frac{g}{f}\frac{d\eta}{dx} = -\frac{g'}{f}\frac{dh}{dx}, \tag{2.3}$$

where v is along channel velocity in the upper layer, f is the Coriolis frequency, and g' is the reduced gravity at the interface. Equation (2.3) can be rearranged and reduced gravity substituted in, $g' = g(\rho_2 - \rho_1)/\rho_2$, where ρ_1 and ρ_2 are the densities of the upper and lower layers, giving

$$\frac{d\eta}{dx} = -\frac{(\rho_2 - \rho_1)}{\rho_2}\frac{dh}{dx}. \tag{2.4}$$

Taking the density of the upper and lower layers as the mean density above and below the 6°C isotherm, $\rho_1 = 1027.36$ kg m^{-3} and $\rho_2 = 1027.92$ kg m^{-3}, therefore the ratio between the slope of sea surface and the slope of the pycnocline is 5.4×10^{-4}.

To determine if the slope of the pycnocline fits geostrophic theory, the slope of the sea surface at the time of the section occupations is required. Here the sea surface height anomaly (SSHA) measured by satellite altimeters[2] is used and the slope of the SSHA across the section calculated by least-squares linear regression. This is compared to the slope of the 6°C isotherm with the time-mean slope removed because only time-varying flows can be resolved from SSHA measurements (Fig. 2.13). Typical amplitudes of SSHA slope are around 2000 times smaller than the amplitude of thermocline slope, the right order of magnitude when compared to geostrophy; however, the phase relationship between the time series is not clear given the different (and varying) sampling frequencies.

The correlation between the slope of SSHA across the section at the times of occupation and the slope of the 6°C isotherm is shown in Figure 2.14. Despite the large scatter there is a rough negative correlation; least-squares linear regression through the data points, with the slope of the 6°C isotherm as the response, has a gradient of -1.8×10^3 ($R^2 = 0.21$). The gradient predicted by geostrophy is also -1.8×10^3, suggesting geostrophic theory for a two-layer watercolumn approximation can account for a small part of the observed pycnocline variability.

Potential mechanisms for this correlation are mesoscale meanders and eddies in the front between NAW and MNAW. These features have been observed in satellite SST images and in-situ data by Sherwin et al. (1999), who suggest that

[2]A gridded sea surface height data product is used, combining altimetry tracks from ERS1, Topex/Posidon, Jason, and Envisat. The anomaly is the difference from the 1992-1997 average. All standard corrections are applied including an inverse barometer correction and a tide model. The data were provided by Chris Hughes (POL).

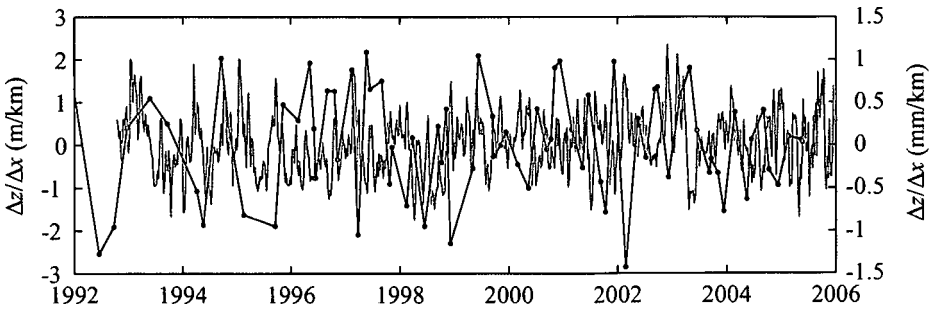

Figure 2.13: Slope of the 6°C isotherm (black, left axis) and slope of the sea surface height anomaly (grey, right axis). In both cases a positive slope is up towards to the southeast.

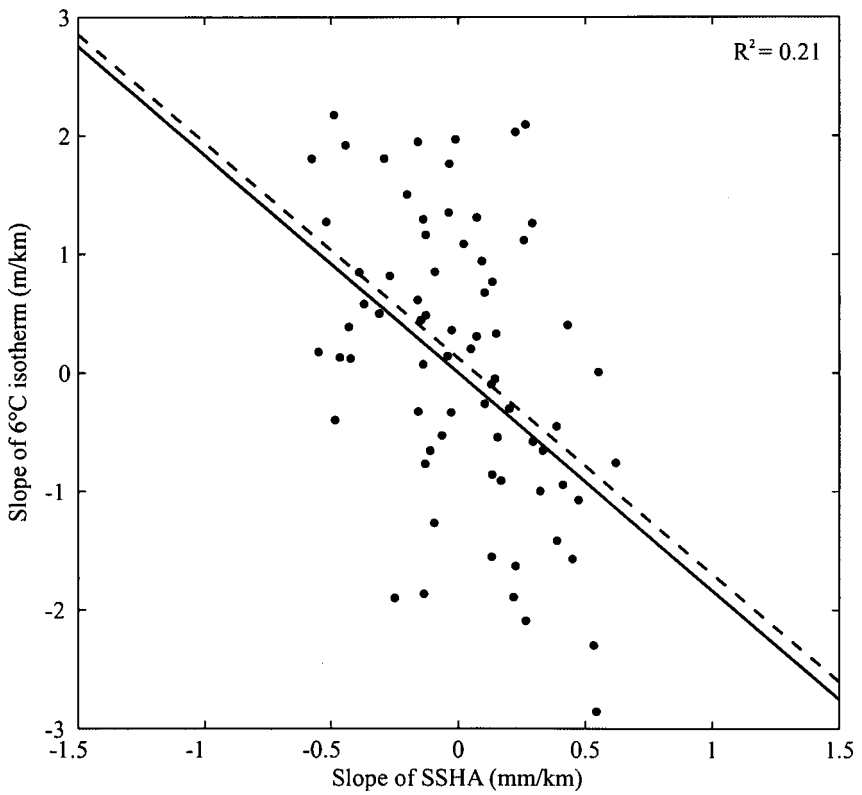

Figure 2.14: Correlation between the slope of the 6°C isotherm (pycnocline slope) and slope of the sea surface height anomaly. The dashed line is a least-squares linear regression. The solid line is the relationship predicted by geostrophy.

movements of the surface waters coincide with considerable movement of deeper water masses. Sherwin et al. (2006) identify peaks in eddy kinetic energy along the shelf slope from satellite altimetry data that coincide with stationary anti-cyclonic meanders in the slope current (one close to the Fair Isle-Munken line). They use the baroclinic instability model (Mysak and Schott, 1977) to explain why the meanders do not propagate along the slope, and suggest that cyclonic eddies are formed as the meanders decay, helping to mix NAW and MNAW.

2.5 Water mass changes

Changes in the properties of deep and intermediate water masses in the Faroe-Shetland Channel have previously been reported by Turrell et al. (1999). The proportion of NSDW in the composition of FSCBW has decreased due to a reduction in the formation of deep water in the Greenland Sea and Iceland Sea central gyres, leading to a decrease in the salinity of FSCBW by 0.01 psu per decade since the mid 1970s. The salinity of NSAIW has also decreased, by 0.02 psu per decade, due to changes in atmospheric forcing leading to an increased influx of fresh Arctic water into the Nordic Seas.

2.5.1 Salinity maximum

An increase in the temperature and salinity of NAW in the slope current is noted by Hughes et al. (2006a) from the FRS dataset (1994 to 2005), but no values are quoted for the trends. They identify NAW as the salinity maximum over the West Shetland slope from each section occupation and find significant seasonal cycles in both potential temperature and salinity; temperature has an amplitude and 0.5°C and is highest in September; salinity has an amplitude of 0.02 psu and is highest in August.

Using the same identification method and dataset, seasonal cycles in the potential temperature and salinity of NAW are found here that as expected are in agreement with Hughes et al. Significant trends of 0.07 psu and 0.4°C per decade are identified after the seasonal cycles are removed (Fig. 2.15); inter-annual variability in salinity, with possible 6-year periodicy, is also apparent. Hughes et al. also find the depth of the NAW core varies seasonally, reaching a maximum around October, but its position over the shelf break remains constant. Change in the heat and salt flux of NAW is dominated by a decrease in the volume flux of 0.6 Sv per decade.

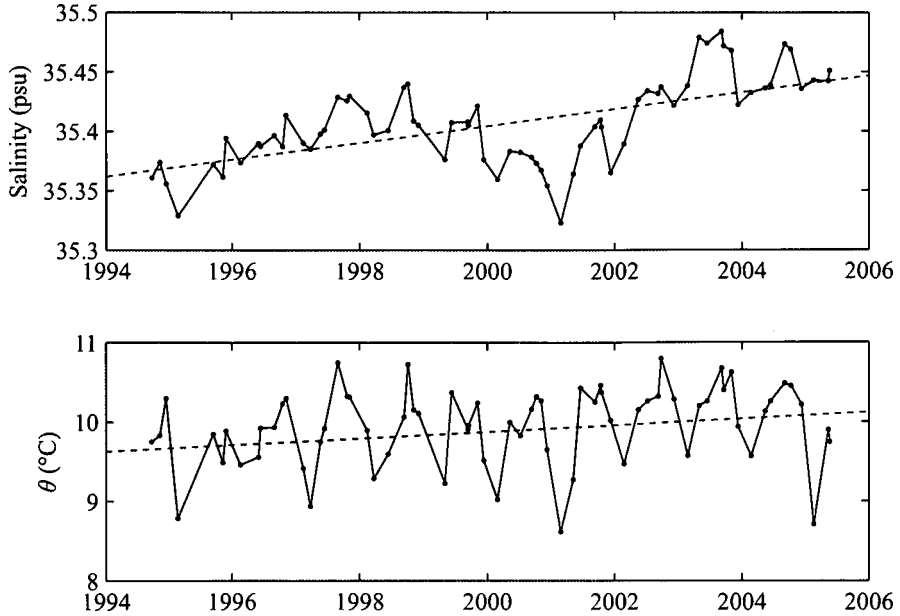

Figure 2.15: Salinity and potential temperature at the salinity maximum over the West Shetland slope. The dashed lines are the trends.

The variation in the properties of NAW can be observed in θ-S profiles from different years (Fig. 2.17). The salinity maximum is noticeably more saline in 2003 than the other years shown.

2.5.2 Salinity minimum

Following the work of Hughes et al., the method of water mass identification is applied to NSAIW at the salinity minimum over the channel axis. For the majority of the 1994 to 2005 period the salinity minimum is relatively constant, between 34.88 and 34.9 psu. However, in 1997 the salinity decreases to between 34.81 and 34.87 psu (Fig. 2.16 upper panel). As there are 7 section occupations during 1997, by both FRS and FML, it is unlikely to be instrument or sampling error. In 1998 and 1999 there are four more occupations with salinity minimums < 34.88 psu. The potential temperature at the salinity minimum is also relatively constant (~ 0°C) for the majority of the 1994 to 2005 period, but warmer than 1°C when the salinity is anomalously low and therefore not density compensating (Fig. 2.16 lower panel). Between 2000 and 2005 there are significant trends of $+0.003$ psu and -0.1°C per year in the salinity and temperature of NSAIW, contrary to the freshening trend observed by Turrell et al. (1999).

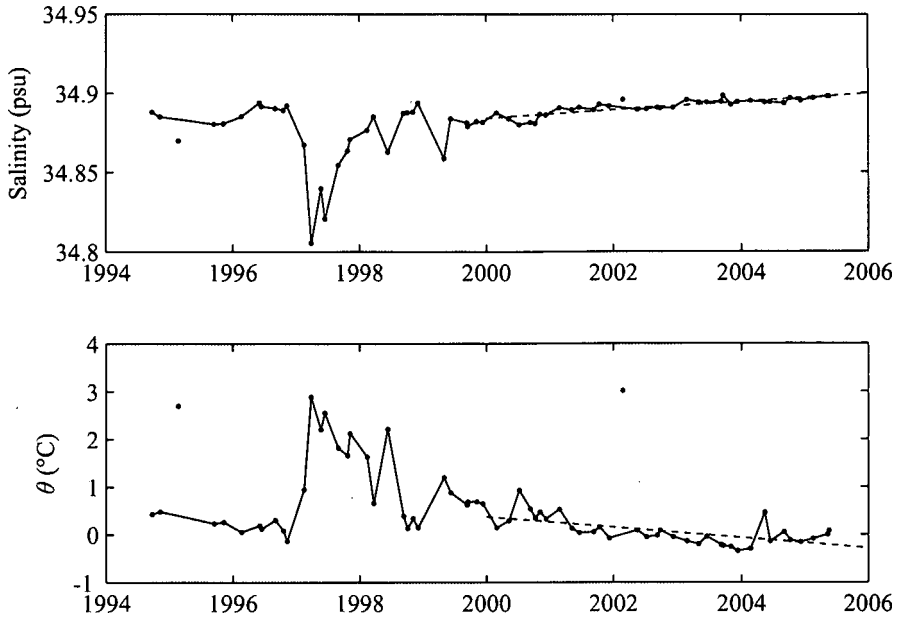

Figure 2.16: Salinity and potential temperature at the salinity minimum over the axis of the Faroe-Shetland Channel. The dashed lines are the trends.

The θ-S profile from 1997 contains a lot of scatter, particularly around the salinity minimum, when compared to other years (Fig. 2.17). As the salinity minimum is ~ 2°C warmer in 1997, the minimum appears to be associated with unusually fresh AI/NIW. In other years, for example 1996 and 2003, AI/NIW is typically warmer and more saline so there is a defined salinity minimum at 0°C associated with NSAIW. A noticeable feature of all the θ-S profiles is increased scatter around the region of AI/NIW when compared to MNAW and NSAIW above and below. This 'looseness' in the profiles is the result of variation in the composition of AI/NIW in the channel.

2.6 Heat and salt content

Changes in the heat and salt content of the waters in the channel are calculated to assess possible changes to the heat and salt flux between the North Atlantic and Norwegian Sea. Only the seasonal cycles and long-term trends are of interest here so heat (E_h) and salt (M_s) content anomalies are calculated using anomalies of temperature and salinity[3] from time-average values, $T'(x,z,t) = T(x,z,t) -$

[3]In this calculation salinity in psu is assumed equal to grams of salt per kilogram.

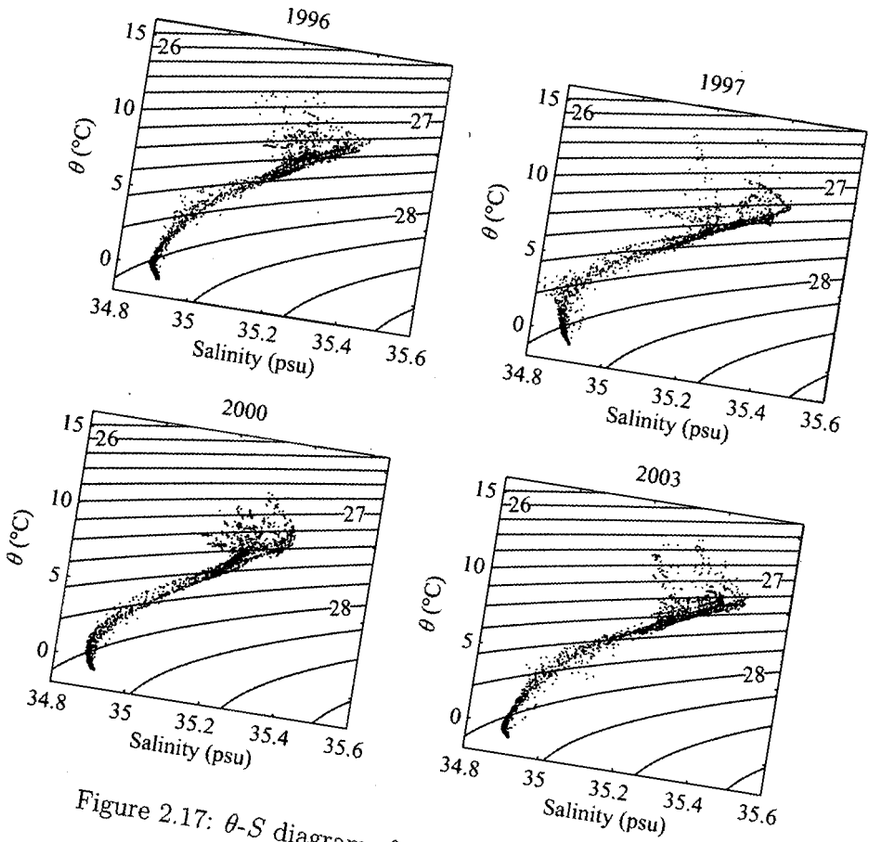

Figure 2.17: θ-S diagrams for four different years.

$\overline{T}(x,z)$ and $S'(x,z,t) = S(x,z,t) - \overline{S}(x,z)$, then integrated through the depth of the watercolumn (H) and across the width of the channel (L),

$$E_h = \int_L^0 \int_{-H}^0 \rho C_P T' \, dx \, dz, \tag{2.5}$$

$$M_s = \int_L^0 \int_{-H}^0 \rho S' \, dx \, dz, \tag{2.6}$$

where ρ is the density and C_P is the specific heat capacity of seawater, a function of temperature, salinity and pressure. As with the pycnocline parameters, the seasonal cycle is fit to the time series and removed if statistically significant, then a trend fit.

The integrated heat content contains a seasonal cycle with an amplitude of 1.6×10^{14} J m^{-1} and maximum in November (Fig. 2.18 upper panel). This is equivalent to a mean temperature change of 0.36°C. There is no significant seasonal cycle in the integrated salt content (not shown). The heat and salt contents have increased by 8.4×10^{13} J m^{-1} and 1.9×10^6 kg m^{-1} per decade during the 1973 to 2005 period (Fig. 2.18 lower panel and Fig. 2.19), the result of an 0.06°C and 0.01 psu per decade increase in the mean temperature and salinity of the waters in the channel. However, between 1995 and 2005 the salt content increased at a higher rate than the previous 20 years, 8.5×10^6 kg m^{-1} per decade. The high salt content in the 1980s and early 1990s is probably a real signal; as the salt content is low in spring and summer when most occupations occur, any aliasing with the seasonal cycle will tend to decrease the salt content. A summary of the seasonal cycles and decadal time-scale trends is shown in Table 2.3.

Property	Seasonal cycle		Decadal change
	Amplitude	Maximum	
Mean temperature	0.36°C	November	+0.06°C
Heat content	1.64×10^{14} J m^{-1}		$+8.44 \times 10^{13}$ J m^{-1}
Mean salinity	-	-	+0.01 psu
Salt content	-		$+1.94 \times 10^6$ kg m^{-1}

Table 2.3: Summary of the seasonal cycles and trends in mean temperature and salinity, and integrated heat and salt content.

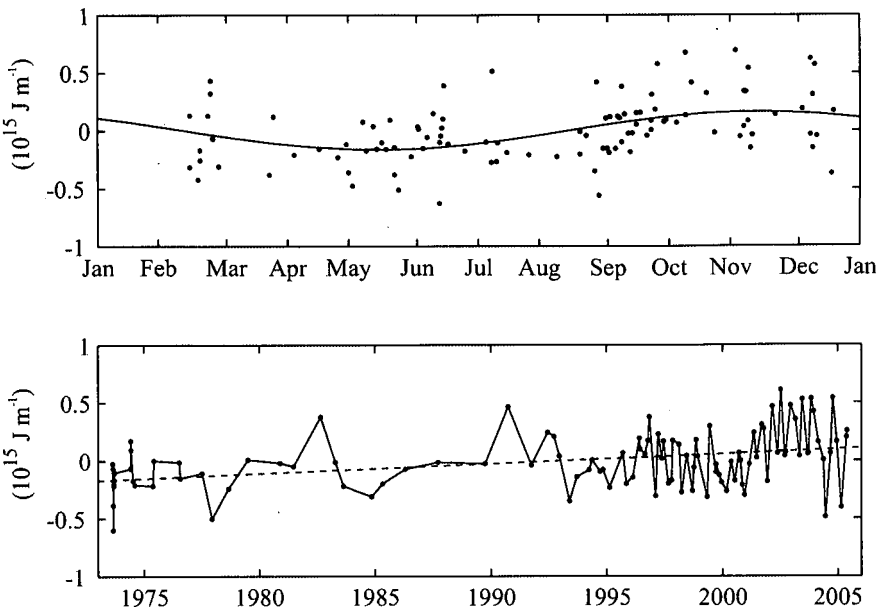

Figure 2.18: Integrated heat content anomalies by month and year. The solid line in the upper panel is the seasonal cycle; the dashed line in the lower panel is the trend.

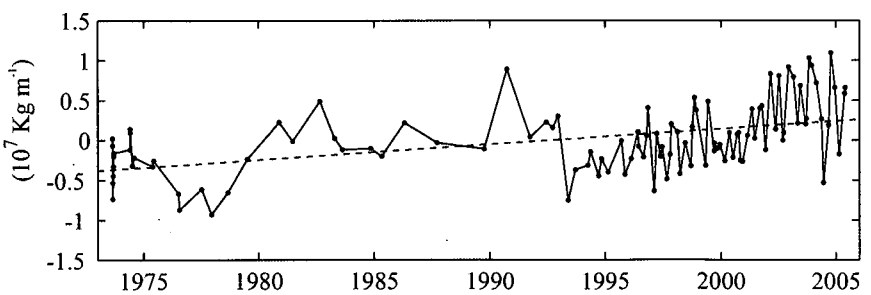

Figure 2.19: Integrated salt content anomalies by year. The dashed line is the trend.

2.7 Summary

The temperature and salinity structure of the Faroe-Shetland Channel changes on day-to-week to decadal time-scales, identified from a 32-year time series (1973 to 2005) of temperature and salinity data from a historic section across the channel. In the surface layer there is a strong seasonal cycle; surface heating in spring and summer leads to the formation of a seasonal thermocline in the upper 200 m that is eroded by wind mixing in autumn and winter. Surface salinity is lowest during the summer months with a subsurface salinity maximum at around 100 m.

The position of the main pycnocline changes on day-to-week time-scales; temperature changes of the order 5°C within a week are observed at fixed levels within the pycnocline, equivalent to vertical isotherm displacements of the order 200 m. There is little correlation between temperature at different locations across the channel suggesting the displacement of isotherms in the pycnocline is not horizontally uniform. Both the depth and thickness of the pycnocline contain a seasonal cycle; pycnocline depth varies by $\sim$ 80 m and is deepest in January; pycnocline thickness varies by around $\sim$ 45 m and is thickest in May. Over the whole 32-year period there is a deepening trend of 17.7 m per decade and thinning trend of 11.7 m per decade. There is no significant seasonal cycle or decadal time-scale trend in pycnocline slope but there is a rough negative correlation between the slope of the pycnocline and the slope of the sea surface, measured by satellite altimeters. Linear least squares regression suggest a relationship that matches geostrophic theory for a two-layer watercolumn approximation but only accounts for 21% of the variance.

There is a increase in the salinity and temperature of NAW in the slope current of 0.07 psu and 0.4°C per decade for the period 1994 to 2005. The salinity of NSAIW decreases by around 0.05 psu in 1997, accompanied by a temperature increase of around 2°C. Between 2000 and 2005 there are trends of +0.003 psu and −0.1°C per year in the salinity and temperature of NSAIW.

The integrated heat content of the waters in the channel contains a seasonal cycle, maximum in November, and a trend of $+8.4 \times 10^{13}$ J m^{-1} per decade over the whole 32-year period, the result of an 0.06°C per decade increase in the mean temperature. The integrated salt content does not contain a significant seasonal cycle but does increase by 1.9×10^{6} kg m^{-1} per decade, the result of an 0.01 psu per decade increase in the mean salinity of the waters in the channel.

With this understanding of the rapid time-scales on which the structure and position of the main pycnocline changes, in the next chapter observations of

internal waves in the pycnocline, made during a slope mixing experiment on the West Shetland slope, are described.

Chapter 3

Slope mixing experiment: *F. S. Poseidon*, cruise 328

3.1 Introduction

Internal waves are suspected to play an important role in supporting turbulent mixing on continental shelf slopes worldwide. In September 2005 a slope mixing experiment was undertaken to make measurements of internal waves, their induced mixing, and bottom boundary layer structure on the shelf slope north of Scotland. Instruments were deployed from *F. S. Poseidon* during cruise 328, from Torshavn in the Faroe Islands to Aberdeen on the east coast of Scotland, between 6^{th} and 25^{th} September.

Four Acoustic Doppler Current Profilers (ADCP), three thermistor moorings, and three specialist instrument packages were deployed on the West Shetland slope, about the 600 m isobath, for twelve days. Full-depth CTD (Conductivity Temperature Depth) and lowered ADCP profiles were recorded hourly at a station adjacent to the moorings, over the 680 m isobath, for 24 hours during the deployment. To ascertain the background hydrography, three full-depth lowered ADCP/CTD sections across the Faroe-Shetland Channel were carried out.

This chapter contains summaries of the instruments deployed during the experiment and initial analysis of the data collected, including observations of internal waves. This analysis forms a basis upon which detailed analyses of mixing rates and internal wave energy fluxes are undertaken in later chapters. The lowered ADCP/CTD profiles from the across-channel sections and the 24-hour repeat station are described in Section 3.2. The mooring time series are described in Section 3.3. Frequency spectra and harmonic tidal analysis of the time series data are shown in Section 3.4. The vertical structure of the internal tide is shown in Section 3.5 and compared with inferred vertical structure modes. A short discus-

sion follows in Section 3.6. Full details of the instrumentation can be found in the cruise report (Huthnance, 2005).

3.2 CTD and lowered ADCP profiles

In total, 105 profiles were recorded with a CTD and lowered ADCP between the 6th and 17th September. They include three sections across the Faroe-Shetland Channel comprising of 17 to 25 profiles each and 25 profiles from a 24-hour repeat station over the West Shetland slope (Fig. 3.1). The first across-channel section was centred on the mooring array (from here on referred to as the Central section), the second to the southwest near the bend in the channel (Southern section), and the third to the northeast (Northern section). The repeat station was located slightly down-slope from the mooring array. The locations and dates of the sections and repeat station are shown in Table B.1.

Profiles were also recorded before each mooring deployment as a matter of routine and an along-channel survey following the 700 m isobath between the Northern and Southern sections was started but aborted after six casts due to bad weather. These profiles are not included in this analysis.

3.2.1 Instrument package and data processing

All casts were made with a SeaBird Electronics (SBE) 911plus CTD, combined with a Paroscientific Digiquartz pressure sensor, SBE 3plus temperature sensor, SBE 4 conductivity sensor, and a SBE Beckmann/YSI oxygen sensor. These were mounted on a 12-bottle rosette frame fitted with a SBE 32 carousel water sampler and twelve, 10-litre OTE bottles. The sampling frequency of all the sensors was 24 Hz. During the course of the cruise, 68 in-situ water samples were taken from the rosette bottles and used to calibrate the salinity data from the CTD. An RD Instruments (RDI) 300 kHz lowered ADCP was mounted on the frame facing downward. The majority of casts profiled the entire water column, to within 4 m of the seabed. The CTD data were processed in 1 m vertical bins using standard SBE software. Potential temperature and potential density were calculated using UNESCO 1983 algorithms; depth was calculated from pressure using the algorithm of Saunders (1981). The lowered ADCP data were used to generate profiles of horizontal current velocity in 4 m vertical bins using standard processing techniques[1]. The oxygen data are not included in this analysis.

[1]The lowered ADCP data were processed by Mark Inall (SAMS) using code provided by Martin Visbeck (IFM-GEOMAR).

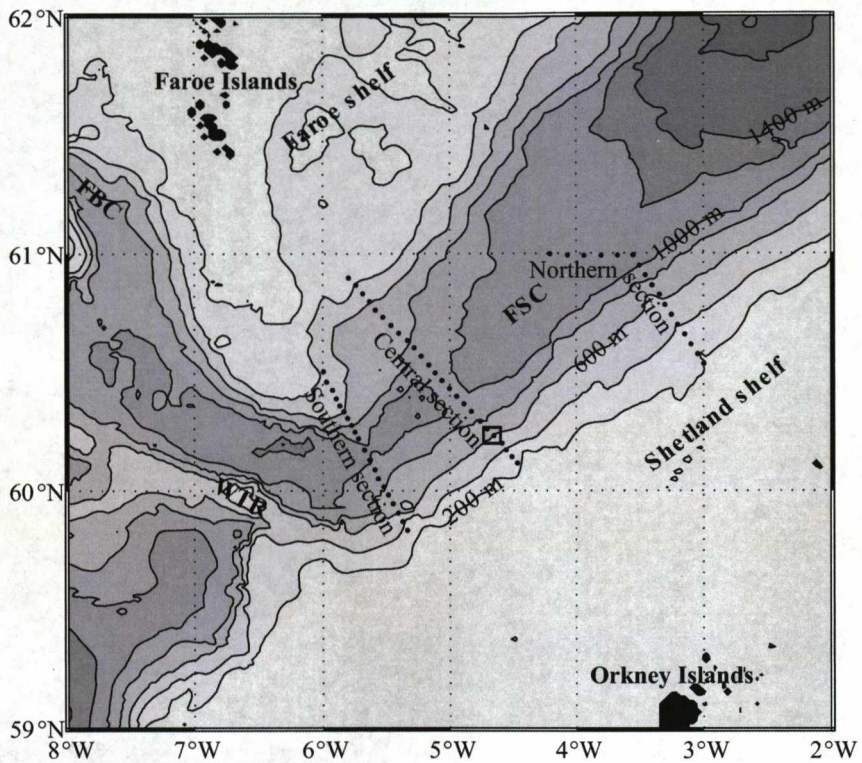

Figure 3.1: Location of the lowered ADCP/CTD casts in the three sections across the Faroe-Shetland Channel made during *F. S. Poseidon*, cruise 328. The square is the location of the moorings and repeat station shown in Figure 3.9. FSC is the Faroe-Shetland Channel; FBC is the Faroe Bank Channel; and WTR is the Wyville Thomson Ridge.

3.2.2 Across-channel sections

Potential temperature in the channel decreases with depth, the largest vertical gradients occurring in the main pycnocline between approximately 300 and 700 m (Fig. 3.2). Salinity is maximum at around 200 m over the West Shetland slope but otherwise also decreases with depth. Qualitatively, this is similar to the 32-year time-averages of temperature and salinity from the Fair Isle-Munken section, northeast of the Central section, shown in Chapter 2. The structure of the main pycnocline deviates from the time-average; in the two complete across-channel sections (Central and Southern) the pycnocline is deeper and thinner; the pycnocline slope, although also down towards the east, is larger over the Faroe slope than the West Shetland slope. However, when compared to the variability observed in the historic dataset, the depth and thickness of the pycnocline is not unusual. The mean depth of the 6°C isotherm (pycnocline depth in Chapter 2) over the West Shetland slope from the Central and Southern sections is 599 m, deeper than the mean from the historic data (432 m) but within three standard deviations. The mean vertical distance between the 6°C and 2°C isotherms (pycnocline thickness) is 83 m, thinner than the mean from the the historic data (132 m) but within two standard deviations.

Isopycnals below the 27.6 isopycnal slope up against the West Shetland slope while isopycnals above the 27.6 isopycnal continue to slope down towards the east, forming a wedge-shaped density field (Fig. 3.2 middle and lower panels). This 'pinching' of isopycnals has previously been observed in both the Faroe Bank Channel (Borenäs and Lundberg, 1988; Saunders, 1990; Borenäs et al., 2001) and the Faroe-Shetland Channel (van Aken and Eisma, 1987; Saunders, 1990).

In the Faroe Bank Channel the phenomenon is explained by Johnson and Sanford (1992) as an effect of secondary circulation in the deep outflow, created by an Ekman flow in the bottom boundary layer and at the interface, and mixing at the interface from shear instabilities. An alternative explanation is presented by Hogg (1983, 1985); conservation of potential vorticity in an inviscid, rotating, three-layer flow through a constriction may lead to a dynamical balance where the intermediate layer assumes a wedge shape. Borenäs et al. (2001) conclude that it is likely both processes play a role in maintaining the wedge-shaped stratification in the Faroe Bank Channel, however, in the Faroe-Shetland Channel the presence of intermediate water masses may favour the latter theory.

The main pycnocline in the Northern section is shallower, around 400 m, than in the Central and Southern sections ($\sim$ 600 m). The isopycnals slope slightly upwards towards the east over the centre of the channel and downwards over the

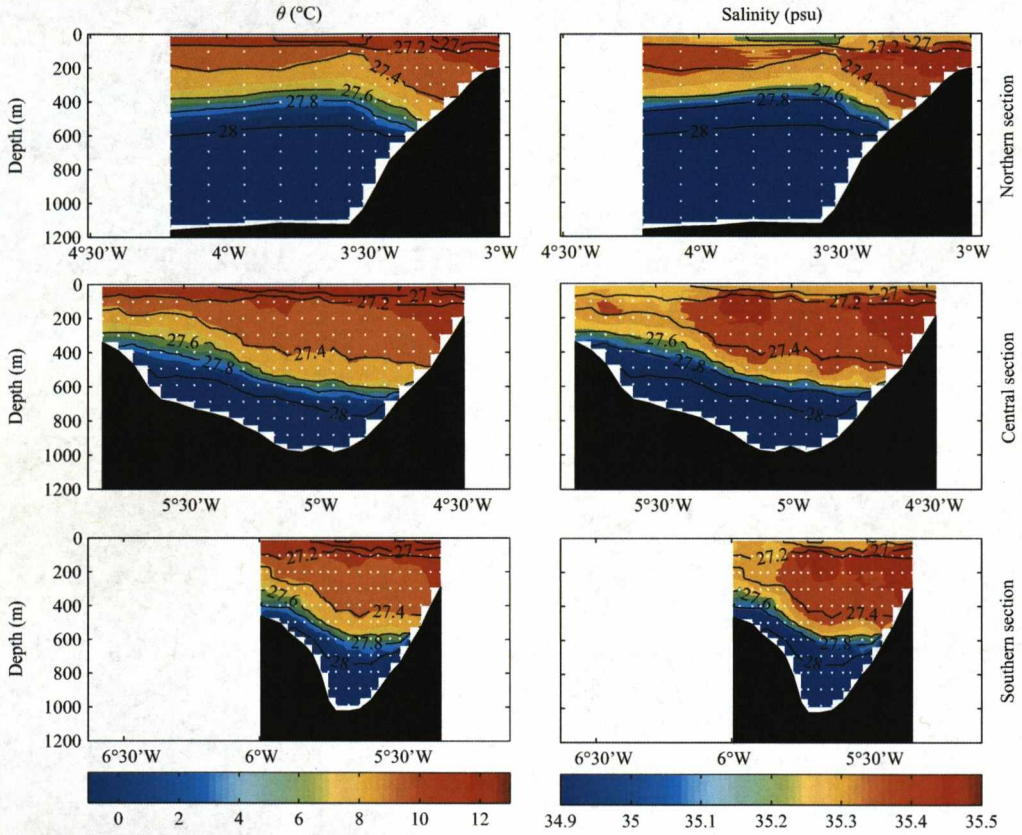

Figure 3.2: Potential temperature and salinity from the three across-channel sections. The black lines are contours of σ_θ.

West Shetland slope. The difference in the structure of the pycnocline may be an effect of either temporal or spatial variability as the Northern section was occupied over four days later than the Central and Southern sections. As described in Chapter 2, the depth of isotherms in the main pycnocline commonly change on time scales of the order 100 m in a few days. The Northern section is also further apart from the Central section than the Southern and Central sections, being approximately halfway between the Fair Isle-Munken line and another historical section, the Nolso-Flugga line (Turrell et al., 1999). The potential temperature structure in the Northern section is more comparable to sections from these historical lines, e.g. Sherwin et al. (1999), than the other sections shown here.

The core of high salinity NAW near the shelf break at the top of the West Shetland slope can clearly be identified. A second high salinity core, at around 200 m over the centre of the channel, is observed in both the Central and Southern sections; the result of a mesoscale eddy, possibly formed from instabilities in the slope current as discussed by Sherwin et al. (1999, 2006). The order 50 km horizontal length-scale of the eddy can be inferred from coincident satellite SST images (not shown).

In the upper 150 m a seasonal thermocline is present, as expected for late summer, with surface temperature typically increasing to the southeast and highest above the two high salinity cores. There is a surface salinity minimum in the Northern section above the shoaling main pycnocline. This may also be the result of mesoscale activity but there is no corresponding signature in near-surface temperature.

Buoyancy frequency squared (N^2) is calculated for each CTD profile (Fig. 3.3). In the main pycnocline and seasonal thermocline N^2 is up to 10^{-4} s^{-2}. Below the main pycnocline there is a mass of low buoyancy deep water ($N^2 \simeq 10^{-6}$ s^{-2}). The volume of this water mass is larger in the Northern section than the other two sections, suggesting, either there is an acceleration of deep water as it flows south, or there is deep recirculation to the northeast. In the Central and Southern sections there is a buoyancy minimum ($N^2 \simeq 5 \times 10^{-6}$ s^{-2}) between the main pycnocline and the seasonal thermocline over the centre of the channel and the West Shetland slope; over the upper Faroe shelf the watercolumn is more uniformly stratified with buoyancy frequencies of the order 10^{-5} s^{-2}. The volume of the upper buoyancy minimum is decreased in the Northern section, restricted to the upper West Shetland slope.

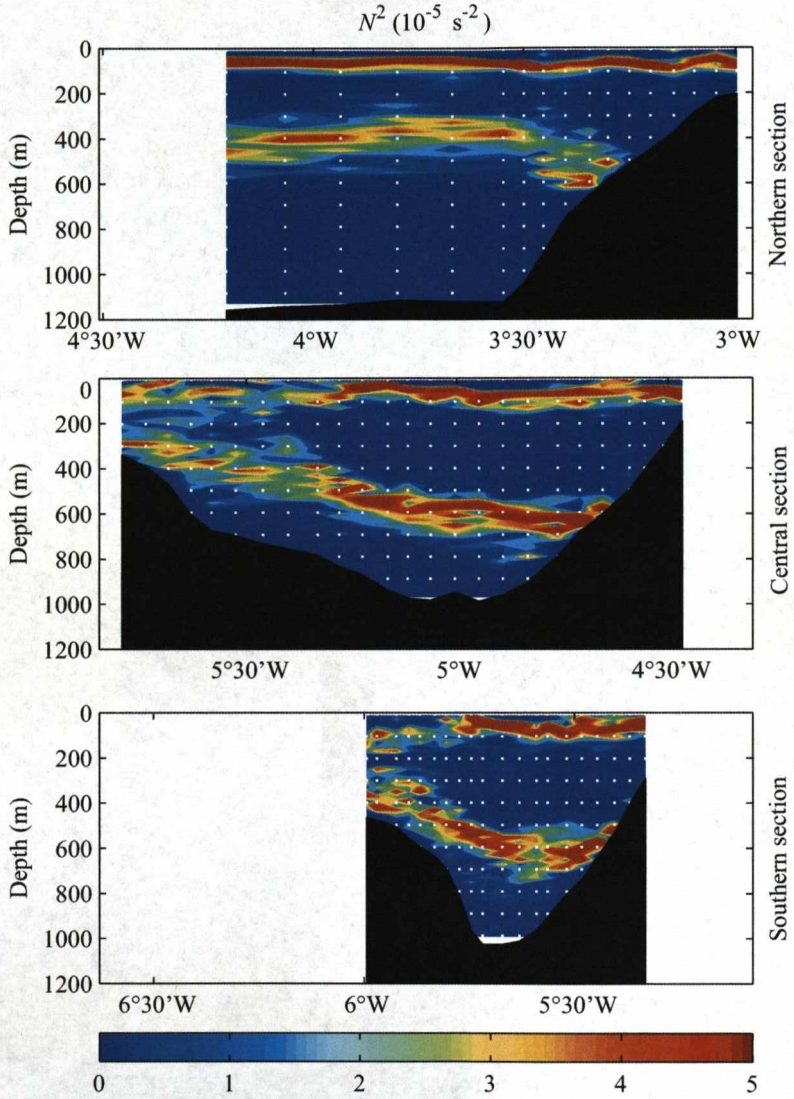

Figure 3.3: Buoyancy frequency from the three across-channel sections.

3.2.3 Repeat station

The 24-hour repeat station is located over the 680 m isobath to sample through the main pycnocline close to where it intersects the West Shetland slope. The pycnocline is found at 600 m, with the isopycnals diverging slightly over the 24 hours (Fig. 3.4). A semi-diurnal vertical displacement of the pycnocline with an amplitude of the order 10 m is observed, suggesting an internal tide is present along the slope. The generation region may be local, for example the shelf break, or a remote location. An internal tide in the Faroe-Shetland Channel has previously been observed by Sherwin (1991), who proposed the Wyville Thomson Ridge as the generation region.

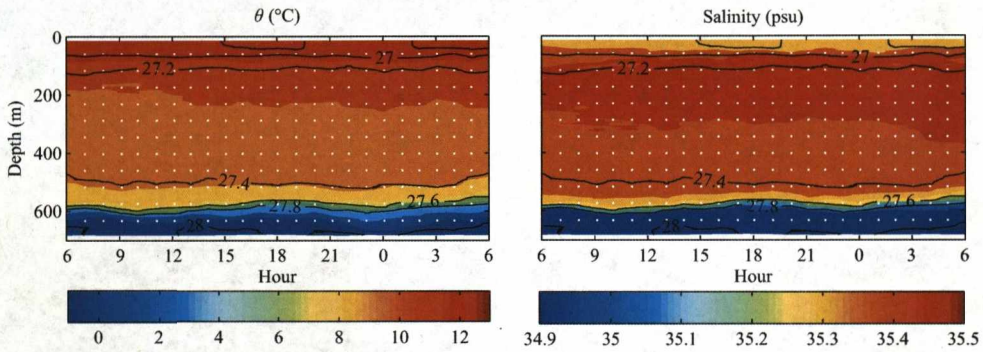

Figure 3.4: Potential temperature and salinity from the repeat station. The black lines are contours of σ_θ.

The orientation of the slope is approximately 51° clockwise from north so throughout this thesis horizontal velocity vectors are rotated to separate along-slope and across-slope flow. Positive along-slope is to the northeast, towards the Norwegian sea, while positive across-slope is to the southeast, up the slope.

There is high semi-diurnal variability in horizontal current velocity with the strongest currents, > 0.25 m s^{-1}, below the main pycnocline (Fig. 3.5 upper panel). The direction of flow below the pycnocline is primarily up the slope (southeast) and along-slope directed to the northeast. In the upper 350 m there is a northeast along-slope flow that is in phase and of a comparable magnitude (~ 0.2 m s^{-1}) to that below the pycnocline; the time-averaged flow in these layers is to the northeast. Between 350 and 550 m the time-averaged along-slope flow is

to the southwest. Across the slope, the time-averaged flow is down-slope above the pycnocline and up-slope below it.

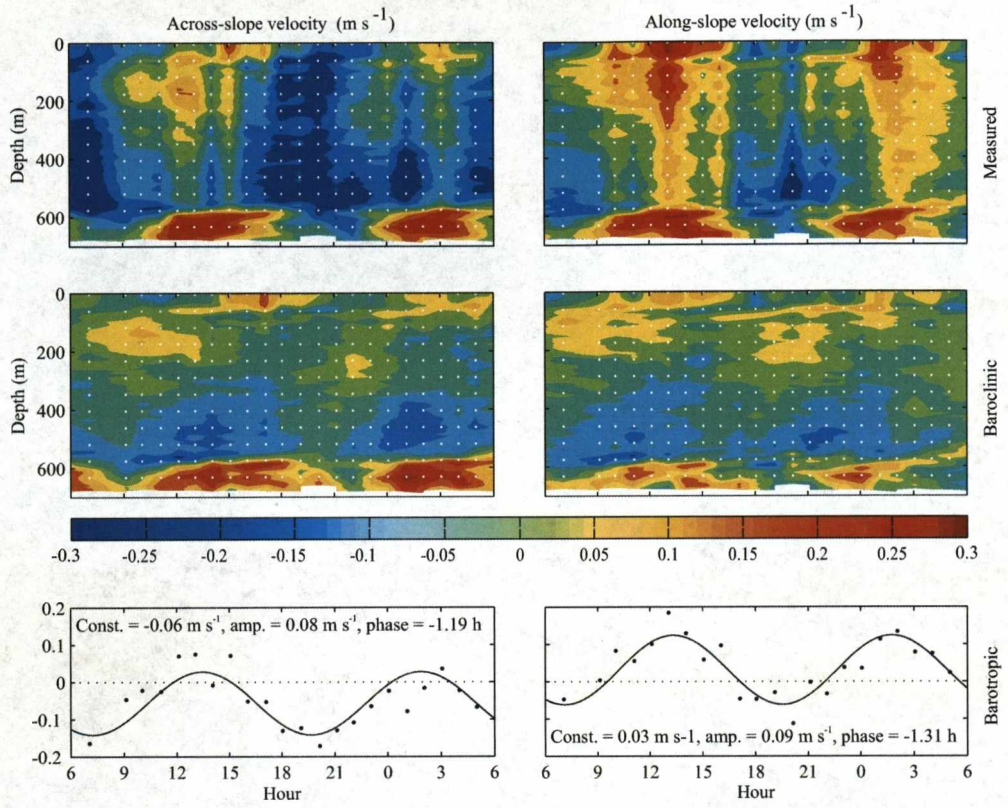

Figure 3.5: Across and along-slope current velocities from the repeat station. The upper panels show the measured velocities, the middle panels show the baroclinic velocities, and the points on the lower panels show the barotropic velocities. Positive is to the southeast (up-slope) for across-slope velocity and to the northeast for along-slope velocity. The lines on the lower panels are M_2 fits to barotropic velocity.

The full-depth horizontal velocity time series, $\mathbf{u}(z,t)$, is split into barotropic (bt) and baroclinic (bc) components, $\mathbf{u}(z,t) = \mathbf{u}_{\mathrm{bt}}(t) + \mathbf{u}_{\mathrm{bc}}(z,t)$. The barotropic component,

$$\mathbf{u}_{\mathrm{bt}}(t) = \frac{1}{H}\int_{-H}^{0} \mathbf{u}(z,t)\, dz, \tag{3.1}$$

where H is the total depth of the watercolumn, is roughly sinusoidal for both along and across-slope components (Fig. 3.5 lower panel), with semi-diurnal tidal am-

plitudes of the order 0.1 m s^{-1}. The time-averaged barotropic flow is 0.06 m s^{-1} down-slope and 0.03 m s^{-1} along the slope to the Northeast. The baroclinic (internal) component is larger across-slope than along-slope; in the former direction is of a comparable magnitude to the barotropic tide with horizontal velocities ~ 0.15 m s^{-1} below 350 m (Fig. 3.5 middle panel). The along-slope flow has a less coherent baroclinic semi-diurnal signal than the across-slope flow and is primarily barotropic.

Buoyancy frequency squared and the horizontal shear squared, $S^2 = (du/dz)^2 + (dv/dz)^2$, is calculated for each CTD and lowered ADCP profile (Fig. 3.6). Buoyancy is relatively uniform with time in the main pycnocline ($> 10^{-4}$ s^{-2}) and the seasonal thermocline ($\sim 10^{-4}$ s^{-2}). However horizontal shear is strongest, $> 10^{-4}$ s^{-2}, in the main pycnocline during the up-slope (and northeast) phase of the barotropic tide and rises away from the seabed with time. Horizontal shear is weaker, $\sim 5 \times 10^{-4}$ s^{-2}, in the seasonal thermocline. The strong shear through the main pycnocline may cause instabilities and mixing.

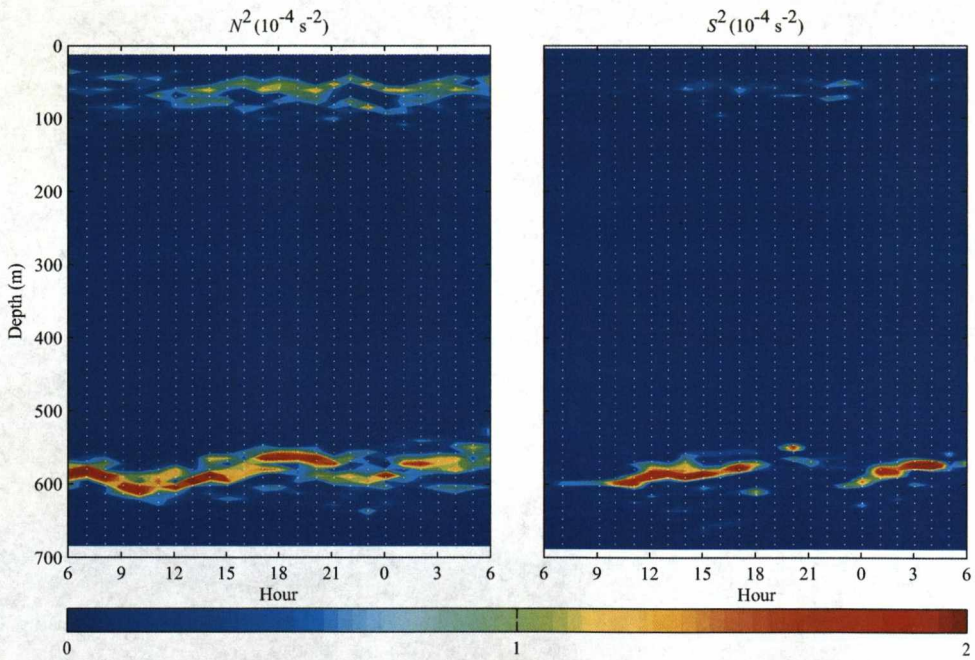

Figure 3.6: Buoyancy frequency and horizontal shear from the repeat station.

To assess the likelihood of the observed shear causing instabilities, the gradient Richardson number, Ri = N^2/S^2, is calculated at the shortest resolved length-scale, limited by the bin size of lowered ADCP to 4 m. The typical threshold for the onset of turbulence, Ri < 0.25, is met in 15% of bins; the most frequent occurrences are in the range 0.5 < Ri < 1 (Fig. 3.7). This suggests that the observed shear causes some instabilities and mixing, however, most instabilities are likely to occur at length-scales < 4 m.

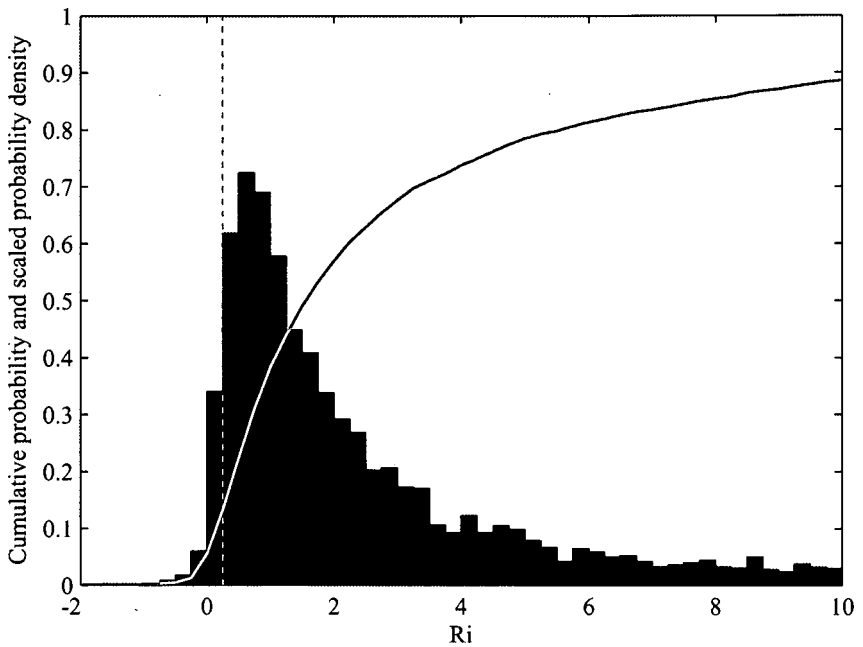

Figure 3.7: Cumulative probability distribution (grey line) and scaled probability density distribution (black bars) of Richardson number from the repeat station. The dashed grey line marks Ri = 0.25.

3.2.4 Temperature-salinity relationship

The θ-S diagrams for the three across-channel sections (Fig. 3.8) clearly show the NAW salinity maximum, the salinity minimum associated with NSAIW, and the FSCBW end-member. The 'tightness' of FSCBW in θ-S space shows the water mass is homogeneous despite its large volume. The influence of MNAW is identified by freshening of the salinity maximum across the channel towards

the Faroe Islands. AI/NIW is harder to identify directly from the θ-S diagrams but the mixing between NSAIW and NAW/MNAW is not linear so this water mass must be present in some proportion. The Northern section has a more pronounced 'kink' around 4°C than the other sections, suggesting a greater influence of AI/NIW. The presence of intermediate water masses in the channel may be a cause of the isopycnal pinching against the West Shetland slope, as observed in the Faroe Bank Channel (Borenäs et al., 2001).

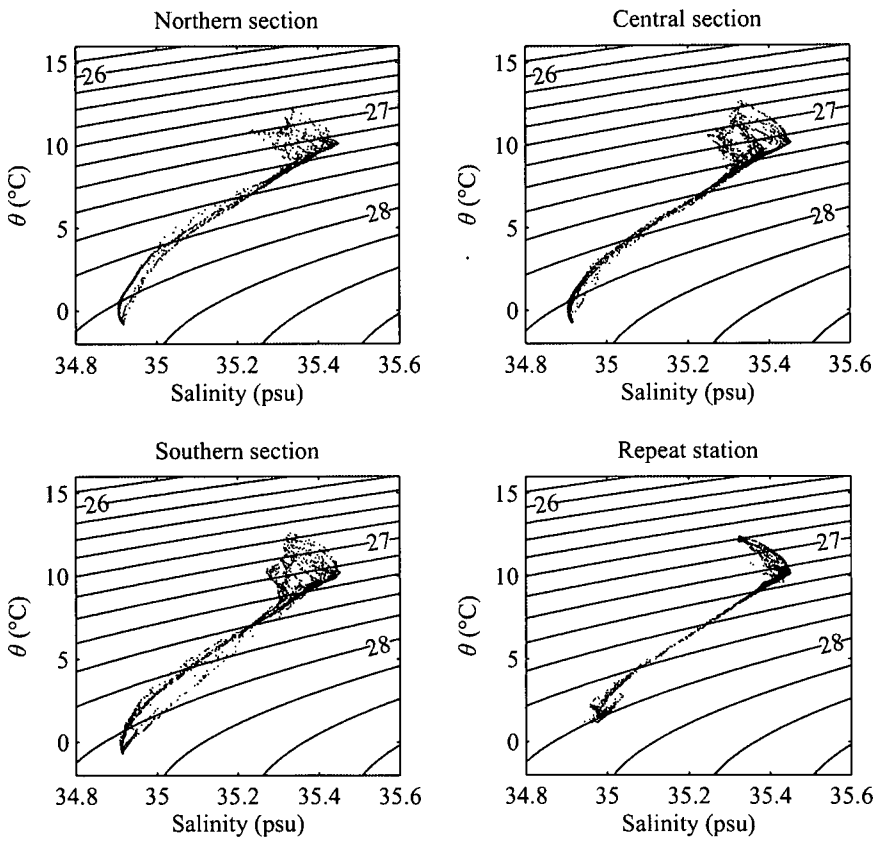

Figure 3.8: θ-S diagrams for the three across-channel sections and the repeat station.

Although most deep casts pass through NSAIW, some casts along the Northern and Central sections show mixing directly between FSCBW and AI/NIW. A

few casts over the West Shetland slope along the Southern section also suggest direct mixing between FSCBW and NAW/MNAW.

As expected over the West Shetland slope, the θ-S diagram for the repeat station shows little variability at the salinity maximum, consistent with a lack of MNAW. There is high variability near the seabed that could be the result of enhanced mixing through the main pycnocline or advection of dense water masses up the slope by the barotropic tide. No FSCBW is present, the densest water is closer to AI/NIW.

3.3 Mooring time series

Internal wave activity was expected to be high in the main pycnocline following observations of an internal tide in the channel (Sherwin, 1991) and non-linear internal wave trains at the seabed, propagating up the West Shetland slope (Hosegood and van Haren, 2004; Hosegood et al., 2004). To make measurements of these internal waves an array of instruments was deployed on the slope from 8th to 21st September[2]. As the array was designed to make high resolution measurements, the mooring lengths and instrument ranges were short. It was therefore critical to make the deployments close to where the main pycnocline meets the slope. Internal wave trains were previously observed below 450 m (Hosegood and van Haren, 2004) so the array was intended to be deployed about the 500 m isobath. However, preliminary CTD profiles over the slope showed the main pycnocline to be deeper than expected, $\sim$ 600 m. This is not unexpected following the high variability in the depth of the main pycnocline described in Chapter 2. Instead, the array was deployed further down the slope, about the 600 m isobath, so the instruments would sample through the main pycnocline.

3.3.1 Instrumentation

Four moored ADCPs were arranged in a square $\sim$ 5 km across (Fig. 3.9), facing upward. 50-m thermistor moorings were deployed next to the ADCP moorings at the 'East', 'South', and 'West' corners of the square. The thermistors were attached approximately 4 m apart along the mooring cable and on the 'West' and 'East' moorings a CTD logger was attached 4 m above the seabed. The location, dates, and instrumentation attached to each mooring are shown in Table B.2. All the ADCPs and most of the thermistors had 2-minute sampling (some thermistors

[2]The 'North' ADCP mooring could not be recovered during the cruise but was recovered later, on 30th September, and so provides a longer time series.

were set to sample every 4 minutes due to memory constraints); the CTD loggers sampled every minute. This novel arrangement of instruments, in a 3-dimensional mooring array rather than a single line of moorings, allows both the speed and direction of internal waves to be resolved, provided individual waves are observed in three or more of the mooring time series. The specialist instrument packages (STABLE, HOMER, and NIOZ lander) were deployed in the centre of the square along the 600 m isobath. The data from these instruments are not included in this analysis. The ADCP data were processed using standard processing techniques[3]. The thermistors were not calibrated before the cruise, so corrections were applied to match the near-bed vertical temperature profile from the CTD casts made before the deployments.

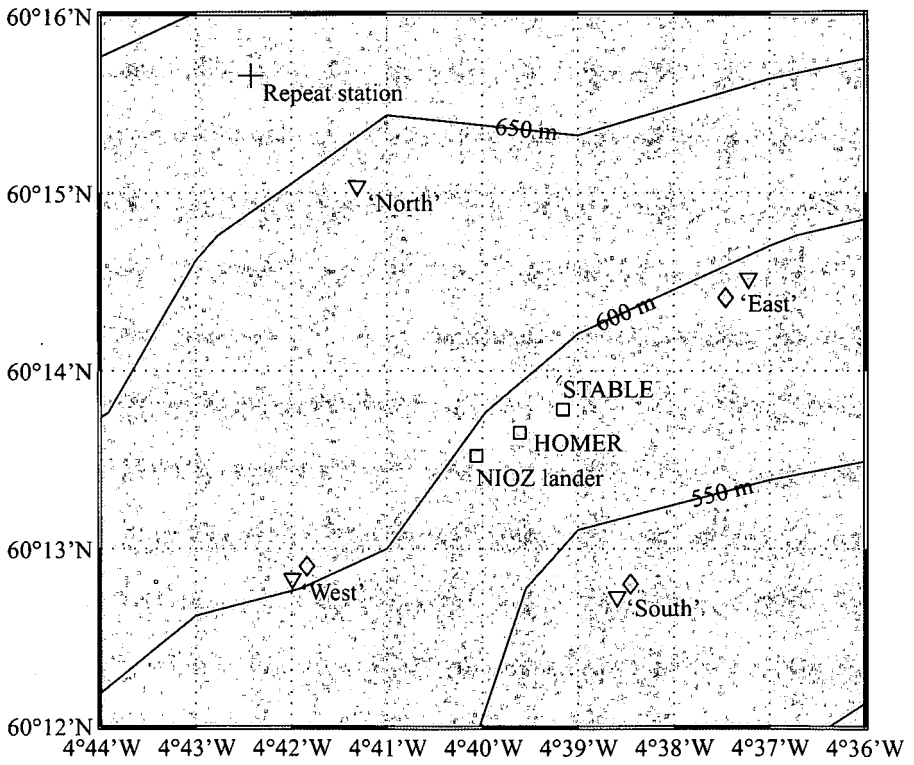

Figure 3.9: Location of the moorings and repeat station on the West Shetland slope. The triangles are the moored ADCPs and the diamonds are the thermistor moorings.

[3]The ADCP data were processed by John Howarth (POL).

3.3.2 Thermistor moorings

The temperature time series from the three thermistor moorings are shown in Figures 3.10, 3.11, and 3.12. High semi-diurnal variability is a common feature of all three time series with typical temperature changes of 2-3°C. This could either be a manifestation of the internal tide in the main pycnocline or across-slope advection of the pycnocline by the barotropic tide. 3°C changes in temperature are observed in the pycnocline from the CTD profiles at the repeat station so the internal tide can account for much of the semi-diurnal variability. However, the existence of 2°C and 8°C water near the seabed in both the 'West' and 'East' thermistor moorings implies that some longer period advection occurs.

In all three time series there is a trend of decreasing temperature during the first 8 days then increasing temperature during the last 4 days. The pattern is coherent between the moorings and reflects shallowing then deepening of the pycnocline over the slope. This longer time-scale variability is likely the result of mesoscale activity, as described in Chapter 2. An unfortunate effect of the pycnocline displacement is that during the second half of the time series only the base of the pycnocline is sampled by the 'West' and 'East' thermistor moorings.

Higher frequency internal wave variability is intermittently observed in the time series. The period of the waves is typically between 15 and 30 minutes with temperature changes of the order 1°C. During the first four and last three days of the time series, groups of internal waves appear at roughly semi-diurnal intervals, correlated with the cold phase of the semi-diurnal cycle, so are likely to be tidally forced. In the middle of the time series, when the pycnocline is shallow, the waves appear with no apparent periodicity.

Near-bed temperature, salinity, and pressure was recorded by the CTD loggers on the 'West' and 'East' thermistor moorings and potential density calculated. Semi-diurnal variability is again evident at the beginning and end of the time series and high-frequency fluctuations, from the passing of internal waves, are observed (Fig. 3.10 and 3.11). The near-bed pressure is also used to approximate sea surface elevation. The barotropic tide is easily resolved and five tidal constituents fit by harmonic analysis[4] (see Section 1.4.2). The pressure resolution of the instruments was insufficient to resolve the pressure perturbations associated with the passing of internal waves, however, the phase relation between the barotropic tide and the high frequency internal waves can be assessed. Although

[4]The tidal constituents fit are M_2, K_1, S_2, O_1, and N_2. Although the different diurnal and semi-diurnal constituents cannot be separately resolved from a 12-day time series, including the extra constituents improves the overall fit to observed pressure.

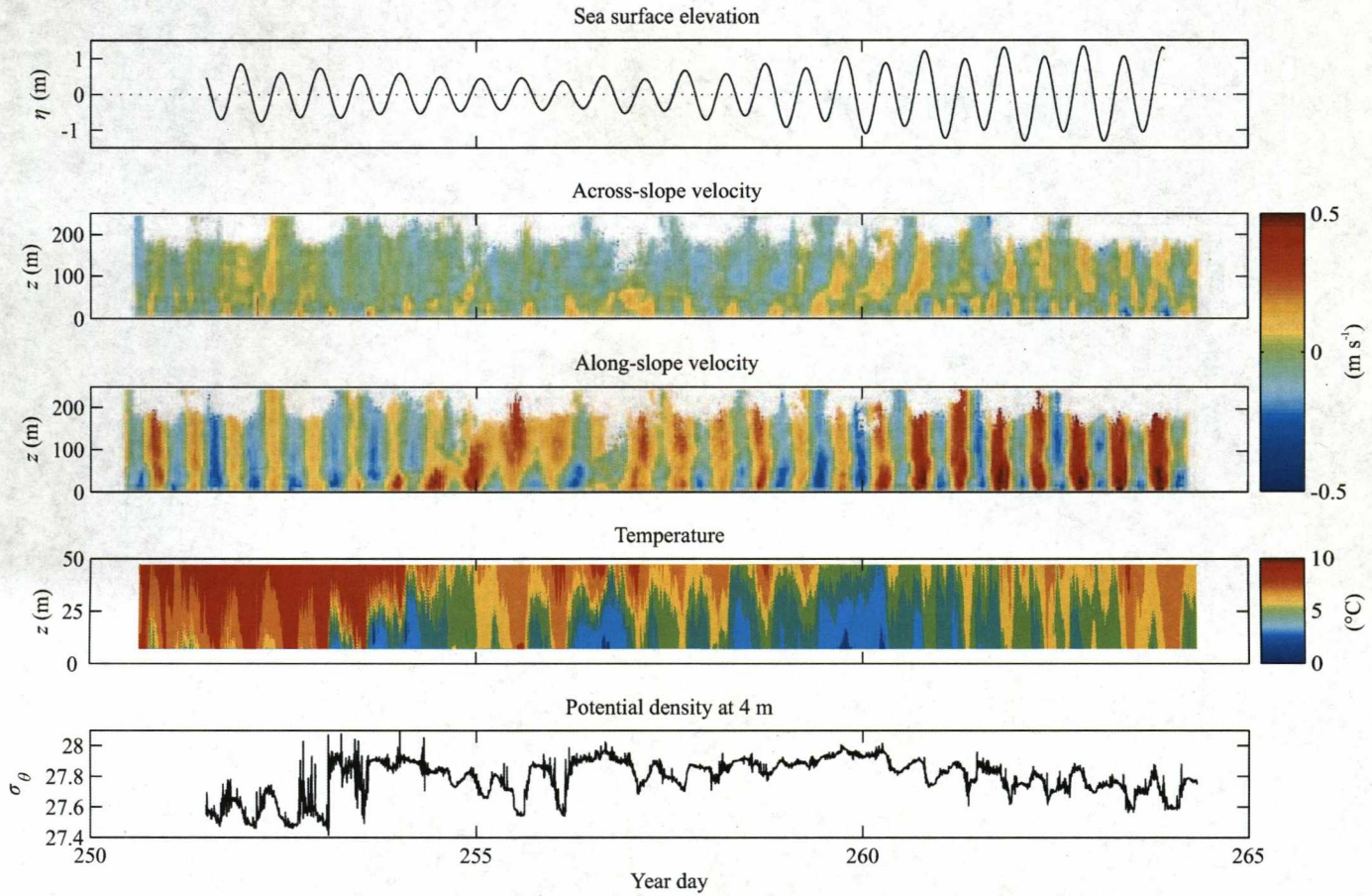

Figure 3.10: 'West' ADCP and thermistor mooring time series: sea surface elevation, horizontal current velocity, temperature, and near-bed potential density.

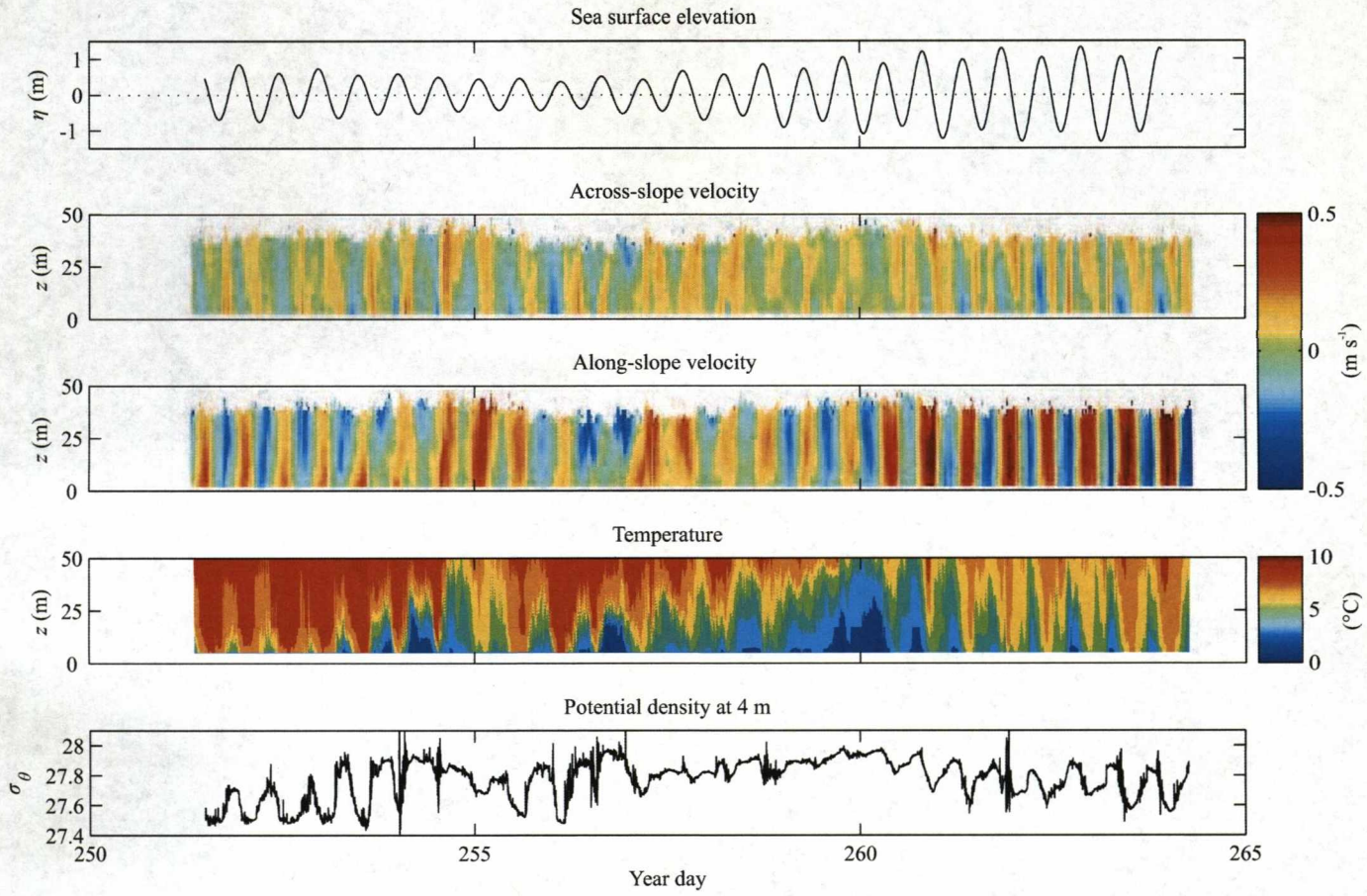

Figure 3.11: 'East' ADCP and thermistor mooring time series: sea surface elevation, horizontal current velocity, temperature, and near-bed potential density.

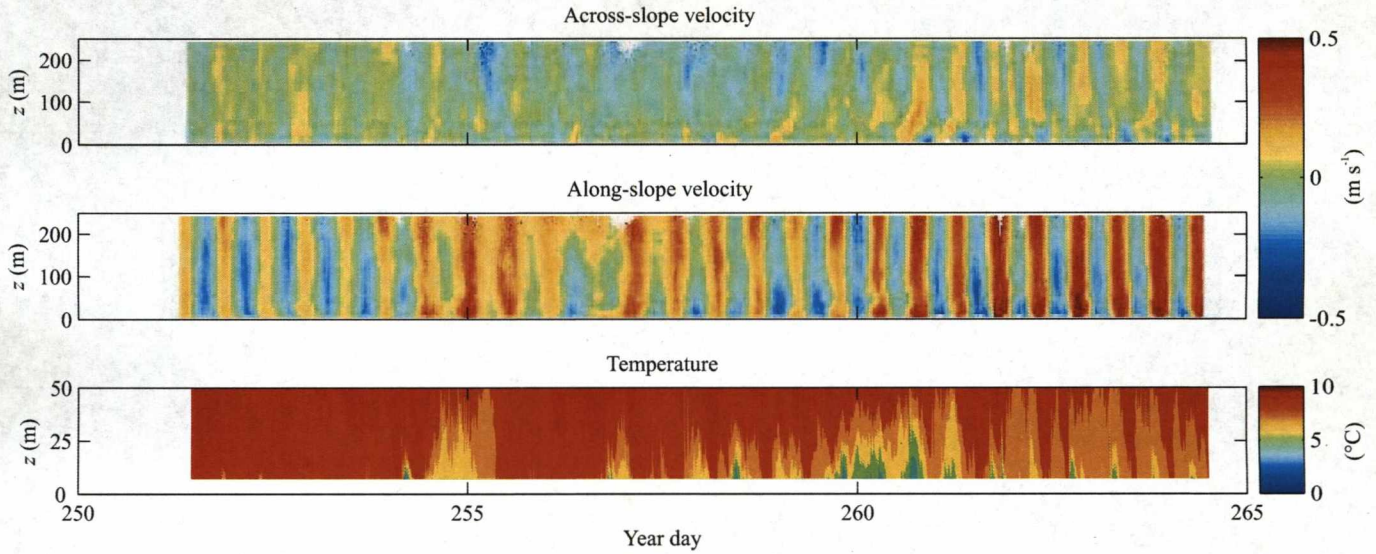

Figure 3.12: 'South' ADCP and thermistor mooring time series: horizontal current velocity and temperature.

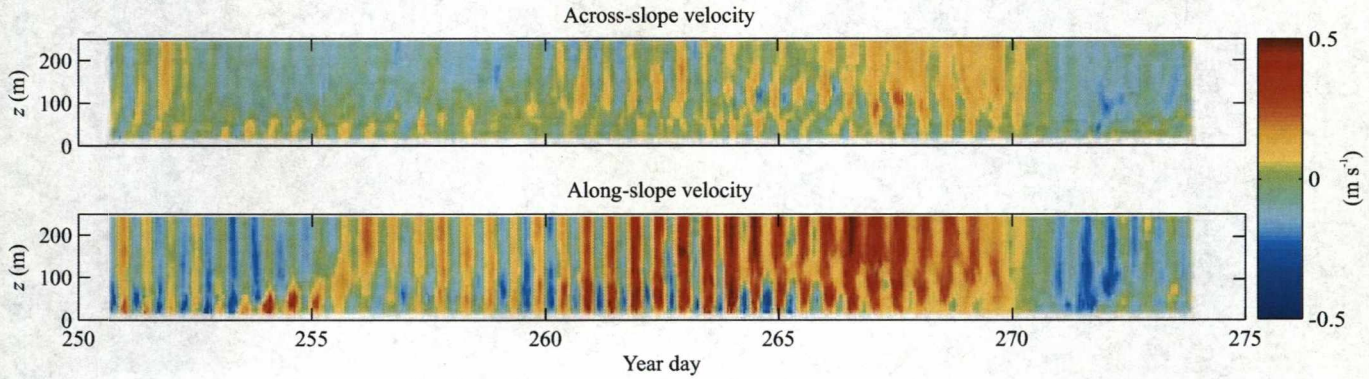

Figure 3.13: 'North' ADCP mooring time series: horizontal current velocity.

internal wave groups sometimes appear in the time series at roughly semi-diurnal intervals, the phase relation with the barotropic tide is variable, suggesting they are not generated locally, but at a remote location and propagate into the region.

To calculate the amplitude of the internal waves, density is approximated from the thermistor time series so that the vertical displacement of isopycnals can be calculated. Although internal wave amplitude can be determined from the displacement of isotherms, inferring density simplifies the calculation of energy densities (Chapter 5). Time series of salinity are approximated from the temperature time series by applying a linear T-S relationship inferred from the CTD loggers ($S = 34.88 + 0.05T$), then the approximate density calculated.

The vertical displacement of isopycnals is calculated by decomposing the density time series into time-average values and anomalies so that $\rho'(z,t) = \rho(z,t) - \overline{\rho}(z)$. The vertical isopycnal displacement is then $\xi = -\rho'(d\overline{\rho}/dz)^{-1}$, where $d\overline{\rho}/dz$ is the time-average vertical density gradient. The amplitudes of the high-frequency internal waves are up to 50 m, large compared to the depth of the lower layer, suggesting a certain degree of non-linearity. There is an amplitude dependence of phase velocity with non-linear waves, large amplitude waves travel faster than smaller amplitude waves, leading to the formation of rank-ordered packets. These are observed in the first four and last three days of the time series. The lack of coherence between the waves observed at the three locations implies wavelengths $\ll 5$ km.

Where stratification is maintained near the seabed, strong disturbances are expected to manifest themselves as bottom-trapped waves of elevation (Klymak and Moum, 2003). This appears to generally be the case at this location although as the internal wave field is complex it is not always possible to determine the isopycnal rest state. Some of the waves occur singularly in the form of solitary waves, while others occur in trains in the form of cnoidal waves (Fig. 3.14). On a few occasions the isopycnals do not return to their original rest state after the solitary wave or cnoidal wave train has passed. These waves, with the properties both of internal solitary waves and of turbulent internal bores, were previously observed in the channel by Hosegood and van Haren (2004), who termed them 'solibores'.

3.3.3 ADCP moorings

The horizontal velocity time series from the four moored ADCPs are shown in Figures 3.10, 3.11, 3.12, and 3.13. As the 'East' ADCP is high frequency its range is limited to ~ 40 m and so only samples the lower layer and the base of the main

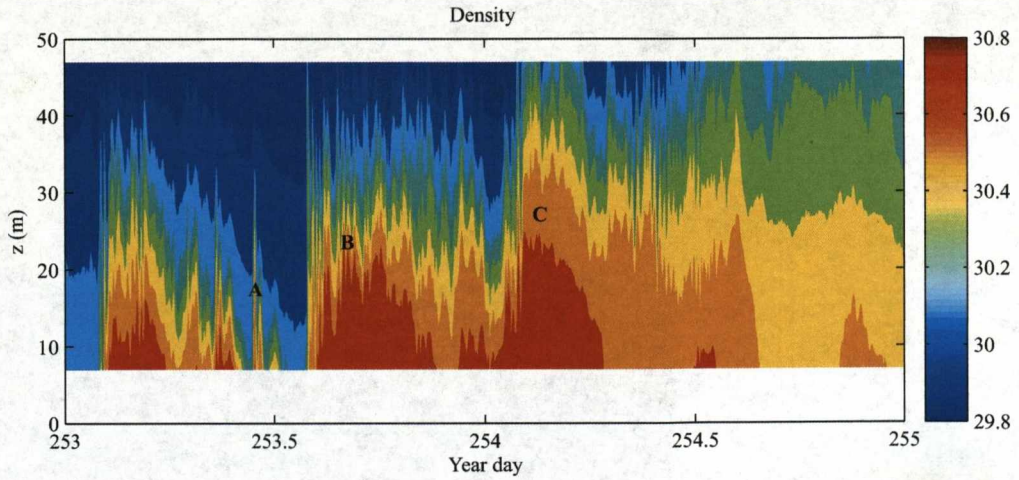

Figure 3.14: Examples of non-linear internal wave forms, A: solitary wave, B: cnoidal wave train, and C: solibore.

pycnocline. The three other ADCPs are lower frequency with ranges of 200 to 250 m and therefore sample approximately the lower third of the watercolumn.

The along-slope flow is strongly semi-diurnal and in phase with sea surface elevation. The time series begins after spring tide; neap tide is on day 255 and the next spring on day 262. Maximum near-bed along-slope velocities during springs are 0.6 m s^{-1} towards the northeast with tidal amplitudes $\sim$ 0.4 m s^{-1}. During neaps the tidal amplitude is $<$ 0.2 m s^{-1}. From the three long-range ADCP time series, there is strong coherence in along-slope velocity in the bottom 200 m, suggesting the flow is primarily barotropic. This is in agreement with the lowered ADCP profiles from the repeat station.

Across-slope velocities are typically smaller than along the slope, $<$ 0.2 m s^{-1}, with less semi-diurnal variability. In the time series from the long-range ADCPs a $\sim$ 180° phase shift is observed at around 50 m above the bottom, the approximate position of the main pycnocline, with the lower layer leading the upper layer, and is evidence of a mode-1 internal tide. Quarter-diurnal period variability is observed in the bottom 50 m of all four time series between year days 260 and 265.

The longer 23-day time series from the 'North' ADCP shows an interesting feature after year day 265 (Fig. 3.13). Between year days 266 and 270 , before neap tide, the along-slope velocity becomes almost entirely positive (i.e. to the northeast) then between year days 270 and 273, after neap tide, switches to

primarily negative (southwest). A similar switch from positive to negative flow is observed in the across-slope velocity time series.

3.4 Time series analysis

3.4.1 Frequency spectra

The frequency spectra of horizontal velocity and vertical isopycnal displacement, vertically averaged in the bottom 50 m, are calculated from the mooring time series using Welch's periodogram. The time series is detrended and a fast fourier transform (FFT) applied in a 5-day Hanning window with 50% overlap. The spectra from each window are averaged and squared to generate power spectra. At the latitude of the experiment site (60.2°N) the inertial frequency is 1.27×10^{-4} rad s^{-1} (13.8-hour period) and so requires a time series longer than 7.8 days to be distinguished from the M_2 tide. The 5-day window therefore excludes the separate resolution of M_2 and near-inertial signals.

The horizontal velocity spectra from all four moored ADCPs show energy cascade gradients between -1.3 to -1.8 (Fig. 3.15), close to the often observed -5/3 for isotropic turbulence (e.g. Holbrook and Fer 2005; Govender et al. 2004). A strong semi-diurnal signal is observed in all the along-slope velocity spectra as well as the 'East' and 'South' across-slope spectra. A quarter-diurnal signal is also observed in the 'West' and 'East' across-slope spectra.

The vertical isopycnal displacement spectra also show energy cascade gradients close to -5/3 (-1.5 to -1.6) up to frequencies of 10^2 cpd (7.3×10^{-3} rad s^{-1}). At higher frequencies the gradient increases, -5.2 and -6.2 for the 'West' and 'East' moorings respectively, and -3.6 for the 'South' mooring. This change in gradient coincides with the upper limit of the frequency band the non-linear internal waves are observed in. Semi and quarter-diurnal signals are observed in all three vertical displacement spectra.

The frequency spectrum of near-bed pressure is also calculated, but because the time series is dominated by semi-diurnal and longer period variability, a full-length Hanning window is used to resolve lower frequency oscillations (Fig. 3.16). As expected the largest signal is at the frequency of the semi-diurnal M_2 tide and a second peak is observed at diurnal periods close to the frequency of the K_1 tide. No clear near-inertial signal is observed, as expected because near-inertial variability tends to occur in current velocity rather than pressure.

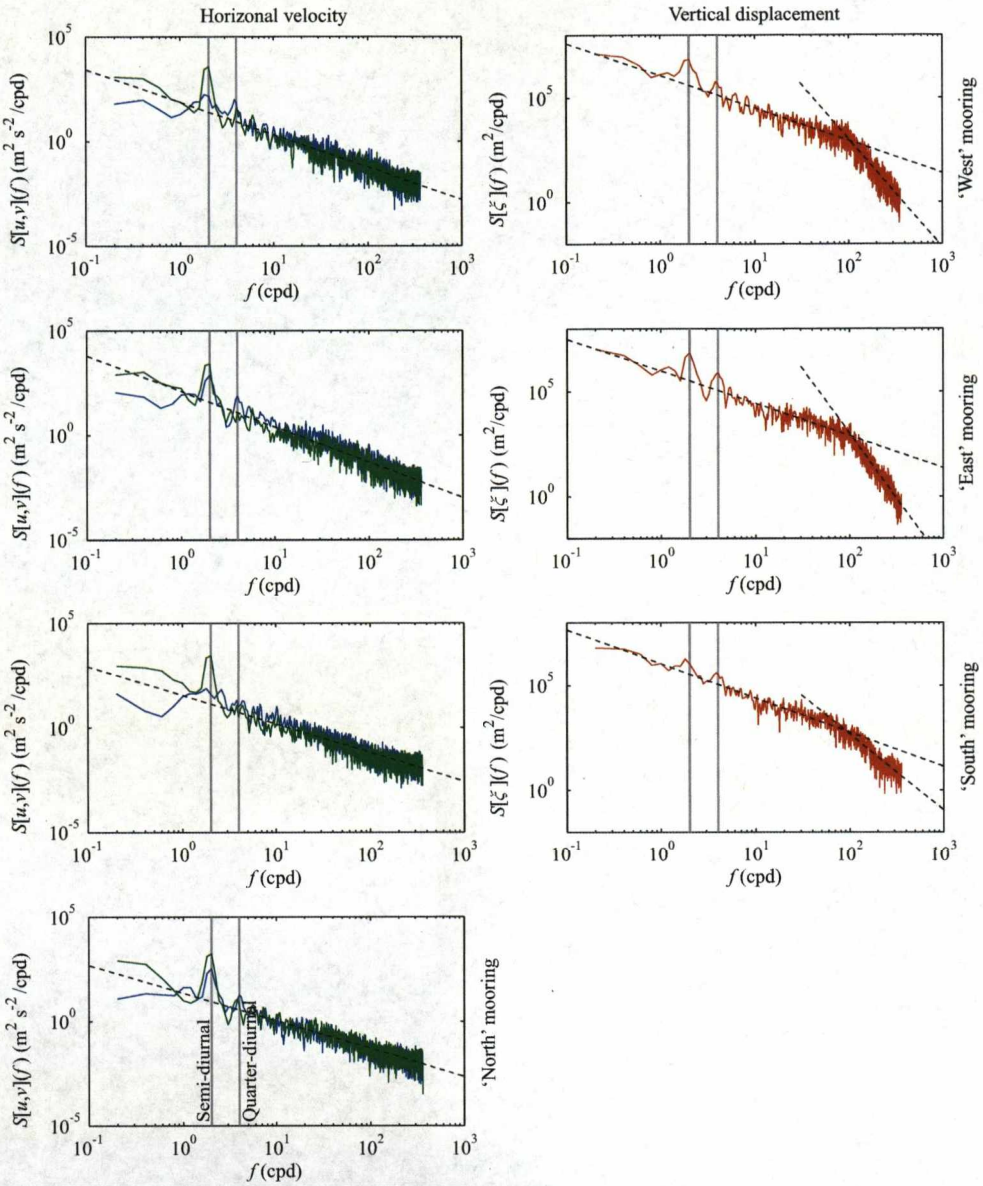

Figure 3.15: Power spectra of across-slope velocity (green) along-slope velocity (blue) and vertical isopycnal displacement (red) from the mooring time series. The dashed lines are the gradients of the energy cascade. The grey lines mark the semi-diurnal and quarter-diurnal frequencies.

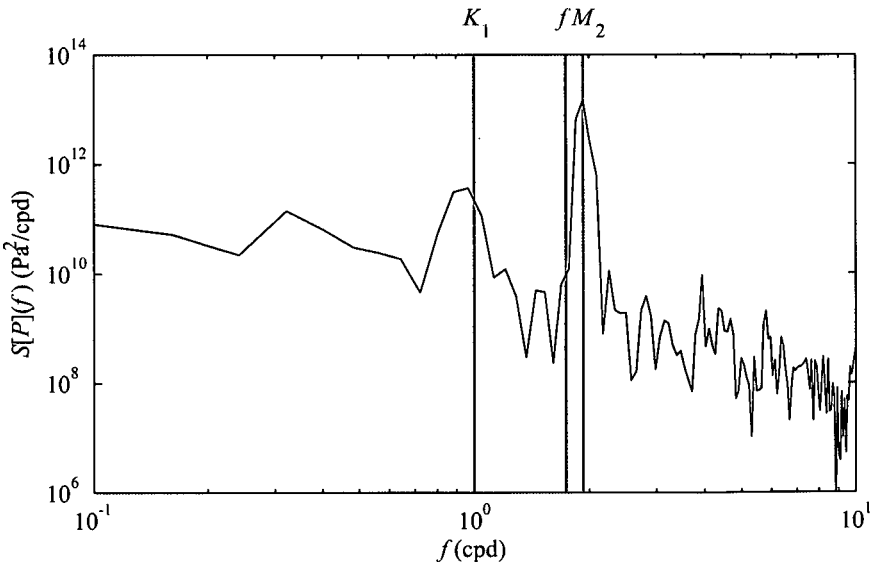

Figure 3.16: Power spectra of near-bed pressure from the CTD loggers on the 'West' and 'East' thermistor moorings. The grey lines mark the M_2, K_1, and inertial (f) frequencies.

3.4.2 Harmonic tidal analysis

Harmonic analysis is applied to the mooring time series to calculate the amplitudes and relative phases of the tidal constituents identified in the frequency spectra. Harmonic tidal analysis has the general form

$$x(t) = \overline{x} + \sum_{i=1}^{N} [A_i \cos(\omega_i t) + B_i \sin(\omega_i t)] + x_r(t), \tag{3.2}$$

where $x(t)$ is the variable, $\overline{x}$ is the time-average constant, i is the tidal constituent, ω_i is the angular frequency of the constituent, and $x_r(t)$ is the residual with zero time-mean (Emery and Thomson, 2001). The constants $\overline{x}$, A_i, and B_i are found by linear least-squares regression. Equation (3.2) can be rewritten

$$x(t) = \overline{x} + \sum_{i=1}^{N} [x_{0i} \cos(\omega_i t - \phi_i)] + x_r(t), \tag{3.3}$$

where $x_{0i} = (A_i^2 + B_i^2)^{1/2}$ is the amplitude of the tidal constituent and $\phi_i = \tan^{-1}(B_i/A_i)$ is the phase lag. The number of tidal constituents that can be separately resolved is limited by the length of the time series (T). Two constituents with different angular frequencies (ω) can be clearly separated if $|\Delta\omega|\, T/2\pi > R$,

where R is typically one. This requirement can be relaxed (i.e. $R < 1$) to estimate the relative amplitude and phase between two close constituents. As the mooring time series contain a lot of noise (non-tidal variability), $R = 1$ is used to decide which constituents are fit. The mooring time series is 12 days long, so the semi-diurnal M_2 and diurnal K_1 constituents of the equilibrium tide can be clearly separated but the semi-diurnal S_2 and diurnal O_1 constituents are too close to the M_2 and K_1 constituents respectively. However, there is a clear quarter-diurnal signal in the vertical displacement time series so the first harmonic of the M_2 tide, the quarter diurnal M_4 tide, is also included in the regression. The angular frequencies of the fitted constituents are shown in Table 3.1.

Constituent	Symbol	Period (hours)	Angular freq. (10^{-5} rad s^{-1})
Principal lunar semi-diurnal	M_2	12.42	14.05
Luni-solar diurnal	K_1	23.93	7.29
Principal lunar quarter-diurnal	M_4	6.21	28.11

Table 3.1: The period and angular frequency of the tidal constituents fit by harmonic analysis.

As with the frequency spectra, the tidal constituents are fit to the horizontal velocity and vertical isopycnal displacement time series, vertically averaged in the bottom 50 m, and the near-bed pressure time series. The pressure amplitudes for the M_2 and K_1 tides are 7.21 and 0.95×10^3 Pa respectively, a ratio of nearly 8. There is negligible M_4 pressure variability.

Coherent amplitudes and phases between the moorings are only observed for the M_2 tide, for which the along-slope velocity amplitude is 17.3 ± 3.0 cm s^{-1} and the phase ± 0.14 hours (Table 3.2). The amplitudes of across-slope velocity and vertical displacement are 3.9 ± 1.4 cm s^{-1} and 3.2 ± 1.2 m respectively but the phases are incoherent between the moorings. For the K_1 tide the along-slope amplitude is 1.4 ± 0.6 cm s^{-1}, the across-slope amplitude 0.8 ± 0.3 cm s^{-1}, and the vertical displacement amplitude 1.7 ± 0.7 m. Only the along-slope M_2-to-K_1 ratio is consistent with pressure, the ratios for the other two variables are smaller.

The largest velocity amplitudes for the M_4 tide are across the slope but the amplitude is variable, between 2.2 cm s^{-1} ('West') and 0.8 cm s^{-1} ('North'). The

		Const.	M_2		K_1		M_4	
			x_0	ϕ	x_0	ϕ	x_0	ϕ
P		-	7.21	-0.64	0.95	-0.56	0.05	-1.14
'West'	u	-0.30	2.58	-2.15	0.48	-1.82	2.22	-1.40
	v	3.87	19.92	0.49	1.85	5.08	0.78	0.39
	ξ	-	3.86	-0.92	0.76	-4.04	1.46	-0.38
'East'	u	2.13	5.28	2.82	0.97	1.34	1.41	1.24
	v	3.78	20.21	0.39	1.20	-2.14	0.58	-0.49
	ξ	-	4.41	0.22	0.83	4.51	0.19	-1.38
'South'	u	-1.22	3.00	0.34	1.16	2.37	0.97	0.02
	v	3.65	18.41	0.61	1.96	5.73	0.67	0.01
	ξ	-	2.04	1.28	2.10	5.64	0.51	1.00
'North'	u	0.15	4.04	2.34	0.65	-4.20	0.81	0.86
	v	2.11	14.29	0.33	0.74	5.66	0.59	1.27

Table 3.2: The amplitudes (x_0) and phase lags (ϕ) of the tidal constituents fit to across-slope velocity (u), along-slope velocity (v), and vertical isopycnal displacement (ξ) from the mooring time series by harmonic analysis. Const. is the time-average constant. Pressures are in 10^3 Pa; velocities in cm s^{-1}; vertical displacements in m; and phases in hours.

along-slope amplitude is smaller, 0.7 ± 0.1 cm s^{-1}, but consistent between the moorings. The vertical isopycnal displacement is also highly variable, between 1.5 m for the 'West' mooring and 0.2 m for the 'East' mooring.

The time-average velocities are consistent, 3.7 ± 0.1 cm s^{-1}, along-slope between the 'West', 'East', and 'South' moorings, but the for the 'North' mooring is only 2.1 cm s^{-1}. These values are small compared to the along-slope velocity amplitudes for the M_2 tide and typical residual flow in the slope current (20 to 30 cm s^{-1}) measured by (Hughes et al., 2006b). Across-slope, the time-average velocities change sign between moorings. The time-average is inherently zero for pressure (as the time-means are removed to compensate for different deployment depths) and vertical displacement.

3.5 Internal tide vertical structure

The vertical structure of semi-diurnal internal tide is assessed by fitting the M_2 tidal constituent to horizontal velocity and vertical isopycnal displacement from the repeat station lowered ADCP/CTD profiles. Only the M_2 tide is fit because it has by far the largest amplitude. Fits are made to depth-averaged barotropic

velocity, and baroclinic velocity and vertical displacement at each level. As only a single tidal constituent is fit, the harmonic analysis has a simpler form, e.g. for vertical isopycnal displacement

$$\xi(z,t) = \overline{\xi}(z) + \xi_0(z)\,\cos(\omega_{M_2}t - \phi(z)) + \xi_r(z,t). \tag{3.4}$$

The barotropic velocity amplitudes for the M_2 tide are 0.08 and 0.09 m s^{-1} for the across and along-slope components and the phases are separated by less than 10 minutes (Fig. 3.17). The baroclinic velocity amplitudes are largest, > 0.1 m s^{-1}, in and below the main pycnocline, tending to zero at the bottom. Between the seasonal thermocline and main pycnocline the amplitude is ~ 0.03 m s^{-1}, increasing to > 0.06 m s^{-1} near the surface. Similarly, the vertical displacement is largest in the pycnocline, approaching 10 m, but decreases to 2 m at the bottom and near zero at 450 m. Above 450 m the amplitude is ~ 1 m, increasing to > 4 m at the surface. The fact that ξ does not go to zero at the surface and the bottom suggests some horizontal advection of isopycnals by the barotropic tide occurs (probably across-slope as that is the direction the horizontal density gradients are largest).

The phases of baroclinic velocity for the M_2 tide display much variability with a general trend of increasing phase lag with depth. This phase lag is in agreement with observations from the moored ADCPs. In the upper 100 m and below 400 m, the phases of the vertical displacements also display a trend of decreasing phase lag with depth. Between 100 and 500 m, however, the trend is of increasing phase lag with depth.

The time-averaged constants of baroclinic velocity are positive (up-slope and along-slope to the northeast) above 300 m and below 600 m but negative (down-slope and along-slope to the southwest) between. Maximum time-averaged baroclinic velocities below the main pycnocline are of the same order as the baroclinic velocity amplitudes in the lower layer.

For comparison with the vertical structure of the internal tide, vertical structure modes are calculated for the time-averaged buoyancy frequency profile from the repeat station (Fig. 3.18). Although the application of vertical structure modes is limited to flat bottom cases, the slope at the experiment site is small (0.02) and so useful comparisons may still be made. Other deviations from vertical structure modes may arise from horizontal density gradients and along-slope currents. Solutions to the Sturm-Liouville equation are found using software developed by John Klinck (Old Dominion University) and the first three internal wave modes are shown in Figure 3.19. The first mode horizontal velocity structure

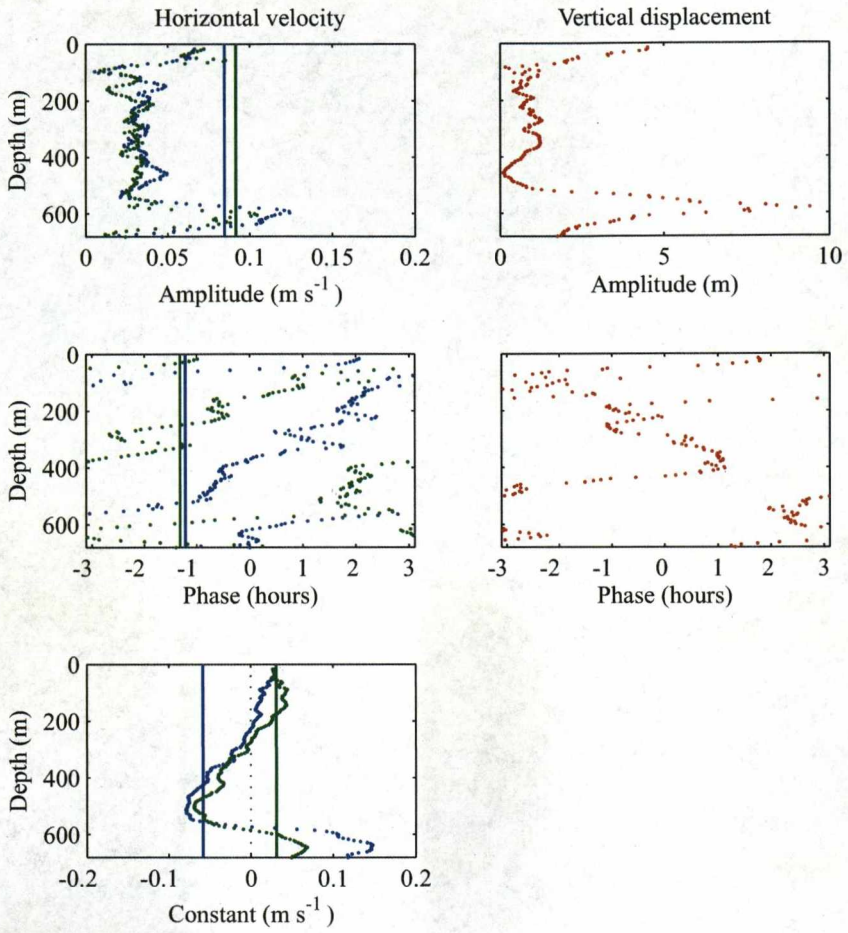

Figure 3.17: The amplitude, phase lag, and time-average constant of the M_2 tidal constituent fit to across-slope velocity (green) along-slope velocity (blue) and vertical isopycnal displacement (red) from the repeat station lowered ADCP/CTD profiles. For horizontal velocity the solid lines are depth-averaged barotropic velocity and the dots are baroclinic velocity at each level.

predicts the large baroclinic velocities observed in and below the main pycnocline and the smaller baroclinic velocities at the surface. However, the first mode vertical velocity structure is very different from the observed vertical displacements. Although the maximum is in the pycnocline and decreases to zero at the bottom (the observed vertical displacement tends towards zero at the bottom), high vertical velocities are predicted directly above the pycnocline that are not observed in vertical displacement. In addition, the predicted vertical velocities go to zero at the surface, whereas observed vertical displacements increase towards the surface.

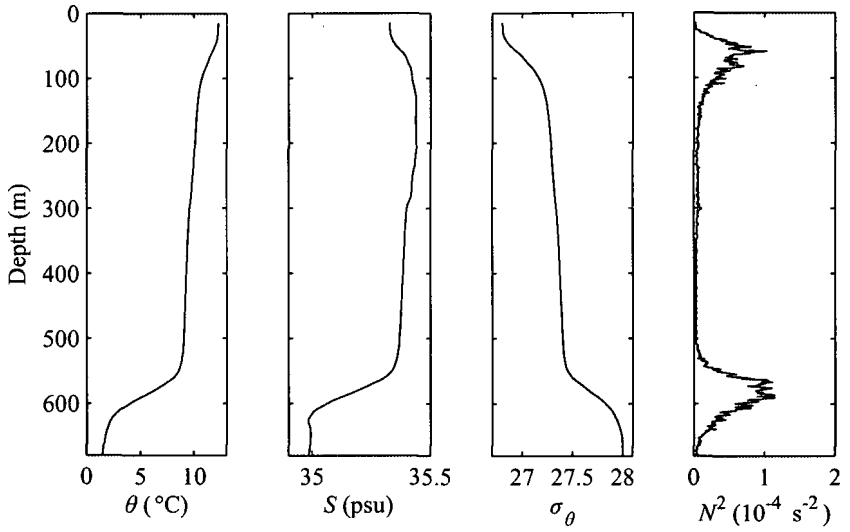

Figure 3.18: Time-averaged potential temperature, salinity, potential density, and buoyancy frequency profiles from the repeat station.

The fact that the observed vertical displacement goes to zero at mid-depths suggests that higher modes of internal wave variability maybe present. The second mode predicts zero vertical velocity at the right depth, but larger vertical velocities in the upper layer than in the main pycnocline; observed vertical displacements are small in the upper layer. Higher internal wave modes are discounted because vertical velocity goes to zero deeper than 450 m.

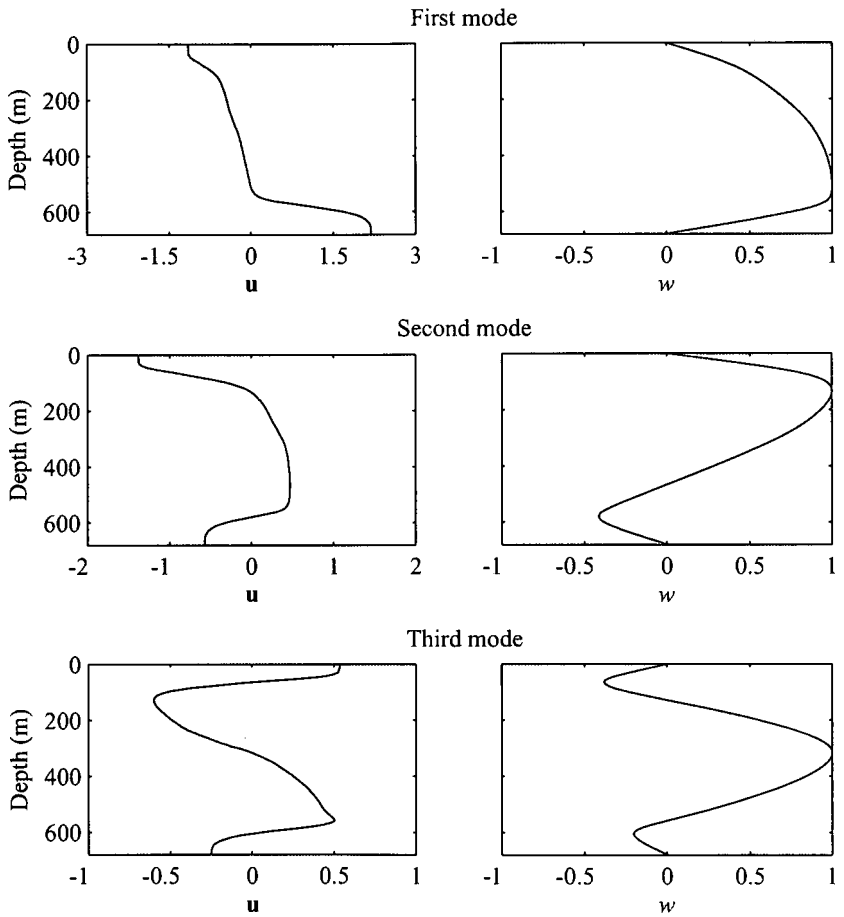

Figure 3.19: Vertical structure modes of horizontal and vertical velocities for the time-averaged buoyancy frequency profile from the repeat station.

3.6 Discussion and conclusions

The aim of the slope mixing experiment was to make measurements of internal waves, their induced mixing, and bottom boundary layer structure over the West Shetland slope. Excellent measurements of internal waves were achieved through a combination of moored instruments and lowered ADCP/CTD casts. Measurements of turbulent mixing by internal waves is limited to indirect methods because no direct turbulence measurements are available. A microstructure profiler was mounted on the specialist instrument package HOMER, but unfortunately the sensor module, along with all the microstructure data, was lost during recovery. Bottom boundary layer forms were intended to be measured by the specialist instrument package STABLE. Unfortunately, all the high-frequency, near-bed current and temperature data became corrupted during the cruise and was irretrievable.

The internal wave field contains a semi-diurnal baroclinic tide of a comparable magnitude to the barotropic tide and intermittent higher-frequency, non-linear internal waves that are bottom-trapped by the main pycnocline maintained close to the seabed. The internal tide is observed in the mooring time series and in the lowered ADCP/CTD profiles from the repeat station. In the mooring time series the presence of an internal tide is suggested by a semi-diurnal vertical displacement of isotherms (and inferred isopycnals) and a $\sim 180°$ phase shift in across-slope velocity. However, the true baroclinic component of the tide can only be determined from the full-depth profiles. The largest semi-diurnal vertical isopycnal displacements, of the order 10 m, are observed in the main pycnocline and the largest baroclinic velocity amplitudes, > 0.1 m s^{-1}, are observed in and below the pycnocline. This is in agreement with a mode-1 internal tide. However, vertical displacement goes to zero at mid-depths suggesting that the higher modes of internal wave variability maybe present. Vertical displacement does not go to zero at the surface and the bottom, suggesting that some horizontal advection of isopycnals by the barotropic tide occurs. The vertical displacement and across-slope velocity time series from the moorings also contain quarter-diurnal signals.

Previous observations of the internal tide in the Faro-Shetland Channel by Sherwin (1991) were made at a station at the southwestern end of the channel, near the base of the Wyville Thomson Ridge. M_2 period vertical displacements of 37 m were observed in the main pycnocline at 580 m. Baroclinic horizontal velocities were 0.1 m s^{-1} above and 0.2 m s^{-1} below the pycnocline. These are several times larger than observed here, but the observations of Sherwin were

made local to the Wyville Thomson Ridge, the proposed generation region. By comparison, the site of the slope mixing experiment is approximately 110 km to the east, by which point some dispersion and/or dissipation of the internal tide will have occurred. The internal tide is linear in the centre of the channel (where observations were made), but Sherwin speculates that it is likely to be non-linear at the boundaries and the energy associated with the internal tide may be dissipated by mixing on the shelf slope.

The near-bed internal wave field over the West Shetland slope was well sampled by the moored ADCPs and thermistor moorings during the slope mixing experiment. High-frequency, non-linear internal waves are observed intermittently in the temperature time series and have the form of solitary waves, cnoidal wave trains, and solibores. Wave amplitudes are up to 50 m while the wave periods are typically in the range 15 to 30 minutes. During some sections of the time series the wave trains appear at roughly semi-diurnal intervals in the mooring time series but the phase relation with the local barotropic tide is variable, suggesting they are generated by the tide at a remote location. Hosegood and van Haren (2004) observed similar non-linear internal wave trains propagating up the West Shetland slope and proposed the passage of a non-linear Kelvin wave as a generation mechanism for the hydraulic jumps. They discount internal tide forcing because the periodicity of the solibores was typically four days, but here semi-diurnal periodicity is evident for over half the time series.

Klymak and Moum (2003) made direct turbulence measurements through similar bottom-trapped internal solitary waves on the Oregon continental shelf using a microstructure profiler. They identified high turbulent kinetic energy dissipation rates, $\sim 10^{-6}$ W kg^{-1}, in the bottom boundary layer. Hosegood and van Haren (2004) also measured high turbulent kinetic energy dissipation rates, order 10^{-7} W kg^{-1}, within the intruding dense water, and maximum vertical diffusivities of the order 10^{-1} m^{-2} s^{-1}. However, average diffusivities were several orders of magnitude smaller, suggesting that solibores are not important for supporting deep ocean mixing. The more frequent occurrence of non-linear internal waves trains in this dataset (typically two per day as opposed to one every four days) may change this view. However, Hosegood et al. (2004) suggest solibores are the dominant sediment transport mechanism on the shelf slope. During the passing of a solibore, they measured sediment fluxes up the slope of the order 10^2 greater than background levels.

Klymak and Moum (2003) propose the source of the turbulence is either shear instabilities in the pycnocline or bottom stress. Here, high levels of shear,

$> 10^{-4}$ s^{-2}, are observed in the pycnocline but the threshold Richardson number for the onset of turbulence is only occasionally met. It is therefore likely that any enhanced mixing associated with the near-bed, non-linear internal waves is the result of bottom stress. Klymak and Moum also note the dissipation rates suggests a decay time-scale longer than it takes the waves to reach the shore, suggesting internal wave breaking further up the sloping shelf. This process is also likely on the West Shetland slope because the near-bed buoyancy frequency further up the slope is less than the angular frequency of the waves.

In summary, a semi-diurnal internal tide and near-bed, non-linear internal waves are observed on the West-Shetland slope. These waves are suspected to play an important role in supporting turbulent mixing on the slope, either through gradual dissipation of internal wave energy by shear instabilities and bottom stress, or rapid conversion to turbulent kinetic energy by internal wave breaking. Indirect estimates of turbulent mixing from the lowered ADCP and CTD profiles are made in Chapter 4 and energy fluxes associated with the observed internal waves are calculated in Chapter 5.

Chapter 4

Mixing parameters

4.1 Introduction

Mixing of water mass properties, such as temperature and salinity, affects ocean circulation from to local to global scales. In estuaries, the pattern of circulation is determined by how rapidly the freshwater and seawater mix, while on global scales, mixing of heat downwards into the ocean interior is required to allow upwelling of deep water that closes the Meridional Overturning Circulation. By transporting nutrients from the deep ocean to the euphotic surface layer, ocean mixing is also a key control on primary production and carbon drawdown.

In the absence of mechanical inputs of energy, heat and salt diffuse slowly by molecular processes; typical molecular diffusivities of heat and salt are of the order 10^{-7} and 10^{-9} m^2 s^{-1}. In weakly turbulent regions the difference in molecular diffusivities leads to double diffusive phenomenon, such as salt fingering and salt layering, if the temperature and salinity gradients have opposing effects on density (see Turner 1973 for a review). In the ocean, mixing is maintained above molecular levels by inputs of kinetic energy, primarily wind and tidal forcing. Instabilities in sheared flows cause turbulent eddies that cascade kinetic energy to progressively smaller scales and at the same time transporting parcels of water and their associated properties down property gradients. The energy is eventually dissipated at molecular scales by viscosity. As most down-gradient exchange occurs at small scales, mixing of water mass properties by eddies is generally parameterised as eddy diffusivities. This is particularly important in numerical ocean models because turbulent eddies often occur at sub-grid scales.

Direct measurements of diapycnal (across density surfaces) eddy diffusivity in the interior of the open ocean, from the dispersion of chemical tracer and measurements of small-scale turbulence, suggest typical values are of the order 10^{-5} m^2 s^{-1} (Ledwell et al., 1993; Toole et al., 1994), many orders of magnitude

smaller than eddy diffusivities along isopycnals, estimated to be > 100 m^2 s^{-1} (Kawabe, 2008; Armi and Stommel, 1983). Mixing across density surfaces requires more energy than mixing along isopycnals because work must be done on buoyancy.

Indirect estimates of diapycnal diffusivity, from the balance of deep convection and global upwelling against the strength of abyssal stratification (Munk, 1966), suggest average values of 10^{-4} m^2 s^{-1} in the deep ocean, an order of magnitude larger than direct measurements. This estimate is reduced to 3×10^{-5} m^2 s^{-1} by including Southern Ocean upwelling (Webb and Suginohara, 2001). One explanation for the inconsistency between direct and indirect estimates, is that there are areas of enhanced mixing at the ocean boundaries and mixed water is transported into the interior along isopycnal surfaces (Munk and Wunsch, 1998); indeed, in the Brazil Basin diapycnal diffusivity has been found to be several orders of magnitudes higher over the rough topography of the Mid-Atlantic Ridge than over the smoothly abyssal plain (Polzin et al., 1997; Ledwell et al., 2000). Enhanced diapycnal diffusivities have also been found over rough topography in the Nordic seas and Southern Ocean (Naveira Garabato et al., 2004a,b), and over the Kerguelen Plateau (Park et al., 2008). Although these and other areas of rough topography may contribute significantly, further work is required to close the global deep ocean mixing budget.

Diapycnal eddy diffusivity, κ_ρ, can be inferred from the rate of turbulent kinetic energy (TKE) dissipation, ϵ, by the empirical relationship

$$\kappa_\rho = \Gamma \frac{\epsilon}{N^2}, \tag{4.1}$$

where N is buoyancy frequency and Γ is mixing efficiency, the ratio of turbulent kinetic energy converted to potential energy to the energy dissipated (Osborn, 1980).

Accurate estimates of TKE dissipation require direct turbulence measurements from a microstructure profiler (Schmitt et al., 1988). However, the microstructure dataset is sparse due to the cost of the instruments and the expertise required for their deployment. Therefore, indirect methods are often used to estimate TKE dissipation from CTD or ADCP data. These datasets are extensive and could be used to constrain the level of mixing over large areas of the ocean.

In this chapter, CTD and lowered ADCP profiles from the slope mixing experiment (see Chapter 3) are used to infer TKE dissipation rates and diapycnal eddy diffusivities on the West Shetland slope. Two independent methods are used: Thorpe scale analysis of density overturns (Section 4.2) and a finescale pa-

rameterisation of vertical shear and strain (Section 4.3). The results are compared and the method limitations discussed in Section 4.4.

4.2 Thorpe scaling

The rate of TKE dissipation is inferred from vertical profiles of potential density using a method developed by Thorpe (1977) that relates the length-scale of density overturns to the Ozmidov scale,

$$L_O = \sqrt{\frac{\epsilon}{N^3}}, \tag{4.2}$$

the dissipation length-scale (Ozmidov, 1965). The length-scale of density overturns is calculated by reordering all the samples in each potential density profile so that the watercolumn is statically stable. The vertical distance that each sample is moved during the reordering process is the Thorpe displacement (L). Figure 4.1 shows the measured and reordered density profile through a single overturn, and the corresponding Thorpe displacements. The Thorpe scale (L_T) is the rms Thorpe displacement over a section of profile containing a complete overturn[1], and is empirically related to the Ozmidov scale by $L_O = 0.8L_T$ (Dillon, 1982). Substituting this relationship into Equation (4.2), ϵ can be inferred from L_T and N,

$$\epsilon = 0.64{L_T}^2 N^3. \tag{4.3}$$

To be representative of the stratification against which the overturn is straining, N should be calculated over the depth range of the overturn from the reordered potential density profile (Fer et al., 2004). Then, from Equations (4.1) and (4.3), and using a typical mixing efficiency $\Gamma = 0.2$ (Osborn, 1980; Oakey, 1982), diapycnal eddy diffusivity can be estimated

$$\kappa_\rho \simeq 0.1{L_T}^2 N. \tag{4.4}$$

The resolution of Thorpe displacements by the CTD may be limited by either the depth (pressure) or the density (temperature and salinity) resolution depending on the stratification (Stansfield et al., 2001), and puts a lower bound on the TKE dissipation rates that can be inferred. The actual resolution of the CTD is the largest of the depth resolution, Δz_{inst}, and the density resolution scaled by the background density gradient, $\Delta\rho_{\text{inst}}(d\rho/dz)^{-1}$. To minimise Δz_{inst},

[1] A complete overturn is defined as a section of profile where all the samples above are less dense than the samples in the section and all the samples below are denser than the samples in the section (see Figure 4.1)

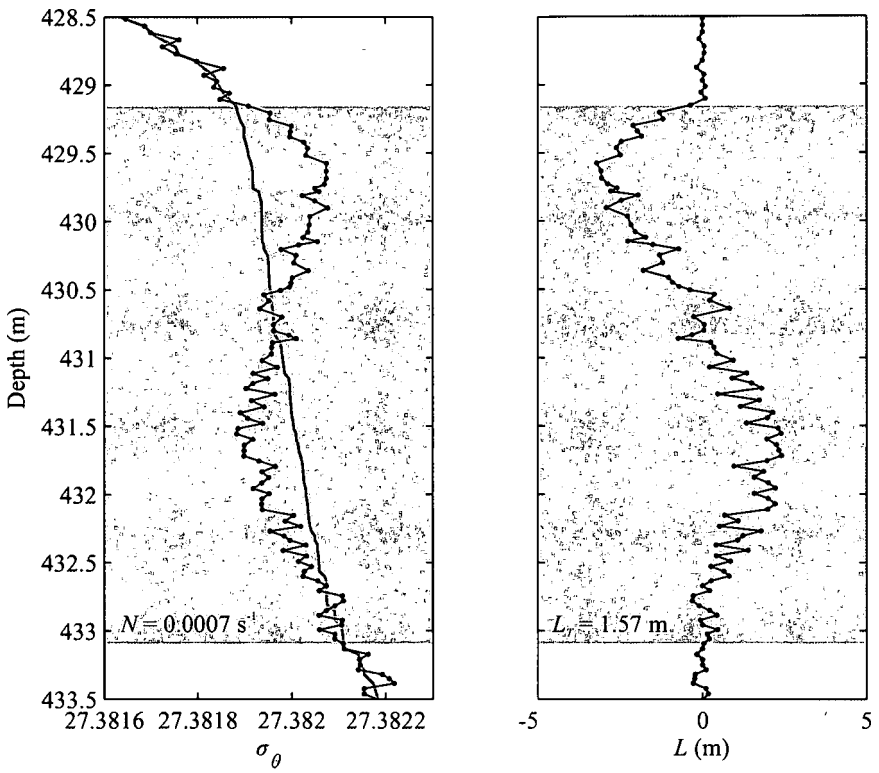

Figure 4.1: Measured (black) and reordered (grey) potential density profiles, and Thorpe displacements through a typical example turbulent overturn. The grey areas mark the vertical extent of the complete overturn.

the original 24 Hz sampling frequency of the SBE 911plus CTD is retained during processing. For the typical CTD descent rate of 1 m s^{-1}, this equates to ~ 0.04 m resolution. However the resolution of the pressure sensor limits Δz_{inst} to 0.11 m. $\Delta\rho_{\text{inst}}$ is quoted at 0.0004 kg m^{-3}, giving resolution of Thorpe displacements < 1.5 m away from the surface and bottom boundary layers where $d\rho/dz$ goes to zero. Where $N^2 > 3.5 \times 10^{-5}$ s^{-2}, such as in the main pycnocline and seasonal thermocline, depth resolution is the limiting factor; in between the regions of stratification density resolution is the limiting factor.

An important consideration when using standard CTD equipment is the generation of turbulence in the wake of the instrument package as it descends. This is a problem during the up cast, because the CTD is moving through water that has previously been mixed by the instrument package during the down cast, and if the descent of the CTD is halted rapidly. The same problem occurs if the descent rate of the CTD is seriously affected by vertical ship motion. In heavy seas, heaving of the ship can cause the CTD to temporarily ascend during the downcast, forming short pressure reversals. Mounting the sensors on the bottom of the frame reduces the influence of wake generated turbulence and three screening procedures were included during processing to minimise the number of wake generated turbulent overturns in the dataset:

1. Only the down casts were processed and periods when the CTD was held at a constant depth (either just below the surface or near the seabed) were flagged.

2. Pressure reversals were removed by only retaining samples with a higher pressure than all previous samples from the cast.

3. Casts or sections of casts with frequent pressure reversals or rapid changes in descent rate where flagged.

Fifteen CTD casts were flagged unsuitable for Thorpe scaling by the screening procedures, mainly due to a large number of pressure reversals caused by heavy seas. In addition, the upper 100 m and lower 50 m of most casts were flagged because the descent rate was < 1 m s^{-1}, increasing the likelihood of pressure reversals. In total, only 72 casts passed the screening process with sections $\geq$ 400 m unflagged.

Measured density profiles may contain spurious density inversions from instrumental noise that must be distinguished from real turbulent overturns to accurately infer the rate of TKE dissipation. Some inversions may result from

differences between the temperature and conductivity sensor response times or the thermal lag of the conductivity cell (Lueck and Picklo, 1990; Morison et al., 1994); both effects are corrected for during processing. Alternatively, Thorpe displacements can be calculated from potential temperature profiles, but this method risks spurious temperature inversions associated with density compensating salinity intrusions. This problem is avoided by using potential density profiles.

Other spurious density inversions may result from random instrumental noise. Spikes in the temperature profiles are removed by calculating a 25-point ($\sim$ 1 m) running mean and standard deviation. Any value more than three standard deviations away from the mean is replaced by the mean value (Stansfield et al., 2001). The salinity profiles have a higher random noise level than the temperature profiles as well as frequent spikes. The salinity spikes are removed by the same process as the temperature spikes but with a 125-point ($\sim$ 5 m) window and a threshold of one standard deviation. A wide window and strict standard deviation threshold is required because the frequent spikes contribute significantly to standard deviation of the windowed data. The random instrumental noise in the salinity profiles is reduced by averaging with a 125-point running mean. Density in the channel is primarily determined by temperature so this averaging does not have large effect on the density profiles, but does remove any compensating salinity intrusions that are smaller than noise level. As salinity noise is large compared to the size of salinity inversions implied by potential temperature diagnosed overturns, this is the best compromise.

Finally a 'run-length' test is applied to each density overturn (Galbraith and Kelley, 1996)[2]. Individual density overturns are identified from the Thorpe fluctuation profile,

$$\rho'(z) = \rho(z) - \hat{\rho}(z), \tag{4.5}$$

where $\rho(z)$ is the measured density profile and $\hat{\rho}(z)$ is the reordered density profile. The sum of Thorpe fluctuations over an entire overturn is zero so the cumulative sum is used to separate the profile into sections, each containing a complete overturn.

[2]Galbraith and Kelley (1996) also describe a 'water mass' test, but this method assumes a smooth θ-S covariation in the overturning region that does not hold in the channel due to the complex water mass structure.

4.2.1 Run-length test

The run-length of a series is calculated by examining a series sequentially and grouping adjacent values with the same sign into 'runs'. The number of data points in each run is the run-length. The probability density function (PDF) of run-length for a random, uncorrelated series with an equal number of positive and negative values is

$$P(n) = 2^{-n}, \tag{4.6}$$

where $P(n)$ is the probability of a run-length n. Therefore, if a density inversion is caused by random instrumental noise, the PDF of Thorpe fluctuation run-length should be 2^{-n}. However, real turbulent overturns are likely to have a long positive run of Thorpe fluctuations followed by a long negative run, so if a real overturn is present in the section the probability of longer runs will be larger than 2^{-n}. For the run-length test, the rms run-length is calculated for each section of Thorpe fluctuation profile and if longer than the rms run-length expected for a random uncorrelated time series,

$$(\sum_{1}^{\infty} n^2 2^{-n})^{1/2} = \sqrt{6}, \tag{4.7}$$

the overturn is considered real (Timmermans et al., 2003).

Johnson and Garrett (2004) raise two important issues with using run-length to distinguish between noise and real turbulent overturns. Firstly, reordering the profile so that density increases monotonically with depth introduces a bias towards long runs near the top and bottom of the profile. The proportion of the profile that is affected by the bias depends on the amplitude of the noise and the background stratification, increasing as the noise amplitude approaches the total, top-to-bottom, density difference. In this regime the rms run-length is expected to be longer than for a random uncorrelated time series. Here, only profile sections longer than 400 m are used; the ends of the sections are typically in regions of strong stratification, beginning in the seasonal thermocline and ending in the main pycnocline, so the bias towards longer runs is minimised.

Secondly, if the noise amplitude is smaller than the average density difference between consecutive samples, noise will not necessarily result in density inversions, introducing a bias towards short runs. In this regime the rms run-length is expected to be shorter than for a random uncorrelated time series. In the main pycnocline the average density difference between consecutive samples is of the order 4×10^{-4} kg m^{-3} (compared to a noise amplitude of 0.003 kg m^{-3}), so rejecting a density inversion on the basis that the rms run-length is less than $\sqrt{6}$ will result in the rejection of some small but real turbulent overturns. However,

in the absence of an alternative statistical method, $\sqrt{6}$ is maintained as the expected run-length with the caveat that the values inferred may be overestimated in the main pycnocline.

4.2.2 Temporal and spatial averaging

Due to the heterogeneous nature of turbulent overturns in time and space, Thorpe scales must be averaged over a large domain to attain values of TKE dissipation rate and diapycnal eddy diffusivity that can be meaningfully compared to macroscale processes such as internal waves. For example, if ϵ is calculated from the Thorpe scale across a single overturn, it is only relevant to that overturning event.

The most suitable casts for Thorpe scaling are those from the repeat station as some time-averaging can be included. Fortunately, most of the casts from the repeat station passed the screening process relatively unflagged. Thorpe displacements for the repeat station casts are shown in Figure 4.2. Only these casts included in this analysis.

L_T, N, ϵ, and κ_ρ are vertically averaged in two ways. Firstly, the variables are averaged in 50 m vertical bins, from 50 to 650 m. Secondly, the variables are averaged in three layers with relatively constant background buoyancy frequencies: the seasonal thermocline (50-150 m); the main pycnocline (550-650 m); and the buoyancy minimum between the two stratified layers (150-550 m). In both cases each vertical bin is time-averaged through the 24 casts[3] from the repeat station and the standard error (standard deviation divided by the square root of the number of samples) calculated.

4.2.3 Errors

Errors in the estimation of ϵ and κ_ρ from Thorpe scales arise firstly from the accuracy of the CTD in the measurement of L_T, estimated to be 0.3 m. There is a small error in the calculation of N due to the resolution of density and depth and $\sim$ 60% uncertainty in the empirical constant relating L_O to L_T (Ferron et al., 1998). The temporal sampling error is estimated as the standard error between the 24 casts. Including all sources of uncertainty, ϵ can be calculated from equation (4.3) within a factor of 3 (Fer et al., 2004)

There is also uncertainty in the mixing efficiency used for Equation (4.1), Γ being dependent on the type of instability causing the turbulence (Wijesekara et al., 1993). From the literature, estimates of Γ in the open ocean vary between 0.15

[3]One cast was completely flagged during screening.

and 0.3, increasing the uncertainty in the calculation of κ_ρ from Equation (4.4) to a factor of 4.

4.2.4 Results

Before approaching the time-averaged results it is of interest to at look the casts individually. The largest Thorpe displacements occur at around 200 m, below the seasonal thermocline (Fig. 4.2). Displacements approaching 40 m are observed which seem unusually large given the displacements are typically < 10 m elsewhere. As the large displacements occur where the background buoyancy frequency is minimum, there is a possibility the density inversions may be the result of instrumental noise. However, the two largest overturning events (hours 19 and 20 at ~ 200 m) contain long runs of negative displacements followed by long runs of positive displacements, characteristic of real turbulent overturns. Other large Thorpe displacements occur below 650 m in a well mixed bottom boundary layer. As the background buoyancy frequency goes to zero, the layer is unsuitable for Thorpe scale analysis.

Thorpe scales of individual overturns range from 0.02 m to 15 m but for more than 75% of overturns $L_T < 1$ m (Fig. 4.3). The most frequent occurences are between 0.1 and 0.3 m. Figure 4.4 shows Thorpe scale calculated for a single cast from the repeat station (hour 9). There is a large scatter between zero and 2 m, but most overturns with Thorpe scales larger than 2 m are in the buoyancy minimum. The buoyancy frequency profile also contains considerable scatter, particularly in the main pycnocline where the buoyancy across overturns at similar depths varies by up to a factor of three. There is typically less scatter at mid-depths, where N is small. As TKE dissipation rate and diapycnal eddy diffusivity are dependent on these two variables, it is not suprising that there is a lot of scatter in the inferred values. ϵ varies between 10^{-12} and 10^{-6} W kg^{-1}, with the most frequent values of the order 5×10^{-11} W kg^{-1}. κ_ρ varies between 10^{-7} and 10^{-2} m^2 s^{-1}, with the most frequent values of the order 5×10^{-6} m^2 s^{-1}.

Averaged in 50 m vertical bins and and time-averaged through all the casts from the repeat station, a coherent pattern emerges (Fig. 4.5). L_T is longest, 1.4 m, at around 200 m, decreasing to 0.4 m in the seasonal thermocline and 0.6 in the main pycnocline. Due primarily to the sensitivity to N, ϵ is largest in the main pycnocline ($\sim 4 \times 10^{-8}$ W kg^{-1}) and seasonal thermocline ($\sim 2 \times 10^{-8}$ W kg^{-1}). Between 100 and 550 m $\epsilon < 10^{-8}$ W kg^{-1}, and at a minimum of 10^{-9} W kg^{-1} around 400 m. κ_ρ is less sensitive to N so is maximum, 6×10^{-4} m^2 s^{-1}, at the

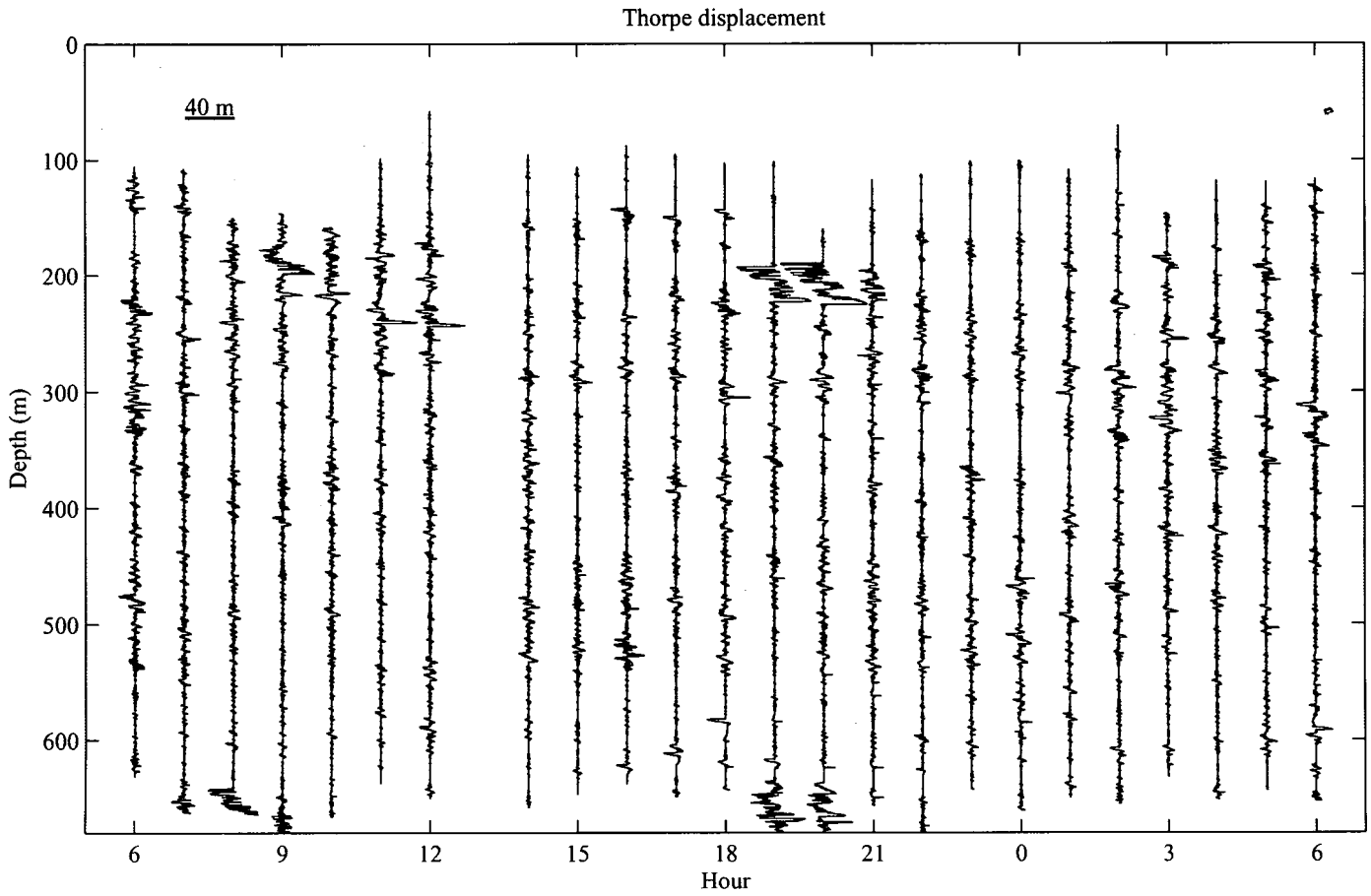

Figure 4.2: Thorpe displacements for all the casts from the repeat station that passed the screening process.

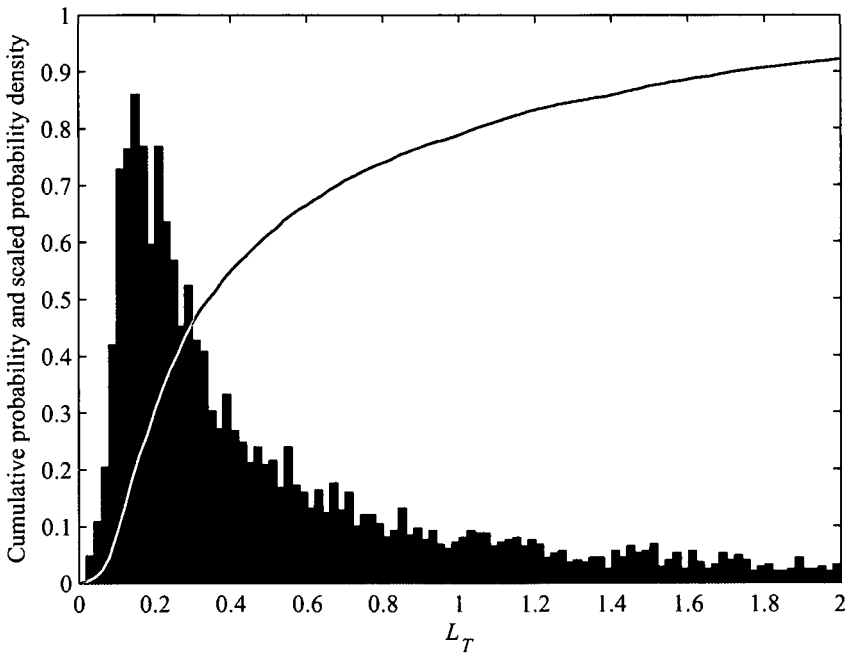

Figure 4.3: Cumulative probability distribution (grey line) and scaled probability density distribution (black bars) of Thorpe scale.

same depth at L_T, decreasing to 10^{-4} m^2 s^{-1} in the seasonal thermocline and at around 400 m. In the main pycnocline κ_ρ increases to 3×10^{-4} m^2 s^{-1}.

For comparison with the following finescale parameterisation the mixing parameters are vertically averaged in three layers (see Section 4.2.2). TKE dissipation rate and diapycnal eddy diffusivity are both largest in the main pycnocline ($2.9 \pm 0.5 \times 10^{-8}$ W kg^{-1} and $2.5 \pm 0.3 \times 10^{-4}$ m^2 s^{-1} respectively), where the average Thorpe scale is 0.59 ± 0.03 m (Table 4.1). L_T is longest, 0.80 ± 0.02 m, in the buoyancy minimum, but because N is small, ϵ is an order of magnitude smaller than in the pycnocline. Despite κ_ρ being maximum around 200 m, the lower diffusivities at other depths in the buoyancy minimum decrease the average to $1.9 \pm 0.1 \times 10^{-4}$ m^2 s^{-1}. In the seasonal thermocline, L_T is minimum, 0.46 ± 0.06 m, equivalent to a dissipation rate of $0.5 \pm 0.3 \times 10^{-8}$ W kg^{-1} and a diffusivity of $1.2 \pm 0.4 \times 10^{-4}$ m^2 s^{-1}.

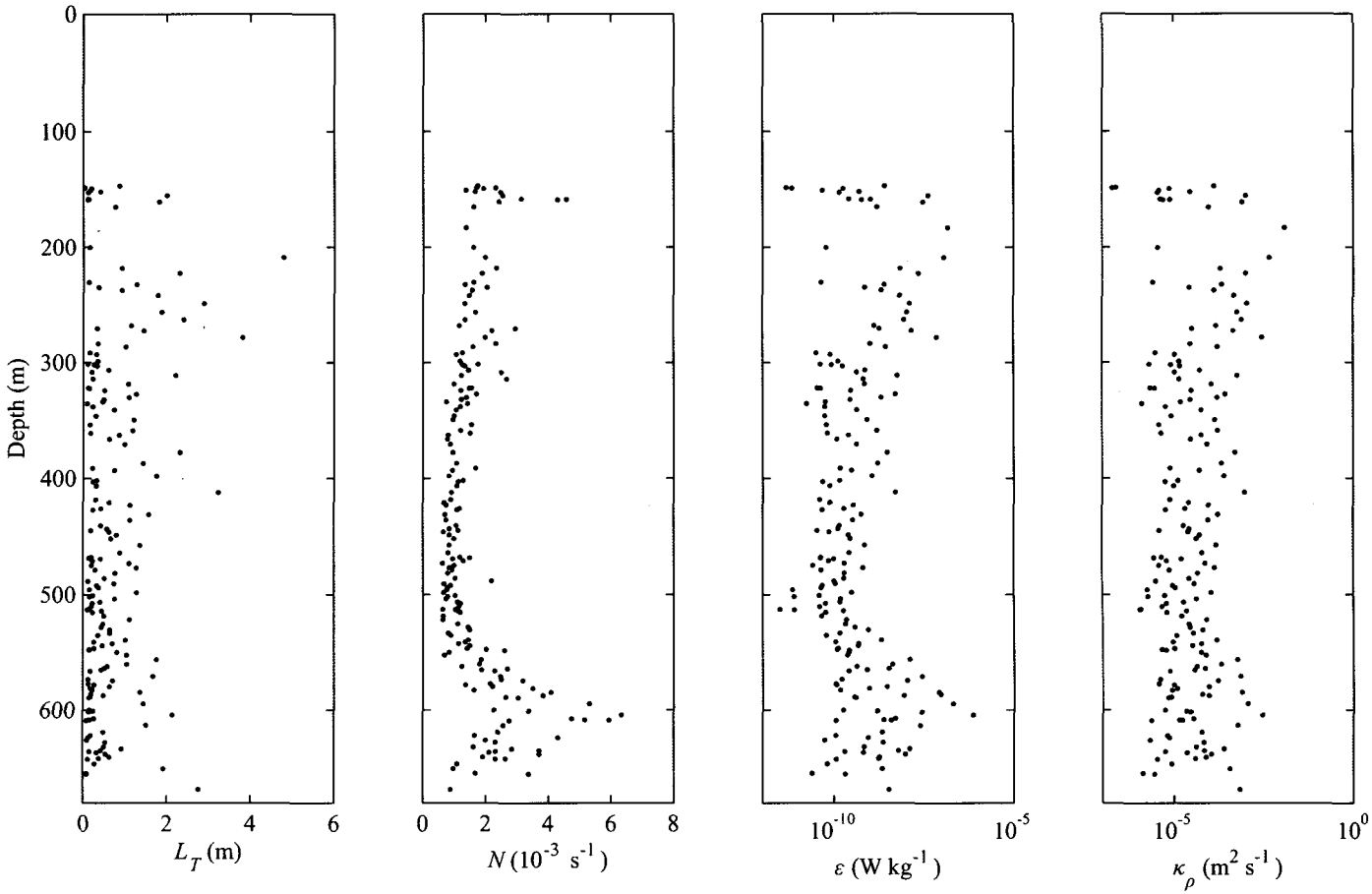

Figure 4.4: Thorpe scale, buoyancy frequency, TKE dissipation rate, and diapycnal eddy diffusivity for a single cast from the repeat station (hour 9).

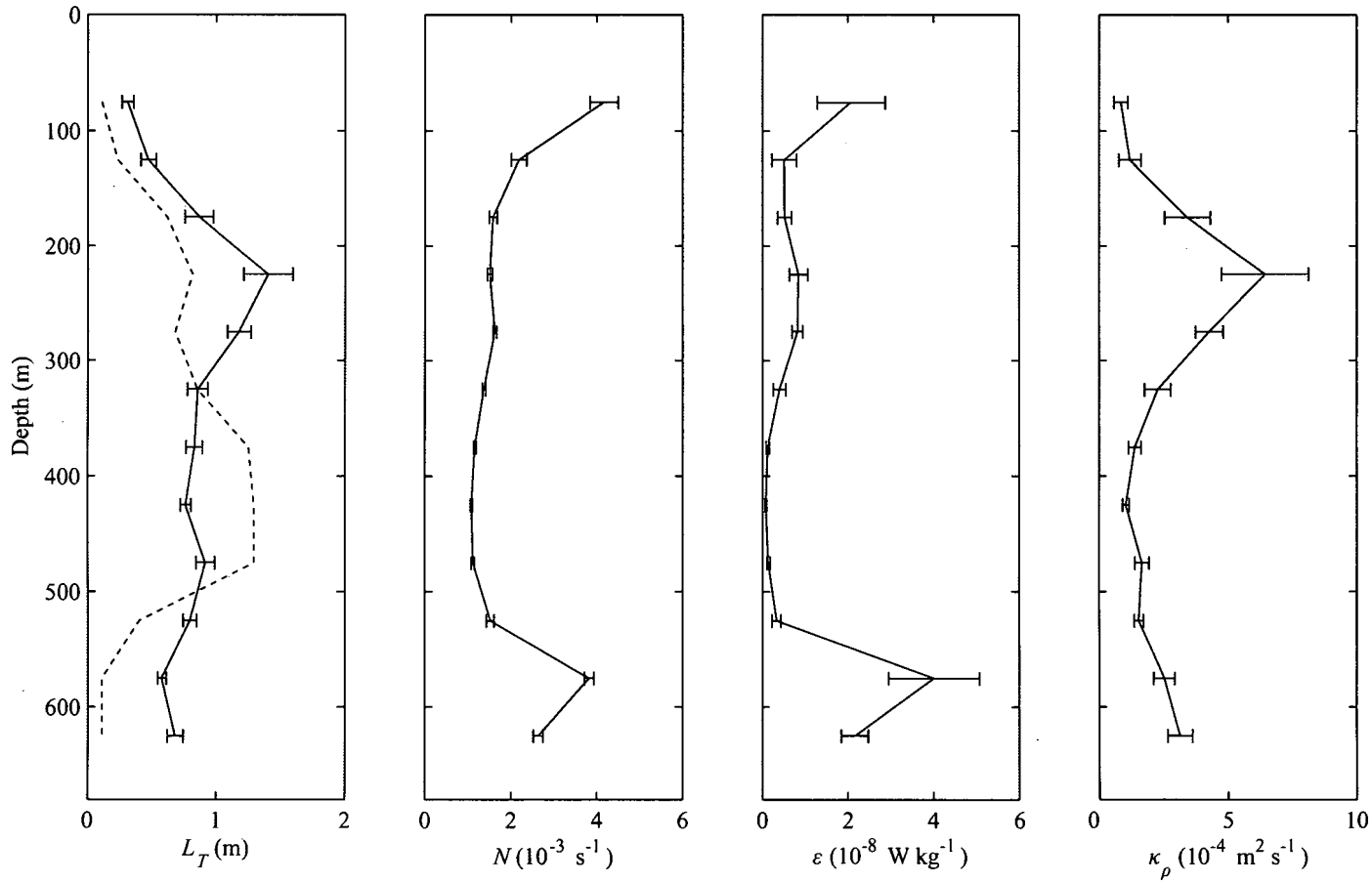

Figure 4.5: Thorpe scale, buoyancy frequency, TKE dissipation rate, and diapycnal eddy diffusivity in 50 m vertical bins during the repeat station. The error bars are the standard error. The dashed line is the CTD resolution limit.

Layer (m)	L_T (m)	N (10^{-3} s^{-1})	ϵ Thorpe (10^{-8} W kg^{-1})	κ_ρ Thorpe (10^{-4} m^2 s^{-1})
50-150	0.46 ± 0.06	2.29 ± 0.19	0.54 ± 0.28	1.17 ± 0.42
150-550	0.80 ± 0.02	1.36 ± 0.02	0.29 ± 0.03	1.86 ± 0.13
550-650	0.59 ± 0.03	3.30 ± 0.05	2.88 ± 0.46	2.48 ± 0.25

Table 4.1: Summary of Thorpe scales, buoyancy frequencies, TKE dissipation rates, and diapycnal eddy diffusivities in three layers: the seasonal thermocline (50-150 m); the main pycnocline (550-650 m); and the buoyancy minimum between the two stratified layers (150-550 m). The uncertainty is the standard error.

4.3 Finescale parameterisation

To provide a comparison for the mixing estimates inferred from the Thorpe scale analysis, independent estimates of TKE dissipation rate are made using the Gregg-Henyey finescale parameterisation, based on the Garrett and Munk (GM) model of the background internal wave field (Garrett and Munk, 1975; Cairns and Williams, 1976). In the parameterisation, ϵ is dependent on the spectra of vertical shear and strain, computed from the lowered ADCP and CTD profiles, compared with the GM model following the method of Henyey et al. (1986), Gregg (1989), and Polzin et al. (1995). For the shear parameterisation,

$$\epsilon_{\text{ shear}} = \epsilon_0 \times \frac{f}{f_0} \times \frac{\cosh^{-1}(N/f)}{\cosh^{-1}(N_0/f_0)} \times \frac{N^2}{N_0^2} \times \frac{\langle V_z^2 \rangle^2}{\langle V_{z\,\text{GM}}^2 \rangle^2} \times F_1(R_\omega), \tag{4.8}$$

where $\langle V_z^2 \rangle$ is the measured variance of vertical shear ($d\mathbf{u}/dz$); $\langle V_{z\,\text{GM}}^2 \rangle$ is the variance of vertical shear from the GM model; $\epsilon_0 = 7.8 \times 10^{-10}$ W kg^{-1}, $f_0 = 7.29 \times 10^{-5}$ s^{-1}, and $N_0 = 5.24 \times 10^{-3}$ s^{-1} are characteristic constants from the model. For the equivalent strain parameterisation,

$$\epsilon_{\text{ strain}} = \epsilon_0 \times \frac{f}{f_0} \times \frac{\cosh^{-1}(N/f)}{\cosh^{-1}(N_0/f_0)} \times \frac{N^2}{N_0^2} \times \frac{\langle \xi_z^2 \rangle^2}{\langle \xi_{z\,\text{GM}}^2 \rangle^2} \times F_2(R_\omega), \tag{4.9}$$

where $\langle \xi_z^2 \rangle$ is the measured variance of vertical strain ($d\xi/dz$) and $\langle \xi_{z\,\text{GM}}^2 \rangle$ is the variance of vertical strain from the GM model. In both parameterisations, the last term, $F_{1,2}(R_\omega)$, corrects for small deviations from the GM spectra. Following Kunze et al. (2006), for the shear parameterisation

$$F_1(R_\omega) = \frac{3(R_\omega + 1)}{2\sqrt{2} R_\omega \sqrt{R_\omega - 1}}, \tag{4.10}$$

and for the strain parameterisation

$$F_2(R_\omega) = \frac{R_\omega(R_\omega + 1)}{6\sqrt{2}\sqrt{R_\omega - 1}}, \tag{4.11}$$

where R_ω is the shear-to-strain ratio, an estimate of the frequency content of the internal wave field. R_ω is typically calculated from the shear and strain variances,

$$R_\omega = \frac{\langle V_z^2 \rangle}{N^2 \langle \xi_z^2 \rangle}, \tag{4.12}$$

(e.g. Naveira Garabato et al. 2004a,b; Kunze et al. 2006), but for time series data an alternative definition can be used following Polzin et al. (1996),

$$R_\omega = \frac{\sum [(u_z - \langle u_z \rangle)^2 + (v_z - \langle v_z \rangle)^2) / \langle N^2 \rangle]}{\sum [(\langle N^2 \rangle - N^2) / \langle N^2 \rangle]^2}, \tag{4.13}$$

where u_z and v_z are the vertical gradients of horizontal velocity and $\langle\rangle$ denotes a time-average. For the GM frequency spectrum the shear-to-strain ratio is 3 by design and so $F_{1,2}(R_\omega) = 1$.

The central assumption of parameterisation (4.8) and (4.9) is that in a statistically steady-state internal wave field, turbulent kinetic energy is produced at the same rate as it is transfered from large to small scales by linear wave-wave interactions, and eventually dissipated by internal wave breaking. Most successful previous applications have been for the interior of the open ocean (Gregg et al., 2003; Naveira Garabato et al., 2004a,b; Kunze et al., 2006) while applications in shelf seas and on continental slopes have had limited success (Kunze et al., 2002; MacKinnon and Gregg, 2003; Nash et al., 2004, 2007). It has been suggested that the parameterisation fails on continental shelves because the internal wave field does not satisfy the vertical wavenumber bandwidth assumptions (MacKinnon and Gregg, 2003), and in canyons because wave scattering and near-critical reflection with topography may transfer energy to small scales more efficiently than linear wave-wave interactions (Kunze et al., 2002; Carter and Gregg, 2002). However, the shear parameterisation has been shown to be consistent with direct turbulence measurements on the continental slope off Virginia (Nash et al., 2004) and Thorpe scale analysis on the Oregon continental slope (Nash et al., 2007).

To lower the noise level, some averaging of the spectra is required. Therefore parameterisation (4.8) and (4.9) are only applied to the 25 casts from the repeat station and the spectra time-averaged in five 5-cast groups[4]. $\langle V_z^2 \rangle$ is computed from vertical profiles of horizontal velocity in the same three layers as the Thorpe

[4]One group contains only four shear profiles because the lowered ADCP failed to record during one cast.

scale analysis. Only long-wavelength variability is included in the variance estimate so both up and down casts are utilised and processed separately, doubling the number of realisations. Each segment is detrended and the power spectra, $S[u,v](k_z)$, calculated using Welch's periodogram with a Hanning window. The spectra are then averaged in time and between the up and down casts. The vertical shear spectrum, $S[V_z](k_z)$, is calculated from the horizontal velocity spectra

$$S[V_z](k_z) = k_z^2(S[u](k_z) + S[v](k_z)) \tag{4.14}$$

where k_z is the angular vertical wavenumber. $S[V_z](k_z)$ is corrected for high wavenumber attenuation due to data processing (Polzin et al., 2002) before the spectrum is integrated to obtain the vertical shear variance,

$$\langle V_z^2 \rangle = \int_{k_z\ \mathrm{min}}^{k_z\ \mathrm{max}} S[V_z](k_z)\ dk_z. \tag{4.15}$$

The lower integration limit is the lowest resolved vertical wavenumber and so varies between the layers (0.063 rad m^{-1} for the seasonal thermocline and main pycnocline and 0.016 rad m^{-1} for the buoyancy minimum). The upper integration limit is fixed at $k_z = 0.126$ rad m^{-1} (equivalent to a vertical wavelength of 50 m) because this is typically the spectral maximum and avoids contamination by instrument noise at shorter wavelengths. In the seasonal thermocline and main pycnocline only two wavenumbers contribute to shear variance (8 in the buoyancy minimum). Although low, this is the same number as used by Kunze et al. (2006) in a global-scale study.

For the equivalent strain parameterisation, $\langle \xi_z^2 \rangle$ is computed from vertical profiles of potential density. The power spectra of potential density, $S[\rho](k_z)$, are obtained in the same way as for horizontal velocity but only the down casts are used. The vertical strain spectrum, $S[\xi_z](k_z)$, is calculated from potential density spectrum and normalised by the background potential density gradient

$$S[\xi_z](k_z) = \frac{k_z^2 S[\rho](k_z)}{(d\rho/dz)^2}. \tag{4.16}$$

To obtain the vertical strain variance, the strain spectrum is integrated between the same limits as the shear spectrum,

$$\langle \xi_z^2 \rangle = \int_{k_z\ \mathrm{min}}^{k_z\ \mathrm{max}} S[\xi_z](k_z)\ dk_z. \tag{4.17}$$

As the data form a time series at a single location, the shear-to-strain ratio is calculated for each layer from Equation (4.13) with all casts included in the time-average. R_ω is 1.72, 1.70, and 1.62 in the layers 50-150 m, 150-550 m, and

550-650 m respectively, smaller than typically found in the open ocean interior (Kunze et al., 2006; Naveira Garabato et al., 2004a,b), but of the same order as found over Kerguelen Plateau by Park et al. (2008) where the water depth is similar. Assuming a typical ratio of 1.7, $F_1(R_\omega) \simeq 2$ and $F_2(R_\omega) \simeq 0.65$. However, this correction introduces a mis-match in the inferred dissipation rates of approximately a factor of 3, so ultimately $F_{1,2}(R_\omega) = 1$ is used.

For the finescale parameterisation, N is the background buoyancy frequency (notated here N_b) and is calculated from the mean density gradient over the depth range of each layer, for each group of casts. This typically is larger than the local buoyancy frequency across overturns, used for the Thorpe scale analysis. For both shear and strain parameterisations, diapycnal eddy diffusivity is calculated from Equation (4.1) using N_b and a mixing efficiency of 0.2. In each layer N_b, ϵ, and κ_ρ are time-averaged between the five groups of casts and the standard error calculated.

4.3.1 GM model spectra

From Gregg and Kunze (1991), the vertical power spectra of horizontal velocity and vertical displacement for the GM model are

$$S[u](k_z) = \frac{3Eb^3N_0^2}{2\pi j_*(1 + k_z/k_{z*})^2}, \tag{4.18}$$

$$S[\xi](k_z) = \frac{Eb^3N_0^2}{2\pi j_* N^2(1 + k_z/k_{z*})^2}, \tag{4.19}$$

where $E = 6.3 \times 10^{-5}$ is a dimensionless energy level; $b = 1300$ m is the scale depth of the thermocline; $N_0 = 5.24 \times 10^{-3}$ rad s^{-1} is a reference buoyancy frequency; and N is the measured background buoyancy frequency. k_{z*} is a reference vertical wavenumber,

$$k_{z*} = \frac{\pi j_* N}{bN_0}, \tag{4.20}$$

where $j_* = 3$ is a reference mode number. To account for the high wavenumber roll-off of shear and strain spectra (Gregg, 1977; Gargett et al., 1981), the model spectra are modified following Munk (1981) to

$$S[u](k_z) \rightarrow S[u](k_z)\frac{k_{z\ \mathrm{crit}}}{k_z} \quad \text{for} \quad k_z \geq k_{z\ \mathrm{crit}}, \tag{4.21}$$

$$S[\xi](k_z) \rightarrow S[\xi](k_z)\frac{k_{z\ \mathrm{crit}}}{k_z} \quad \text{for} \quad k_z \geq k_{z\ \mathrm{crit}}, \tag{4.22}$$

where $k_{z\ \mathrm{crit}} = 0.6$ rad m^{-1} is a critical wavenumber. The GM spectra of vertical shear and vertical strain are then

$$S[V_z](k_z) = k_z^2 S[u](k_z), \tag{4.23}$$

$$S[\xi_z](k_z) = k_z^2 S[\xi](k_z). \tag{4.24}$$

The variances of vertical shear and vertical strain from the GM model are obtained from Equations (4.15) and (4.17) by integrating $S[V_z](k_z)$ and $S[\xi_z](k_z)$ between the same limits as the measured shear and strain.

4.3.2 Errors

The temporal sampling error is estimated as the standard error between the five groups of casts. The total uncertainty in the calculation of ϵ from parameterisation (4.8) and (4.9) is estimated to be a factor of 3 (Polzin et al., 2002). Including the uncertainty in the mixing efficiency used for Equation (4.1), κ_ρ can be calculated within a factor of 4.

4.3.3 Results

The measured spectra of vertical shear are typically above the GM spectra, except for the lowest resolved wavenumbers, where some realisations are below (Fig. 4.6). At wavenumbers above 0.4 rad m^{-1} measured shear variance increases rapidly because of the spectral correction for high wavenumber attenuation. This diversion from GM does not have a significant effect on the shear variance included in parameterisation (4.8) because $S[V_z](k_z)$ is only integrated up to 0.126 rad m^{-1}. The spread of the spectra for the five realisations is around a factor of 5 below the upper integration limit, leading to a spread in $\langle V_z^2 \rangle$ of less than a factor of 3.

The measured spectra of vertical strain typically decrease with increasing wavenumber, being above the GM spectra at the lowest resolved wavenumbers and typically below GM at the highest wavenumbers. The gradient of the variance cascade is between -0.4 and -0.9; by comparison the high wavenumber roll-off gradient of the GM spectrum is -0.1. The spread of the spectra for the five realisations is up to an order of magnitude below the upper integration limit, leading to a spread in $\langle \xi_z^2 \rangle$ of less than a factor of 6.

In all layers, the TKE dissipation rates and diapycnal eddy diffusivities inferred from parameterisations (4.8) and (4.9) are consistent and within the bounds of uncertainty. In the main pycnocline, ϵ is 7.3 ± 2.1 and $4.5 \pm 2.0 \times 10^{-8}$ W kg^{-1} from shear and strain respectively (Tables 4.2 and 4.3); the equivalent values of

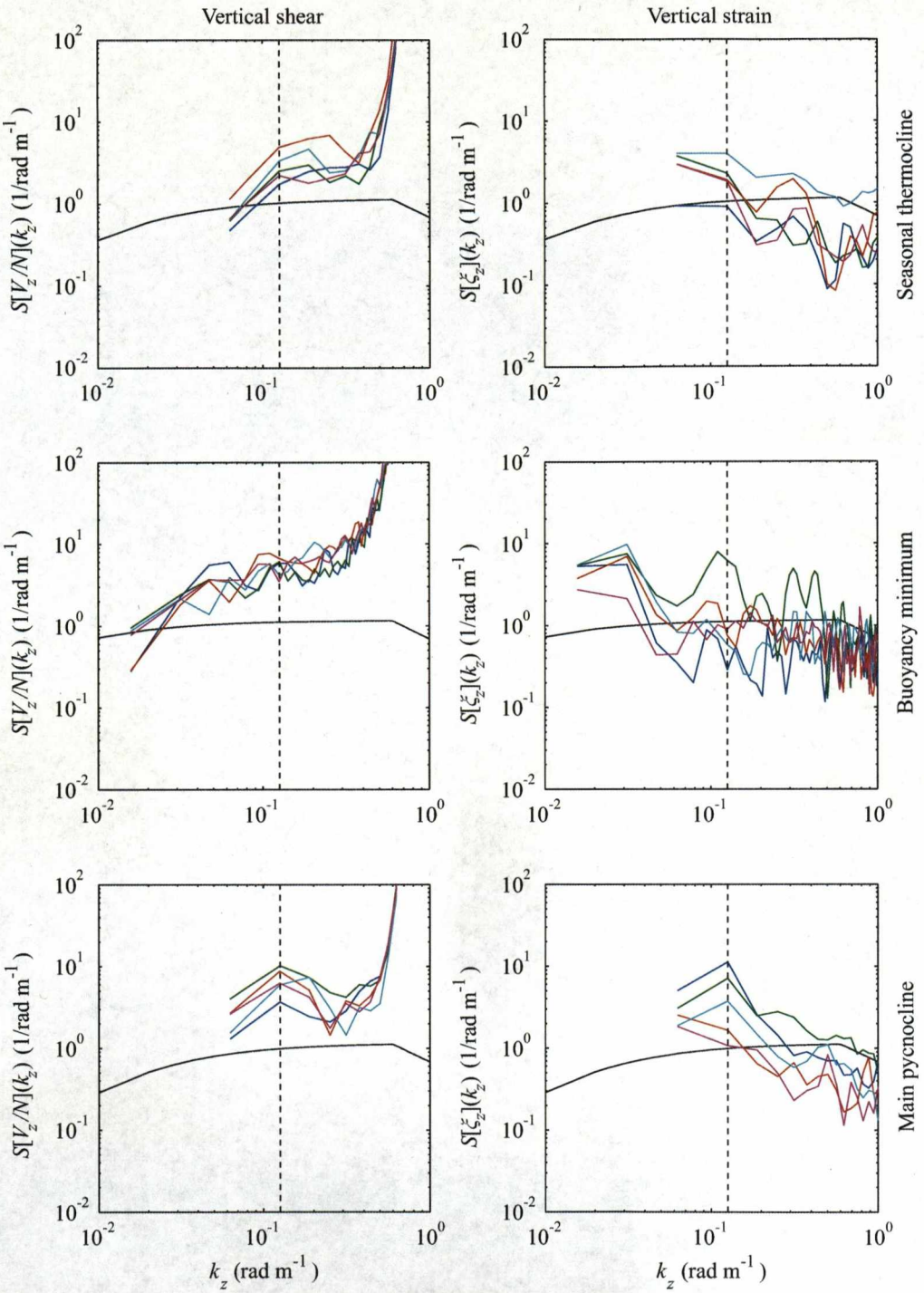

Figure 4.6: Power spectra of vertical shear (normalised by N) and vertical strain for three layers of the watercolumn: the seasonal thermocline; the buoyancy minimum; and the main pycnocline. The black lines are the power spectra from the GM model. The dashed lines mark the upper limit of integration.

Layer (m)	N_b (10^{-3} s^{-1})	ϵ shear (10^{-8} W kg^{-1})	κ_ρ shear (10^{-4} m^2 s^{-1})
50-150	5.69 ± 0.09	0.58 ± 0.21	0.35 ± 0.12
150-550	1.92 ± 0.03	0.16 ± 0.02	0.87 ± 0.10
550-650	7.29 ± 0.30	7.33 ± 2.12	2.85 ± 0.78

Table 4.2: Summary background buoyancy frequencies, TKE dissipation rates, and diapycnal eddy diffusivities in three layers, calculated from the finescale parameterisation of vertical shear. The uncertainty is the standard error.

Layer (m)	N_b (10^{-3} s^{-1})	ϵ strain (10^{-8} W kg^{-1})	κ_ρ strain (10^{-4} m^2 s^{-1})
50-150	5.69 ± 0.09	1.04 ± 0.31	0.62 ± 0.18
150-550	1.92 ± 0.03	0.09 ± 0.04	0.50 ± 0.25
550-650	7.29 ± 0.30	4.47 ± 1.99	1.52 ± 0.59

Table 4.3: Summary background buoyancy frequencies, TKE dissipation rates, and diapycnal eddy diffusivities in three layers, calculated from the finescale parameterisation of vertical strain. The uncertainty is the standard error.

κ_ρ are 2.9 ± 0.8 and $1.5 \pm 0.6 \times 10^{-4}$ m^2 s^{-1}. The seasonal thermocline is the only layer in which ϵ and κ_ρ from the strain parameterisation is larger than that from the shear parameterisation. From strain, $\epsilon = 10 \pm 3 \times 10^{-9}$ W kg^{-1} and $\kappa_\rho = 0.6 \pm 0.2 \times 10^{-4}$ m^2 s^{-1}. From shear $\epsilon = 6 \pm 2 \times 10^{-9}$ W kg^{-1} and $\kappa_\rho = 0.4 \pm 0.1 \times 10^{-4}$ m^2 s^{-1}. ϵ is smallest in the buoyancy minimum layer with dissipation rates of the order 0.1×10^{-8} W kg^{-1} from both shear and strain, however κ_ρ is not minimum, being of the same order as in the seasonal thermocline.

4.4 Discussion and conclusions

TKE dissipation rates from the finescale parameterisations of vertical shear (4.8) and vertical strain (4.9) vary with depth and buoyancy in the same manner as from the Thorpe scaling analysis of density overturns (4.3), but are larger in the main pycnocline and the seasonal thermocline by factors between 1.1 and 2.5, within the bounds of uncertainty. In the buoyancy minimum the dissipation rate from (4.3) is larger than from (4.8) and (4.9) by approximately a factor of 2. Diapycnal eddy diffusivity from the Thorpe scale analysis and the two finescale

parameterisations are within a factor of 2 in the main pycnocline and within a factor of 4 in the seasonal thermocline and buoyancy minimum.

The general agreement between the two independent estimates is promising. The estimates are used to constrain the magnitude of TKE dissipation rate and diapycnal eddy diffusivity on the West Shetland Slope, however, the absence of direct turbulence measurements means the true rate of TKE dissipation remains elusive. Combining the estimates from the two methods, and taking into consideration the errors involved in the calculations, ϵ is estimated to be of the order 5×10^{-8} W kg^{-1} in the main pycnocline; 5×10^{-9} W kg^{-1} in the seasonal thermocline; and 10^{-9} W kg^{-1} in the buoyancy minimum. κ_ρ is of the order 5×10^{-5} m^2 s^{-1} in the seasonal thermocline and buoyancy minimum and 2×10^{-4} m^2 s^{-1} in the main pycnocline. The latter value of diapycnal diffusivity is an order of magnitude larger than typical values for the interior of the open ocean (Ledwell et al., 1993; Toole et al., 1994), but of the same order as measured over rough abyssal topography (Polzin et al., 1997; Ledwell et al., 2000; Naveira Garabato et al., 2004a,b) and seamounts (Toole et al., 1997; Eriksen, 1998; Carter et al., 2006).

For a direct comparison with previous measurements of mixing in the Faroe-Shetland Channel, the above estimates are compared with two previous studies. Mauritzen et al. (2005) used Thorpe scaling to quantify the mixing in the channel from a CTD section along the Fair Isle-Munken line in June 2000. Diapycnal eddy diffusivity was calculated for each of the five water masses present in the channel, varying from 10^{-4} m^2 s^{-1} in the surface waters to 0.1 m^2 s^{-1} in the bottom water. The estimates here are best compared with the three lightest water masses, because the casts at the repeat station, approximately halfway up the shelf slope, did not sample through the densest two water masses. Mixing in these layers is of the order 10^{-4} to 10^{-3} m^2 s^{-1}, comparable to the largest of the diffusivities inferred here.

Direct turbulence measurements were made in a region local to the slope mixing experiment during the PROcesses over the Continental Slope (PROCS) project. Calculations of TKE dissipation rate and vertical diffusivity from microstructure measurements were found to be in agreement with estimates from Thorpe scaling (Hosegood et al., 2005). In the main pycnocline vertical diffusivity was found to be larger than $10^{-4.5}$ m^2 s^{-1}, comparable to the diapycnal eddy diffusivity in the pycnocline, 2×10^{-4} m^2 s^{-1}, inferred here. However, in regions of weak stratification, such as in the slope current and the deep interior below the pycnocline, Hosegood et al. found vertical diffusivity to be larger, around

10^{-3} m^2 s^{-1}. These estimates are at odds with the average diffusivities in the buoyancy minimum, 5×10^{-5} m^2 s^{-1}, inferred here. However, returning to the 50 m vertically averages of ϵ and κ_ρ from the Thorpe scale analysis, diffusivity is actually maximum at around 200 m and approaching 10^{-3} m^2 s^{-1}.

Neither Thorpe scaling or the finescale parameterisation is ideally suited to the available data, but, in the absence of direct turbulent measurements, they are the best tools available to constrain the amount of mixing that occurs in the Faroe-Shetland Channel. Thorpe scaling ideally requires calm conditions to avoid pressure reversals and minimise wake effects. Many of the CTD casts from the slope mixing experiment contain too many pressure reversals to apply the method. To improve the accuracy of Thorpe scaling when using standard CTD equipment, the descent rate should be kept as constant as possible and all precautions made to prevent pressure reversals. The finescale parameterisation is best applied to deeper, oceanic datasets so shear and strain variances can be calculated from longer (> 200 m) sections of profile. The short profile sections through the main pycnocline and seasonal thermocline limited the low wavenumber contribution to shear and strain variance. The influence of the shelf slope on the internal wave field may also have an effect on the resulting dissipation and diffusivity estimates.

Despite the limitations of the methods, the resulting estimates of TKE dissipation rate and diapycnal eddy diffusivity from the two methods are in general agreement (within the bounds of uncertainty) and comparable to previous mixing estimates from the Faroe-Shetland Channel. The estimates are used to constrain the magnitude of ϵ and κ_ρ on the West Shetland slope and, in Chapter 6, are related to the observed internal wave field.

Chapter 5

Internal wave energy fluxes

5.1 Introduction

During the slope mixing experiment, a semi-diurnal internal tide and near-bed, non-linear internal waves were observed on the West Shetland slope (see Chapter 3). These waves are suspected to play an important role in supporting turbulent mixing on the slope, either through gradual dissipation of internal wave energy by shear instabilities and bottom stress, or rapid conversion to turbulent kinetic energy by internal wave breaking. In this chapter, the energy fluxes associated with the observed internal waves are calculated by two different approaches.

To accurately calculate the flux of energy associated with internal waves the density and velocity structure of the wave field must be well sampled in time and space. Suitable measurements may be made using a hydrographic mooring or from a series of temperature, salinity, and velocity profiles such as lowered ADCP/CTD casts or expendable current/temperature profilers. Moorings of thermistors and current meters can provide high temporal resolution but tend to be coarse in the vertical. Lowered ADCP/CTD profiles provide high vertical resolution but the temporal resolution is limited by the time it take to complete each cast. Moored ADCPs provide both high temporal and high vertical resolution of current velocity, but have a limited range which may not cover the full water depth.

The dataset collected during the slope mixing experiment best suited to calculating the internal tide energy flux is the series of full-depth lowered ADCP/CTD profiles from the repeat station, while the higher frequency non-linear waves are best resolved by the three thermistor/ADCP mooring pairs ('East', 'West', and 'South'). In addition, the total horizontal energy flux of the semi-diurnal tide at the experiment site is calculated by utilising the time series of near-bed pressure, measured by the moored CTD loggers. Separation of this energy flux

into barotropic and baroclinic components is found to yield two additional cross-correlation terms.

The general calculation of internal wave energy fluxes is discussed in Section 5.2, including how the surface pressure perturbation may be constrained, and the separation of barotropic and baroclinic variability when the bottom and isopycnals are not horizontal. In Section 5.3 barotropic and baroclinic tidal energy fluxes are calculated from the lowered ADCP/CTD profiles, vertical internal tide energy fluxes calculated, and internal tide characteristics plotted. In Section 5.4 non-linear internal wave energy fluxes are calculated from the thermistor/ADCP mooring pairs. A short discussion follows in Section 5.5.

5.2 Internal wave energy flux calculation

Until recently, internal wave energy fluxes, $\mathbf{F}$, were estimated by measuring the energy density and wave velocity,

$$\mathbf{F} = \mathbf{c}(KE + APE), \tag{5.1}$$

where KE and APE are the kinetic and available potential energy densities of the internal wave and $\mathbf{c}$ is the velocity of energy propagation (e.g. Kunze and Sanford 1984; Mied et al. 1986). In the case of dispersive waves such as internal tides and near-inertial waves, $\mathbf{c}$ is the group velocity ($\mathbf{c_g}$). For low-mode internal waves, the available potential energy density can be calculated

$$APE = \frac{1}{4}\rho_0 N^2 \xi_0^2, \tag{5.2}$$

where ξ_0 is the amplitude of vertical displacement and N is the buoyancy frequency. The vertical displacement is measured from the variability of temperature (or density) at a fixed depth and the vertical gradient such that $\xi_0 = -T_0(dT/dz)^{-1}$, where T_0 is the amplitude of the temperature variability and dT/dz is the background vertical temperature gradient. Similarly, the kinetic energy density can be calculated directly from velocity measurements of the internal wave,

$$KE = \frac{1}{4}\rho_0 \mathbf{u}_0^2, \tag{5.3}$$

where $\mathbf{u}_0$ is the velocity amplitude, or, for low-frequency waves, from the relationship

$$\frac{KE}{APE} = \frac{(\omega^2 + f^2)}{(\omega^2 - f^2)}, \tag{5.4}$$

where ω is the angular frequency of the wave and f is the inertial frequency (Fofonoff, 1969). The group velocity, $\mathbf{c_g} = \partial\omega/\partial\mathbf{k}$, must be determined from the internal wave dispersion relation (1.2), requiring the horizontal and vertical wavenumbers to be known. This method is only possible if the internal wave field is dominated by a single mode and is sampled frequently enough to avoid temporal aliasing (Nash et al., 2005).

Alternatively, internal wave energy fluxes can be calculated from the correlation between velocity and pressure,

$$\mathbf{F} = \langle \mathbf{u}'p' \rangle , \tag{5.5}$$

where $\mathbf{u}'$ is the velocity perturbation and p' is the pressure perturbation, due to passing internal waves (e.g. Kunze et al. 2002; Carter and Gregg 2002, see Nash et al. 2005 for a review). For hydrostatic internal waves ($\omega \ll N$) the pressure perturbation can be calculated from the density anomalies (ρ') by integrating the hydrostatic equation from the surface,

$$p' = p'_{\text{surf}} + \int_z^0 \rho' g \, dz, \tag{5.6}$$

where p'_{surf} is the surface pressure perturbation due to passing internal waves. This method has the advantage that the internal wave field does not need to be as well resolved in time or in the vertical (Nash et al., 2005). It does however require full-depth sampling as Equation (5.6) must be integrated from the surface and the baroclinic component must be calculated from horizontal velocity profiles.

5.2.1 The integration constant problem

There is a fundamental problem with calculating p' from ρ' in that the constant of integration in Equation (5.6), p'_{surf}, cannot be determined from CTD measurements and the vertical distribution of $\mathbf{F}$ is dependent on the constant used. If the bottom is horizontal the baroclinicity condition for pressure, $\int_{-H}^0 p' \, dz = 0$, can be used to constrain p'_{surf} (Kunze et al., 2002) because the vertical structure is independent of the horizontal position. However, if the bottom is sloping, such as on shelf slopes or over seamounts, the baroclinic condition of pressure is incompatible with the baroclinicity condition of horizontal velocity, $\int_{-H}^0 \mathbf{u}' \, dz = 0$, and the constant is impossible to determine from a single location (Gerkema and van Haren, 2007). Therefore, over sloping topography some other assumption must be made to constrain p'_{surf}. Over Great Meteor Seamount, Gerkema and van Haren find the baroclinic currents concentrated in the upper layer of the watercolumn and weak in the lower layer. They therefore make the assumption that

the baroclinic pressure field is also weak in the lower layer and assume $p' = 0$ at the bottom.

If only the vertically integrated internal wave energy flux is of interest, such assumptions are unnecessary as $\int_{-H}^{0} \mathbf{F}\, dz$ is independent of p'_{surf} because the depth integral of $\mathbf{u}'$ is zero by definition (Ray and Mitchum, 1997).

5.2.2 Sloping topography and isopycnals

Over topography, across-slope barotropic tidal flow induces vertical isopycnal displacements (and hence density anomalies) due to the continuity of volume (Baines, 1982); such barotropic displacements should be removed from the baroclinic pressure perturbations to accurately calculate internal wave energy fluxes (Nash et al., 2004; Gerkema and van Haren, 2007). The barotropic component of vertical isopycnal displacement, ξ_{bt}, can be estimated in two ways. Provided the topographic slope gradient is known and uniform at the tidal excursion length scale, and the across-slope barotropic tidal transport is known and assumed spatially uniform, ξ_{bt} can be calculated a priori. Following Nash et al. (2004), the position of the bottom is defined by $h = s_{\text{topog}} x$, where s_{topog} is the topographic slope. As there is no flow normal to the bottom, an across-slope barotropic tidal velocity $u_{\text{bt}} = u_{\text{bt0}} \cos(\omega t - \phi)$ induces a vertical velocity $w_{\text{bt}}(z) = u_{\text{bt}} s(-z/H)$, where H is the total depth of the watercolumn. The vertical displacement is therefore

$$\xi_{\text{bt}}(z,t) = \frac{u_{\text{bt0}} s_{\text{topog}}}{\omega} \left(\frac{-z}{H}\right) \sin(\omega t - \phi). \tag{5.7}$$

Alternatively, ξ_{bt} can be estimated as a linear least-squares fit to $\xi(z)$ with zero at the surface (Kunze et al., 2002). The equivalent density anomaly, $\rho'_{\text{bt}} = -\xi_{\text{bt}} d\overline{\rho}/dz$, should be subtracted from ρ' before calculating p' from Equation (5.6).

Barotropic tidal flow also induces vertical isopycnal displacements at a fixed location by horizontal advection if the isopycnals are not horizontal. This component of ξ can be estimated in a similar way to the component due to sloping topography if the slope of the isopycnals is known. For the special case where the largest isopycnal slope is at the bottom and decreases linearly towards the surface

$$\xi_{\text{bt}}(z,t) = -\frac{u_{\text{bt0}} s_{\text{isopyc}}}{\omega} \left(\frac{-z}{H}\right) \sin(\omega t - \phi), \tag{5.8}$$

where s_{isopync} is the isopycnal slope at the bottom, this is the same form as the topographic slope component. If the isopycnal slope is in the same vertical plane as the topographic slope Equations (5.7) and (5.8) can be combined

$$\xi_{\text{bt}}(z,t) = \frac{u_{\text{bt0}} (s_{\text{topog}} - s_{\text{isopyc}})}{\omega} \left(\frac{-z}{H}\right) \sin(\omega t - \phi). \tag{5.9}$$

If the isopycnal slope at the bottom is of the same sign but smaller than the topographic slope (i.e. approaching parallel) then it acts to reduce the barotropic component of ξ. However, if the isopycnal slope is of the opposite sign then it increases the barotropic component. If the isopycnal slope is known but does not tend to zero at the surface the general solution is

$$\xi_{\mathrm{bt}}(z,t) = \frac{u_{\mathrm{bt0}}}{\omega}\left(s_{\mathrm{topog}}(-z/H) - s_{\mathrm{isopyc}}(z)\right)\,\sin(\omega t - \phi). \tag{5.10}$$

To accurately calculate internal wave energy fluxes where isopycnals are non-horizontal therefore requires information of the horizontal density field. This draws a parallel with the integration constant problem where information on the horizontal velocity field is required to find the surface pressure perturbation over sloping topography (Gerkema and van Haren, 2007).

5.3 Barotropic and baroclinic tidal energy flux

The semi-diurnal internal tide is adequately resolved by the hourly CTD and lowered ADCP profiles from the repeat station to allow the calculation of the energy flux from Equation (5.5). As the profiles are full-depth, the baroclinic velocity perturbation can be accurately determined and the baroclinic pressure perturbation calculated from Equation (5.6).

The barotropic component of vertical isopycnal displacement due to sloping topography, ξ_{bt}, is first calculated a priori. From the repeat station lowered ADCP data, the M_2 across-slope barotropic tidal amplitude (u_{bt0}) is 0.08 m s^{-1}, yielding a tidal excursion of approximately 570 m. The topographic slope gradient at the location of the slope mixing experiment is around 0.02 and detailed swath bathymetry of the area, courtesy of BP and the British Geological Survey, show the slope is relatively uniform at sub-km scales. From Equation (5.7), the M_2 across-slope barotropic tide should induce 12 m vertical isopycnal displacements at the bottom, decreasing linearly towards the surface. These displacements are the same order as those observed in the CTD profiles and so internal wave energy fluxes are sensitive to small errors in the measurement of u_{bt0} and s_{topog}. The alternative method, estimating ξ_{bt} as a linear least-squares fit to $\xi(z)$ with zero at the surface, implies similar vertical isopycnal displacements of 10 m at the bottom and is chosen over the a priori calculation because it is insensitive to the slope gradient and barotropic tidal amplitude.

The barotropic component of ξ due to sloping isopycnals is estimated from a composite potential density section across the the West Shetland slope, including

CTD profiles from the Central section, repeat station, and preliminary casts made before deploying the moorings (Fig. 5.1). The horizontal resolution of the section, $\sim$ 4 km, is too coarse to accurately estimate the isopycnal slope at the tidal excursion length scale but the component due to sloping isopycnals is calculated nevertheless. Below 600 m at the location of the repeat station there is a slight upward slope of isopycnals towards the Southeast, the same direction as the topographic slope, which will have the effect of decreasing ξ_{bt} near the bottom. The isopycnal slope[1] is small (0.003) compared to the topographic slope, only decreasing ξ_{bt} by 2 m, but large enough to account for the discrepancy between two methods of calculating the component due to sloping topography. Through the rest of the watercolumn there is no consistent trend in isopycnal slope when compared to the temporal variability. It is concluded, therefore, that the isopycnal slope cannot be measured accurately enough from the available datasets to reliably calculate the barotropic component of ξ due to sloping isopycnals. It is however small compared to the component due to sloping topography and so neglecting the term will not significantly affect the internal tide energy flux estimates.

For comparison with the baroclinic tide, the barotropic tidal energy flux is also calculated, using the variability in near-bed pressure, measured by the CTD loggers on the 'East' and 'West' thermistor moorings, as an estimate of the total (barotropic plus baroclinic) pressure perturbation.

Semi-diurnal horizontal velocity perturbations and density anomalies are calculated from linear least-square fits of the M_2 tidal constituent (harmonic tidal analysis) to the horizontal velocity and density time series at each level. Only the amplitude and phase is retained so the resulting time series have zero time-means. Similarly, the total pressure perturbation is calculated from an M_2 fit to the near-bed pressure time series.

The horizontal velocity perturbations are then split into barotropic (bt) and baroclinic (bc) components,

$$\mathbf{u}'(z,t) = \mathbf{u}'_{\mathrm{bt}}(t) + \mathbf{u}'_{\mathrm{bc}}(z,t), \tag{5.11}$$

with the barotropic component defined,

$$\mathbf{u}'_{\mathrm{bt}}(t) = \frac{1}{H}\int_{-H}^{0} \mathbf{u}'(z,t)\, dz. \tag{5.12}$$

[1]The isopycnal slope is also calculated from the density time series inferred from the thermistor moorings. Despite the thermistors not being calibrated, the estimated isopycnal slope is of a similar magnitude.

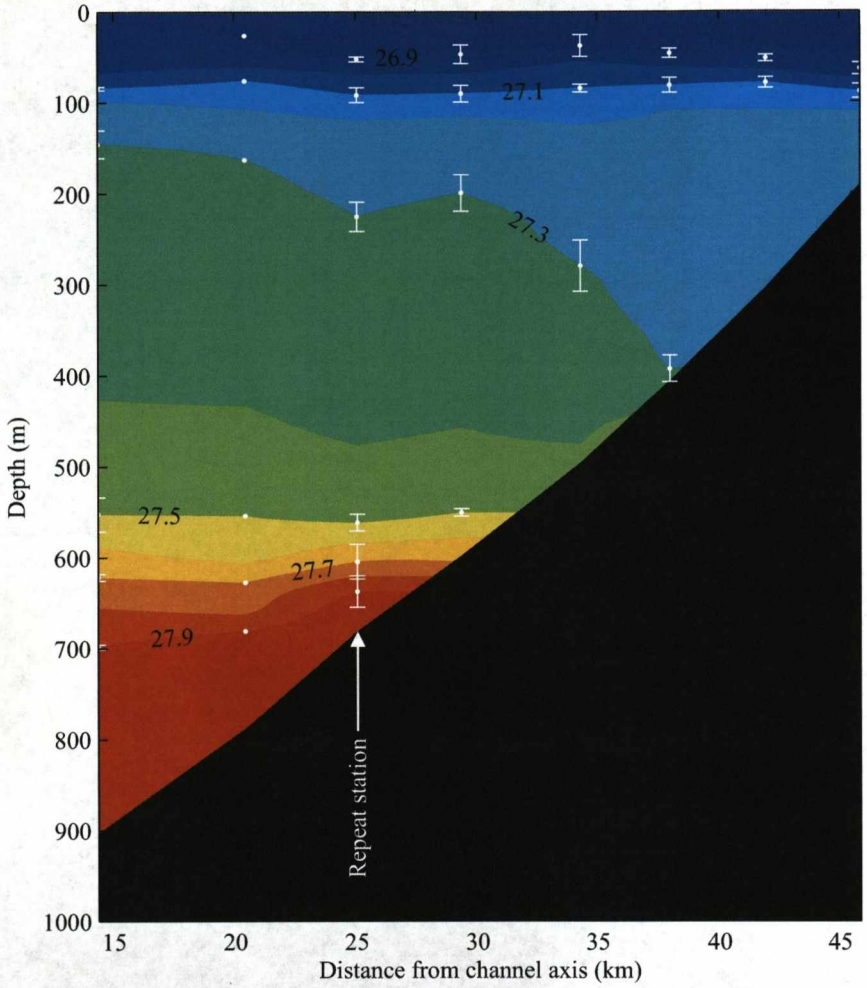

Figure 5.1: A composite σ_θ section across the West Shetland slope, including CTD profiles from the Central section, repeat station, and preliminary casts made before deploying the moorings. Multiple casts made within 24 hours at a single location are not considered independent and so are averaged together first before averaging with independent casts. Where two independent profiles are averaged, error bars show the range of depths selected isopycnal were observed.

The barotropic and baroclinic components of $\mathbf{u}'$ are shown in Figure 5.2. The amplitude of the barotropic component is 0.08 m s^{-1} across the slope and 0.09 m s^{-1} along the slope, and in phase. The amplitudes of the baroclinic components are ~ 0.1 m s^{-1} in and below the main pycnocline, and around 0.06 m s^{-1} in the seasonal thermocline. In both directions the phase lag decreases with depth by a single M_2 period so baroclinic variability in the two stratified regions are roughly in phase, leading the barotropic component by ~ 1 hour along-slope and lagging the barotropic component by ~ 2 hours across-slope.

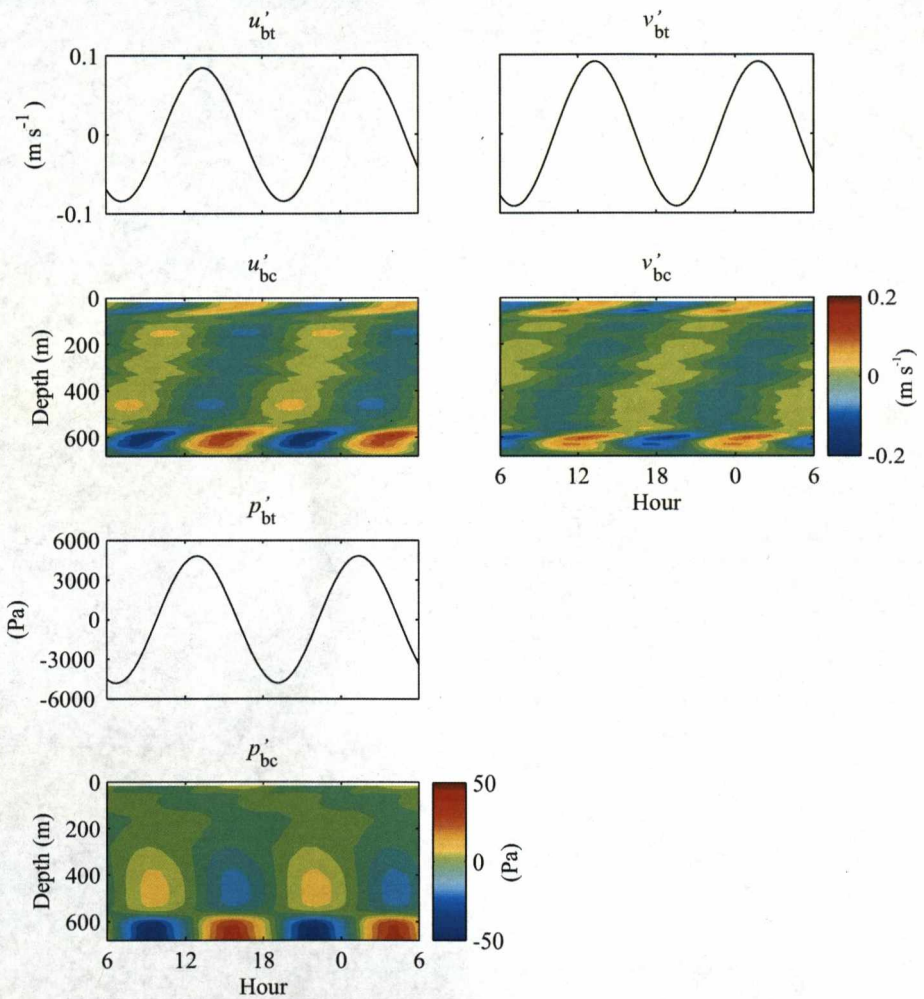

Figure 5.2: Across (u') and along-slope (v') velocity perturbations for the M_2 tide, separated into barotropic (bt) and baroclinic (bc) components. Also shown is the pressure perturbation for the assumption $\int_{-H}^{0} p'\, dz = 0$, separated into barotropic and baroclinic components.

The total pressure perturbation is taken to be p' at $z = -H$ and split into barotropic and baroclinic components,

$$p'(z,t) = p'_{\mathrm{bt}}(t) + p'_{\mathrm{bc}}(z,t), \tag{5.13}$$

by determining the baroclinic component from the density anomalies using Equation (5.6). The barotropic component is then the residual after p'_{bc} at $z = -H$ is subtracted from the total pressure perturbation. The integration constant problem is approached in a similar fashion to Gerkema and van Haren (2007). Four different assumptions about the pressure field are made to constrain p'_{surf}:

1. $p' = 0$ at $z = 0$ ($p'_{\mathrm{surf}} = 0$). The baroclinic velocity perturbations are largest in the lower layer of the watercolumn, below the main pycnocline, and small in the upper layer. So making the assumption that the baroclinic pressure perturbations are also small in the upper layer, it may be sensible to assume $p' = 0$ at the surface rather than at the bottom.

2. $p' = 0$ at $z = -H$. The assumption made by Gerkema and van Haren (2007) because their baroclinic currents were concentrated in the upper layer of the watercolumn, the opposite to what is observed here; this assumption is included for comparison with assumption 1. The value of p'_{surf} for this assumption is of the order 25 Pa.

3. $\int_{-H}^{0} p'\, dz = 0$. Although the baroclinicity condition for pressure is invalid over sloping topography, it may be a useful approximation because the slope gradient is small (0.02). The value of p'_{surf} for this assumption is of the order 10 Pa.

4. $p' = 0$ at $z = -560$ m. Simulation of an M_2 internal tide with stratification and topography modelled on the Faroe-Shetland Channel suggests p' goes to zero between 550 and 570 m over the 680 m isobath (see Chapter 7). The value of p'_{surf} for this assumption is also of the order 10 Pa.

The barotropic and baroclinic components of p' for assumption 3 are shown in Figure 5.2. The magnitude of the baroclinic variability is less than 2% of the barotropic variability, so the amplitude of the barotropic component is close to that of the total pressure perturbation, > 4500 Pa, and is roughly in phase with barotropic velocity. The baroclinic component is largest at the bottom, with an amplitude of around 30 Pa, and lagging the barotropic component by approximately 3 hours.

The total horizontal tidal energy flux is the sum of the barotropic, $\langle \mathbf{u}'_{\rm bt} p'_{\rm bt} \rangle$, and baroclinic, $\langle \mathbf{u}'_{\rm bc} p'_{\rm bc} \rangle$, components and the two cross-correlation terms so that

$$\mathbf{F} = \langle \mathbf{u}' p' \rangle = \langle \mathbf{u}'_{\rm bt} p'_{\rm bt} \rangle + \langle \mathbf{u}'_{\rm bc} p'_{\rm bt} \rangle + \langle \mathbf{u}'_{\rm bt} p'_{\rm bc} \rangle + \langle \mathbf{u}'_{\rm bc} p'_{\rm bc} \rangle \,. \tag{5.14}$$

For accurate assessment, the time-average, $\langle\rangle$, should be at least as long as the tidal period. As the repeat station was only occupied for 24 hours (approximately two tidal periods) all 24 profiles[2] are included in the time-average. Each component is evaluated separately.

5.3.1 Results

By far the largest terms in Equation (5.14) are the barotropic component and the cross-correlation term with barotropic pressure. As $p'_{\rm surf} \ll p'_{\rm bt}$, the constant used has little effect on the value of these terms. Instantaneous barotropic energy fluxes are up to 400 W m^{-2} both across and along the slope (Fig. 5.3) with time-average values of the order 200 W m^{-2} (Fig. 5.4). Vertically integrated through the total depth of the watercolumn, the barotropic energy flux $\simeq$ 133 kW m^{-1} up-slope and $\simeq$ 145 kW m^{-1} along-slope directed to the northeast (Table 5.1).

		Barotropic kW m^{-1}	Baroclinic W m^{-1}
Across-slope	Total	$\simeq$ 132.6	154.7
	Pycnocline	-	99.3 ± 3.6
Along-slope	Total	$\simeq$ 145.3	-44.5
	Pycnocline	-	-22.0 ± 1.4

Table 5.1: Barotropic and baroclinic M_2 tide energy fluxes, integrated through the whole watercolumn. Also shown are the baroclinic energy fluxes integrated through the main pycnocline (550 to 650 m).

The cross-correlation term $\langle \mathbf{u}'_{\rm bc} p'_{\rm bt} \rangle$ also contains instantaneous energy fluxes up to 400 W m^{-2} in the main pycnocline, with time-average values larger than 150 W m^{-2}. The vertical integral is inherently zero because $\int_{-H}^{0} \mathbf{u}'_{\rm bc}\, dz = 0$ and $p'_{\rm bt}$ is constant.

The baroclinic component and the cross-correlation term with baroclinic pressure are typically only 1% of the terms with barotropic pressure. $p'_{\rm surf}$ is of the

[2]The lowered ADCP failed to record during one cast at the repeat station.

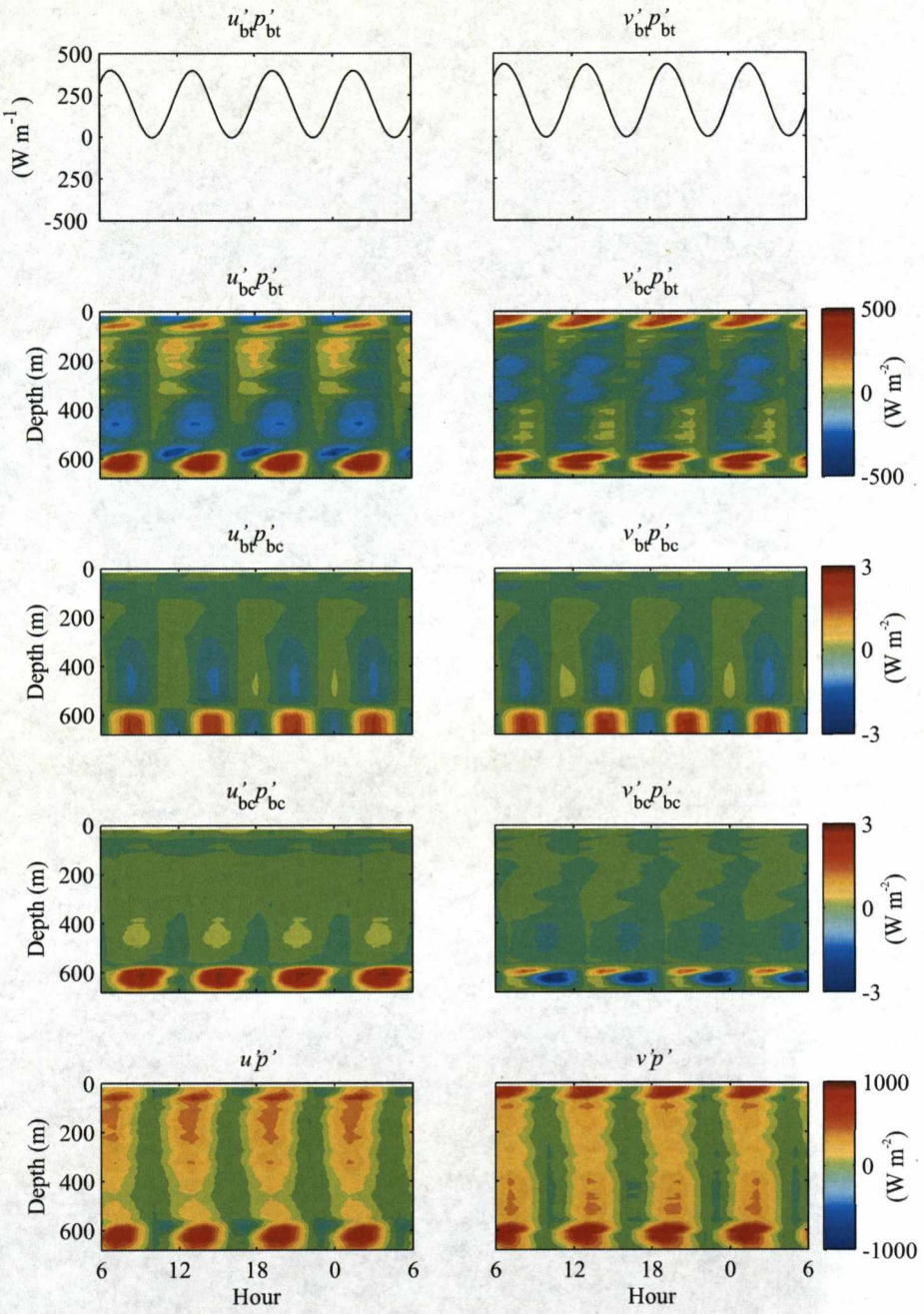

Figure 5.3: Across and along-slope values of $\mathbf{u}'p'$ for the M_2 tide, separated into barotropic, $\mathbf{u}'_{\mathrm{bt}}p'_{\mathrm{bt}}$, and baroclinic, $\mathbf{u}'_{\mathrm{bc}}p'_{\mathrm{bc}}$, components, and the two cross-correlation terms for the assumption $\int_{-H}^{0} p'\, dz = 0$.

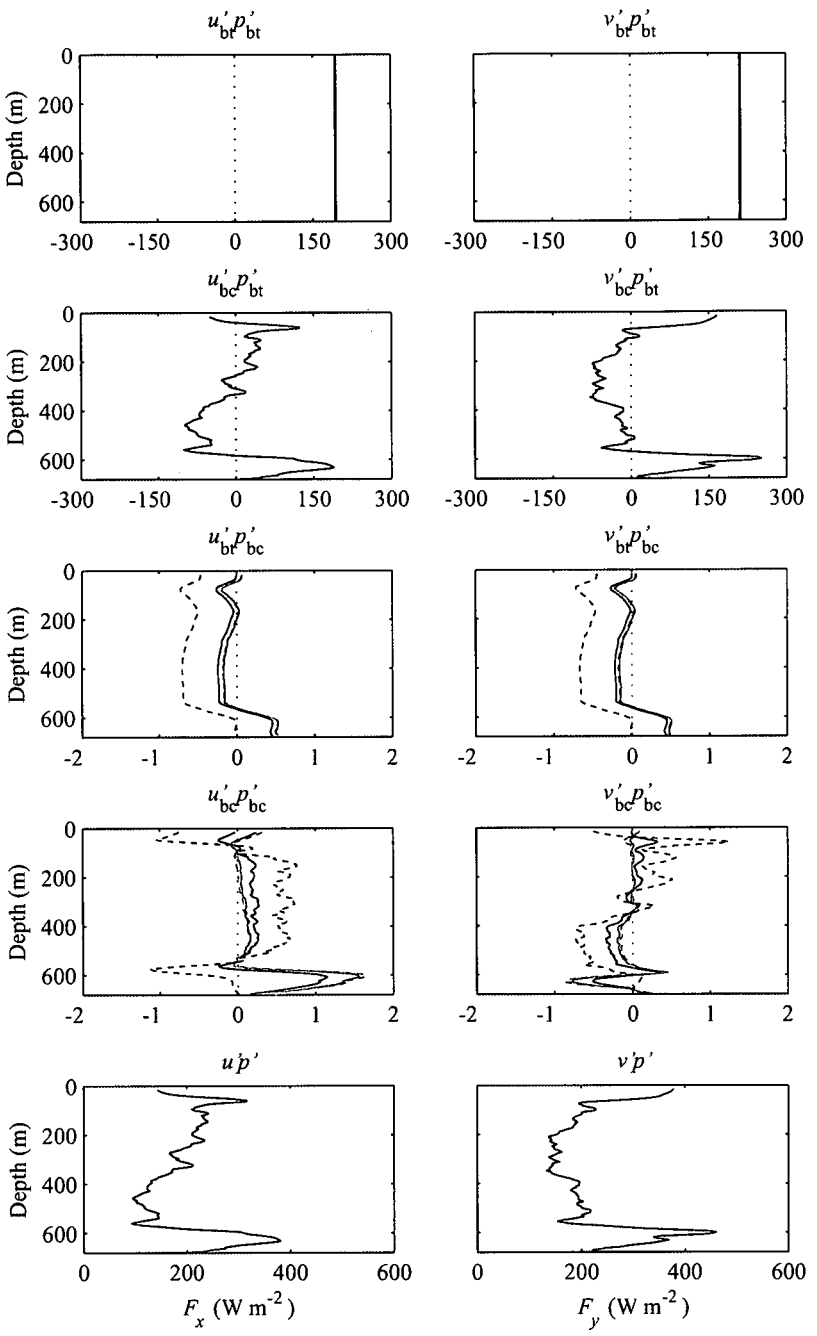

Figure 5.4: Time-average energy flux profiles, $\langle \mathbf{u}'p' \rangle$ for the M_2 tide, separated into barotropic, $\langle \mathbf{u}'_{\rm bt} p'_{\rm bt} \rangle$, and baroclinic, $\langle \mathbf{u}'_{\rm bc} p'_{\rm bc} \rangle$, components and the two cross-correlation terms. The black lines are for the assumption $p' = 0$ at $z = 0$; the dashed black lines are for the assumption $p' = 0$ at $z = -H$; the solid grey lines are for the assumption $\int_{-H}^{0} p' \, dz = 0$; the dashed grey lines are for the assumption $p' = 0$ at $z = -560$ m.

same order as p'_{bc} so the constant used has a large effect on the value of these terms. There is very close agreement between the time-averaged baroclinic energy flux profiles for assumptions 3 and 4, both are ~ 1.5 W m^{-2} up-slope in the main pycnocline and < 1 W m^{-2} along-slope to the southwest below 600 m. Above 550 m both horizontal components of the energy flux are close to zero that fits assumption 1 of small baroclinic pressure perturbations in the upper layer. Assumption 1 yields an energy flux profile qualitatively similar to assumptions 3 and 4, but smaller in the pycnocline and lower layer, and larger in the upper layer. Assumption 2 yields an energy flux profile that bears no resemblance to the velocity or density variability; in neither direction is the energy flux close to zero in the upper layer, and in the lower layer the across-slope energy flux is the opposite sign to that for assumptions 1, 3, and 4. Assumption 2 is therefore discounted in further analyses. The excellent agreement of assumption 3 with assumption 4, the model 'truth', suggests the baroclinicity condition for pressure yields the best approximation of p'_{surf} at this location. The total baroclinic energy flux, integrated from the surface to the seabed, is independent of the value of p'_{surf}, 155 W m^{-1} up-slope and 44 W m^{-1} along-slope to the southwest (Table 5.1). From the energy flux profiles for assumptions (3) and (4), the energy flux integrated through the main pycnocline (550-650 m) is 99 ± 4 W m^{-1} up-slope and 22 ± 1 W m^{-1} along-slope to the southwest.

The vertical distribution of the cross-correlation term $\langle \mathbf{u}'_{bt} p'_{bc} \rangle$ is determined by p'_{bc} and so the absolute values are sensitive to p'_{surf}. The vertical integral is inherently zero for assumption 3, because $\int_{-H}^{0} p'_{bc}\, dz = 0$ and $\mathbf{u}'_{bt}$ is uniform, but of the order 50 and 10 W m^{-1}, down-slope and along-slope to the southwest, for assumptions 1 and 4 respectively.

Combining the four terms, the total tidal energy flux is dominated by the barotropic component and the cross-correlation term with barotropic pressure. $\langle \mathbf{u}'p' \rangle$ is independent of the value of p'_{surf} because the constant is both added to p'_{bc} and subtracted from p'_{bt}. Instantaneous energy fluxes in the main pycnocline are up to 800 W m^{-2}, with time-average values larger than 350 W m^{-2}. The vertical integral of $\langle \mathbf{u}'p' \rangle$, 130 kW m^{-1} up-slope and 143 kW m^{-1} along-slope to the northeast, is dominated by the barotropic component with the other terms contributing less than 0.2% of the total energy flux. The main pycnocline contribution to the total tidal energy flux is 26 kW m^{-1} up-slope and 32 kW m^{-1} along-slope to the northeast.

5.3.2 Vertical internal tide energy flux

The vertical energy flux, $F_z = \langle w'p' \rangle$, for the M_2 internal tide is calculated by inferring vertical velocity perturbations from vertical isopycnal displacement, $w' = d\xi/dt$. Semi-diurnal vertical isopycnal displacements are calculated from the M_2 fits to density; the barotropic component, ξ_{bt}, is subtracted. p' is the baroclinic pressure perturbation (p'_{bc}) and the same four assumptions stated in Section 5.3 are made to constrain p'_{surf}.

The largest vertical isopycnal displacements ($\sim$ 20 m) occur at mid-depth, around 350 m, and are in phase with the baroclinic pressure perturbation at that depth (Fig. 5.5). These imply vertical velocity perturbations up to 0.3 cm s^{-1} that lead the pressure perturbation by approximately 3 hours. The largest instantaneous vertical internal tide energy fluxes are at mid depth and in the main pycnocline (0.01 W m^{-2}), the latter due to the large pressure perturbations in the lower layer. Time-averaged, the vertical internal tide energy flux is of the order one hundredth of the magnitude of the horizontal baroclinic energy flux, comparable with s_{topog}. There is again close agreement between the energy flux profiles for assumptions 3 and 4, with assumption 1 diverging slightly above 300 m. Between 280 and 490 m the energy flux is < 0.005 W m^{-2} upwards, and between 490 and 540 m < 0.005 W m^{-2} downwards. There is a convergence of internal tide energy in the main pycnocline. From the energy flux profiles for assumptions 3 and 4, the vertical energy flux is $78 \pm 2 \times 10^{-4}$ W m^{-2} at the base of the pycnocline (650 m) but only $6 \pm 5 \times 10^{-4}$ W m^{-2} at the top of the pycnocline (550 m).

5.3.3 Internal tide characteristics

The slope of the of the M_2 internal tide characteristic is calculated for a smoothed N^2 field from the Central section, using the internal wave dispersion relation (1.2). Two possible internal tide ray paths, originating at the same point over the Faroe shelf, are shown in Figure 5.6. Ray path A starts in a downward direction, reflects subcritically with the lower the Faroe slope, reflects with the surface, and then subcritically again with the upper West Shetland slope, exiting the domain over the Shetland shelf. Ray path B starts in an upward direction, reflects with the surface, reflects subcritically with the lower West Shetland slope, then supercritically with West Shetland slope near the intersection with the main pycnocline. The ray path then reflects with the surface and subcritically with the lower Faroe slope before exiting the domain over the Faroe shelf. This is an

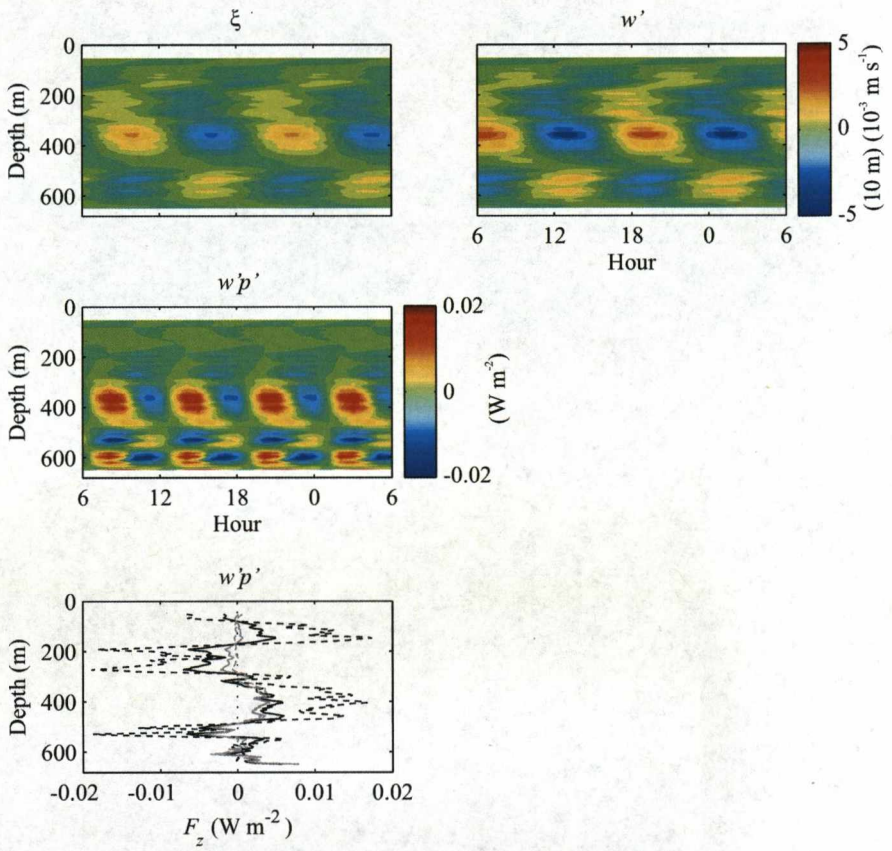

Figure 5.5: Vertical isopycnal displacement and vertical velocity for the M_2 tide. Also shown is the vertical internal tide energy flux for the assumption $\int_{-H}^{0} p'\, dz = 0$, and time-average energy flux profiles. The black lines are for the assumption $p' = 0$ at $z = 0$; the dashed black lines are for the assumption $p' = 0$ at $z = -H$; the solid grey lines are for the assumption $\int_{-H}^{0} p'\, dz = 0$; the dashed grey lines are for the assumption $p' = 0$ at $z = -560$ m.

example of 'geometric focusing', previously observed in laboratory experiments by Maas et al. (1997). The sub-super-subcritical reflective behavior of the M_2 internal tide with the West Shetland slope implies two bands of near-critical slope between the subcritical and supercritical regions. In these bands high dissipation of internal tide energy is expected, through shear instabilities and internal wave breaking.

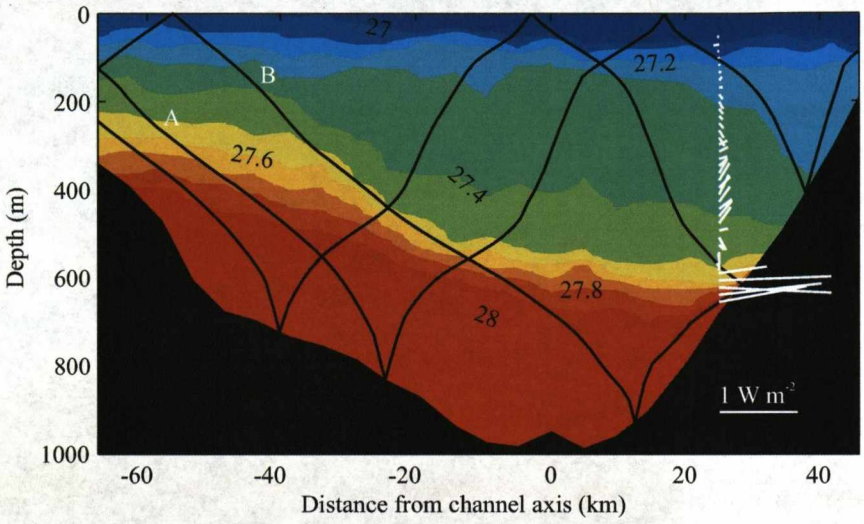

Figure 5.6: Characteristic ray paths of the M_2 internal tide in the Faroe-Shetland Channel (black lines) overlaid on the across-channel distribution of σ_θ. The white lines show the across-slope M_2 internal tide energy flux.

Internal wave characteristics approach horizontal as N^2 increases, so the ray paths converge in the main pycnocline and diverge in the buoyancy minimum. This is in agreement with across-slope M_2 internal tide energy flux (plotted with the M_2 internal tide ray paths in Figure 5.6), which is maximum in the pycnocline.

5.4 Non-linear internal wave energy flux

Calculation of the energy flux associated with the near-bed, non-linear internal waves is complicated by their variable frequency and intermittent occurrence. The period of the waves observed in the mooring time series (typically 15 to 30 minutes) means they are insufficiently resolved for the energy flux to be cal-

culated from the hourly lowered ADCP/CTD profiles. The 2-minute temporal resolution of the moored instruments is adequate for resolving waves with periods > 4 minutes and the 4 m separation of thermistors provides excellent vertical resolution.

Moum et al. (2007) calculate the horizontal energy flux of non-linear internal waves as the sum of non-linear advection of wave energy ($E = KE + APE$) and the pressure-velocity work term,

$$F = \langle uE \rangle + \langle up \rangle \,. \tag{5.15}$$

The non-linear advection term can be calculated from the mooring data. However, calculation of the pressure-velocity work term is problematic because p includes internal hydrostatic ($p = \int_z^0 \rho' g \; dz$), external hydrostatic (p_{surf}), and non-hydrostatic terms. Even if the external hydrostatic and non-hydrostatic terms are assumed small, the internal hydrostatic term cannot be calculated because the high-frequency density variability is only measured in the bottom 50 m. Although the method does not require the density structure of the internal wave field to be well resolved in the vertical, it does require some information about the overlying watercolumn. The lower layer and main pycnocline are well sampled by the thermistor moorings, but the temperature (and hence density) variability in the upper layer is unknown and so the hydrostatic equation cannot be integrated from the surface. Nash et al. (2005) suggest fitting vertical structure modes to generate full-depth profiles from datasets with discrete vertical sampling. This approach proves unsuccessful with this dataset because of the short length of the thermistors moorings and strong near-bed stratification.

An addition complication comes from lack of full-depth velocity profiles to separate the barotropic and baroclinic components. The moored ADCPs have a maximum range of 250 m, less than half the depth of the watercolumn, so separation of the flow using the baroclinicity condition for horizontal velocity is not possible. Although this would be a problem for the calculation of linear internal wave energy fluxes, Moum et al. (2007) find $\int_{-H}^0 u \; dz \neq 0$ for non-linear internal waves[3] and so the velocity perturbations due to passing internal waves must be distinguished from the background flow by some other means.

Moum et al. (2007) demonstrate that the simplification

$$F = c \, \langle E \rangle \,, \tag{5.16}$$

[3]This implies there is a net flow associated with non-linear internal waves, analogous to Stokes drift.

equivalent to Equation (5.1), holds for observations of non-linear internal waves on the Oregon continental shelf. This simplification is used here to estimate the non-linear internal wave energy flux from the mooring data, but requires an estimation of the velocity with which the energy propagates. If the observed waves are considered non-dispersive, a good approximation for bottom trapped internal waves of elevation because the wavelength is short relative to the lower layer depth, there is no distinction between phase and group velocity and so the energy propagates at the velocity of the waveform.

The wave velocity (c) of the non-linear internal waves is determined from observations of individual waves in multiple mooring time series. This is possible because the instruments are arranged in a 3-dimensional mooring array rather than a single line of moorings. The leading wave[4] of five wave trains is observed in all three thermistor time series (Fig. 5.7), the times of the observations are shown in Table 5.2. The inferred velocities of four of the five waves are between 0.24 and 0.3 m s^{-1}, and all the velocity vectors are within 7° of each other. The mean velocity of the waves between the moorings is 0.27 m s^{-1} at an angle of 132° up the shelf slope, within 10° of perpendicular to the isobaths (Fig. 5.8). Wave D is considered an outlier and so is excluded from the mean. This wave velocity implies wavelengths between 250 and 500 m. Amplitude-to-wavelength ratios are up to 0.2, reinforcing the non-linear nature of the waves.

Wave	Year day			Speed	Direction
	'West'	'East'	'South'	(m s^{-1})	(°)
A	251.693	251.737	251.805	0.244	134.3
B	252.159	252.205	252.259	0.283	132.0
C	252.692	252.753	252.800	0.276	128.0
D	253.086	253.182	253.266	0.163	129.2
E	253.581	253.621	253.675	0.295	133.2
				0.27 ± 0.01	132 ± 1

Table 5.2: Times of appearance in the three temperature time series of the leading wave in five non-linear internal wave trains, and the inferred velocities. The last row contains the mean speed and direction (excluding wave D); the uncertainty is the standard error.

[4]There will be some dispersion due to the amplitude dependence of phase velocity inherent with non-linear waves. This bias is small because, by observing the leading wave, the inferred velocity is for the fastest wave in the train which has the largest amplitude and hence the highest energy density.

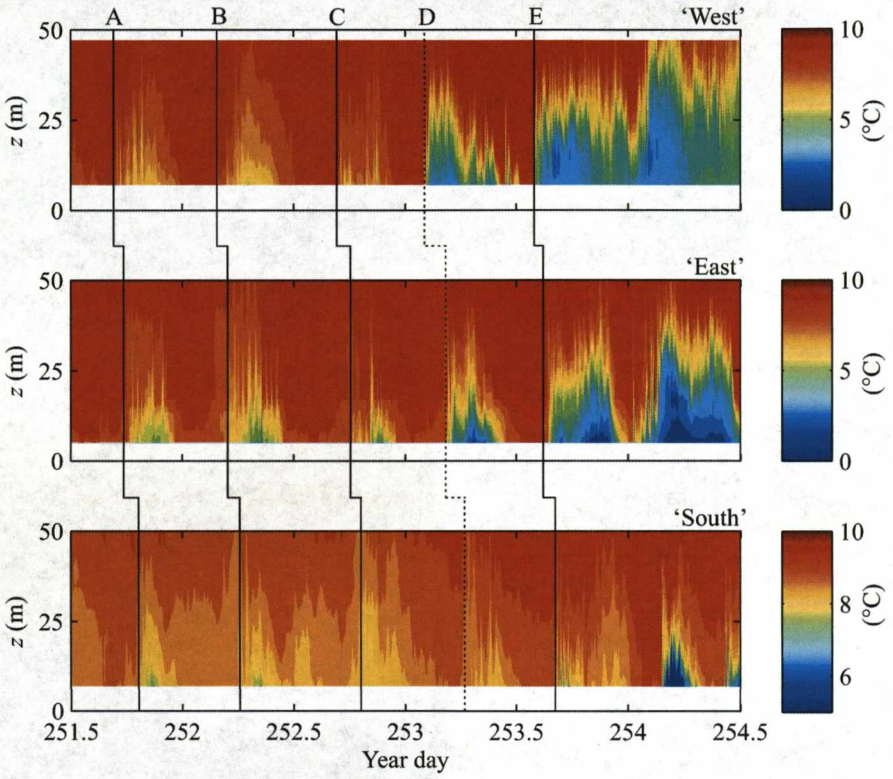

Figure 5.7: Times of appearance in the three temperature time series of the leading wave in five non-linear internal wave trains. Wave D is significantly slower than the other waves (dashed line).

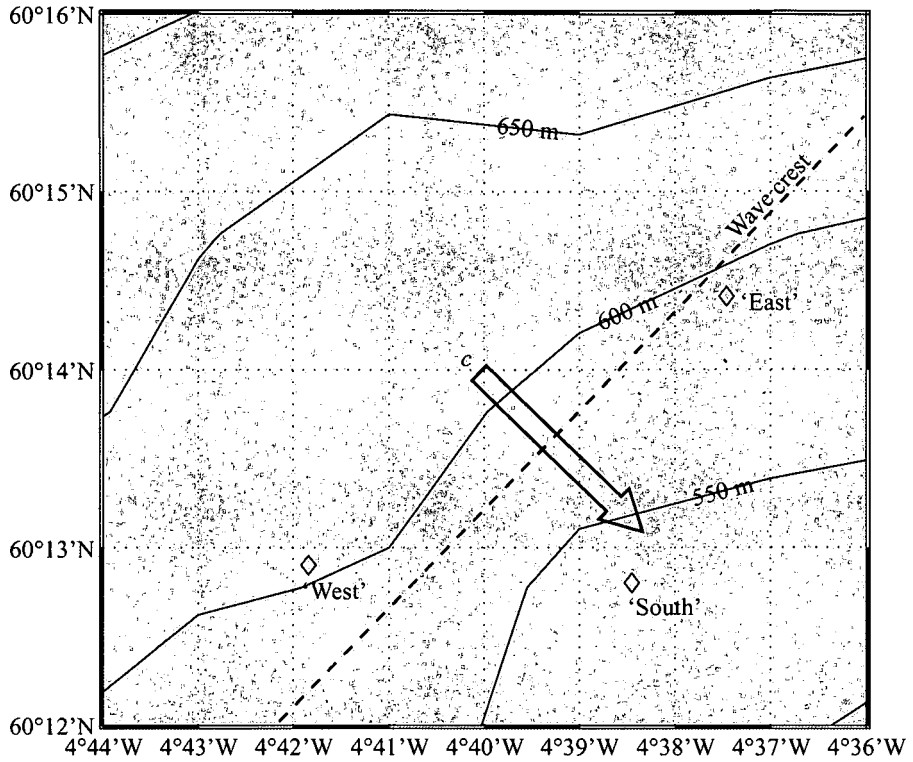

Figure 5.8: The inferred direction of non-linear internal wave propagation relative to the thermistor moorings.

Available potential energy density is calculated

$$APE = \frac{1}{2}\rho_0 N^2 \xi^2, \tag{5.17}$$

where $\xi = -\rho'(d\overline{\rho}/dz)^{-1}$ is the vertical displacement of isopycnals from their rest state due to passing internal waves. To remove the across-slope advection of the pycnocline by the barotropic tide from the energy calculation, the density anomaly is calculated $\rho'(z,t) = \rho(z,t) - \overline{\rho}(z,t)$, where $\rho(z,t)$ is the density approximated from the thermistor time series and $\overline{\rho}(z,t)$ is a 2-hour running median. Using this method, $\overline{\rho}$ accurately follows the roughly semi-diurnal across-slope advection of dense water (Fig. 5.9). A running median is used instead of a running mean so that $\overline{\rho}$ does not increase prematurely before the passage of large solitary waves or the leading wave of a wave train.

As the non-linear internal waves are propagating roughly perpendicular to the slope, only the across-slope energy flux (F_x) is considered. The kinetic energy

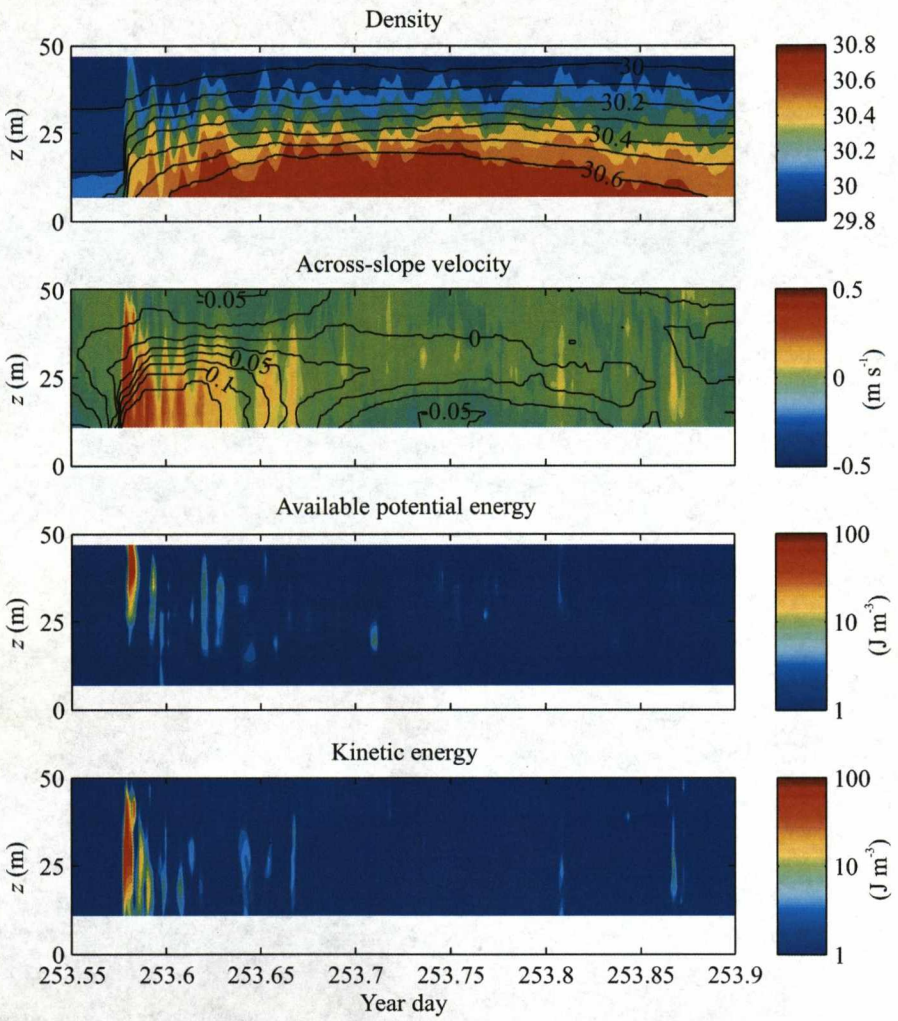

Figure 5.9: An example of density, across-slope velocity, available potential energy density, and kinetic energy density for a non-linear internal wave train from the 'West' mooring pair. The black lines on the upper two panels are contours of 2-hour running median values.

density is therefore calculated

$$KE = \frac{1}{2}\rho_0 u'u'. \tag{5.18}$$

The across-slope velocity perturbation is calculated $u'(z,t) = u(z,t) - \overline{u}(z,t)$, where $u(z,t)$ is the velocity measured by the ADCP and $\overline{u}(z,t)$ is a 2-hour running median (Fig. 5.9).

The kinetic and potential energy densities are vertically integrated from the seabed to 50 m above the bottom; then the wave-averaged energy flux is calculated from Equation (5.16) with 30-minute time-averages (15 realisations),

$$F_x = c\left\langle \int_0^{50} KE\, dz + \int_0^{50} APE\, dz \right\rangle. \tag{5.19}$$

This approach yields three time series of the across-slope energy flux associated with the near-bed, high-frequency internal waves, one from each thermistor/ADCP mooring pair.

5.4.1 Results

There is good correlation between the kinetic and available potential energy density from each mooring pair, with KE generally larger than APE (Fig. 5.10, 5.11, and 5.12). Most APE peaks coincide with peaks in KE although not all KE peaks coincide with peaks in APE. This is particularly evident in the time series from the 'South' moorings and may be because only the lower layer is well sampled by the 50-m thermistor moorings. Internal wave variability is often observed higher than 50 m above the bottom in the 'West', 'South', and 'North' ADCP time series. There are also periods where APE goes to zero but KE is non-zero due to noise in the ADCP data.

Most large energy peaks coincide with the leading wave of a train or individual solitary waves. Instantaneous energies are occasionally over 1 kJ m^{-2} but mean values for the three mooring pairs are of the order 30 J m^{-2} for KE and 10 J m^{-2} for APE. The average KE/APE ratio, averaged in 12-hour bins, is 3.3 (Fig. 5.13). This is larger than $\langle KE \rangle$ / $\langle APE \rangle \simeq 1.5$ estimated by Klymak and Moum (2003) and $\langle KE \rangle \simeq \langle APE \rangle$ observed by Moum et al. (2007) on the Oregon continental shelf, but again may be due to ADCP noise or the fact that only the lower layer is sampled. Evidence for the latter comes from model simulations of high-frequency internal waves on a shelf slope (see Chapter 7) where horizontal velocities (and hence KE) are amplified in the lower layer but vertical isopycnal displacements (and hence APE) are amplified above the pycnocline.

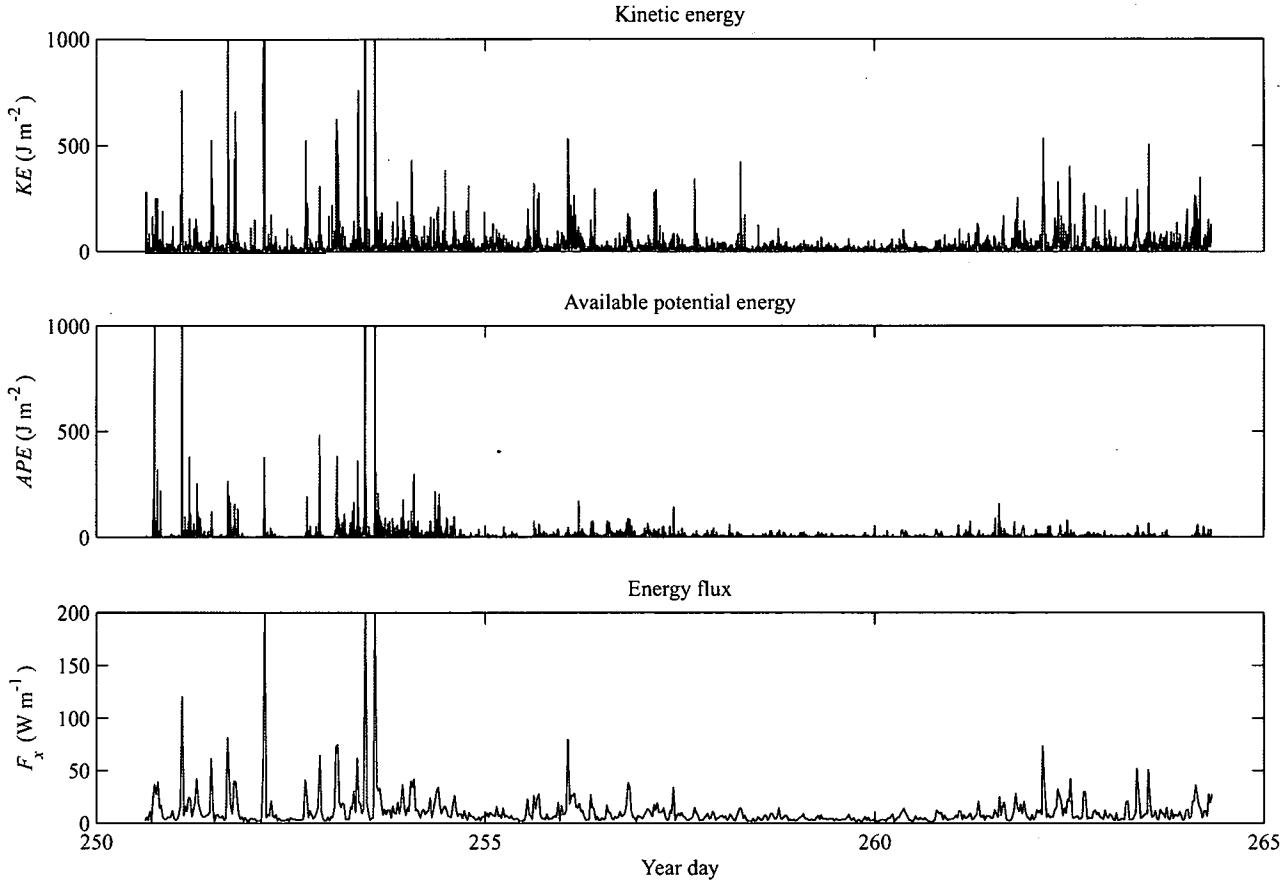

Figure 5.10: Kinetic and available potential energy density integrated from the seabed to 50 m above the bottom, and non-linear internal wave energy flux; from the 'West' mooring pair.

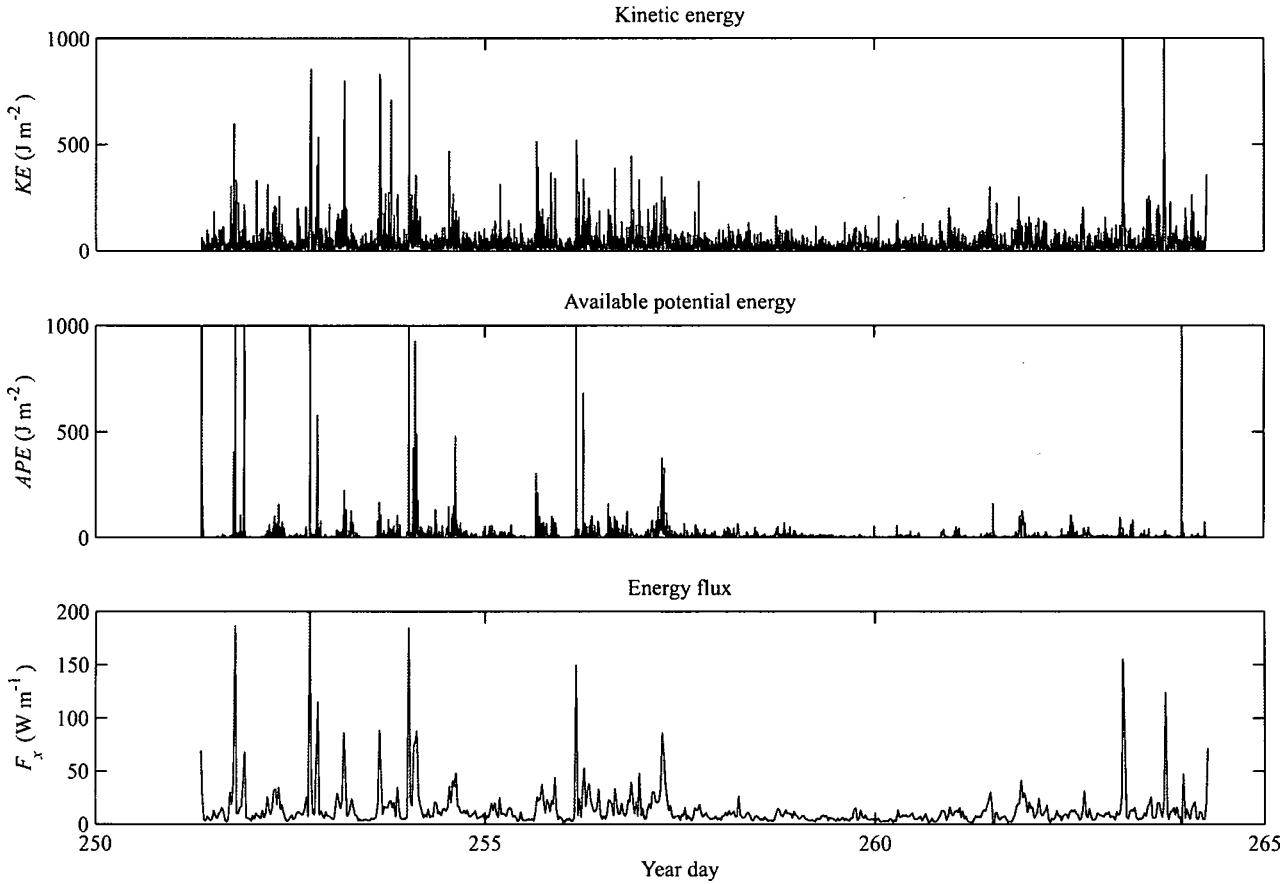

Figure 5.11: Kinetic and available potential energy density integrated from the seabed to 50 m above the bottom, and non-linear internal wave energy flux; from the 'East' mooring pair.

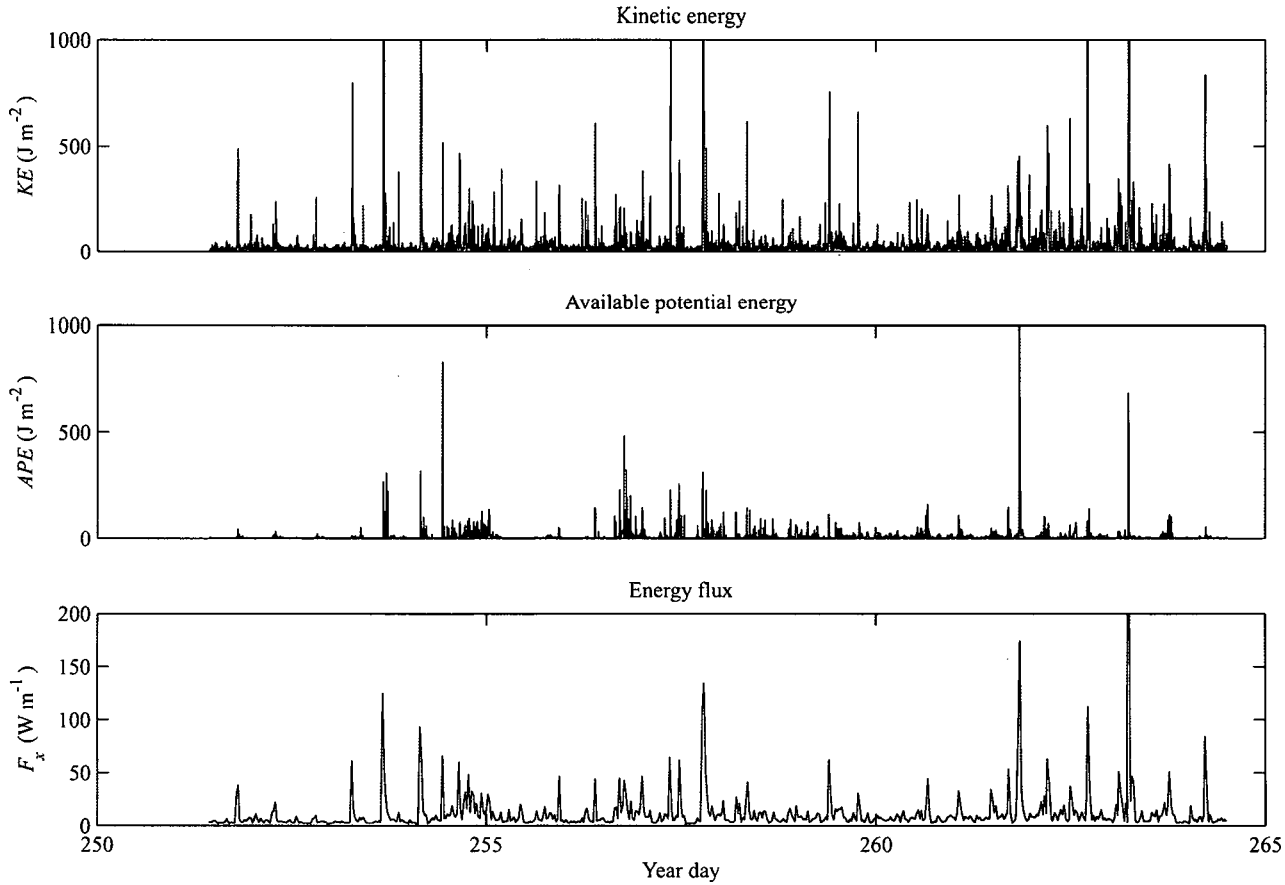

Figure 5.12: Kinetic and available potential energy density integrated from the seabed to 50 m above the bottom, and non-linear internal wave energy flux; from the 'South' mooring pair.

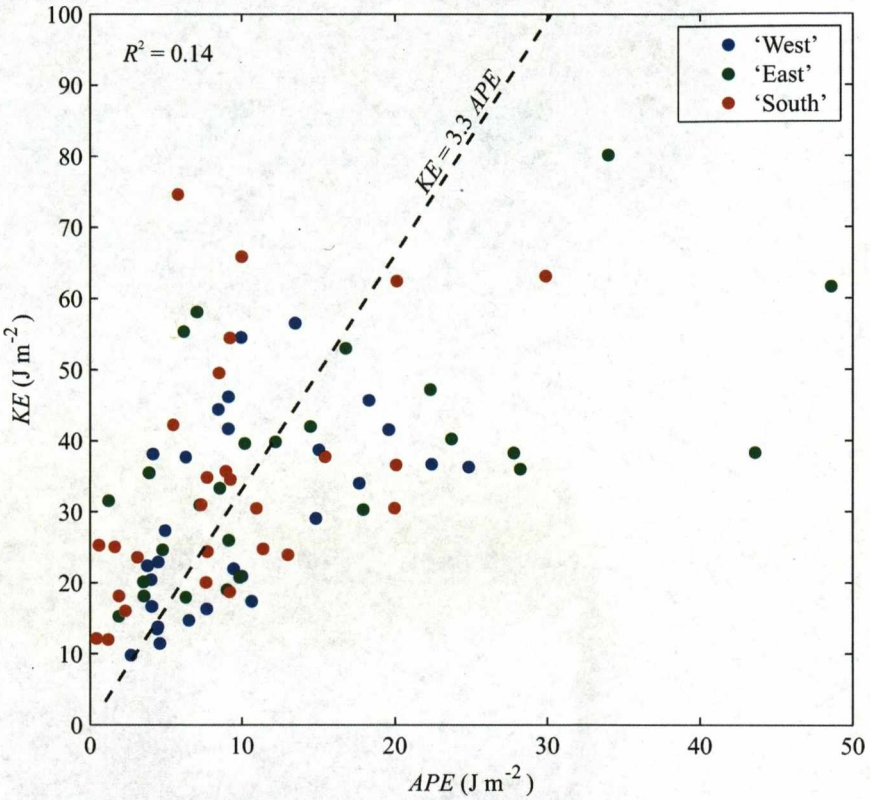

Figure 5.13: Kinetic energy density plotted against available potential energy density, integrated from the seabed to 50 m above the bottom and averaged in 12-hour bins, for the three mooring pairs. The dashed line is a linear regression through the origin of all the data points; the average KE/APE ratio is 3.3.

Maximum wave-averaged energy fluxes reach $\sim$ 200 W m^{-1}, but are typically of the order 10 W m^{-1} (Fig. 5.10, 5.11, and 5.12). The most energetic period is before year day 255, with other large energy peaks near the end of the time series. Between year days 258 and 261 the energy fluxes inferred from the 'West' and 'East' mooring pairs are consistently smaller than 20 W m^{-1}, but this coincides with the period that the pycnocline is shallowest, and only the base is sampled by these thermistor moorings. The time series from the 'South' mooring pair, furthest up the slope, contains more evenly distributed high energy events but misses the energetic period at the beginning of the time series, when the pycnocline was deepest. This suggest significant dissipation of internal wave energy on the slope because the the moorings are $<$ 5 km apart.

5.5 Discussion and conclusions

The energy flux associated with the baroclinic tide on the West Shetland slope is small compared to that of the barotropic tide. Across-slope fluxes for the M_2 tide are 155 W m^{-1} for the baroclinic component but 133 kW m^{-1} for the barotropic component, almost a thousand times larger, with most of the barotropic energy coming from the pressure term. Vertical isopycnal displacements are of the order 10 m in the main pycnocline but surface height perturbations, inferred from the near-bottom pressure time series, are almost 1 m during the same period. There is excellent agreement between the baroclinic energy flux profile for the assumption of the baroclinicity condition for pressure and the profile for the assumption of zero pressure perturbation at mid-depth based a model simulations. This suggests the baroclinicity condition for pressure yields the best approximation of p'_{surf} at this location.

The behaviour of the M_2 internal tide on reflection with the shelf slope is supercritical near the intersection with the main pycnocline, but subcritical for the lower slope, below the pycnocline, and the upper slope near the shelf break. This suggest some reflection of the internal tide in the pycnocline back into deeper water and high dissipation of internal tide energy in the bands of near-critical slope between the subcritical and supercritical regions.

The physical interpretation of the two cross-correlation terms in the tidal energy flux is currently unknown. A similar decomposition of the internal tide into semi-diurnal, near-inertial, GM, and advective components is made by Nash et al. (2005), resulting in 16 separate terms. However, the author is unaware of any previous work decomposing the total tidal energy flux into barotropic

and baroclinic components. The cross-correlation and the baroclinic terms may all be considered part of the baroclinic energy flux because they cannot exist without stratification (Baines, 1982). However, the cross-correlation terms both have vertical integrals of zero[5] and so may be neglected in full-depth energy budgets. As both barotropic and baroclinic variability is required for the cross-correlation terms to exist, they may be related to the transfer of energy from the barotropic tide to the baroclinic tide. Alternatively, they can be taken as evidence that the separation of variability into barotropic and baroclinic components is rather artificial (T. Gerkema, personal communication), especially over sloping topography because the vertical structure of velocity and pressure cannot be separated from horizontal position (Gerkema and van Haren, 2007).

The only known previous estimates of internal tide energy flux in the region local to the slope mixing experiment were made by Sherwin (1991), from observations and a model of internal generation over the Wyville Thomson Ridge. At a station near the base of the ridge, a northward mode-1 M_2 internal tide energy flux of 4.7 kW m^{-1} is estimated, twice that predicted by the model (2.2 kW m^{-1}) and over an order of magnitude larger than calculated here. However, Sherwin also made new estimates of the internal tide energy flux using the data of Helland-Hansen (1930) from three other stations, one at 61°N, 2°30′W over the 500 m isobath of the West Shetland slope, northeast of the site of the slope mixing experiment. At this station the mode-1 M_2 internal tide energy flux is estimated 137 W m^{-1}, comparable to that calculated here. To the southwest of the Wyville Thomson ridge, where the shelf slope descends into the Rockall Trough, Sherwin (1988) estimated the onshore mode-1 internal tide energy flux at the shelf break to be 104 W m^{-1}, again comparable to that calculated here.

Although the internal tide energy flux at the base of the Wyville Thomson ridge is over an order of magnitude larger than at the site of the slope mixing experiment, energy fluxes of this magnitude are not uncommon. The recent Hawaii Ocean Mixing Experiment (HOME) found the internal tide energy flux away from the Hawaii ridge crest to be 5 to 6 kW m^{-1} (Nash et al., 2006) with $\sim$ 16 kW m^{-1} across the 3000 m isobath (Lee et al., 2006). Other estimates of large internal tide energy fluxes include 5 kW m^{-1} at the mouth of Monterey Submarine Canyon (Kunze et al., 2002), 1 kW m^{-1} on the Mid-Atlantic Bight (Nash et al., 2004), and 2.4 kW m^{-1} away from Great Meteor Seamount (Gerkema and van Haren, 2007).

[5]The baroclinicity condition for pressure must be assumed if $\int_{-H}^{0} \langle \mathbf{u}'_{\mathrm{bt}} p'_{\mathrm{bc}} \rangle = 0$.

During the passage of non-linear internal wave trains or large solitary waves, the up-slope energy flux in the bottom 50 m reaches ~ 200 W m^{-1} on the West Shetland slope, the same order as across-slope baroclinic tidal energy flux integrated through the whole watercolumn. This suggests that, when the near-bed internal wave field is energetic, these features are at least as important as the internal tide for mixing on the shelf slope. Although time-average energy fluxes are typically of the order 10 W m^{-1}, the non-linear internal waves are bottom-trapped and so must dissipate or break in the local area because the near-bed buoyancy frequency further up the slope is less than the angular frequency of the waves. Evidence for high local internal wave energy dissipation comes from occasions of large upslope energy fluxes at the 'West' and 'East' moorings that are not evident at the 'South' moorings < 5 km up the slope.

For comparison, the onshore energy flux associated with the internal solitary waves observed on the Oregon continental shelf by Klymak and Moum (2003) is estimated to be of the order 100 W m^{-1} (Moum et al., 2007) and similar to the onshore semi-diurnal internal tide energy flux at the shelf break. This is an order of magnitude larger than the time-averaged non-linear internal wave energy flux calculated here, but comparable to the peak fluxes during the passing of wave trains.

The dissipation of internal wave energy on the West Shetland slope is discussed in Chapter 6 and reconciled with the independent estimates of TKE dissipation rate from Chapter 4. The reflection and dissipation of internal wave energy on the slope is investigated using a numerical model in Chapter 7.

Chapter 6

Mixing and dissipation of internal wave energy on the West Shetland slope

6.1 Introduction

The internal wave field on the West Shetland slope contains both a semi-diurnal internal tide and near-bed, non-linear internal waves. In this chapter, the role of these internal waves in supporting mixing on the slope is assessed, focusing on the following questions: 'How much turbulent mixing occurs on the slope?'; 'What are the sources of energy for mixing?'; and 'Can internal wave energy fluxes account for the measured mixing?'.

To make measurements of internal waves and their induced mixing, an array of thermistor and ADCP moorings were deployed on the West Shetland slope and a series of full-depth lowered ADCP/CTD casts taken (Fig. 6.1, summarised in Chapter 3). In Chapter 4 the CTD and lowered ADCP profiles are used to make independent estimates of the rate of TKE dissipation, from Thorpe scale analysis of density overturns and using a finescale parameterisation of vertical shear and strain. In Chapter 5 the internal tide energy flux is calculated from the full-depth lowered ADCP/CTD profiles and the non-linear internal wave energy flux is calculated from the thermistor and ADCP mooring time series. This chapter[1] is a synthesis of the previous three chapters with an extended discussion on the dissipation of internal wave energy and other sources of energy for mixing. Initial observations of internal waves are described in Section 6.2. The estimates

[1]This chapter is based on the manuscript:

Hall, R., J. Huthnance, and R. G. Williams: Mixing and dissipation of internal wave energy on a shelf slope. In revision for *Journal of Physical Oceanography.*

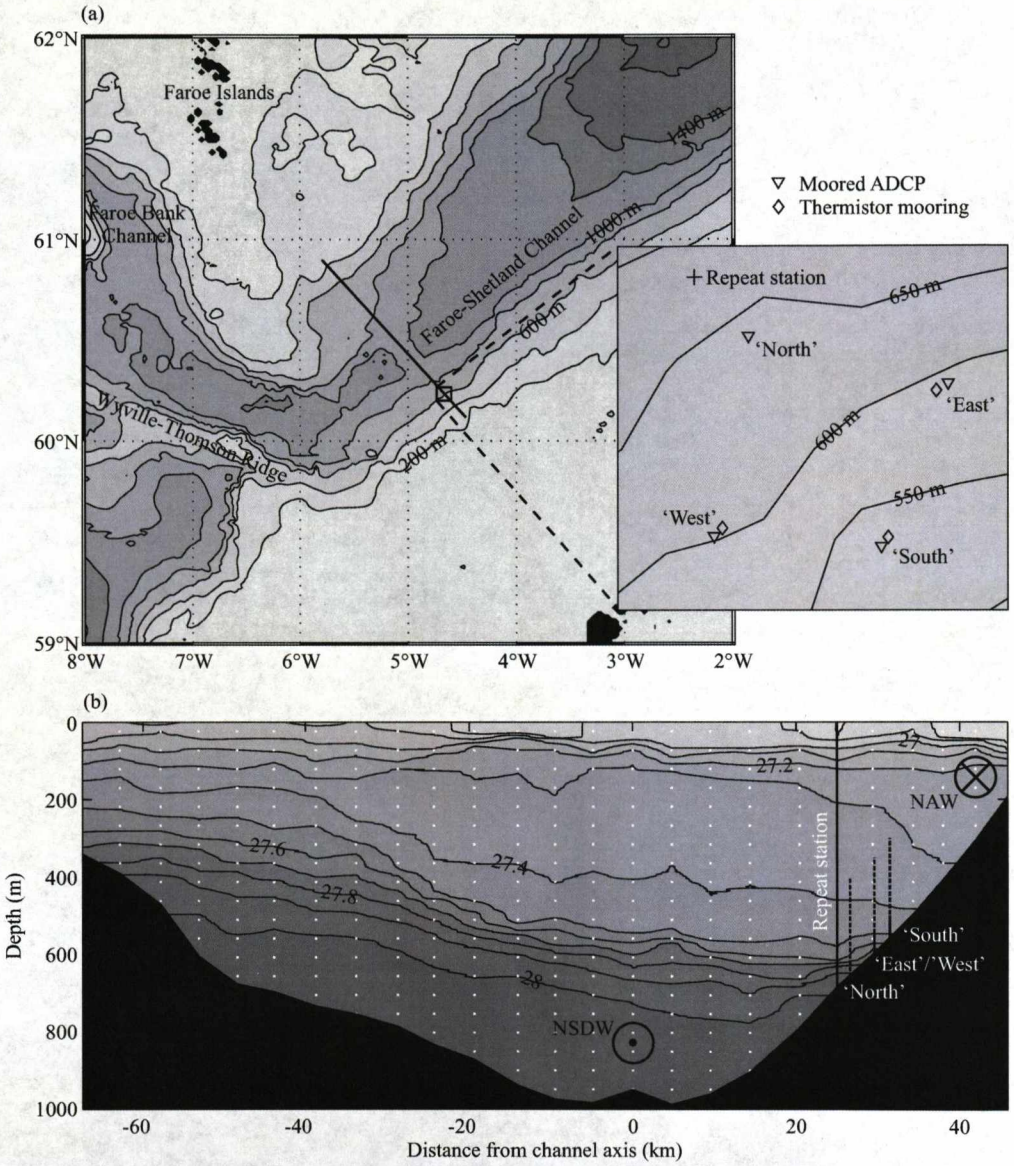

Figure 6.1: (a) Topography of the Faroe-Shetland Channel and the location of the mooring array on the West Shetland slope. Inset: the location of individual moorings in the array and the lowered ADCP/CTD repeat station. (b) Across-channel distribution of σ_θ with the locations of casts and moorings (the white dotted lines are single casts from the across-channel section).

of TKE dissipation rate and inferred diapycnal eddy diffusivities are reviewed in Section 6.3. Sources of energy for mixing, including turbulence from bottom friction on barotropic tidal currents; surface forcing by the wind; the internal tide; and near-bed, non-linear internal waves are considered in Section 6.4. The larger-scale context and the potential sources of the internal waves on the slope are discussed in Section 6.5.

6.2 Internal wave observations

At the location of the lowered ADCP/CTD repeat station the main pycnocline is observed at about 600 m, less than 100 m above the seabed (Fig. 6.2). Vertical displacement of the pycnocline suggests a semi-diurnal internal tide present along the slope, with an amplitude of the order 10 m. Horizontal current velocities are strongly semi-diurnal and concentrated in the lower layer, below the pycnocline, with velocity amplitudes of the order 0.1 m s^{-1}. The internal tide may be generated locally, at the shelf break, or at a remote location. Linear least-square fits of the M_2 tide to the depth-averaged flow show the barotropic tidal amplitude is 0.08 and 0.09 m s^{-1} across and along the slope respectively. The time-average barotropic flow is 0.06 m s^{-1} down the slope and 0.03 m s^{-1} along-slope directed to the northeast.

Higher frequency, non-linear internal waves appear intermittently in the mooring time series (Fig. 6.3b,c). As the pycnocline is maintained close to the seabed, most of the observed internal waves are bottom-trapped waves of elevation (Klymak and Moum, 2003). Some of the waves occur singularly in the form of solitary waves, while others occur in trains in the form of cnoidal waves. On a few occasions the isopycnals do not return to their original rest state after the solitary wave or cnoidal wave train has passed (Fig. 6.3d), suggesting solibore like behavior (Hosegood and van Haren, 2004).

Each train begins with a large amplitude (up to 50 m) wave of elevation; subsequent waves generally decrease in amplitude and typically have periods between 15 and 30 minutes. This variation is expected because the large amplitude waves travel faster than the smaller amplitude waves, forming rank-ordered packets. During some periods of the mooring time series, the trains appear at roughly semi-diurnal intervals so are likely to be tidally forced. However, the trains have varied phase relations with the local barotropic tide (Fig. 6.3a) suggesting they are not generated locally, but at a remote location and propagate into the region.

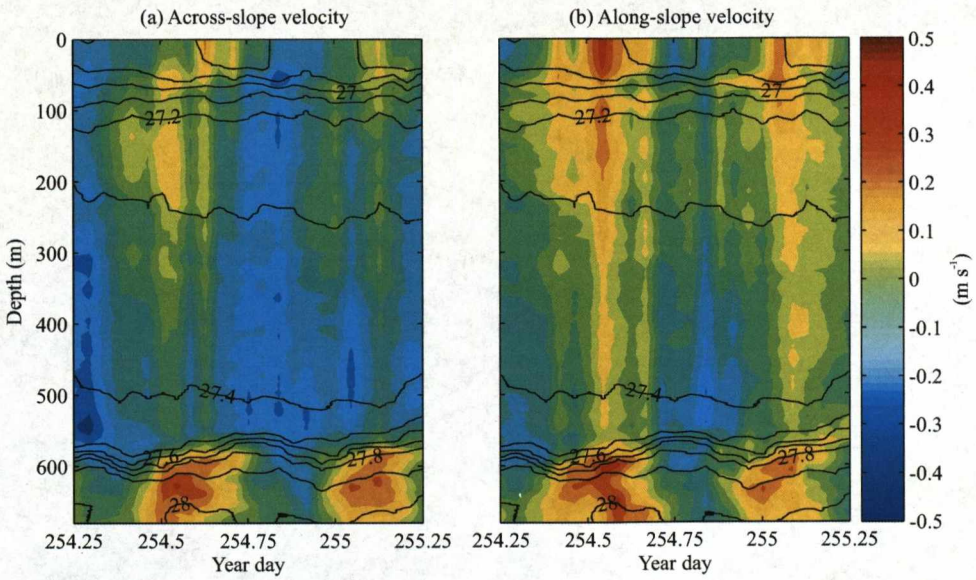

Figure 6.2: (a) Across-slope and (b) along-slope velocity from the lowered ADCP during the repeat station over the 680 m isobath. The black lines are contours of σ_θ from the CTD.

The velocities of the non-linear waves are measured by tracking the leading wave in each train between the three thermistor moorings. The mean velocity of the leading waves is 0.27 m s^{-1} at an angle of 132° up the shelf slope, within 10° of perpendicular to the isobaths. This wave velocity implies wavelengths between 250 and 500 m. Wave amplitudes are large compared to the depth of the lower layer, and amplitude-to-wavelength ratios are up to 0.2, reinforcing the non-linear nature of the waves.

6.3 Mixing estimates

To investigate how much turbulent mixing occurs on the slope, independent estimates of TKE dissipation rate are made from Thorpe scale analysis of density overturns and using a finescale parameterisation of vertical shear and strain. The diapycnal eddy diffusivity is then inferred from the dissipation rate.

6.3.1 Density overturns

The rate of TKE dissipation (ϵ) is inferred from vertical profiles of potential density by relating the Ozmidov scale, $L_O = (\epsilon/N^3)^{1/2}$, (Ozmidov, 1965) to the

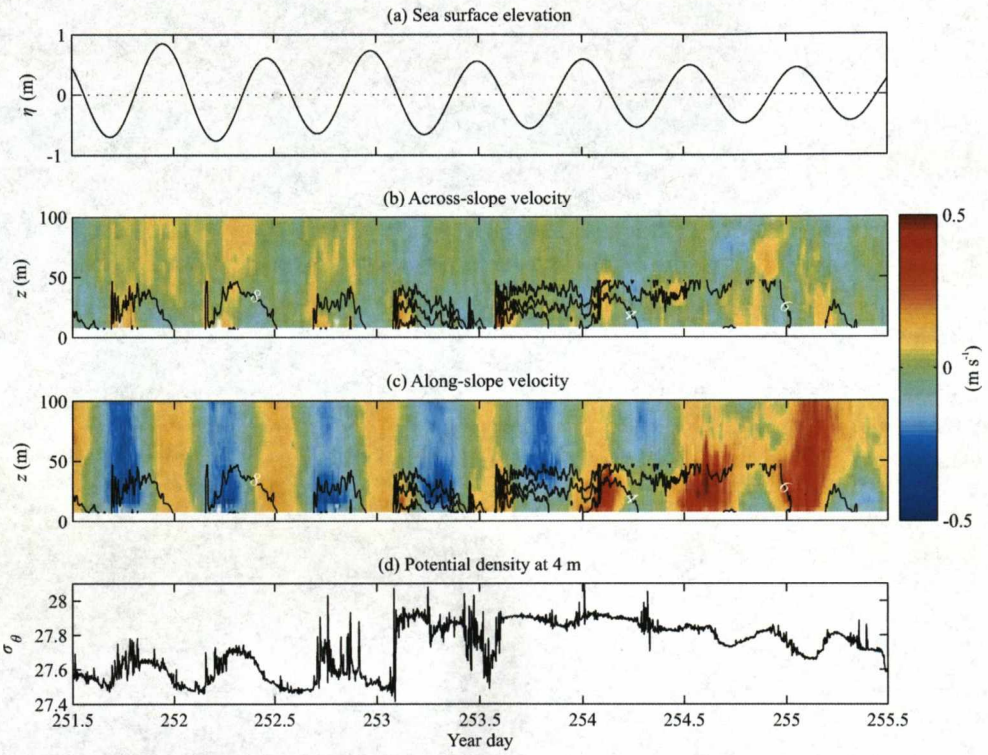

Figure 6.3: (a) Sea surface elevation approximated from near-bed pressure recorded by the moored CTD loggers. (b) Across-slope and (c) along-slope velocity from the 'West' moored ADCP. The black lines are contours of temperature (every 2°C) from the 'West' thermistor mooring. (d) Potential density at 4 m above the seabed from the CTD logger on the 'West' thermistor mooring.

Thorpe scale, L_T, (Thorpe, 1977) by the empirical relation $L_O = 0.8L_T$ (Dillon, 1982), giving

$$\epsilon = 0.64{L_T}^2 N^3, \tag{6.1}$$

where N is the buoyancy frequency over the depth range of each overturn. L_T is the rms distance the samples are moved in the vertical (Thorpe displacements) as the density profiles are reordered to make them statically stable.

L_T, N, and ϵ are first averaged in 50 m vertical bins for each cast then the time-average and standard error calculated for each bin from the 25 casts (Fig. 6.4a). The longest overturn scales occur below the seasonal thermocline, at around 200 m, where L_T approaches 1.5 m. Between 350 and 500 m, L_T is shorter than the density resolution limit of the CTD ($\sim$ 1.2 m) and so is likely to be strongly affected by noise. However, the Thorpe scale is significantly longer than the 0.11 m depth resolution limit in the main pycnocline, where $L_T > 0.5$ m, and the overturn-scale buoyancy frequency is maximum ($\sim 3 \times 10^{-3}$ s^{-1}). Using these estimates, the TKE dissipation rate in the main pycnocline reaches up to 4×10^{-8} W kg^{-1} (Fig. 6.4c).

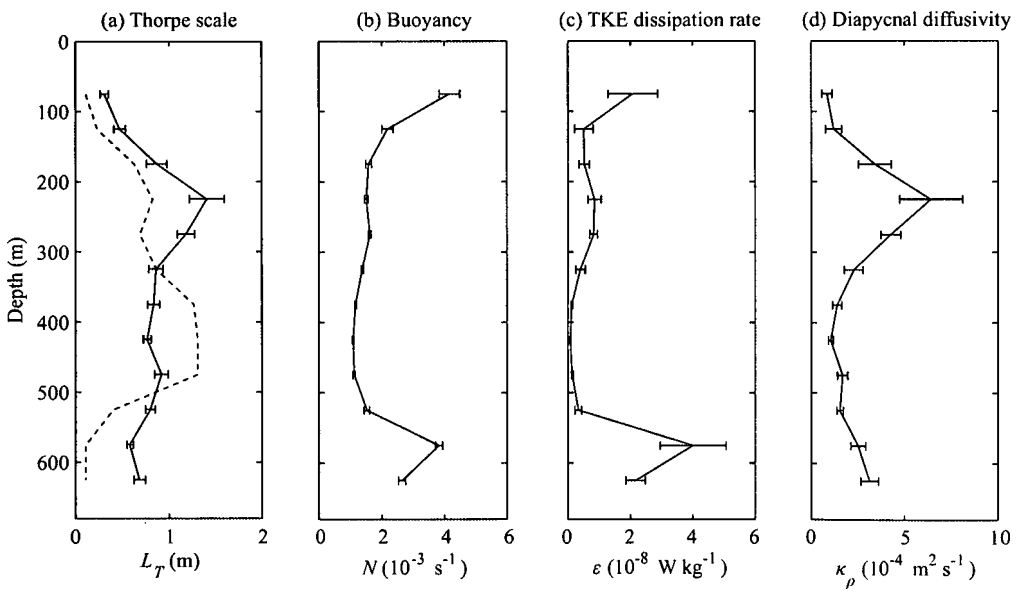

Figure 6.4: (a) Thorpe scale, (b) buoyancy frequency, (c) TKE dissipation rate, and (d) diapycnal eddy diffusivity in 50 m vertical bins. The error bars are the standard error between 25 casts. The dashed line is the CTD resolution limit.

For comparison with the following finescale parameterisation, L_T, N, and ϵ are then averaged in three layers with relatively constant buoyancy frequencies: the seasonal thermocline (50-150 m); the main pycnocline (550-650 m); and the buoyancy minimum between the two stratified layers (150-550 m). The time-average values in each layer are shown in Table 6.1 with the attached standard error as an estimate of the temporal sampling error. Other uncertainties in the calculation arise from the accuracy of the CTD and variability in the empirical constant. Including these additional sources of error, ϵ can be estimated within a factor of 3 (Fer et al., 2004), which is used for the error bars in Figure 6.6a.

Layer (m)	L_T (m)	N (10^{-3} s^{-1})	ϵ Thorpe (10^{-8} W kg^{-1})	κ_ρ Thorpe (10^{-4} m^2 s^{-1})
50-150	0.46 ± 0.06	2.29 ± 0.19	0.54 ± 0.28	1.17 ± 0.42
150-550	0.80 ± 0.02	1.36 ± 0.02	0.29 ± 0.03	1.86 ± 0.13
550-650	0.59 ± 0.03	3.30 ± 0.05	2.88 ± 0.46	2.48 ± 0.25

Table 6.1: Summary of Thorpe scales, buoyancy frequencies, TKE dissipation rates, and diapycnal eddy diffusivities in three layers; the seasonal thermocline (50-150 m); the main pycnocline (550-650 m); and the buoyancy minimum between the two stratified layers (150-550 m). The uncertainty is the standard error between 25 casts.

The average Thorpe scale in the main pycnocline is 0.6 ± 0.03 m, equivalent to a TKE dissipation rate of $3 \pm 0.5 \times 10^{-8}$ W kg^{-1}. L_T is longest, 0.8 ± 0.02 m, in the buoyancy minimum but because N is small, ϵ is an order of magnitude smaller than in the pycnocline. In the seasonal thermocline L_T is minimum, 0.5 ± 0.06 m, but a higher buoyancy frequency means ϵ is of the same order as in the buoyancy minimum. The proximity of L_T to the resolution limit in the upper two layers means the dissipation rates must be interpreted with caution.

6.3.2 Vertical shear and strain

To provide a comparison for the TKE dissipation rates inferred from the Thorpe scale analysis, independent estimates are made using the Gregg-Henyey finescale parameterisation, based on the Garrett and Munk (GM) model of the background internal wave field (Garrett and Munk, 1975; Cairns and Williams, 1976). In the parameterisation, ϵ is dependent on the spectra of vertical shear and strain,

computed from the lowered ADCP and CTD profiles, compared with the GM model following the method of Henyey et al. (1986), Gregg (1989), and Polzin et al. (1995),

$$\epsilon = \epsilon_0 \times \frac{f}{f_0} \times \frac{\cosh^{-1}(N/f)}{\cosh^{-1}(N_0/f_0)} \times \frac{N^2}{N_0^2} \times \frac{\langle V_z^2 \rangle^2}{\langle V_{z\,\mathrm{GM}}^2 \rangle^2} \times F(R_\omega). \qquad (6.2)$$

Here $\langle V_z^2 \rangle$ is the measured power spectrum of vertical shear (or strain for the equivalent calculation) integrated from the lowest resolved vertical wavenumber to $k_z = 0.126$ rad m^{-1} (50 m vertical wavelength); $\langle V_{z\,\mathrm{GM}}^2 \rangle$ is the power spectrum of vertical shear (or strain) from the GM model integrated between the same limits; ϵ_0, f_0, and N_0 are characteristic constants from the model. The last term, $F(R_\omega)$, corrects the parameterisation for small deviations from the GM spectra and is a function of frequency content of the internal wave field, estimated from the shear-to-strain ratio.

To infer values of ϵ from (6.2) that can be directly compared with ϵ from (6.1), the power spectra of vertical shear and strain are computed in the same three layers as the Thorpe scale and time-averaged in five 5-cast groups (Fig. 6.5). Both the up and down casts from the lowered ADCP are utilised and the shear spectra are corrected for high wavenumber attenuation due to data processing (Polzin et al., 2002). Unlike the Thorpe scale analysis, N is the background buoyancy frequency (notated here N_b) and is calculated from the mean density gradient through each layer for each group of casts.

Time-average values of N_b and ϵ in each layer are shown in Tables 6.2 and 6.3 with the attached standard error between the five groups as an estimate of the temporal sampling error. The total uncertainty in the calculation of ϵ is estimated to be a factor of 3 (Polzin et al., 2002), which is used for the error bars in Figure 6.6a.

In all layers, the TKE dissipation rates inferred from the shear and strain parameterisations are consistent and within the bounds of uncertainty. In the main pycnocline, the dissipation rates are 7 ± 2 and $4 \pm 2 \times 10^{-8}$ W kg^{-1} from shear and strain respectively. ϵ is smallest in the buoyancy minimum layer with dissipation rates of order 10^{-9} W kg^{-1}. The seasonal thermocline is the only layer in which ϵ from the strain parameterisation is larger than that from the shear parameterisation (10 ± 3 and $6 \pm 2 \times 10^{-9}$ W kg^{-1} respectively).

TKE dissipation rates from (6.2) vary with depth and buoyancy in the same manner as from (6.1), but are larger in the main pycnocline and the seasonal thermocline by factors between 1.1 and 2.5, within the bounds of uncertainty. In the buoyancy minimum the dissipation rate from (6.1) is larger than from (6.2) by

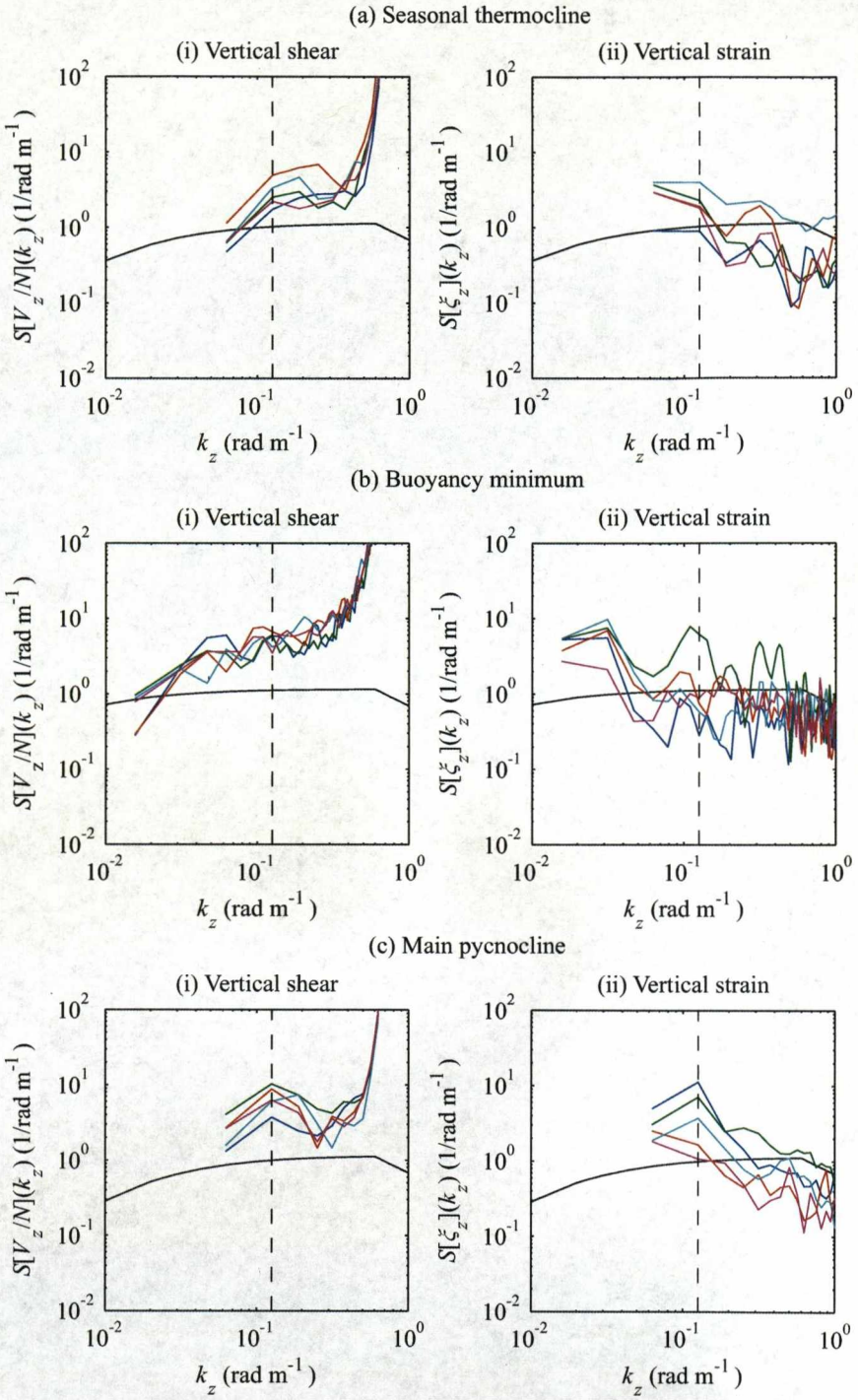

Figure 6.5: Power spectra of (i) vertical shear normalised by N and (ii) vertical strain for three layers of the watercolumn: (a) the seasonal thermocline; (b) the buoyancy minimum; and (c) the main pycnocline. The black lines are the power spectra from the GM model. The dashed lines mark the upper limit of integration.

Layer (m)	N_b (10^{-3} s^{-1})	ϵ shear (W kg^{-1})	κ_ρ shear (10^{-4} m^2 s^{-1})
50-150	5.69 ± 0.09	0.58 ± 0.21	0.35 ± 0.12
150-550	1.92 ± 0.03	0.16 ± 0.02	0.87 ± 0.10
550-650	7.29 ± 0.30	7.33 ± 2.12	2.85 ± 0.78

Table 6.2: Summary background buoyancy frequencies, TKE dissipation rates, and diapycnal eddy diffusivities in three layers, calculated from the finescale parameterisation of vertical shear. The uncertainty is the standard error between five groups of casts.

Layer (m)	N_b (10^{-3} s^{-1})	ϵ strain (W kg^{-1})	κ_ρ strain (10^{-4} m^2 s^{-1})
50-150	5.69 ± 0.09	1.04 ± 0.31	0.62 ± 0.18
150-550	1.92 ± 0.03	0.09 ± 0.04	0.50 ± 0.25
550-650	7.29 ± 0.30	4.47 ± 1.99	1.52 ± 0.59

Table 6.3: Summary background buoyancy frequencies, TKE dissipation rates, and diapycnal eddy diffusivities in three layers, calculated from the finescale parameterisation of vertical strain. The uncertainty is the standard error between five groups of casts.

approximately a factor of 2. The general agreement between the two independent estimates is promising and, in the absence of direct turbulence measurements, suggests the true dissipation rate is of the order 5×10^{-8} W kg^{-1} in the main pycnocline; 5×10^{-9} W kg^{-1} in the seasonal thermocline; and 10^{-9} W kg^{-1} in the buoyancy minimum.

6.3.3 Diapycnal eddy diffusivity

Diapycnal eddy diffusivity (κ_ρ) is the mixing parameter commonly used in ocean circulation models and is related to ϵ by $\kappa_\rho = \Gamma\epsilon/N^2$ (Osborn, 1980), where Γ is the mixing efficiency. For $\Gamma = 0.2$ (Oakey, 1982) and the background buoyancy frequencies shown in Tables 6.2 and 6.3, the diagnosed dissipation rates are equivalent to diapycnal diffusivities of the order 5×10^{-5} m^2 s^{-1} in the seasonal thermocline and buoyancy minimum, and 2×10^{-4} m^2 s^{-1} in the main pycnocline. The latter is an order of magnitude larger than typical values for the interior of the open ocean (Ledwell et al., 1993; Toole et al., 1994), but of the same order as measured over rough abyssal topography (Polzin et al., 1997; Led-

well et al., 2000) and seamounts (Toole et al., 1997; Eriksen, 1998). Estimates of mixing efficiency typically vary between 0.15 and 0.3 (Fer et al., 2004) so the total uncertainty in κ_ρ is estimated to be a factor of 4, which is used for the error bars in Figure 6.6b.

Given the high estimates of TKE dissipation rate and diapycnal eddy diffusivity in the pycnocline, this poses the question of how the high level of mixing is sustained and what are the sources of energy.

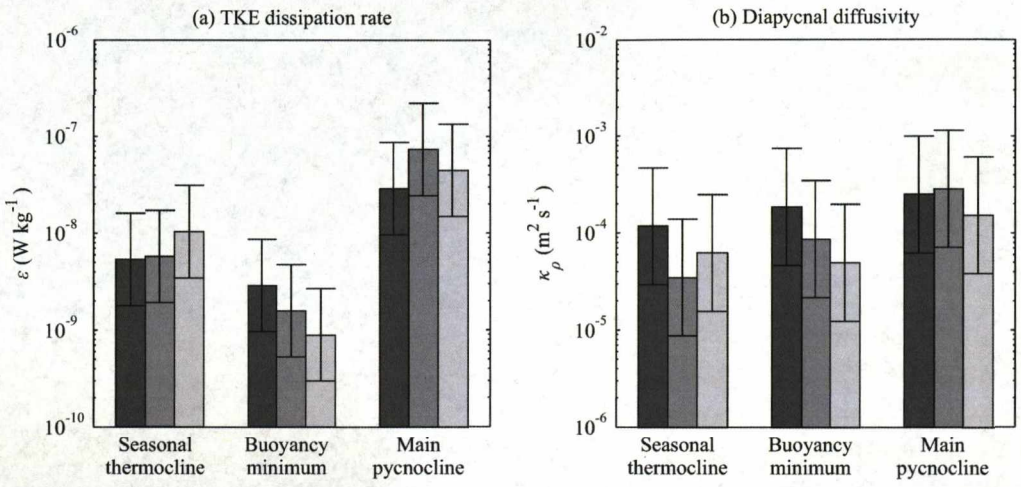

Figure 6.6: (a) TKE dissipation rates and (b) diapycnal eddy diffusivities in three layers inferred from the scale of density overturns (dark grey), vertical shear (grey), and vertical strain (light grey). The error bars show the total uncertainty in the estimates.

6.4 Energy sources

The energy for mixing on the slope might originate from four possible sources: turbulence from bottom friction on barotropic tidal currents; surface forcing by the wind; the internal tide; and near-bed, non-linear internal waves. The high semi-diurnal variability in and below the main pycnocline suggests the internal tide is important, while the bottom-trapped non-linear internal wave field appears to be energetic, but intermittent in time. Each possible source is now discussed in turn.

6.4.1 Bottom friction and surface forcing

The work of bottom friction on barotropic tidal currents generates TKE in the bottom boundary layer, but is not transferred to mixing as efficiently as through internal wave breaking; estimates of mixing efficiency for the barotropic tide are small, e.g. 0.0037 (Simpson and Hunter, 1974), compared with the internal tide, $\sim$ 0.2 (Sandstrom and Oakey, 1995). We estimate the source of TKE at the bottom boundary to be ~ 0.002 W m^{-2} using $D = \rho C_d \langle \mathbf{u}^3 \rangle$, where $\mathbf{u}$ is barotropic tidal current velocity from the full-depth lowered ADCP profiles and $C_d = 0.0025$ is the drag coefficient. The vertical propagation of energy is limited by the main pycnocline because turbulence is inhibited by stratification, therefore the TKE must be dissipated locally. Assuming that the TKE generated at the bottom boundary penetrates upwards no further than 150 m (the top of the pycnocline) suggests the barotropic tide can account for a dissipation rate of 1.2×10^{-8} W kg^{-1}, several times smaller than inferred from the Thorpe scale analysis and finescale parameterisation in the pycnocline.

Wind energy input of TKE to the ocean, $W = \langle \tau \mathbf{u}_g \rangle$ where τ is the wind stress and $\mathbf{u}_g$ is the geostrophic velocity at the sea surface, is typically 0.01 W m^{-2} (Huthnance, 1995). However, this estimate assumes all small-scale motions are dissipated within the surface mixed layer (Wunsch, 1998) and so will not contribute to mixing in the main pycnocline. Energy from mechanical forcing at the surface can be transported below the mixed layer by near-inertial internal waves which have been shown to provide a significant input of energy into the global ocean (Alford, 2003a), comparable to that of internal tides (Egbert and Ray, 2000, 2001). At this location they are discounted as a significant source of energy to the main pycnocline because spectral analysis of the moored ADCPs data shows little variance at near-inertial and sub-inertial frequencies.

6.4.2 Internal tide

The internal tide energy flux is calculated $\mathbf{F} = \langle \mathbf{u}' p' \rangle$, where $\mathbf{u}'$ is the velocity perturbation and p' is the pressure perturbation, due to passing internal waves, following Kunze et al. (2002), Carter and Gregg (2002), and Nash et al. (2005). Semi-diurnal velocity perturbations and density anomalies (ρ') are found from linear least-square fits of the M_2 tidal constituent to horizontal velocity and density from the full-depth lowered ADCP/CTD profiles. Baroclinic velocity perturbations are calculated by subtracting the depth-averaged flow from the velocity perturbations, and baroclinic pressure perturbations are calculated by integrat-

ing the hydrostatic equation from the surface, $p' = p'_{\text{surf}} + \int_z^0 \rho' g \, dz$, where p'_{surf} is surface pressure perturbation due to passing internal waves. Semi-diurnal vertical isopycnal displacements are calculated from the M_2 fits to density then vertical velocity perturbations inferred $w' = d\xi/dt$.

The total horizontal internal tide energy flux, integrated from the surface to the seabed, is 155 W m^{-1} up-slope and 44 W m^{-1} along-slope to the southwest (Fig. 6.7a,b). The energy flux integrated through the main pycnocline (550-650 m) is 99 ± 4 W m^{-1} up-slope and 22 ± 1 W m^{-1} along-slope to the southwest. The vertical internal tide energy flux is of the order one hundredth of the magnitude of the horizontal energy flux (Fig. 6.7c). The vertical energy flux is $78 \pm 2 \times 10^{-4}$ W m^{-2} at the base of the pycnocline (650 m) but only $6 \pm 5 \times 10^{-4}$ W m^{-2} at the top of the pycnocline (550 m).

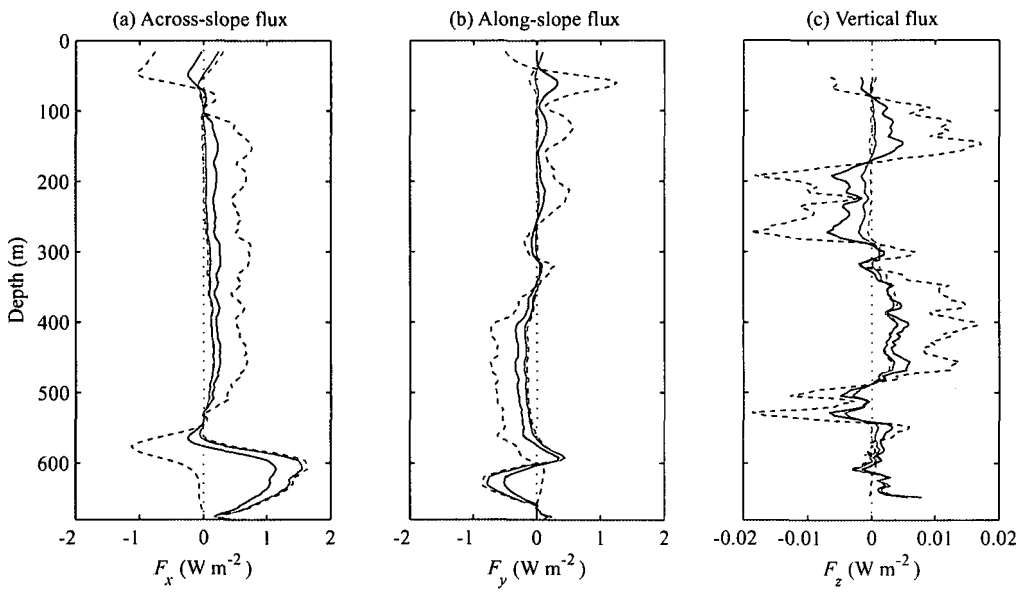

Figure 6.7: (a) Across-slope, (b) along-slope, and (c) vertical M_2 internal tide energy fluxes. The black lines are for the assumption $p' = 0$ at $z = 0$; the dashed black lines are for the assumption $p' = 0$ at $z = -H$; the solid grey lines are for the assumption $\int_{-H}^0 p' \, dz = 0$; the dashed grey lines are for the assumption $p' = 0$ at $z = -560$ m.

6.4.3 Non-linear internal waves

The energy fluxes associated with the high-frequency, non-linear internal waves observed in the thermistor and ADCP mooring time series are calculated using the energy flux relation

$$F_x = c\,\langle KE + APE\rangle\,, \tag{6.3}$$

where $KE = \frac{1}{2}\rho_0 u'u'$ is the kinetic energy density of the wave; $APE = \frac{1}{2}\rho_0 N^2\xi^2$ is the available potential energy density; and c is the internal wave velocity (Moum et al., 2007). u' and ξ are the across-slope velocity perturbations and vertical isopycnal displacements, due to passing internal waves, found by decomposing the velocity and density time series into time-average values and anomalies so that $u' = u - \overline{u}$ and $\rho' = \rho - \overline{\rho}$. The time-average values ($\overline{u}$ and $\overline{\rho}$) are calculated using a 2-hour running median. Using this method, $\overline{\rho}$ accurately follows the roughly semi-diurnal across-slope advection of the dense water and removes it from the energy calculation. Relation (6.3) is used instead of $\langle \mathbf{u}'p'\rangle$ because the mooring array was designed to sample through the main pycnocline at high resolution and so the overlying density structure and barotropic velocities are not measured. We consider only the across-slope energy flux for the non-linear waves as the mean wave velocity is almost perpendicular to the isobaths. For each mooring pair KE and APE are integrated from the seabed up to 50 m above the bottom; then the wave-averaged energy flux is calculated from (6.3) with 30-minute time averages.

Maximum wave-averaged energy fluxes reach ~ 200 W m^{-1}, but are typically of the order 10 W m^{-1} (Fig. 6.8c). During the period of the repeat station when the mixing estimates were made, the energy flux was low, but relatively uniform. Mean values for this period are consistent between the three mooring pairs: 11 ± 1 W m^{-2} for the 'West' moorings; 14 ± 1 W m^{-1} for the 'East' moorings; and 15 ± 2 W m^{-2} for the 'South' moorings. The uncertainty is the standard error between the 48 flux estimates during the 24 hour period. As the non-linear waves propagate perpendicular to the slope, the difference between the 'East' and 'West' moorings on the same isobath is another measure of the uncertainty in the calculation. Thus, at the time of the repeat station, the non-linear internal wave energy flux in the bottom 50 m is estimated to be 10 to 15 W m^{-1}.

6.4.4 Internal wave energy dissipation

In this section we consider how the internal tide and near-bed, non-linear internal wave energy is dissipated. As turbulent mixing is likely where internal waves undergo critical reflection with sloping topography, the reflective behaviour

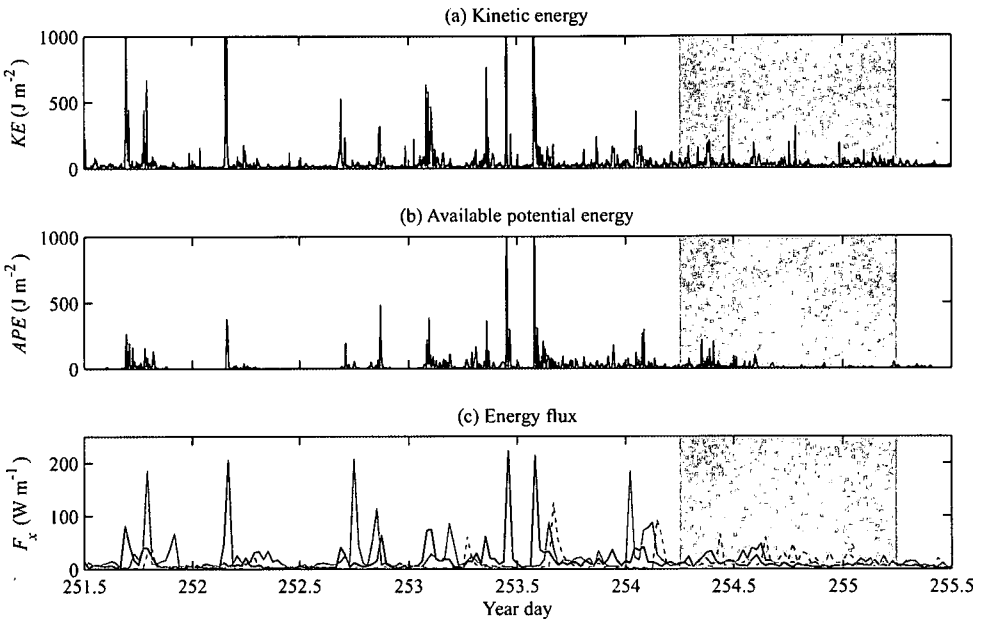

Figure 6.8: (a) Kinetic and (b) available potential energy associated with non-linear internal waves, integrated from the seabed up to 50 m above the bottom, from the 'West' mooring pair. (c) Non-linear internal wave energy fluxes from the three thermistor/ADCP mooring pairs. The solid line is the 'West' mooring pair; the grey line is the 'East' mooring pair; and the dashed grey line is the 'South' mooring pair. The shaded area shows the period of the repeat station when mixing estimates where made.

of the M_2 internal tide is predicted from the ratio of the topographic slope ($s_{\text{topog}} = dh/dx$, where h is the position of the bottom) to the near-bed internal tide characteristic slope, $\alpha = s_{\text{topog}}/s_{\text{wave}}$. s_{wave} is calculated from the internal wave dispersion relation (1.2), for $N = N_{\text{nb}}$, the near-bed buoyancy frequency. Away from the main pycnocline there is a well mixed bottom boundary layer ~ 50 m thick. We therefore take N_{nb} to be the mean buoyancy frequency in the lower 50 m of the watercolumn. Away from the pycnocline, N_{nb}^2 is close to zero, however, where the pycnocline intersects the slope, stratification is maintained near the seabed and N_{nb}^2 increases up to 5×10^{-5} s^{-2}.

The lower reaches of shelf slope is subcritical ($\alpha < 1$) to the M_2 internal tide, becoming supercritical ($\alpha > 1$) ~ 20 km from the axis of the channel as the slope gradient and the near-bed buoyancy frequency increase (Fig. 6.9). At ~ 35 km from the channel axis the gradient and buoyancy frequency decrease and the slope returns subcritical. This variation implies that, in the pycnocline, the internal tide will be reflected back into deeper water, while above and below the pycnocline, the internal tide will continue to propagate up the slope. Some internal tide energy will be dissipated in the bands of near-critical slope ($\alpha \simeq 1$) between the subcritical and supercritical regions. The internal tide energy flux, calculated in Section 6.4.2, is the net energy flux of the incident and reflected waves; it therefore accounts for any internal tide reflection in the pycnocline. The fraction of internal tide energy that is reflected is assessed in Chapter 7.

The high-frequency, non-linear internal waves are bottom-trapped and so must dissipate or break in the local area because the near-bed buoyancy frequency further up the slope is less than the angular frequency of the waves.

Given the up-slope energy fluxes associated with the internal tide and near-bed, non-linear internal waves, we now consider where the energy is dissipated. As the largest internal tide energy fluxes are found in the main pycnocline and the non-linear internal waves are restricted to the pycnocline by their frequency, we make an assumption that the whole up-slope energy flux in the pycnocline is dissipated in a region bounded by the location of the energy flux estimate, the shelf slope, and the top and base of the pycnocline. The bulk TKE energy dissipation rate in this region is then estimated $\epsilon_{\text{bulk}} \simeq F_{\text{net}}/(\rho A)$, where F_{net} is the net energy flux into the region and A is the area.

For the internal tide, a net energy flux of 125 ± 9 W m^{-1} is calculated, including the vertical fluxes at the base and top of the pycnocline. The area of the dissipation region is estimated to be 6.5×10^5 m^2, for a pycnocline thickness of 100 m and the measured slope gradient, 0.02 (Fig. 6.10). Allowing a

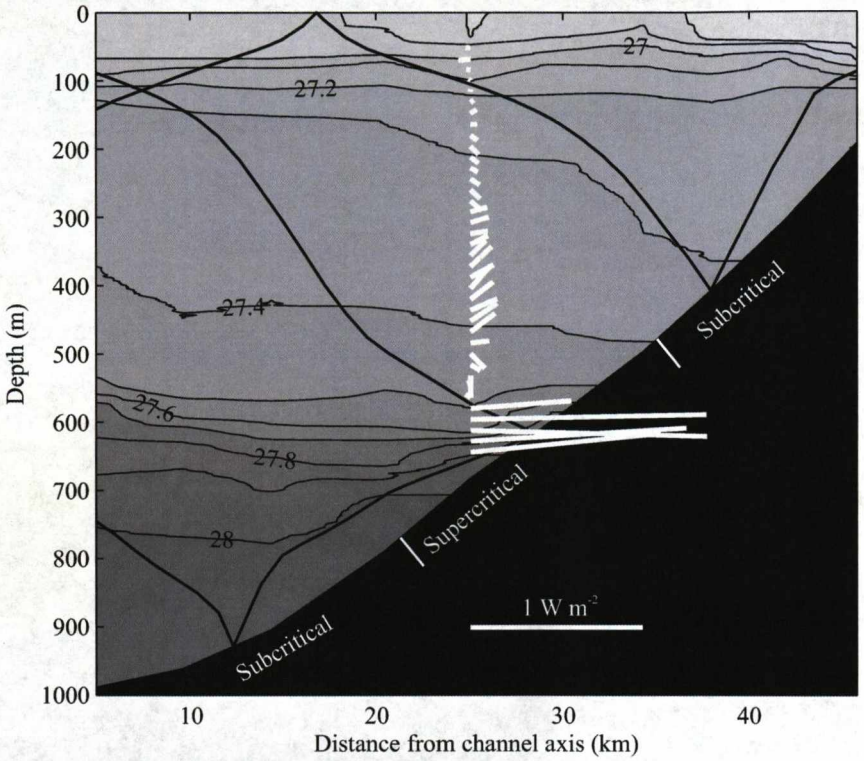

Figure 6.9: Characteristic ray paths of the M_2 internal tide in the Faroe-Shetland Channel (black lines) overlaid on the across-channel distribution of σ_θ. The white lines show the across-slope M_2 internal tide energy flux.

10% error in the area of the dissipation region yields a bulk dissipation rate of $1.9 \pm 0.3 \times 10^{-7}$ W kg^{-1}. This is a factor of four larger than the TKE dissipation rate inferred from the Thorpe scale analysis and finescale parameterisation in the pycnocline (of the order 5×10^{-8} W kg^{-1}).

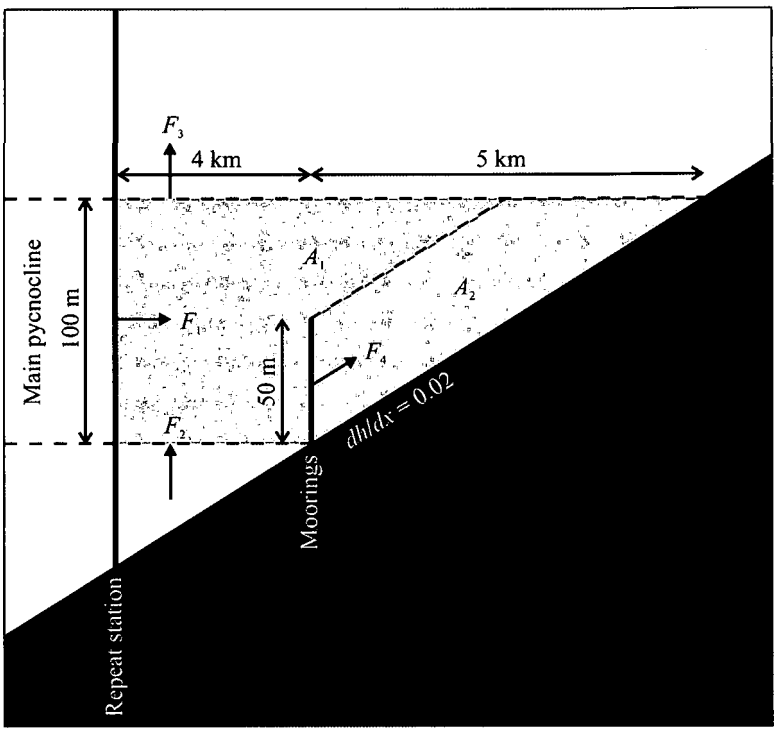

Figure 6.10: Schematic of internal wave energy dissipation. For the internal tide the net energy flux into the region of dissipation, $F_{\text{net}} = F_1 + F_2 - F_3$ and the area of the region, $A_1 = 100$ m $\times$ 4 km + 100 m $\times$ 5 km $\times$ 1/2. For the non-linear internal waves the net energy flux, $F_{\text{net}} = F_4$ and the area $A_2 =$ 50 m $\times$ 5 km $\times$ 3/4.

The up-slope energy flux associated with the the non-linear internal waves is only 10 to 15 W m^{-1}, but the area of the dissipation region is also estimated to be smaller, 1.9×10^5 m^2, because the energy flux estimates are made further up the slope than for the internal tide (Fig. 6.10). Again allowing a 10% error in the area of the dissipation region yields a bulk TKE dissipation rate between 4.7 and 8.7×10^{-8} W kg^{-1}. The TKE dissipation rate inferred from the Thorpe

scale analysis and finescale parameterisation in the pycnocline is at the low end of this range.

6.5 Discussion and conclusions

In this chapter we have assessed the role of internal waves in supporting mixing on the West Shetland slope. The amount of turbulent mixing that occurs on the slope is inferred from Thorpe scale analysis of density overturns and using a finescale parameterisation of vertical shear and strain. The TKE dissipation rate and diapycnal eddy diffusivity are maximum in the main pycnocline, of the order 5×10^{-8} W kg^{-1} and 2×10^{-4} m^2 s^{-1} respectively; the latter is an order of magnitude larger than background levels.

We suggest that the high rate of TKE dissipation in the pycnocline can be sustained by the horizontal energy fluxes associated with the semi-diurnal internal tide and near-bed, non-linear internal waves, if it is assumed that the whole up-slope energy flux in the pycnocline is dissipated in the region between the location of the energy flux estimate and the shelf slope. The net internal tide energy flux into this region is 125 ± 9 W m^{-1}, yielding a bulk TKE dissipation rate of $1.9 \pm 0.3 \times 10^{-7}$ W kg^{-1}. The up-slope non-linear internal wave energy flux is 10 to 15 W m^{-1}, yielding a bulk TKE dissipation rate between 4.7 and 8.7×10^{-8} W kg^{-1}.

The source of TKE at the bottom boundary from the work of bottom friction on barotropic tidal currents is small compared to the horizontal energy fluxes and can only account for a fraction of the measured mixing. Near-inertial internal waves are also discounted because there is little variability at near and sub-inertial frequencies.

It is unlikely that the internal tide and non-linear internal wave trains are generated locally, at the shelf break, because: (1) the non-linear wave trains are observed to propagate up the slope; (2) the trains have varied phase relations with the local barotropic tide; and (3) the internal tide energy flux has a large up-slope component in the pycnocline. We therefore suggest that the internal waves are generated at a remote location and propagate into the region along the pycnocline before reflecting or breaking on the shelf slope. The Wyville Thomson Ridge, 110 km west of the mooring site, is a likely generation region of the internal tide in the Faroe-Shetland Channel, as proposed by Sherwin (1991). The trains of high-frequency internal waves also appear to be tidally forced and may be a non-linear manifestation of the internal tide.

If enhanced mixing by internal wave breaking is typical of the main pycnocline along continental shelf slopes, this mechanism could make a significant contribution to mixing globally, as substantial internal wave energy fluxes have been measured in other regions. The recent Hawaii Ocean Mixing Experiment (HOME) found the internal tide energy flux away from the crest of the Hawaiian Ridge to be 5 to 6 kW m^{-1} (Nash et al., 2006) with $\sim$ 16 kW m^{-1} across the 3000 m isobath (Lee et al., 2006). Other estimates of internal tide energy fluxes include 0.1 kW m^{-1} on the continental shelf West of Scotland (Sherwin, 1988), 5 kW m^{-1} at the mouth of Monterey Submarine Canyon (Kunze et al., 2002), 1 kW m^{-1} on the continental slope off Virginia (Nash et al., 2004), and 2.4 kW m^{-1} away from Great Meteor Seamount (Gerkema and van Haren, 2007).

All internal wave energy must eventually be dissipated, either in shelf seas or the deep ocean. As the transfer of energy from internal waves to turbulent mixing is more efficient than from the barotropic tide or surface forcing by the wind, relatively small energy fluxes could make large contributions to global mixing, especially given that in energetic regions internal wave energy fluxes are of the order kW m^{-1} as opposed to order 10-100 W m^{-1} measured here. Moreover, internal wave energy tends to be dissipated in stratified regions where the most work on buoyancy needs to be done.

In summary, the semi-diurnal internal tide and near-bed, non-linear internal waves are both important mechanisms supporting mixing on the West Shetland slope. Mixing in the main pycnocline is enhanced above background levels by the dissipation of internal tide and non-linear internal wave energy on the slope. This facilitates exchange across the shelf edge and modification of exchanging water masses in the Faroe-Shetland Channel. Three questions remain open: How much of the internal tide energy is reflected and how much is dissipated?'; 'Do the observed high-frequency internal waves dissipate simply because the buoyancy frequency further up the slope is to low to support them, or are there other limiting factors?'; and 'Is the internal wave energy dissipated primarily in the main pycnocline, as assumed in the bulk dissipation calculations?'. These will be discussed in the next chapter using a numerical model to investigate the propagation of internal wave energy on the slope.

Chapter 7

Internal wave reflection and energy dissipation in a numerical model

7.1 Introduction

In the previous chapter, the energy fluxes associated with the semi-diurnal internal tide and high-frequency, non-linear internal waves on the West Shetland slope are calculated and reconciled with independent estimates of the rate of TKE dissipation by assuming that all the energy in the pycnocline is dissipated on the slope. In this chapter, numerical model simulations of internal waves approaching a continental shelf slope are conducted to assess how much energy is reflected and how much is dissipated, depending on the slope topography, background stratification, internal wave frequency, and internal wave mode. These simulations are used to help answer three questions left open after the observational study:

1. On the West Shetland slope, how much internal tide energy is reflected and how much is dissipated?

2. Do the observed high-frequency internal waves dissipate because the buoyancy frequency further up the slope is too low to support them?

3. Where in the watercolumn is the internal wave energy dissipated?

The Massachusetts Institute of Technology general circulation model (see Marshall et al. 1997a,b; Adcroft et al. 1997) is used following the work of Legg and Adcroft (2003) on internal wave breaking on continental slopes; primary changes to the model configuration are non-uniform stratification, varied internal wave frequency, and higher modes. In Section 7.2 the configuration of the model is explained as well as the variables changed for the different runs: slope topography;

background stratification; and open boundary forcing. In Section 7.3 the diagnostics used to assess the performance of the model are described. The results of the model runs are shown in Section 7.4. A discussion of the above questions follows in Section 7.5.

7.2 Numerical model configuration

The model is run in non-hydrostatic mode with rotation. All three components of the velocity are included but the model is only configured in two-dimensions (x,z). A linear equation of state is used and therefore buoyancy frequency is a linear function of the vertical potential temperature and salinity gradients,

$$N^2 = g\alpha\frac{d\theta}{dz} - g\beta\frac{dS}{dz}, \tag{7.1}$$

where $\alpha = 2 \times 10^{-4}$ °C^{-1} is the thermal expansion coefficient for temperature and $\beta = 7.4 \times 10^{-4}$ psu^{-1} is the saline expansion coefficient for salinity. Turbulent diffusivities are not explicitly calculated. Viscosity is uniform ($\nu_h = 10^{-2}$ m^2 s^{-1} and $\nu_z = 10^{-3}$ m^2 s^{-1}), as is horizontal diffusivity ($\kappa_h = 10$ m^2 s^{-1}). However, vertical diffusivity is calculated implicitly; where the watercolumn is stably stratified $\kappa_z = 0$, so that the stratification is not eroded, but is increased to 10 m^2 s^{-1} if statically unstable conditions develop to quickly redistribute buoyancy in the vertical.

The initial conditions are no flow and a horizontally uniform temperature and salinity fields that form stable stratification. Several different temperature and salinity profiles are used, described in Section 7.2.1. The boundary conditions for velocity are no slip at the bottom; no stress at the surface; no flow normal to the topography; and a linear free surface is solved for. The boundary conditions for temperature and salinity are no flux at the surface and bottom.

The maximum depth of the watercolumn is 1000 m and total length of domain (east to west) varies between 100 km and 800 km. The topography consists of a 1000 m deep region with a flat bottom on the western side of the domain, a shelf slope to the east, and a shallow, 200 m deep continental shelf on the eastern side of the domain. The western boundary is open and forced by oscillating velocities and temperature/salinity anomalies, described in Section 7.2.2, that generate eastward propagating internal waves; the eastward boundary is closed by a vertical wall. The gradient and profile of the shelf slope is varied, as described in Section 7.2.3. Topography is represented by a partial step shaved cell

method (Adcroft and Marshall, 1997); the minimum fractional size of cells is 0.05, equivalent to a minimum cell height of 1 m.

7.2.1 Stratification

Five background stratification profiles are investigated, the simplest case of uniform stratification; a non-uniform profile with strong stratification in a pycnocline at mid-depth, based on observed temperature and salinity profiles in the Faroe-Shetland Channel; and three non-uniform profiles with weaker stratification in the pycnocline, but the pycnocline at different depths. For uniform stratification, buoyancy frequency is prescribed ($N^2 = 2.4 \times 10^{-6}$ rad s^{-2}) and for uniform salinity ($S = 35$ psu) the vertical potential temperature gradient inferred,

$$\theta_z = \frac{N^2}{g\alpha}. \tag{7.2}$$

A normalised potential temperature profile is then defined,

$$\theta(z) = \theta_z z - \overline{\theta_z z}. \tag{7.3}$$

For strong pycnocline stratification, idealised potential temperature and salinity profiles, $\theta(z)$ and $S(z)$, are generated using observed temperature and salinity profiles from the middle of the Faroe-Shetland Channel along the Central section. The empirical expression

$$\theta(z) = a + bz + c \tanh\left(d2\pi\left(1 + \frac{z}{e}\right)\right) \tag{7.4}$$

is fit to the observed potential temperature profile (Fig. 7.1), $a = 5.25$ determines the absolute temperature; $b = 1.5 \times 10^{-3}$ is the minimum temperature gradient; $c = 4.5$ determines the temperature difference between the upper and lower layers; $d = 1$ determines the thickness of the pycnocline, and $e = 600$ is the depth of the pycnocline. The temperature gradient through the pycnocline is a function of c and d. Salinity is fixed to covary linearly with potential temperature, $S = 0.05\theta + 34.9$. As a result, the idealised salinity profile is not as close to observations as the temperature profile; the model does not have negative vertical salinity gradients as seen in the upper 100 m and lower 250 m in observations. The buoyancy frequency profile is calculated from Equation (7.1); N^2 varies from 2.4×10^{-6} rad s^{-2} at the surface and the bottom to 7.6×10^{-5} rad s^{-2} in the pycnocline.

For weak pycnocline stratification, the same expression is used to generate potential temperature profiles, but with $c = 0.35$; $d = \frac{2}{3}, 1, 1\frac{1}{3}$; and $e = 400, 600, 800$.

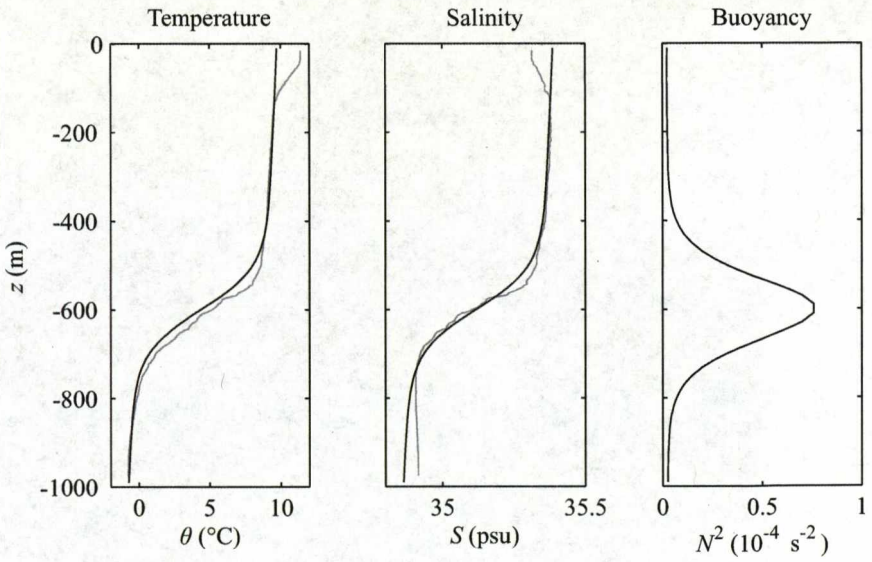

Figure 7.1: Potential temperature, salinity and, buoyancy frequency profiles for the strong pycnocline stratification runs. The grey lines are the observed potential temperature and salinity profiles from the Faroe-Shetland Channel.

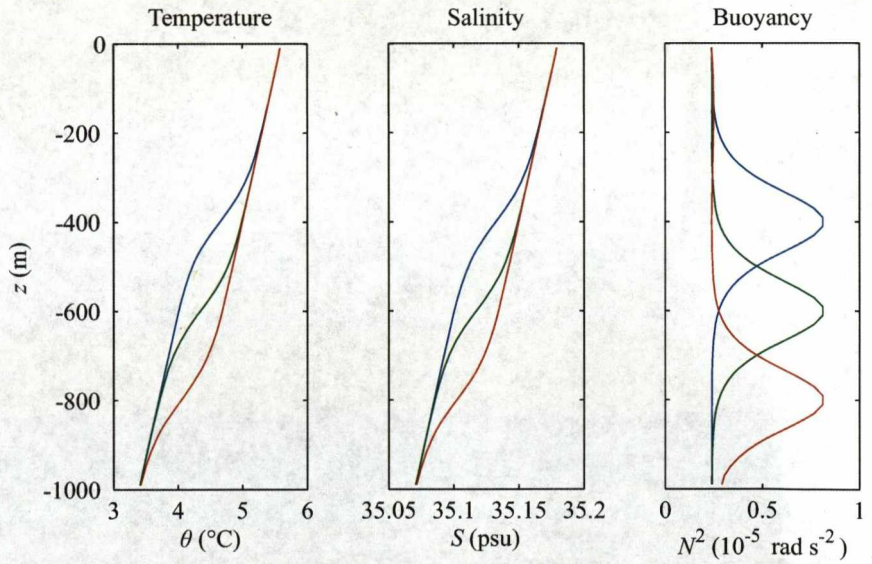

Figure 7.2: Potential temperature, salinity and, buoyancy frequency profiles for the weak pycnocline stratification runs. The blue line is for *LowN400*; the green line is for *LowN600*, and the red line is for *LowN800*.

Salinity again covaries linearly with potential temperature. The resulting buoyancy frequency profiles have the same background value as the strong pycnocline stratification profile but with maximum of only 8.1×10^{-6} rad s^{-2}, located at $z = -400$, -600, and -800 m (Fig. 7.2).

7.2.2 Open boundary forcing

Oscillating velocities and temperature/salinity anomalies are prescribed at the open boundary to satisfy linear internal wave equations. The eastward (u), northward (v), and vertical (w) velocities are defined

$$u(0,z,t) = U_0\, F(z)\, \sin(\omega t), \tag{7.5}$$

$$v(0,z,t) = U_0 \frac{f}{\omega}\, F(z)\, \cos(\omega t), \tag{7.6}$$

$$w(0,z,t) = -U_0 \left(\frac{\omega^2 - f^2}{N^2 - \omega^2}\right)^{1/2} G(z)\, \cos(\omega t), \tag{7.7}$$

where $U_0 = 0.1$ m s^{-1} is the velocity amplitude of the internal wave; ω is the angular frequency of the internal wave, and $f = 1.25 \times 10^{-4}$ rad s^{-1} is the Coriolis frequency. $F(z)$ and $G(z)$ are the vertical structures of horizontal and vertical velocity respectively for first, second, or third mode internal waves, calculated for the background buoyancy frequency profile (Fig. 7.3 and 7.4). For uniform stratification, $F(z) = \cos(k_z z)$ and $G(z) = \sin(k_z z)$, where $k_z = n\pi/H$ is the vertical wavenumber for a n^{th} mode internal wave. $H = 1000$ m is the total depth of the watercolumn.

The potential temperature (θ) and salinity (S) at the open boundary are defined

$$\theta(0,z,t) = \theta_0(z) + U_0 \frac{N}{g\alpha(1 - 1/r)} \left(\frac{\omega^2 - f^2}{\omega^2}\right)^{1/2} G(z)\, \sin(\omega t), \tag{7.8}$$

$$S(0,z,t) = S_0(z) + U_0 \frac{N}{g\beta(r - 1)} \left(\frac{\omega^2 - f^2}{\omega^2}\right)^{1/2} G(z)\, \sin(\omega t), \tag{7.9}$$

where $\theta_0(z)$ and $S_0(z)$ are the prescribed background potential temperature and salinity profiles and $r = (\alpha/\beta)(d\theta/dS)$ is ratio of the temperature term to the salinity term in Equation (7.1). For the uniform stratification salinity is also uniform so $r \to \infty$ and $N/g\alpha(1 - 1/r)$ in Equation (7.8) simplifies to $N/g\alpha$. In Equation (7.9), $N/g\beta(r - 1)$ goes to zero and so there is no salinity forcing. For the non-uniform stratification profiles, temperature and salinity covary linearly

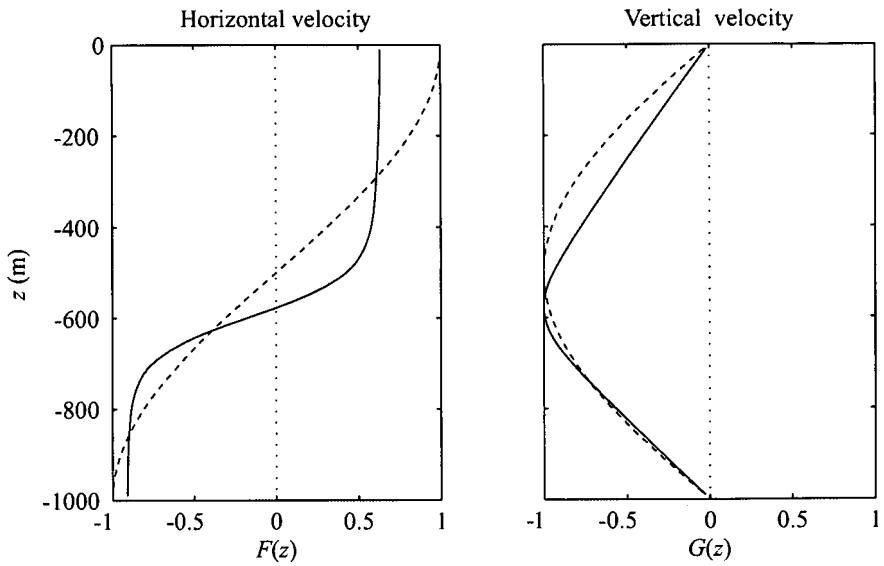

Figure 7.3: Vertical structure of horizontal and vertical velocity of mode-1 internal waves. The solid lines are for the strong pycnocline stratification runs; the dashed lines are for the uniform stratification runs.

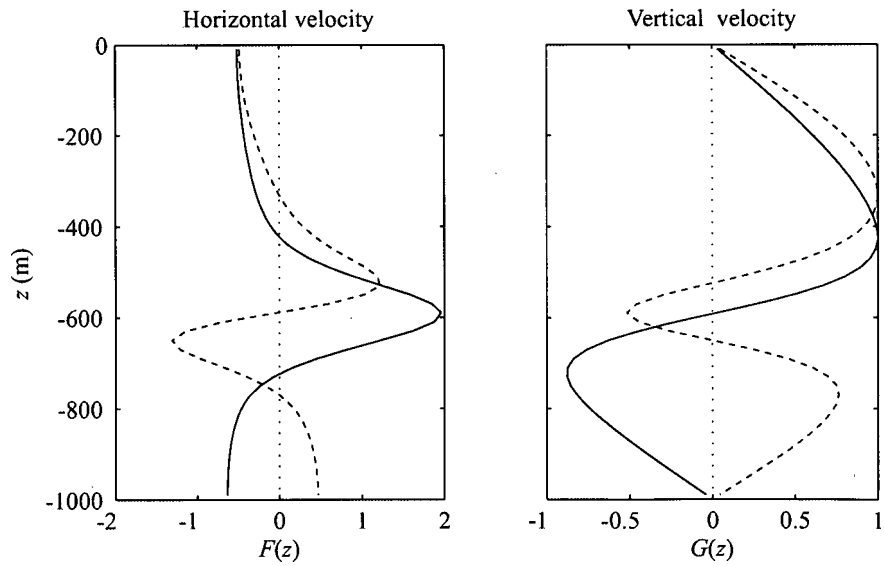

Figure 7.4: Vertical structure of horizontal and vertical velocity of mode-2 (solid lines) and mode-3 (dashed lines) internal waves for the strong pycnocline stratification runs.

so that $d\theta/dS = 20°\text{C/psu}$ and thus $r = 5.4$, i.e. temperature is the primary control on density.

The forcing at the open boundary generates a linear internal wave of the form

$$u(x, z, t) = -U_0 \, F(z) \, \sin(k_x x - \omega t), \tag{7.10}$$

where k_x is the horizontal wave number given by the internal wave dispersion relation (1.2). To avoid transients the open boundary forcing is ramped up over one tidal period. Three forcing frequencies are investigated: $\omega = 1.41 \times 10^{-4}$ rad s^{-1} ($T = 12.42$ hours, where T is wave period) for a semi-diurnal M_2 internal tide; $\omega = 2.81 \times 10^{-4}$ rad s^{-1} ($T = 6.21$ hours) for the first harmonic of M_2, a quarter-diurnal M_4 internal tide; and $\omega = 1.45 \times 10^{-3}$ rad s^{-1} ($T = 1.2$ hours) for high-frequency internal waves close to N, the upper limit of free internal waves. The ratio of the internal wave frequency to the buoyancy frequency, $\mu = \omega/N$, is 0.09 for the uniform stratification cases but varies with depth for the non-uniform stratification profiles.

7.2.3 Slope topography

Four shelf slope profiles are investigated, three linear and one sinusoidal (Fig. 7.5). To investigate the effect of slope steepness, linear shelf slope profiles with different gradients are used to represent different internal wave reflection regimes. The behaviour of an internal wave upon reflection with topography is determined by the ratio of the topographic slope ($s_{\text{topog}} = dh/dx$, where h is the position of the bottom) to the internal wave characteristic slope, $\alpha = s_{\text{topog}}/s_{\text{wave}}$. s_{wave} is calculated from the internal wave dispersion relation (1.2).

The three linear shelf slopes have gradients of 0.02, 0.04, and 0.08; for M_2 frequency internal waves and a uniform buoyancy frequency of 2.4×10^{-6} rad s^{-2}, these slopes have α-values of approximately 0.5 (subcritical), 1 (critical), and 2 (supercritical). For non-uniform stratification profiles α varies with depth, as well as the local topographic slope and internal wave frequency.

To investigate the interaction between the depth of the pycnocline and the local topographic slope an idealised sinusoidal shelf slope profile is used, fit to bathymetry data from the West Shetland slope, $h = -400 \cos(6 \times 10^{-5} x) - 600$. $s_{\text{topog}} = 0$ at the base of the slope, increasing to 0.024 in the middle of the slope, and decreasing back to zero at the shelf break.

A second non-dimensional parameter related to the slope topography is $\gamma = L_{\text{topog}}/\lambda_x$, where L_{topog} is the horizontal length-scale of the shelf slope (base of the slope to the shelf break) and λ_x is the horizontal wavelength of the internal

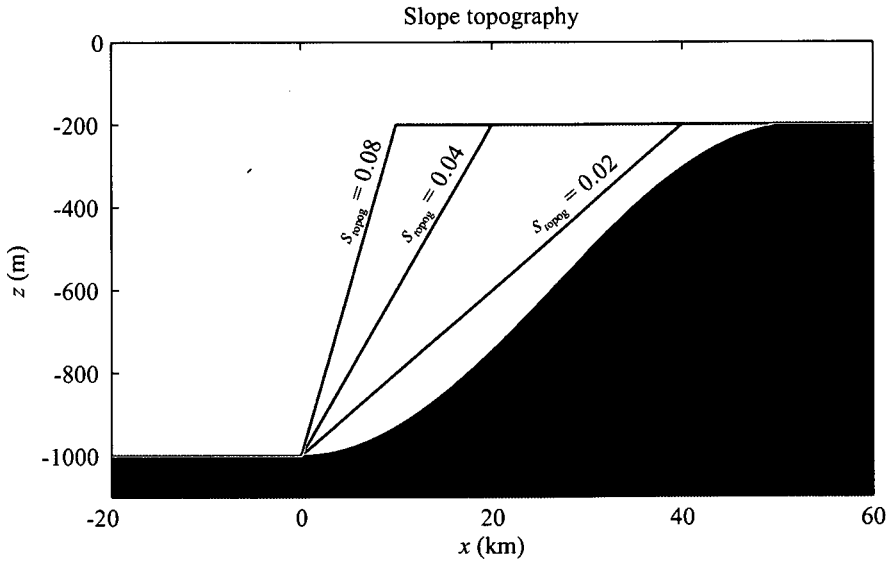

Figure 7.5: Four shelf slope profiles used in the numerical model. The grey lines are linear shelf slopes with different gradients: $s_{\text{topog}} = 0.04$ is near-critical to the internal wave characteristic slope for M_2 frequency forcing and uniform buoyancy frequency, $N^2 = 2.4 \times 10^{-6}$ rad s^{-2}; $s_{\text{topog}} = 0.02$ is subcritical; and $s_{\text{topog}} = 0.08$ is supercritical. The black shaded area is a sinusoidal shelf slope profile fitted to bathymetry data from the West Shetland slope.

wave. The three linear shelf slopes have length-scales of 40, 20, and 10 km; for a uniform buoyancy frequency of 2.4×10^{-6} rad s^{-2}, mode-1 M_2 frequency internal waves have 48 km horizontal wavelengths, implying γ-values of 0.8, 0.4, and 0.2 respectively. A final non-dimensional parameter is the ratio of the depth of the watercolumn on continental shelf to the depth of the watercolumn off-shelf $(-h/H)$, which is 0.8 for all configurations.

7.2.4 Model runs

Eleven model runs are made with different combinations of slope topography, background stratification, forcing frequency, and mode structure. The variables changed between runs are shown in Table 7.1, while the resulting internal wave characteristic slope and other non-dimensional parameters are shown in Table 7.2.

Three runs are made with uniform stratification, mode-1 M_2 frequency forcing, and linear shelf slopes with different gradients. These are referred to as *UniNsub* ($\alpha \simeq 0.5$), *UniNcrit* ($\alpha \simeq 1$), and *UniNsuper* ($\alpha \simeq 2$). Three runs are made with weak pycnocline stratification, mode-1 M_2 frequency forcing, and a

Run	Stratification			Forcing		Topography	
	Type	N^2	$z_{\max\ N^2}$	ω	Mode	Type	s_{topog}
UniNsub	Uni.	0.2	-	1.41	1	Lin.	0.02
UniNcrit	Uni.	0.2	-	1.41	1	Lin.	0.04
UniNsuper	Uni.	0.2	-	1.41	1	Lin.	0.08
LowN400	Var.	0.2-0.8	−400	1.41	1	Sin.	≤ 0.02
LowN600	Var.	0.2-0.8	−600	1.41	1	Sin.	≤ 0.02
LowN800	Var.	0.2-0.8	−800	1.41	1	Sin.	≤ 0.02
HighN	Var.	0.2-7.6	−600	1.41	1	Sin.	≤ 0.02
HighNm4	Var.	0.2-7.6	−600	2.81	1	Sin.	≤ 0.02
HighNhf	Var.	0.2-7.6	−600	14.54	1	Sin.	≤ 0.02
HighNmode2	Var.	0.2-7.6	−600	1.41	2	Sin.	≤ 0.02
HighNmode3	Var.	0.2-7.6	−600	1.41	3	Sin.	≤ 0.02

Table 7.1: A summary of the variables changed between model runs. Uni. is uniform; Var. is variable; Lin. is linear; and Sin. is sinusoidal. Buoyancy frequencies (N^2) are in 10^{-5} rad s^{-2}; z in m; and internal wave frequencies in 10^{-4} rad s^{-1}.

Run	s_{wave}	α	γ	μ
UniNsub	0.04	$\simeq 0.5$	0.8	0.09
UniNcrit	0.04	$\simeq 1$	0.4	0.09
UniNsuper	0.04	$\simeq 2$	0.2	0.09
LowN400	0.02-0.04	≤ 0.9	0.8	0.05-0.09
LowN600	0.02-0.04	≤ 1.1	0.8	0.05-0.09
LowN800	0.02-0.04	≤ 0.9	0.9	0.05-0.09
HighN	0.01-0.04	≤ 3.3	0.3	0.02-0.09
HighNm4	0.03-0.17	≤ 0.8	1.2	0.03-0.18
HighNhf	0.17-2.72	≤ 0.1	7.4	0.17-0.94
HighNmode2	0.01-0.04	≤ 3.3	1.0	0.02-0.09
HighNmode3	0.01-0.04	≤ 3.3	1.6	0.02-0.09

Table 7.2: A summary of internal wave characteristic slope (s_{wave}) and other non-dimensional parameters for all model runs. α is the ratio of the topographic slope to the internal wave characteristic slope; γ is the ratio of the horizontal length-scale of the slope to the horizontal wavelength of the internal wave; and μ is the ratio of internal wave frequency to buoyancy frequency.

sinusoidal shelf slope, but with the pycnocline at different depths. The vertical displacement shifts the pycnocline from subcritical to supercritical regimes by changing the local topographic slope at the point of intersection. For the run with the pycnocline at 600 m (*LowN600*) the maximum α-value is 1.1, but, for the runs with the pycnocline at 400 m and 800 m (*LowN400* and *LowN800*), the maximum α-value is 0.9 (Fig. 7.6). Three runs are made with strong pycnocline stratification and a sinusoidal shelf slope, but different mode-1 forcing frequencies. These simulate a semi-diurnal M_2 internal tide (*HighN*); a quarter-diurnal M_4 internal tide (*HighNm4*); and high-frequency internal waves close to N (*HighNhf*). For *HighN*, $\alpha > 1$ in the pycnocline but < 1 above 400 m and below 800 m; for *HighNm4* the maximum α-value is 0.8; and for *HighNhf* $\alpha \ll 1$ at all depths (Fig. 7.7). Finally, two runs are made with the same configuration as *HighN* but with mode-2 (*HighNmode2*) and mode-3 (*HighNmode3*) forcing.

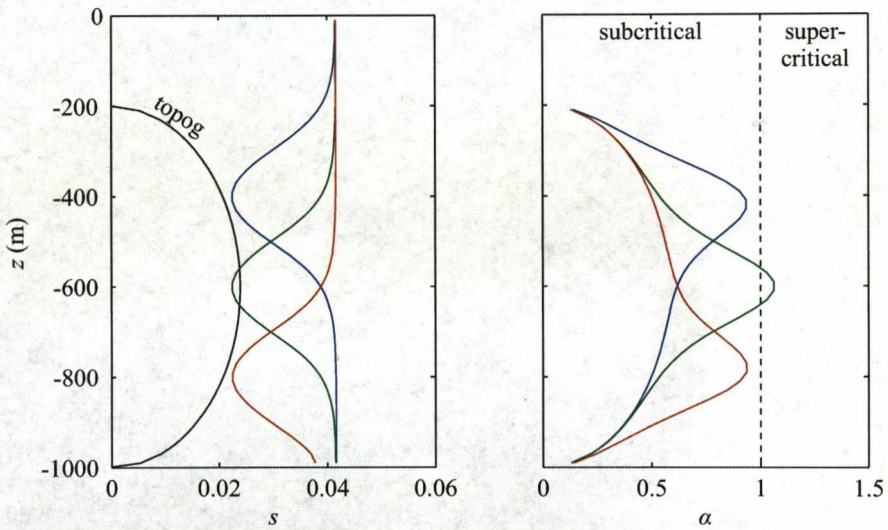

Figure 7.6: Topographic and internal wave characteristic slopes, and α-values for the weak pycnocline stratification runs. The blue line is for *LowN400*; the green line is for *LowN600*, and the red line is for *LowN800*. The dashed line in the right hand plot is the critical α-value.

The continental shelf is made sufficiently long so that westward propagating internal waves, from reflection with the eastern boundary, do not interfere with the region of interest, the area over the shelf slope. After reflection with the slope,

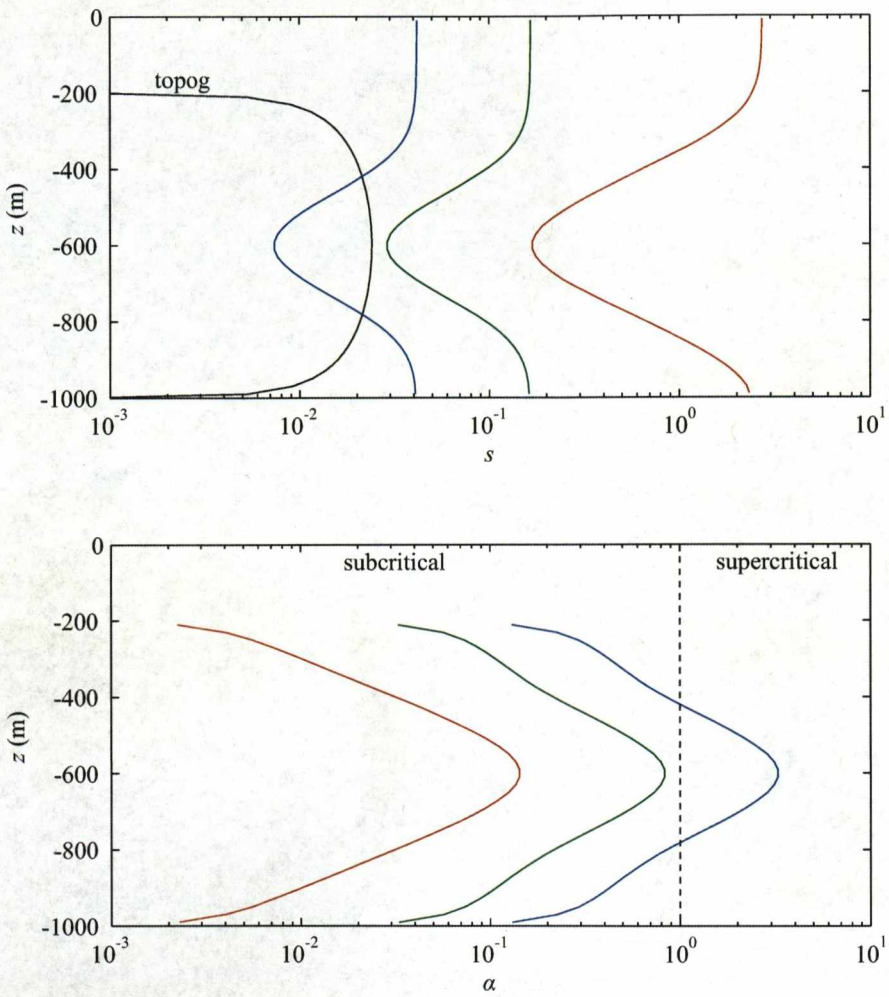

Figure 7.7: Topographic and internal wave characteristic slopes, and α-values for the strong pycnocline stratification runs. The blue line is for *HighN*; the green line is for *HighNm4*; and the red line is for *HighNhf*. The dashed line in the lower plot is the critical α-value.

westward propagating internal waves may re-reflect with the western boundary so the distance between the slope and the western boundary must be substantial. To maintain consistency between the runs, the base of the slope, $x = 0$, is located $4\lambda_x$ from the western boundary. The total length of the domain and the location of the slope are therefore dependent on the horizontal wavelength and are shown in Table C.1.

The horizontal resolution is varied depending on the frequency of the boundary forcing (500 m for M_2 frequency forcing); the vertical resolution is 20 m for all runs. The model is run for 36 wave periods with a time-step of 100 s. As the initial conditions are static, the amplitude and wavelength of the internal waves increases gradually over the first few wave cycles. Full amplitude internal waves typically reach the base of the shelf slope after approximately 24 cycles and boundary reflected internal waves begin to cause interference over the slope after approximately 30 cycles. The resolution for each run is shown in Table C.1.

7.3 Diagnostics

7.3.1 Velocity and density snapshots

To avoid interference from boundary reflected internal waves, only the sections of model run between $t = 24T$ and $t = 30T$ are analysed here. Snapshots of the across-slope velocity, vertical velocity and non-dimensional density ($\rho = \beta S - \alpha\theta$) over the slope are shown are shown for $t = 24.5T$.

7.3.2 Internal wave energy flux

The internal wave energy flux is calculated $\mathbf{F} = \langle \mathbf{u}'p' \rangle$, in the same way as the internal tide energy flux on the West Shetland slope (Chapter 5). The baroclinic across-slope velocity perturbations are calculated

$$u' = u - \frac{1}{T}\int_t^{t+T} u \, dt - \frac{1}{H}\int_{-H}^{0} u \, dz. \tag{7.11}$$

The second term on the right hand side (rhs) is the time-average velocity over one wave period, the third term on the rhs is the barotropic velocity. For this model configuration (with no barotropic or background flow) the second and third terms are zero within the bounds of numerical error so $u' \simeq u$. Similarly, vertical velocity perturbations are calculated

$$w' = w - \frac{1}{T}\int_t^{t+T} w \, dt. \tag{7.12}$$

As with across-slope velocity, the time-average is close to zero so $w' \simeq w$.

Density is not explicitly output by the model, but density anomalies (ρ') can be calculated from potential temperature and salinity anomalies,

$$\rho' = \beta \rho_0 S' - \alpha \rho_0 \theta'. \tag{7.13}$$

The potential temperature and salinity anomalies are calculated

$$S' = S - \frac{1}{T} \int_t^{t+T} S \, dt, \tag{7.14}$$

$$\theta' = \theta - \frac{1}{T} \int_t^{t+T} \theta \, dt, \tag{7.15}$$

then the baroclinic pressure perturbations calculated

$$p' = \int_0^{\eta} \rho_0 g \, dz + \int_z^0 \rho' g \, dz, \tag{7.16}$$

where η is free surface height. The first term on the rhs is the surface pressure perturbation, the second term on the rhs is the internal pressure perturbation. Finally, the internal wave energy flux (across-slope and vertical) is calculated

$$\mathbf{F} = \frac{1}{T} \int_t^{t+T} \mathbf{u}' p' \, dt. \tag{7.17}$$

Energy flux profiles are calculated at each horizontal grid point at $t = 24T$ and the convergence of internal wave energy diagnosed

$$F_{\text{con}} = -\frac{\partial F_x}{\partial x} - \frac{\partial F_z}{\partial z}, \tag{7.18}$$

where positive values denote a convergence of energy and negative values denote a divergence.

To separate the incident and reflected internal waves in runs with regions of supercritical slope a series of control runs were made with no topography other than the vertical wall at the eastward boundary. Internal wave energy flux profiles are calculated for these runs at $t = 24T$, $x = -5$ km, near the base of the shelf slope. These are compared to the energy flux profile at the same location from the runs with topography. The energy flux profile from the control run is unaffected by topography so is considered the incident wave. The energy flux profile from the run with topography contains both the incident and reflected wave so the residual after subtracting the energy flux profile from the control run is considered the reflected wave.

7.3.3 Kinetic and available potential energy

For the model runs with internal waves closest to those observed on the West Shetland slope, *HighN* and *HighNhf*, kinetic and available potential energy are calculated and integrated over the area above slope. The available potential energy density and kinetic energy density of the internal waves are defined

$$APE = \frac{1}{2}\rho_0 \frac{b^2}{N^2}, \tag{7.19}$$

$$KE = \frac{1}{2}\rho_0 \left(u^2 + v^2 + w^2\right), \tag{7.20}$$

where $b = -g\rho'/\rho_0$ is buoyancy. These definitions are consistent with Equations (5.2) and (5.3). The integrated kinetic and available potential energy are then

$$APE(t) = \int_{x_1}^{x_2} \int_{-H}^{0} APE(x,z,t)\, dz\, dx, \tag{7.21}$$

$$KE(t) = \int_{x_1}^{x_2} \int_{-H}^{0} KE(x,z,t)\, dz\, dx, \tag{7.22}$$

where $x_1 = -5$ km, near the base of the slope, and $x_2 = 55$ km, on the continental shelf near the shelf break. The values of KE and APE vary considerably as internal waves enter the area so are time-averaged over each wave cycle between $24T$ and $30T$.

Following Legg and Adcroft (2003), the flux of energy into the area above the slope is a summation of the advection of kinetic and available potential energy, diffusion of kinetic energy, kinetic energy transport at the free surface, pressure transport of kinetic energy (the internal wave energy flux, as calculated is Section 7.3.2), and dissipation of kinetic energy by viscosity. The pressure transport term is by far the largest and is diagnosed every wave cycle between $24T$ and $30T$ as the vertical integral of across-slope energy flux, $\int_{-H}^{0} F_x\, dz$, at x_1 minus the integrated energy flux at x_2.

The last term, kinetic energy dissipation by viscosity, is equivalent to the rate of TKE dissipation (ϵ), measured on the West Shetland slope in Chapter 4. For comparison, the rate of kinetic energy dissipation in the model is diagnosed

$$\epsilon = \nu_h \left[\left(\frac{\partial u}{\partial x}\right)^2 + \left(\frac{\partial v}{\partial x}\right)^2 + \left(\frac{\partial w}{\partial x}\right)^2 \right] + \nu_z \left[\left(\frac{\partial u}{\partial z}\right)^2 + \left(\frac{\partial v}{\partial z}\right)^2 + \left(\frac{\partial w}{\partial z}\right)^2 \right]. \tag{7.23}$$

To be consistent with KE and APE, ϵ is multiplied by ρ_0, integrated through the watercolumn and from x_1 to x_2, then time-averaged over each wave cycle.

For comparison with the equivalent mixing parameter on the West Shetland slope, diapycnal diffusivity is then calculated from the rate of kinetic energy

dissipation using the relation $\kappa_\rho = \Gamma\epsilon/N^2$ (Osborn, 1980), where $\Gamma = 0.2$ is the mixing efficiency. This diagnostic is not the active diffusivity in the model. The spatial distribution of KE, APE, ϵ and κ_ρ over the slope are also plotted, time-averaged over six wave periods ($24T$ to $30T$).

7.4 Results

7.4.1 Topographic effects with uniform stratification

Critical slope theory predicts that the amount of internal wave reflection will increase with increasing α, i.e. more internal wave reflection will occur on a supercritical slope than a subcritical slope. This hypothesis is tested using the three runs with uniform stratification and linear shelf slopes with different gradients.

On the subcritical slope (*UniNsub*), horizontal wavelength decreases as the water depth decreases so that on the continental shelf the wavelength is only 6 km, compared to 48 km off the shelf (Fig. 7.8 upper panels). Vertical velocity and isopycnal displacement increase as the water depth decreases, being largest at the shelf break. The vertically integrated across-slope internal wave energy flux is 321.6 W m^{-1} at the base of the slope with a typical mode-1 vertical structure; maximum at the surface and the bottom and decreasing to near-zero at 500 m (Fig. 7.9 upper panel). The energy flux at the shelf break is only 3.8 W m^{-1} and dissipates rapidly. Vertical energy fluxes off the shelf are small but on the slope larger upward energy fluxes are induced near the bottom, associated with a convergence of internal wave energy. As expected, there is little internal wave reflection; the across-slope energy flux profile at the base of the slope is almost identical for the run with topography and the run without topography (Fig. 7.10 upper panels). The energy flux of the incident wave is 322.8 W m^{-1}, the same for all uniform stratification runs, leaving a residual energy flux of 1.3 W m^{-1} to be made up by the reflected wave. There is a small downwards energy flux at the base of the slope, going to zero at the surface and bottom. The presence of topography increases the downward energy flux by approximately a factor of two, but is still of the order 200 times smaller than the across-slope energy flux. For all uniform stratification runs, the vertical energy flux profile is dependent on the distance from the slope.

On the critical slope (*UniNcrit*), the decrease in horizontal wavelength and the increase vertical velocity and isopycnal displacement are of the same order as on the subcritical slope, but occur over a shorter distance (Fig. 7.8 middle panels). Large upward internal wave energy fluxes are again induced on the slope

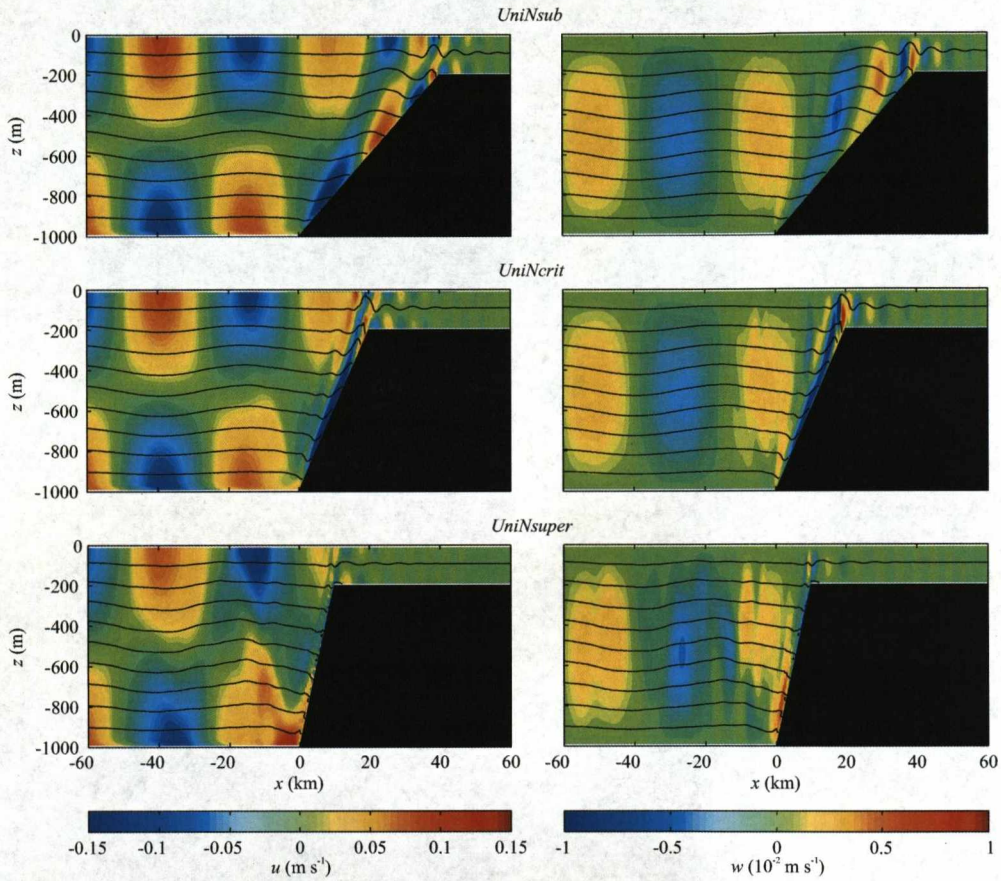

Figure 7.8: Across-slope (left) and vertical (right) velocity for *UniNsub*, *UniNcrit*, and *UniNsuper*. The black lines are contours of non-dimensional density (every 2.5×10^{-5}).

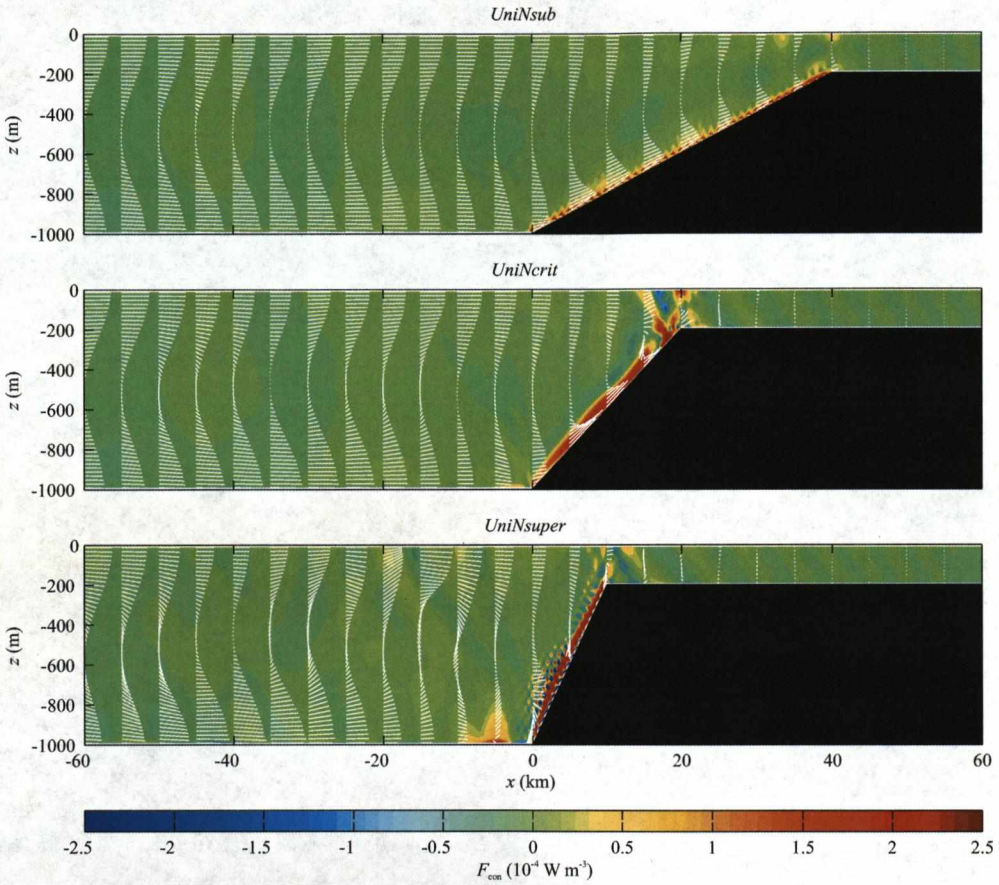

Figure 7.9: Convergence of internal wave energy for *UniNsub*, *UniNcrit*, and *UniNsuper*. The white lines are across-slope and vertical energy flux vectors at each level every 5 km.

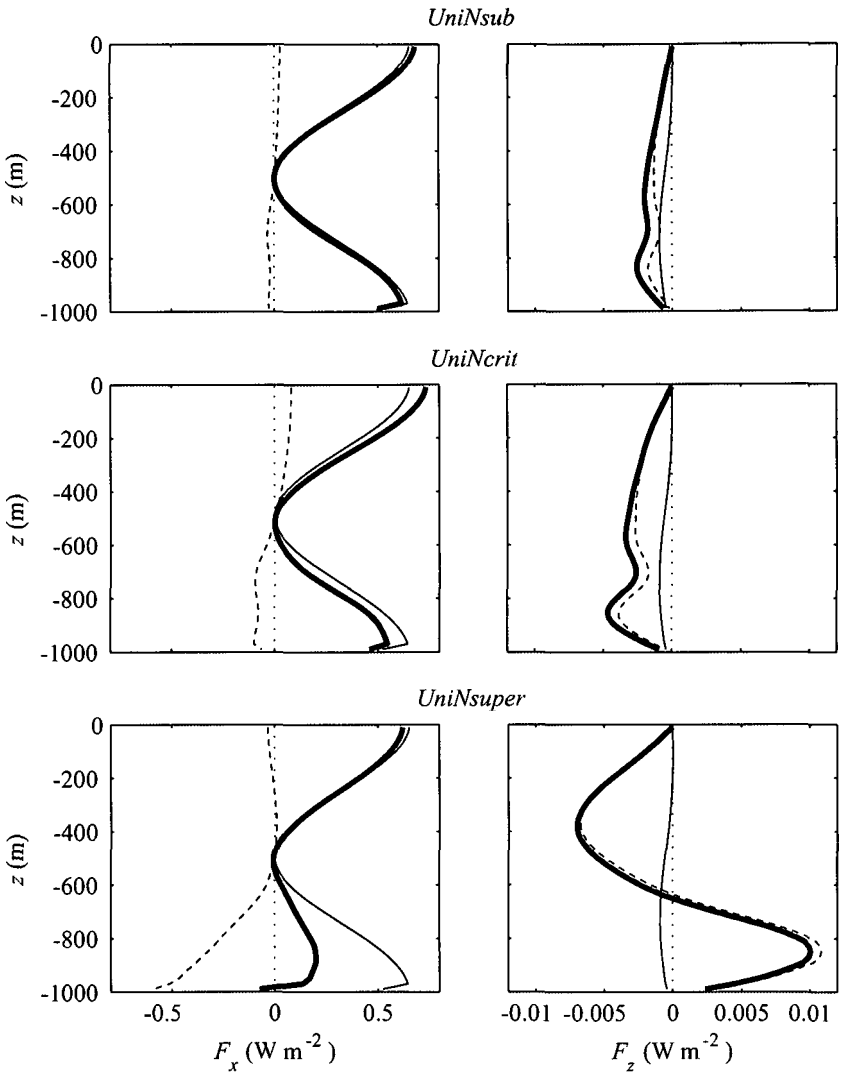

Figure 7.10: Across-slope (left) and vertical (right) internal wave energy fluxes at $x = -5$ km for *UniNsub*, *UniNcrit*, and *UniNsuper*. The thin black lines are for the incident wave; the dashed black lines are for the reflected wave; and the thick black lines are the net energy fluxes.

near the bottom and across-slope energy fluxes amplified, associated with a larger convergence of internal wave energy than on the subcritical slope (Fig. 7.9 middle panel). There are separate areas of energy convergence at the surface, near the shelf break. Some internal wave reflection is evident as modification of the density and velocity fields off the shelf from the mode-1 structure of the incident wave; this is particularly evident in vertical velocity. At the base of the slope the net across-slope energy flux (incident plus reflected) is 316.2 W m^{-1}, so the reflected component is only 6.6 W m^{-1}. The energy flux of the incident wave is smaller than the net energy flux in the upper half of the watercolumn and larger in the lower half (Fig. 7.10 middle panels). This mis-match implies the energy flux of the reflected wave is away from the slope in the lower half of the watercolumn but *towards* the slope in the upper half. The same pattern is apparent to a lesser extent for the subcritical run and may be due to some other effect linked to the presence of topography. There is a downwards energy flux at the base of slope through the whole watercolumn, larger than for the subcritical slope, and almost entirely due to the reflected wave. At the shelf break the across-slope energy flux is 4.6 W m^{-1}, similar to the subcritical run.

On the supercritical slope (*UniNsuper*), internal wave breaking occurs, identified by vertical isopycnal surfaces as buoyancy is redistributed and the unstable part of the watercolumn is mixed (Fig. 7.8 lower panels). However, there is less amplification of vertical velocity and isopycnal displacement at the shelf break when compared to the subcritical and critical runs. On the slope, downward internal wave energy fluxes are induced the near the bottom, associated with a large convergence of internal wave energy (Fig. 7.9 lower panel). There is a separate area of energy convergence at the bottom, near the base of the slope, that is consistent with the supercritical reflection of downward propagating internal wave characteristics. The net across-slope energy flux at the base of the slope is 207.7 W m^{-1}, so a large fraction of the incident wave energy flux is reflected (115.1 W m^{-1}), as predicted by critical slope theory. At the shelf break the energy flux is 1.7 W m^{-1}, even smaller than for the subcritical and critical runs. Off-shelf there is much modification of the velocity and density fields from mode-1 structure by reflected waves; again most evident in vertical velocity. Energy flux profiles off the shelf are also highly modified by the reflected waves with larger vertical energy fluxes than for the subcritical and critical runs. At the base of the slope the across-slope energy flux of the reflected wave is contained in the lower half of the watercolumn; and approximately equal to the incident wave energy flux in the lower layer (Fig. 7.10 lower panels); in the upper layer the energy

flux of the reflected wave is close to zero. However, the vertical structure of the reflected energy flux depends on the distance from the slope. The vertical energy flux at the base of the slope is downwards in the upper half of the watercolumn and upwards in the lower half, almost entirely due to the reflected wave.

Dividing the convergence of internal wave energy by ρ_0 implies dissipation rates of the order 5×10^{-8} W kg^{-1} on the subcritical slope and 2×10^{-7} W kg^{-1} on the critical and supercritical slopes.

7.4.2 Non-uniform stratification and pycnocline depth

For the simplified case, with uniform stratification and a linear shelf slope, the reflective behaviour of the internal waves agrees with critical slope theory. The background stratification profile is now changed to include a weak pycnocline at three different depths and the topography changed to a sinusoidal shelf slope.

For all three runs (*LowN400*, *LowN600*, and *LowN800*), the slope topography is near-critical in the pycnocline and the reflective behaviour of the internal waves is similar. The effect of the slope on the internal wave field is similar to *UniNsub*; horizontal wavelength decreases from 65 km to 6 km as the water depth decreases (Fig. 7.11). Vertical isopycnal displacements off the shelf are smaller than for the uniform stratification runs due to the increased buoyancy frequency. On the slope, the largest vertical velocities occur above the pycnocline, but for all three weak stratification runs, isopycnal displacement at the shelf break is of the same order as for *UniNsub* and *UniNcrit*.

Internal wave energy flux profiles off-shelf vary with the depth of the pycnocline because the vertical structure of internal wave modes is dependent on the buoyancy frequency profile. As with the uniform stratification runs the across-slope energy flux is large at the surface and the bottom, decreasing to near-zero at mid-depths (Fig. 7.12). The depth of the minimum is not exactly coincident with the pycnocline, but does deepen as the depth of the pycnocline increases; for *LowN600*, where the pycnocline is at 600 m, the minimum is slightly shallower at approximately 575 m. For this run the net energy flux at the base of the slope is 371.0 W m^{-1} and almost symmetrical above and below the pycnocline. For the shallow pycnocline run (*LowN400*) the energy flux is almost identical, 371.3 W m^{-1}, but larger in the upper layer than the lower. For the deep pycnocline run (*LowN800*) the energy flux is 348.8 W m^{-1} but larger in the lower layer. The energy flux at the shelf break is small for all three weak stratification runs; 2.9, 2.2, and 2.1 W m^{-1} respectively for *LowN400*, *LowN600*, and *LowN800*.

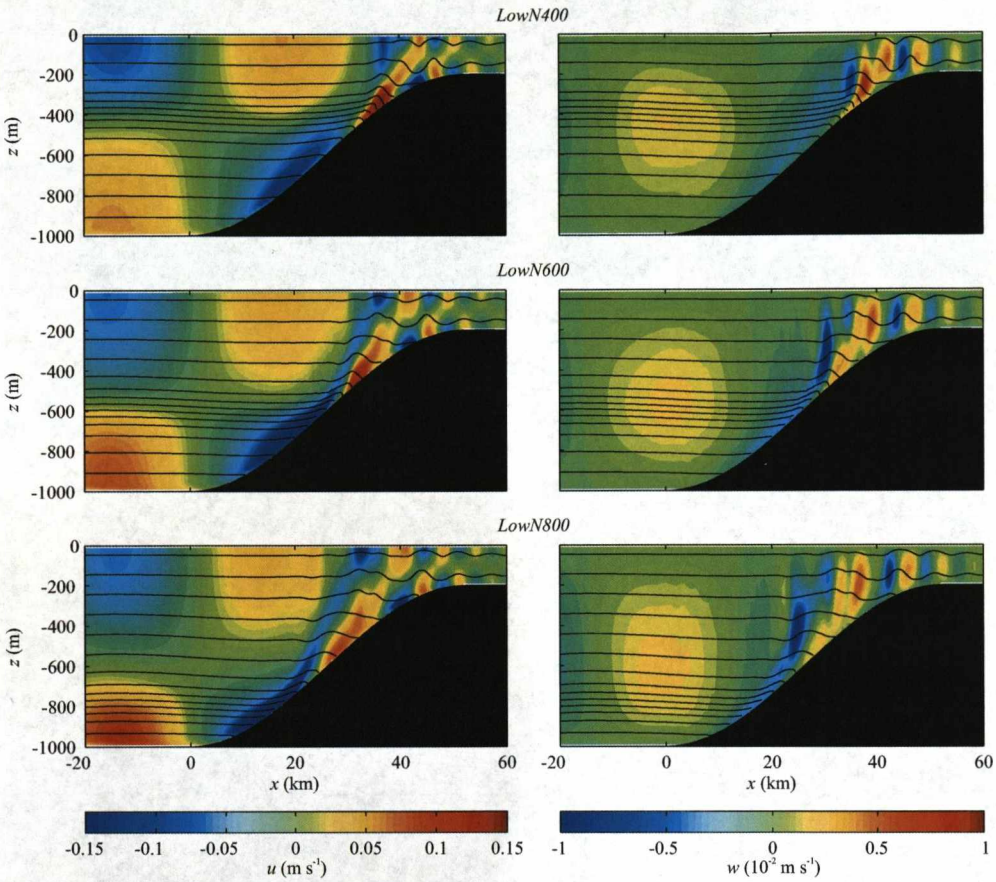

Figure 7.11: Across-slope (left) and vertical (right) velocity for *LowN400*, *LowN600*, and *LowN800*. The black lines are contours of non-dimensional density (every 2.5×10^{-5}).

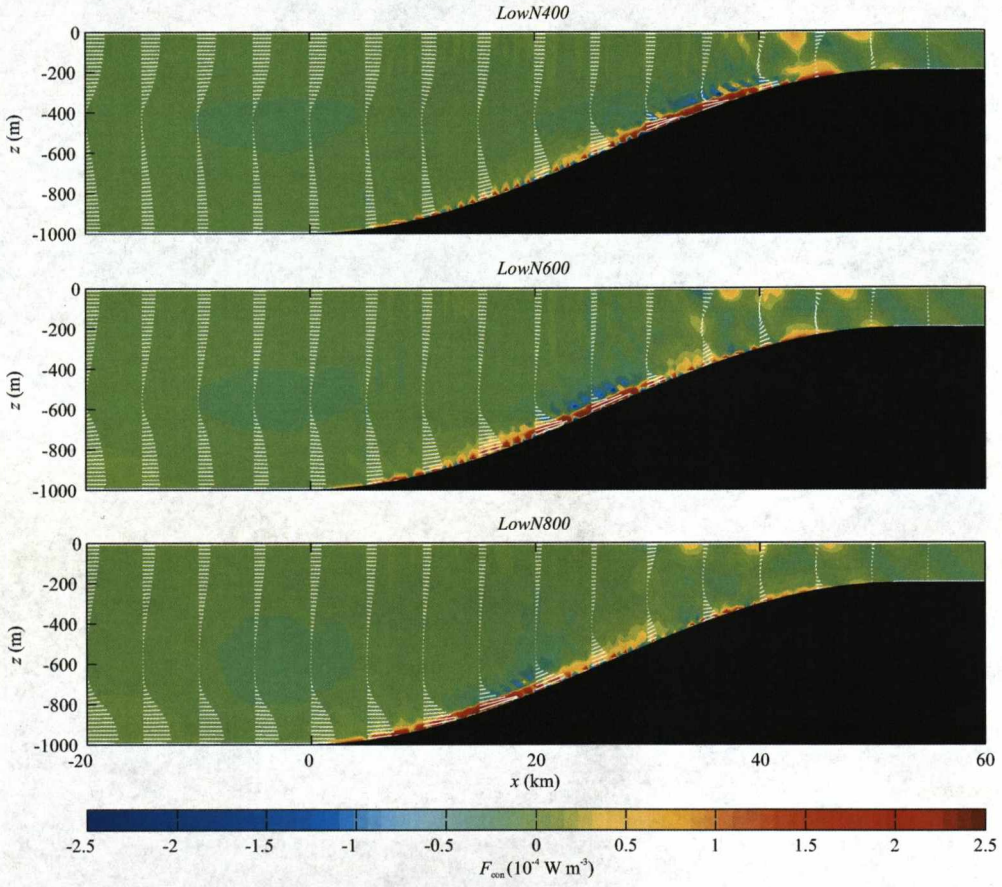

Figure 7.12: Convergence of internal wave energy for *LowN400*, *LowN600*, and *LowN800*. The white lines are across-slope and vertical energy flux vectors at each level every 5 km.

On the slope, upward energy fluxes are induced near the bottom and across-slope energy fluxes amplified. These energy fluxes are largest where the pycnocline intersects the slope as the energy flux minimum shoals to maintain mode-1 vertical structure in shallower water. Thus, the existence of large internal wave energy fluxes in the pycnocline close to intersection with the slope does not require the off-slope energy flux in the pycnocline to be large. Instead they can result from shoaling and amplification of the near-bed energy flux; in this weak stratification case the energy flux in the pycnocline is small until approximately halfway up the slope. There is a convergence of internal wave energy on the slope, maximum at the depth of the pycnocline, that implies dissipation rates of the order 10^{-7} W kg^{-1}.

There is little internal wave reflection in any of the weak stratification runs; off the shelf the velocity and density fields remain unmodified and vertical energy fluxes are small. Even for *LowN600*, where slope is slightly supercritical in the pycnocline, the energy flux profile at the base of the slope is almost identical for the runs with and without topography (not shown). The energy flux of the incident wave is 372.8 W m^{-1}, so only 1.8 W m^{-1} is reflected. As for *UniNsub* and *UniNcrit*, there is a downward energy flux at the base of the slope that is increased by the presence of topography.

7.4.3 Internal wave frequency

The strength of the pycnocline stratification is now increased so that the slope topography is supercritical to the M_2 internal tide between 400 m and 600 m, but subcritical at all depths to the M_4 internal tide and the high-frequency internal waves. The three runs with different forcing frequencies display very different internal wave behaviour. With M_2 forcing the majority of the internal wave energy is reflected back into deep water; with M_4 forcing internal wave breaking occurs on the shelf slope in the pycnocline; and with high-frequency forcing the internal waves become non-linear and dissipate on the slope without breaking.

The M_2 frequency run (*HighN*) is the best approximation of the internal tide on the West Shetland slope, having stratification and topography closest to the observations from the Faroe-Shetland Channel. Horizontal wavelength decreases from 170 km off-shelf to 6 km on the shelf; the former is long because the M_2 angular frequency is close to the inertial frequency and the buoyancy frequency in the pycnocline is large. Vertical isopycnal displacements off the shelf are smaller than for the uniform and weak pycnocline stratification runs due to the increased buoyancy frequency (Fig. 7.13 upper panels). Vertical velocity and isopycnal

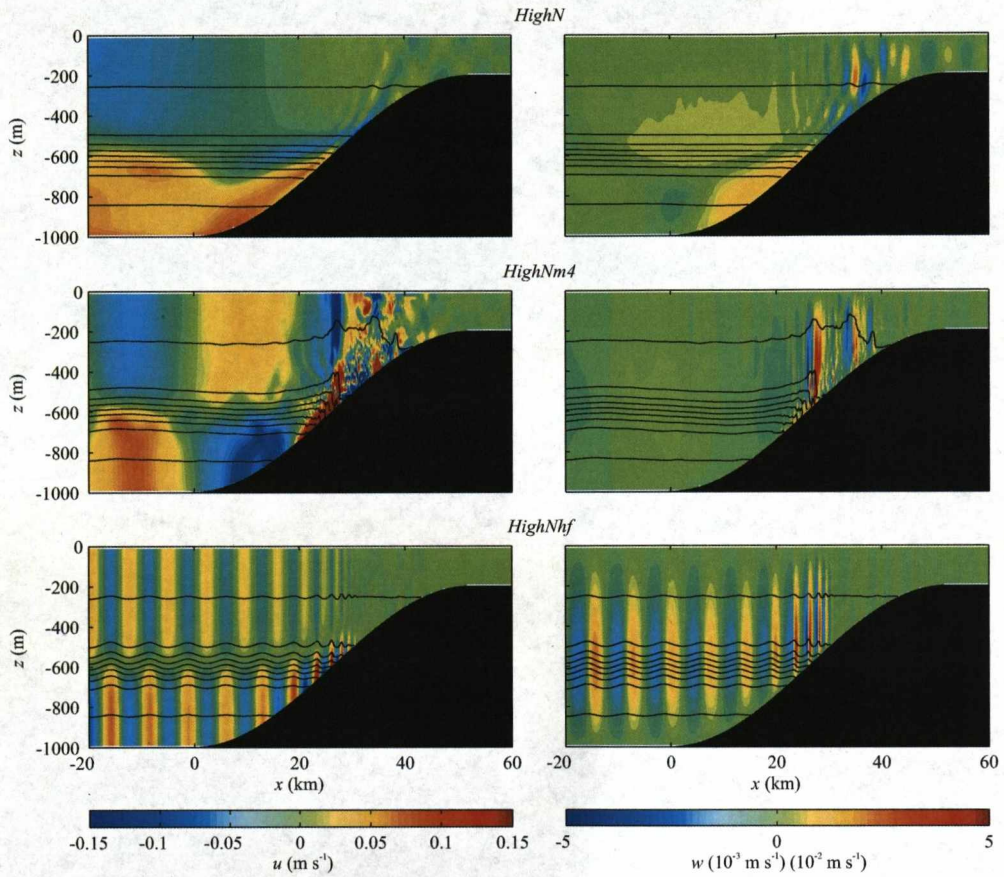

Figure 7.13: Across-slope (left) and vertical (right) velocity for *HighN*, *HighNm4*, and *HighNhf*. The vertical velocity colour scale is 10^{-3} m s^{-1} for *HighN* but 10^{-2} m s^{-1} for *HighNm4* and *HighNhf*. The black lines are contours of non-dimensional density (every 2×10^{-4}).

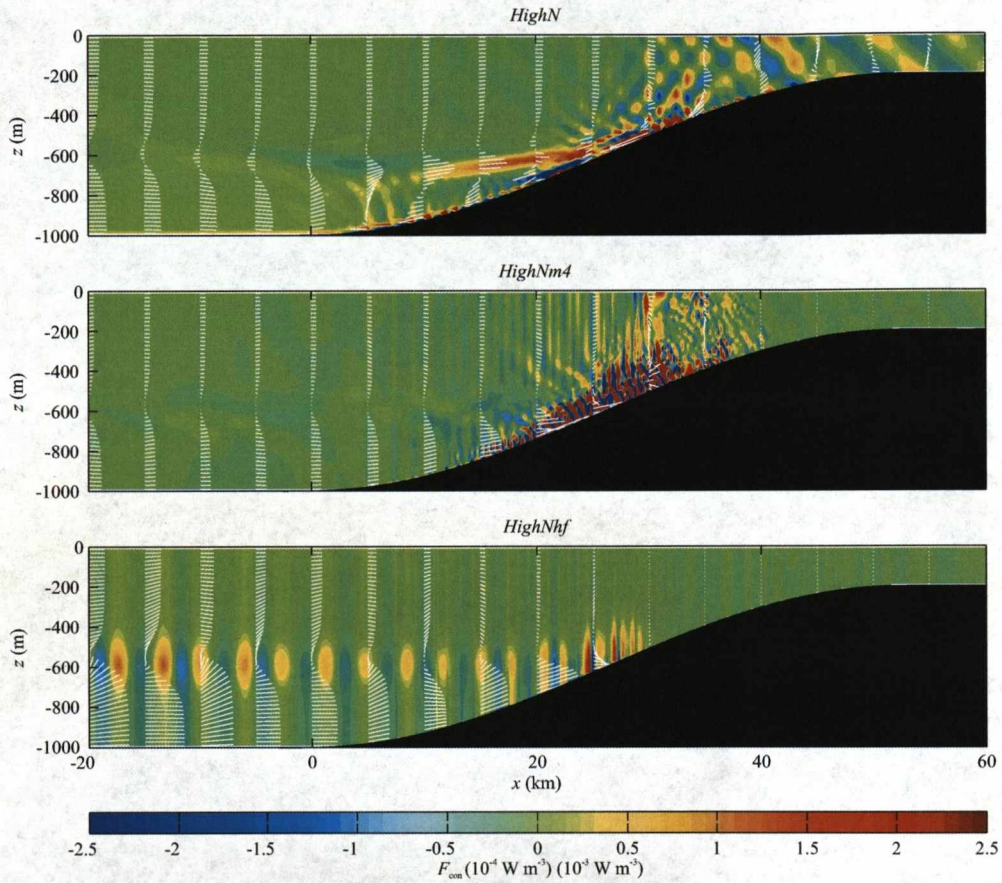

Figure 7.14: Convergence of internal wave energy for *HighN*, *HighNm4*, and *HighNhf*. The energy convergence colour scale is 10^{-4} W m^{-3} for *HighN* but 10^{-3} W m^{-3} for *HighNm4* and *HighNhf*. The white lines are across-slope and vertical energy flux vectors at each level every 5 km.

displacements are largest near the top of the slope and of a similar magnitude to the vertical motions at the shelf break for *UniNsuper*.

Off-shelf, the net internal wave energy flux is towards the slope above and below the pycnocline, but away from the slope in the pycnocline (Fig. 7.14 upper panel), suggesting significant internal wave reflection occurs. On the slope downward energy fluxes are induced near the bottom and the across-slope energy flux is directed down-slope. Both are largest near the intersection with the pycnocline and are associated with a convergence of internal wave energy. Over the lower slope the across-slope energy flux in the pycnocline is directed up-slope, associated with a separate band of energy convergence at around 600 m and implying dissipation rates of the order 10^{-7} W kg^{-1}. At the shelf break the energy flux is only 0.2 W m^{-1}, with adjacent bands of energy convergence and divergence. These divergences of internal wave energy may occur because the internal wave field has not reached a steady state or because the wave period is not an integer multiple of the time-step data is output (every hour for M_2 frequency runs), making aliasing a possibility.

Critical slope theory predicts reflection of internal waves will occur between 400 m and 600 m, potentially explaining the net energy flux away from the slope in the pycnocline off-shelf. Like *UniNsuper*, there is much modification of the velocity and density fields from mode-1 structure by reflected waves, although not evident in Figure 7.13 due to the large horizontal wavelength. The across-slope energy flux of the incident internal wave at the base of the slope is large, 942.2 W m^{-1}, with mode-1 vertical structure (Fig. 7.15 upper panel). The net across-slope energy flux at the base of the slope is only 299.0 W m^{-1}, so the energy flux of the reflected wave is 643.2 W m^{-1}. The reflected energy flux has a similar vertical structure to the incident wave but reversed, near-zero in the pycnocline and away from the slope above and below. Unlike *UniNsuper*, the vertical structure of the reflected energy does not vary significantly with distance from the slope. The net energy flux away from the slope in the pycnocline is due to small differences in the vertical structure of the incident and reflected energy flux profiles. The vertical energy flux is upwards in the pycnocline and downwards above and below, primarily due to the reflected wave. For all non-uniform stratification runs, the vertical energy flux profile is dependent on the distance from the slope.

For the M_4 frequency run (*HighNm4*) horizontal wavelength is 43 km off-shelf but there is no internal wave variability on the shelf (Fig. 7.13 middle panels). Vertical velocities and isopycnal displacements off the shelf are larger than for

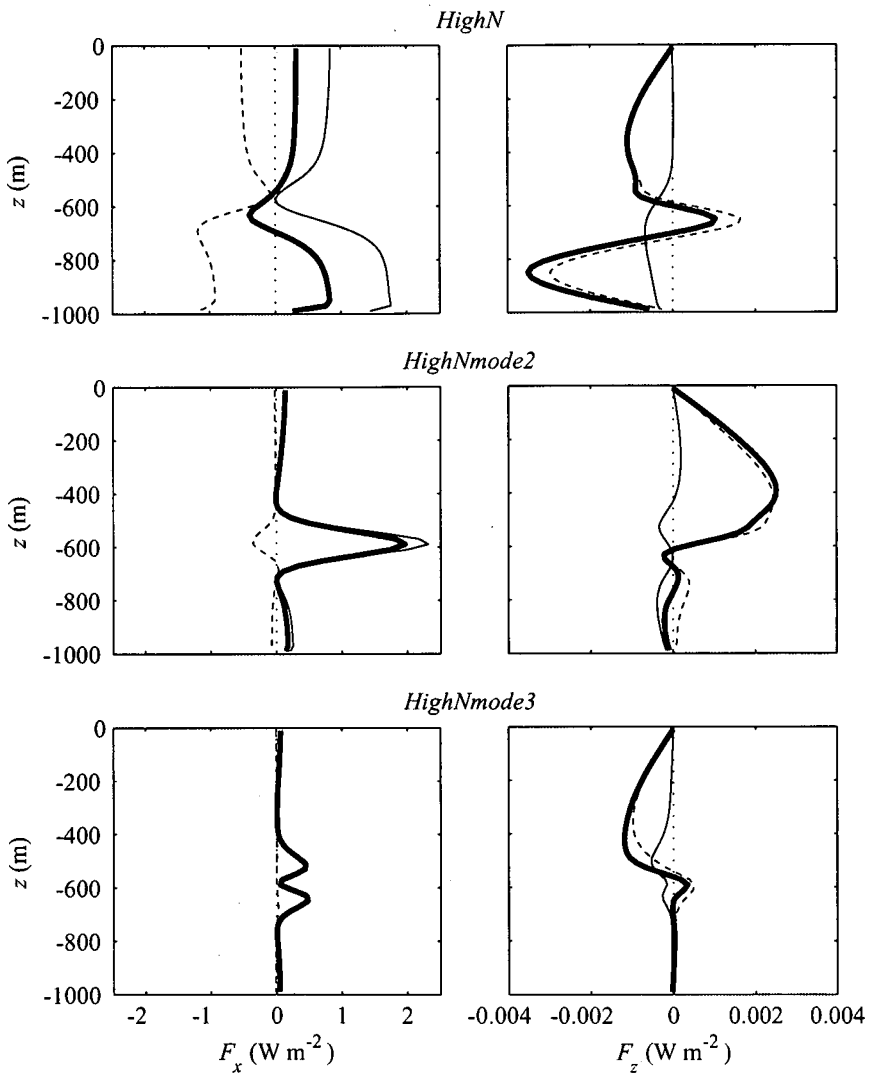

Figure 7.15: Across-slope (left) and vertical (right) internal wave energy fluxes at $x = -5$ km for *HighN*, *HighNmode2*, and *HighNmode3*. The thin black lines are for the incident wave; the dashed black lines are for the reflected wave; and the thick black lines are the net energy fluxes.

HighN due to the higher forcing frequency. On the slope, vertical velocity and isopycnal displacement are rapidly amplified and internal wave breaking occurs in the pycnocline. High vertical velocities above the pycnocline displace the shallower isopycnal surfaces and the waves continues up slope as non-linear waves of elevation. These dissipate before the shelf break is reached. The across-slope internal wave energy flux at the base of the slope is 2.5 kW m^{-1} but no energy reaches the shelf break (Fig. 7.14 middle panel). The energy flux at the base of the slope is larger than for *HighN* because the vertical velocities, isopycnal displacements, and hence energy densities are larger but the horizontal group velocities are almost the same ($\sim$ 2.8 m s^{-1} in the pycnocline). On the slope upward and across-slope energy fluxes are amplified near the bottom, similar to the weak stratification runs. Where internal wave breaking occurs the energy flux calculation breaks down because buoyancy is redistributed and the unstable part of the watercolumn is mixed. It is clear, however, that there is a convergence of internal wave energy on the slope because no energy reaches the shelf break. It is tempting to explain the internal wave breaking as a result of increased wave amplitudes from near-critical reflection with the shelf slope in the pycnocline (Eriksen, 1982, 1985), but no wave breaking occurs in the weak stratification runs which also have near-critical α-values in the pycnocline. The only other run to feature internal wave breaking is *UniNsuper*, but the instabilities are small compared to those in *HighNm4*. Unlike all previous runs, the γ-value for *HighNm4* is larger than one, which may be a factor. However, the following high-frequency run has a γ-value far in excess of one, and no wave breaking occurs.

For the high-frequency run (*HighNhf*), the best approximation of the non-linear internal waves on the West Shetland slope, the horizontal wavelength is 7 km off-shelf and again there is no internal wave variability on the shelf (Fig. 7.13 lower panels). Vertical velocities are over an order of magnitude larger than for *HighN* and increase mid-way up the slope. Across-slope velocities below the pycnocline also increase mid-way up the slope, but both stop abruptly at the 500 m isobath. Vertical isopycnal displacement does not increase greatly over the slope but the waves become non-linear. An asymmetry develops between the peaks and troughs with the form of a second-order Stokes wave. At the base of the slope the across-slope internal wave energy flux is 1.4 kW m^{-1}, larger below the pycnocline than above, but no energy reaches the shelf break (Fig. 7.14 lower panel). The energy flux below the pycnocline is amplified on the lower slope, then decreases to near-zero at the 500 m isobath. There are regions of internal wave

energy convergence and divergence in the pycnocline off-slope but the largest convergences are on the slope, implying dissipation rates up to 2×10^{-6} W kg^{-1}

7.4.4 Internal wave mode

M_2 frequency internal tides with mode-2 and mode-3 vertical structures are now forced at the open boundary to investigate if higher modes allow more internal wave energy to propagate onto the shelf than mode-1.

For both higher mode runs (*HighNmode2* and *HighNmode3*) along-slope velocity is largest in the pycnocline and vertical velocity is largest above and below, the opposite to mode-1 internal waves (Fig. 7.16). Vertical velocity is largest near the top of the slope for *HighNmode2*, similar to *HighN*, but no maximum is evident for *HighNmode3*. It takes longer for full amplitude mode-3 internal waves to reach the slope, so the snapshot at $24.5T$ does not properly capture the internal waves variability.

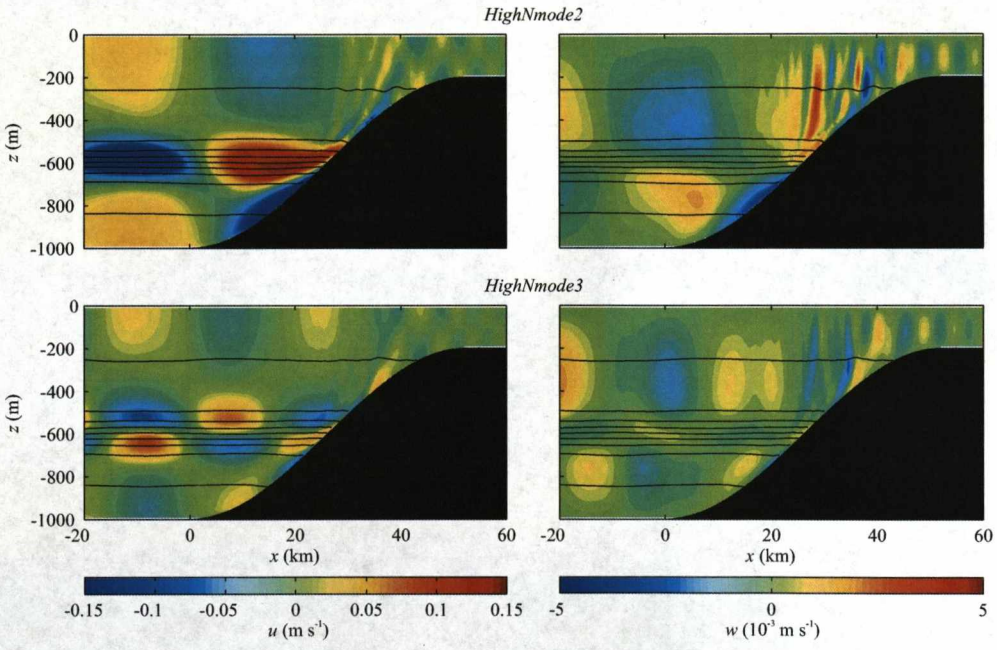

Figure 7.16: Across-slope (left) and vertical (right) velocity for *HighNmode2* and *HighNmode3*. The black lines are contours of non-dimensional density (every 2×10^{-4}).

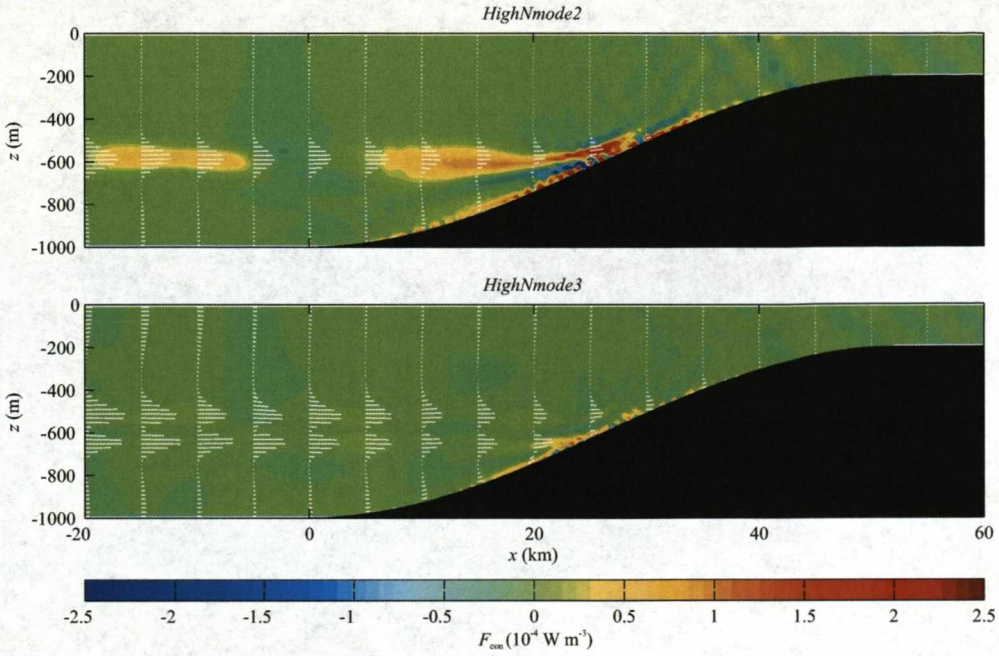

Figure 7.17: Convergence of internal wave energy for *HighNmode2* and *HighNmode3*. The white lines are across-slope and vertical energy flux vectors at each level every 5 km.

The across-slope internal waves energy fluxes at the base of the slope are 290.1 W m^{-1} for *HighNmode2* and 99.6 W m^{-1} for *HighNmode3*. Both are maximum in the pycnocline but there is one energy flux peak for *HighNmode2* and two for *HighNmode3* (Fig. 7.17). There is a convergence of internal wave energy on the slope, largest near the intersection with the pycnocline, and for *HighNmode2* there is a separate band of energy convergence at around 600 m, similar to *HighN*. These imply dissipation rates of the order 10^{-7} W kg^{-1}.

The mode-2 across-slope energy flux of the incident wave at the base of the slope is 347.3 W m^{-1}. The reflected wave energy flux is therefore 57.2 W m^{-1} and primarily in the pycnocline (Fig. 7.15 middle panels). The mode-2 vertical energy flux is upwards above the pycnocline, almost entirely due to the reflected wave. The mode-3 across-slope energy flux of the incident wave is 99.7 W m^{-1}. This is almost identical to the net energy flux, probably because the reflected wave has not reached the location of the energy flux profiles at the time of the diagnostic (Fig. 7.15 lower panels). The mode-3 vertical energy flux is downwards above the pycnocline, almost entirely due to the reflected wave.

At the shelf break the across-slope energy flux is 0.6 W m^{-1} for mode-2 and 0.1 W m^{-1} for mode-3 internal waves. These small energy fluxes suggests that higher modes do not allow significantly more internal wave energy to propagate onto the shelf than mode-1.

7.4.5 On-slope time series

The upper panel of Figure 7.18 shows a time series of across-slope velocity and non-dimensional density at the 680 m isobath, approximately halfway up the slope, for *HighN*. Velocity is largest in the pycnocline and near the bottom while vertical isopycnal displacement increases with depth. Except in the bottom 50 m, the phase lag of velocity decreases with depth so that the flow at the surface and at the bottom are 180° out of phase.

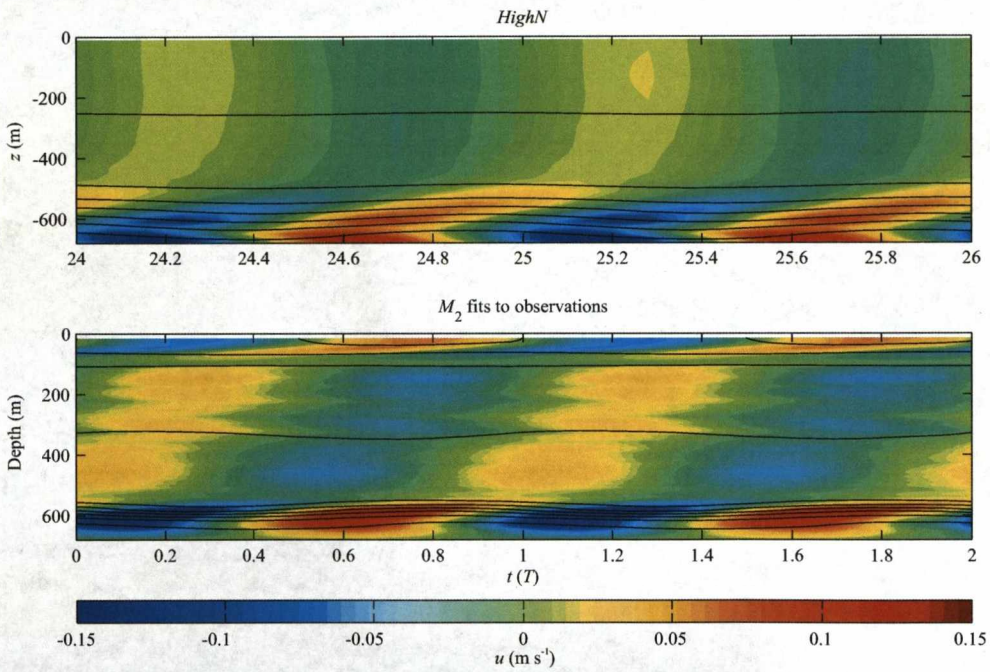

Figure 7.18: Upper panel: Across-slope velocity time series at the 680 m isobath for *HighN*. The black lines are contours of non-dimensional density (every 2×10^{-4}). Lower panel: M_2 fits to across-slope baroclinic velocity at the lowered ADCP/CTD repeat station on the West Shetland slope. The black lines are contours of non-dimensional density (every 2×10^{-4}), calculated from M_2 fits to potential temperature and salinity.

The 680 m isobath is chosen for the time series because it is the location on the West Shetland slope of the lowered ADCP/CTD repeat station during the slope mixing experiment. The lower panel of Figure 7.18 shows M_2 fits to across-slope baroclinic velocity at the repeat station. Non-dimensional density is also plotted, calculated from M_2 fits to potential temperature and salinity. The *HighN* time series compares favourably to the observations, ignoring the seasonal thermocline and currents within that are not included in the model. At mid-depths the observed velocities are larger than modelled by approximately a factor of 2 but in the main pycnocline the observed and modelled velocities are well matched in amplitude and phase[1]. In the model the main pycnocline is thicker than the observations, but this is because the background stratification is modelled on potential temperature and salinity profiles from the middle of the Faroe-Shetland Channel where the pycnocline is thicker than over the West Shetland slope.

The high across-slope velocities in the lower 150 m are not simply due to the proximity of the pycnocline to the bottom. As discussed above, horizontal velocities below the pycnocline are amplified on the slope to maintain mode-1 vertical structure in shallower water. However, a pycnocline is not required for this effect to occur. With uniform stratification the vertical structure of horizontal velocity for mode-1 internal waves goes to zero at half the total water depth (see Fig 7.3) so the same amplification of across-slope velocities occurs in the lower half of the watercolumn. An across-slope velocity maximum at around 600 m and decreasing velocity phase lag with depth also feature in the 680 m isobath time series for *UniNsuper* (not shown). This uniform stratification example suggests the supercriticality of the slope is the important factor, rather than the proximity of the pycnocline to the bottom. Of course the existence of a pycnocline will tend to decrease the internal wave characteristic slope and so decrease the topographic slope required for supercriticality.

Figure 7.19 shows a time series of across-slope velocity and non-dimensional density at the 600 m isobath for *HighNhf*. The asymmetry between the peaks and troughs of the non-linear internal waves is evident in the pycnocline.

[1]The amplitude of the forcing at the open boundary is not precisely tuned to match the internal tide observations. The forcing amplitude ($U_0 = 0.1$ m s^{-1}) is chosen because it generates internal waves with isopycnal displacement amplitudes of the same order (10 m) as observed on the West Shetland slope.

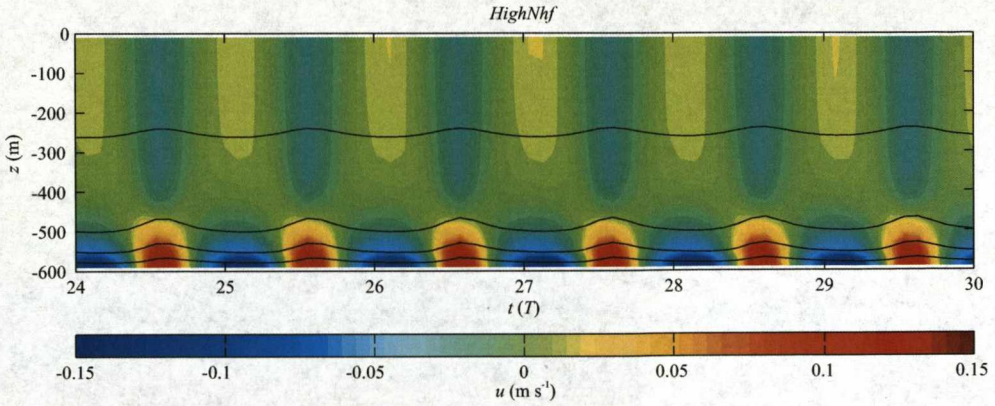

Figure 7.19: Across-slope velocity time series and the 600 m isobath for *HighNhf*. The black lines are contours of non-dimensional density (every 2×10^{-4}).

7.4.6 Energy budget

In this section the evolution of the total energy contained within the area above the slope is investigated for the model runs with internal waves closest to those observed on the West Shetland slope. The rate of change of the total energy is compared with the net flux of internal wave energy into the area and the total dissipation of kinetic energy by viscosity.

For *HighN* the total kinetic and available potential energy increases between $24T$ and $30T$, from 6.1 to 9.2×10^{-7} J m^{-1} (Fig. 7.20 upper panels). This build of energy is expected because the internal wave field over the slope has not reached a steady state. The KE/APE ratio is approximately 5, compared to $KE/APE = (\omega^2 + f^2)/(\omega^2 - f^2) = 8.9$ from Fofonoff (1969). The net internal wave energy flux into the area above the slope is around 250 W m^{-1} between $24T$ and $28T$, decreasing to < 100 W m^{-1} by $30T$. In contrast, the total kinetic energy dissipation by viscosity in the area above the slope increases steadily from 10 to 18 W m^{-1} with the increasing velocity variability. The difference between the net internal wave energy flux and the total kinetic energy dissipation accounts for the increase in kinetic and available potential energy.

The spatial distribution of kinetic and available potential energy over the slope for *HighN* are shown in the upper panels of Figure 7.21. As expected for mode-1 internal waves, APE is highest in the pycnocline, where the vertical isopycnal displacements are largest, and KE is largest above and below, where the horizontal velocity is largest. On the slope, where velocities and isopycnal

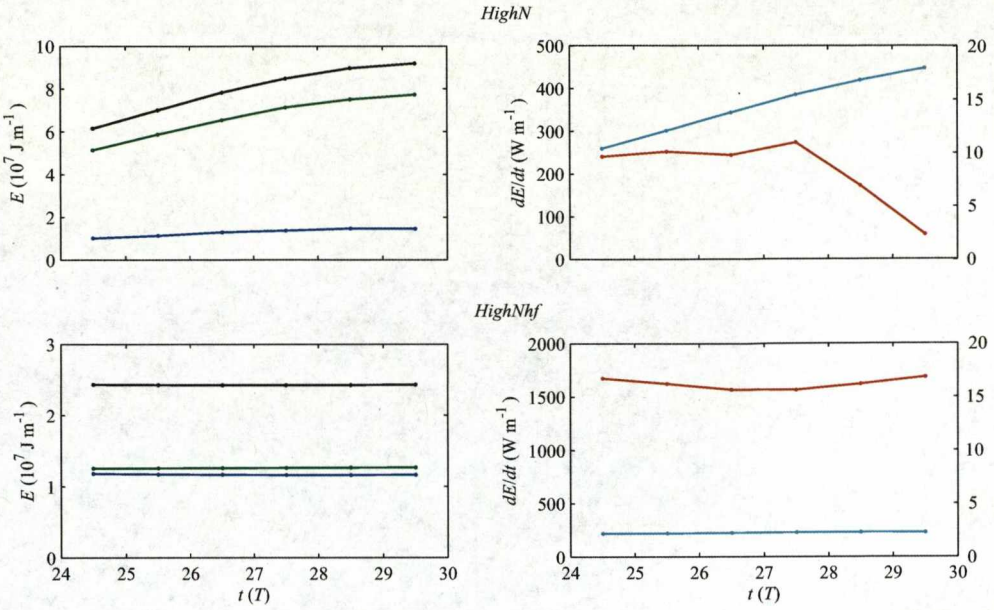

Figure 7.20: Time series of available potential energy (dark blue); kinetic energy (green); total energy (black); and kinetic energy dissipation rate (light blue, right axis), integrated over the area above the slope, for *HighN* and *HighNhf*. Also shown is the net internal wave energy flux into the area above the slope (red, left axis).

displacements are amplified, APE is of the order 5 J m^{-3} and KE, below the pycnocline, is of the order 10 J m^{-3}. Above the pycnocline KE is less than 1 J m^{-3}, decreasing to < 0.1 J m^{-3} on the shelf. Internal wave ray paths, overlaid on the energy fields in Figure 7.21, show an energy convergence in the pycnocline and reflection of internal waves in the pycnocline back into deep water.

The spatial distribution of ϵ and κ_ρ for *HighN* are shown in the upper panels of Figure 7.22. Both kinetic energy dissipation and diapycnal diffusivity are maximum in the pycnocline (of the order 10^{-9} W kg^{-1} and 5×10^{-6} m^2 s^{-1} respectively) and in the bottom boundary layer, where the shear is highest. Dissipation and diffusivity are also enhanced throughout the watercolumn over the upper slope and on the shelf. On-shelf values are of the order 10^{-11} W kg^{-1} and 10^{-6} m^2 s^{-1}, compared to 10^{-13} W kg^{-1} and 10^{-8} m^2 s^{-1} off-shelf above the pycnocline. These values of dissipation are small because the small scale shear, through which most kinetic energy is dissipated in turbulent environments, is not resolved by the model. As a result diapycnal diffusivities are also small, occasionally even less than the molecular diffusivities of heat and salt.

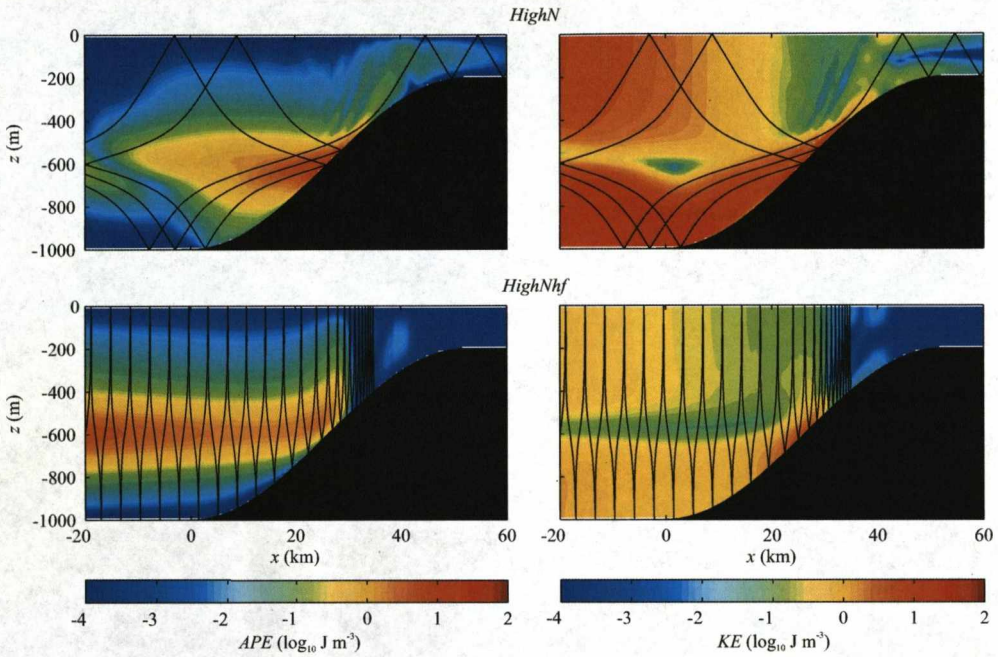

Figure 7.21: Available potential energy density (left) and kinetic energy density (right), time-averaged averaged over six wave periods, for *HighN* and *HighNhf*. The black lines are internal wave characteristic ray paths (not plotted beyond $x = 35$ km for *HighNhf* because they are almost vertical).

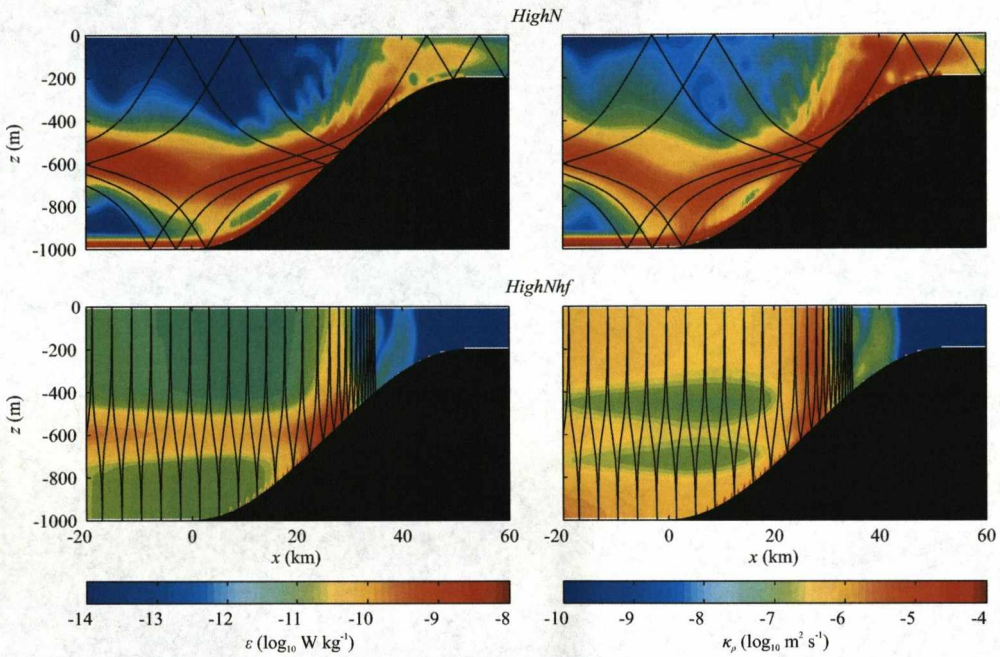

Figure 7.22: Kinetic energy dissipation (left) and diapycnal diffusivity (right), time-averaged averaged over six wave periods, for *HighN* and *HighNhf*. The black lines are internal wave characteristic ray paths (not plotted beyond $x = 35$ km for *HighNhf* because they are almost vertical).

For *HighNhf* the total kinetic and potential energy contained within the area above the slope is relatively constant, around 2.4×10^{-7} J m^{-1}, between $24T$ and $30T$, suggesting the internal wave field over the slope has reached a quasi-steady state (Fig. 7.20 lower panels). $KE/APE = 1.1$, in agreement with $KE/APE = (\omega^2 + f^2)/(\omega^2 - f^2) \simeq 1$. The net internal wave energy flux and total kinetic energy dissipation by viscosity are also relatively constant, around 1.6 kW m^{-1} and 2.3 W m^{-1} respectively. This implies there is a large energy flux into the area above the slope that is not being dissipated by viscosity. The energy budget cannot be closed by including the other energy flux terms (advection and diffusion of energy and energy transport at the free surface) because they are all $< 0.1\%$ of the pressure transport term.

One possible explanation for the mis-match between the energy flux and dissipation rate is that other, not previously considered, energy flux terms are important because the internal waves become non-linear. Following Moum et al. (2007), the energy flux of non-linear internal waves is the sum of non-linear advection of wave energy (kinetic and available potential energy) and the pressure-velocity work term that includes the internal hydrostatic, external hydrostatic, and non-hydrostatic pressure. The advection of kinetic and available potential energy, and the pressure-velocity work term (pressure transport of kinetic energy) are both included in the energy budget but the latter only includes the internal and external hydrostatic pressures. Adding non-hydrostatic pressure to the pressure perturbation calculation, Equation (7.16), gives

$$p' = \int_0^\eta \rho_0 g \, dz + \int_z^0 \rho' g \, dz + \int_z^0 \rho_0 \frac{dw'}{dt} \, dz, \tag{7.24}$$

decreases the pressure-velocity correlation term by 6%. This is not enough to close the energy budget. Another possible explanation for the mis-match is increased numerical dissipation (see Burchard and Rennau 2008) due to the smaller scale of the high-frequency internal waves (Berntsen et al. 2008; J. Berntsen, personal communication).

The spatial distribution of kinetic and available potential energy over the slope for *HighNhf* are shown in the lower panels of Figure 7.21. APE is relatively uniform (of the order 1 J m^{-3}) along the pycnocline but decreases abruptly at the 500 m isobath, where internal wave variability stops. KE also decreases abruptly at the 500 m isobath throughout the watercolumn. Below the pycnocline KE is of the order 1 J m^{-3} and maximum on the lower slope, where velocities are amplified. Above the pycnocline KE is of the order 0.5 J m^{-3}, decreasing towards the slope. Values of APE and KE on the shelf are $< 10^{-4}$ J m^{-3}.

The arrest of high-frequency internal wave energy on the slope can be explained by the dispersion relation, Equation (1.2). The angular frequency of the internal waves is smaller than (but close to) the buoyancy frequency minimum at the surface and the bottom so they can potentially exist on the shelf. However, the horizontal wavelength would be approximately 150 m and the horizontal group velocity only 0.004 m s^{-1} (compared to 2.7 m s^{-1} in the pycnocline off-shelf). The slope of the internal wave characteristic off the shelf goes to 2.72 (almost vertical) at the surface and bottom but is only 0.17 in the pycnocline. The group velocity vector is parallel to the characteristic so the wave energy can only make progress towards the slope in the pycnocline. Up-slope of the intersection with the pycnocline, the characteristic slope is too steep throughout the watercolumn for the wave energy to make significant progress onto the shelf, so the energy is dissipated locally.

The spatial distribution of ϵ and κ_ρ for *HighNhf* are shown in the lower panels of Figure 7.22. Down-slope of the the 500 m isobath kinetic energy dissipation is enhanced throughout the watercolumn. Off the shelf, maximum values (of the order 10^{-10} W kg^{-1}) occur in the pycnocline, where the shear is highest, and increase on the slope up to 10^{-9} W kg^{-1}. Above and below the pycnocline the dissipation rate is of the order 10^{-11} W kg^{-1}, compared to $< 10^{-14}$ W kg^{-1} on the shelf. Diapycnal diffusivity is enhanced throughout the watercolumn off the shelf and over the lower slope; maximum values occur just down-slope of the 500 m isobath (of the order 5×10^{-6} m^2 s^{-1}). Typical values off-shelf are of the order 5×10^{-7} m^2 s^{-1}, compared to $< 10^{-10}$ m^2 s^{-1} on the shelf.

7.5 Discussion and conclusions

In laboratory experiments of internal waves breaking with uniform stratification and critical linear slopes, mixing has been observed in the bottom boundary layer (Ivey and Nokes, 1989) and propagating into the interior of the fluid (Cacchione and Wunsch, 1974). In more recent experiments, mixing has been observed on subcritical and supercritical slopes as well (De Silva et al., 1997; Ivey et al., 2000). The model runs with uniform stratification and linear shelf slopes all exhibit convergence of of internal wave energy in the bottom boundary layer on the slope, in agreement with the above laboratory experiments. The implied dissipation rate is smaller for the subcritical slope than for the critical and supercritical slopes. Separate areas of energy convergence are also observed at bottom, near the base of the slope, and at the surface, near the shelf break. These appear to be related

to reflected internal waves as their location is consistent with reflected internal wave characteristics.

The uniform stratification runs also compare favourably with the *Subcrit*, *Planar*, and *Supercrit* runs from Legg and Adcroft (2003). Their study differs in having a smaller buoyancy frequency ($N^2 = 10^{-6}$ rad s^{-2}); lower amplitude forcing ($U_0 = 0.024$ m s^{-1}); shallower water depth (200 m with a 40 m deep shelf); and higher horizontal resolution relative to the length-scale of the slope. The broad scale distributions of velocity and and density are similar but the Legg and Adcroft runs feature more small scale (turbulent) variability, allowed for by the higher resolution.

The model results are now used help to answer three questions left open after the observational study: 'On the West Shetland slope, how much internal tide energy is reflected and how much is dissipated?'; 'Do the observed high-frequency internal waves dissipate because the buoyancy frequency further up the slope is to small to support them?'; and 'Where in the watercolumn is the internal wave energy dissipated?'. The reflection and dissipation of the internal tide (including the spatial distribution of the dissipation) is discussed first, followed by the dissipation of high-frequency internal waves.

7.5.1 Internal tide reflection

The fraction of internal wave energy approaching the shelf slope that is reflected back into deep water is assessed for different slope topographies and stratification profiles by comparing the across-slope energy fluxes at the base of the slope for runs with and without topography. The incident, reflected, and net energy fluxes are shown in Table 7.3.

The largest reflected energy fluxes occur for runs with the most extensive regions of supercritical topography. However, the profile does not necessarily match the vertical projection of α, i.e. the reflected energy flux does not always occur at depths where the slope is supercritical. The reflected energy flux profile tends to be closely related to incident energy flux profile, suggesting that the internal waves maintain their mode structure upon reflection and so the reflective behaviour cannot be explained simply by critical slope theory. Internal wave characteristics are useful for describing the reflective behaviour of internal waves with wavelengths much shorter than the water depth. However, the modal structure must be considered for wavelengths comparable or longer than the water depth.

Run	$\int_{-H}^{0} F_x\, dz$ off-shelf			$\int_{-H}^{0} F_x\, dz$ on-shelf
	Incident	Reflected	Net	(Net)
UniNsub	322.8	1.3	321.6	3.8
UniNcrit	322.8	6.6	316.2	4.6
UniNsuper	322.8	115.1	207.7	1.7
LowN400	-	-	371.3	2.9
LowN600	372.8	1.8	371.0	2.2
LowN800	-	-	348.8	2.1
HighN	942.2	643.2	299.0	0.2
HighNm4	-	-	2495.8	0.0
HighNhf	-	-	1415.2	0.0
HighNmode2	347.3	57.2	290.1	0.6
HighNmode3	99.7	0.2	99.6	0.1

Table 7.3: Vertically integrated internal wave energy fluxes 5 km from the base of the slope (off-shelf) and within 5 km of the shelf break (on-shelf). The off-shelf flux is separated into incident (towards the slope) and reflected (away from the slope) components so that Net = Incident − Reflected. All energy fluxes are in W m^{-1}.

The reflected component of the energy flux is likely to be underestimated for most runs because maximum internal wave amplitude at the base of the slope has only just been reached at the time of the diagnostic, and so the reflected wave may have had a smaller original amplitude. Control runs without topography were only made for runs with supercritical topography, however, internal wave reflection can be assessed for all runs from the modification of energy flux profiles of the shelf from the mode structure of the incident wave.

With uniform stratification and a linear shelf slope, more internal wave energy is reflected as the slope gradient and α-value increases, as predicted by critical slope theory. For the supercritical slope, 36% of the energy is reflected back into deep water, primarily in the lower half of the watercolumn. In comparison, for the critical slope only 2% of the energy is reflected and $< 1\%$ for the subcritical slope.

With weak pycnocline stratification and a sinusoidal shelf slope, the topography is near-critical to the M_2 internal tide in the pycnocline but little reflection occurs. For the run with the pycnocline at 600 m less than 1% of the internal wave energy is reflected. For the runs with the pycnocline at 400 m and 800 m there is little modification of the energy flux profiles off the shelf. It is therefore assumed little internal wave reflection occurs for these runs either.

With strong pycnocline stratification, the slope is supercritical to the M_2 internal tide between 400 m and 800 m and the fraction of energy reflected is large. For mode-1 internal waves (*HighN*), 68% of the energy is reflected back into deep water, primarilly above and below the pycnocline. The reflected energy flux goes to near-zero in the pycnocline, despite the slope being supercritical, because the incident energy flux goes to near-zero. There is net energy flux away from the slope in the pycnocline, but this results from small differences in the vertical structure of the incident and reflected energy flux profiles. For mode-2 internal waves, 16% of the energy is reflected. Both the incident and reflected energy fluxes are primarily in the pycnocline, where the slope is supercritical. For mode-3 internal waves less than 1% of the energy is reflected but this is probably low because the reflected wave has not yet reached the location of the energy flux profile at the time of the diagnostic. For the M_4 internal tide and high-frequency internal waves the slope is subcritical at all depths and little internal wave reflection is assumed to occur because there is little modification of the energy flux profiles off the shelf.

The internal tide on the West Shetland slope is best approximated by *HighN*; the time series at the 680 m isobath compares favourably to observations at the repeat station. 68% of incident internal wave energy at the base of the slope is reflected for this run, but the fraction is potentially underestimated because a steady state has not been reached at the time of the diagnostic. Although the observed buoyancy frequency in the pycnocline at the repeat station is higher than the maximum background stratification for *HighN* ($N^2 = 10^{-4}$ rad s^{-2} compared to 7.4×10^{-5} rad s^{-2}), the gradient of the West Shetland slope at the 600 m isobath is more gentle (0.02 compared to 0.024). As a result, the maximum α-value for the West Shetland slope is 3.3, the same as for *HighN*. Using buoyancy frequency from the repeat station to calculate α instead of the the near-bed buoyancy frequency from the Central section (as used in Chapter 6), the slope is only supercritical between and 520 and 650 m. This region of slope is a factor of 3 smaller than the supercritical region in *HighN* and so the fraction of incident internal wave energy reflected is also likely to be smaller.

7.5.2 Internal tide dissipation

The fraction of internal wave energy that is dissipated on the shelf slope is assessed by comparing the across-slope energy flux at the base of the slope with the energy flux at the shelf break (Table 7.3). For the runs with uniform stratification, approximately 1% of the net energy flux at the base of the slope reaches the

shelf; the fraction is even less for the runs with low pycnocline stratification ($\sim 0.5\%$) and strong pycnocline stratification ($\sim 0.1\%$).

For *HighN*, the best approximation of the internal tide on the West Shetland slope, the true dissipation rate cannot be inferred from convergences in internal wave energy because a steady state has not been reached at the time of the diagnostic. However, the energy flux on the shelf does not increase greatly at later times, for example at $35T$ the vertically integrated energy flux at the shelf break is 1 W m^{-1}, compared with 0.2 W m^{-1} at $24T$. Such a change is negligible considering the net energy flux at the base of the slope is nearly 300 W m^{-1}. The bulk dissipation rate in the area above the slope from the convergence of internal wave energy is 10^{-8} W kg^{-1}, comparable to measured values of TKE dissipation rate on the West Shetland slope (10^{-9} to 5×10^{-8} W kg^{-1}). Local dissipation rates in the pycnocline are larger than the observations, of the order 10^{-7} W kg^{-1}.

The total kinetic and available potential energy contained within the area above the slope increases during the period $24T$ to $30T$, but is accounted for by the net energy flux into area by internal waves. The average rate of kinetic energy dissipation by viscosity in the area above the slope at the beginning of this period is 2.7×10^{-10} W kg^{-1}; this does not match the dissipation rate inferred from the convergence of internal wave energy because the internal wave field over the slope has not reached a steady state. However, the rate of dissipation by viscosity increases by over 70% during the period $24T$ to $30T$ and eventually settles at 4.7×10^{-10} W kg^{-1} after $30T$. Kinetic energy dissipation is maximum in the pycnocline, as measured on the West Shetland slope, and in the bottom boundary layer. Dissipation is also enhanced throughout the watercolumn over the upper slope and on the shelf, suggesting the dissipation of internal tide energy is important for exchange across the shelf edge as well as through the pycnocline.

7.5.3 High-frequency internal wave dissipation

For the run with high-frequency internal waves (*HighNhf*), the best approximation of the non-linear internal waves on the West Shetland slope, none of the 1.4 kW m^{-1} internal wave energy flux at the base of the slope reaches the shelf despite the topography being subcritical. Although internal waves of this frequency can potentially exist on the shelf, the group velocity vector is almost vertical and so the wave energy cannot propagate horizontally. Off the shelf, wave energy only makes progress towards the slope in the pycnocline, so where the pycnocline intersects the slope the energy is dissipated. The observed non-linear

internal waves must dissipate on the West Shetland slope because the buoyancy frequency further up the slope is too low to support them. However, the model suggests that even if the buoyancy frequency on the upper slope and continental shelf was just high enough to support them (or the waves were of a lower frequency) they would dissipate due to decreasing horizontal group velocity.

The internal wave energy flux at the base of the slope is almost an order of magnitude larger than peak non-linear internal wave energy fluxes measured on the West Shetland slope, primarily because the horizontal group velocity (2.8 m s^{-1}) is an order of magnitude larger than observed. The main difference however, is that the modelled internal wave energy flux is consistent, while the energy flux of the observed waves is highly intermittent. The amplitude of the modelled internal waves at the base of the slope (10 m) is small compared to maximum wave amplitudes observed on the West Shetland slope (50 m). However, the amplitudes of the observed waves are likely to increase as the waves propagate up the slope, due to shoaling of the lower layer and the resulting decrease in phase velocity, so they may have a smaller amplitude when at the base of the slope. The amplitude of the modelled waves increase up to approximately 20 m on the slope.

The bulk dissipation rate in the area above the slope from the convergence of internal wave energy is 5×10^{-8} W kg^{-1}. Local dissipation rates on the slope are up to 2×10^{-6} W kg^{-1}, but values of this magnitude only occur in small areas. A more typical dissipation rate for the pycnocline is 5×10^{-7} W kg^{-1}, but is still order of magnitude larger than measured in the pycnocline on the West Shetland slope (5×10^{-8} W kg^{-1}). The higher than observed dissipation rates may be accounted for by the larger, and consistent, internal wave energy flux.

During the period $24T$ to $30T$ the internal wave field over the slope is in a quasi-steady state, however, there is still a mis-match between the net energy flux into the area above the slope and the total kinetic energy dissipation by viscosity. The average rate of kinetic energy dissipation in the area above the slope is only 5.9×10^{-11} W kg^{-1}, three orders of magnitude smaller than the dissipation rate inferred from the convergence of internal wave energy. Nevertheless, the spatial distribution is promising; kinetic energy dissipation is enhanced throughout the watercolumn down-slope of the 500 m isobath and is maximum in the pycnocline where it intersects the slope.

7.5.4 The integration constant problem revisited

When calculating internal wave energy fluxes, $\mathbf{F} = \langle \mathbf{u}'p' \rangle$, the surface pressure perturbation due to passing internal waves, p'_{surf}, is required to diagnose the correct vertical distribution of energy. This variable cannot be determined from CTD measurements so typically an assumption about the pressure field is made to constrain its value. However, the model is configured with a free surface condition so surface displacements (and hence pressure perturbations) due to passing internal waves can be calculated.

In Chapter 5, four different assumptions about the pressure field were made to calculate the internal tide energy flux at the repeat station on the West Shetland slope. In this section, the model is used to re-assess the validity of the first three assumptions. To review, the first three assumptions made were: (1) $p' = 0$ at $z = 0$ ($p'_{\text{surf}} = 0$); (2) $p' = 0$ at $z = -H$; and (3) $\int_{-H}^{0} p'\, dz = 0$, the baroclinicity condition for pressure. Assumptions (1) and (3) yield qualitatively similar energy flux profiles, while assumption (2) yields a profile that bears no resemblance to the velocity or density variability.

To compare these assumptions, internal wave energy fluxes are calculated at the 680 m isobath for *HighN*, the best approximation of the internal tide on the West Shetland slope. Four across-slope and vertical energy flux profiles are calculated, three using the above assumptions to constrain p'_{surf}, and the true profile using the modelled surface pressure perturbations (Fig. 7.23).

The vertically integrated across-slope energy flux is 73.2 W kg^{-1}, independent of p'_{surf}. This is approximately half the internal tide energy flux measured at the repeat station (154.7 W kg^{-1}), but should be considered good agreement considering the internal wave amplitude is not precisely tuned to the observations. As with the measured energy flux profiles, the largest across-slope energy fluxes are in the pycnocline and lower layer. Assumptions (1) and (3) both yield up-slope fluxes between approximately 500 and 620 m, and down-slope fluxes below 620 m. Above 500 m the flux for assumption (1) is zero and slightly up-slope for assumption (3). The true energy flux profile is similar to the profiles for assumptions (1) and (3) but with a smaller down-slope flux below 620 m and a small down-slope flux around 500 m. As the vertical integral of the energy fluxes are the same, the larger down-slope flux below 480 m is balanced by a larger (but still small) up-slope flux above. Assumption (2) yields a very different energy flux profile, down-slope between 480 and 620 m, and up-slope above and below. Vertical internal wave energy flux profiles are similar for assumptions (1) and (3), and the true profile, downward in the lower layer and tending to zero at the

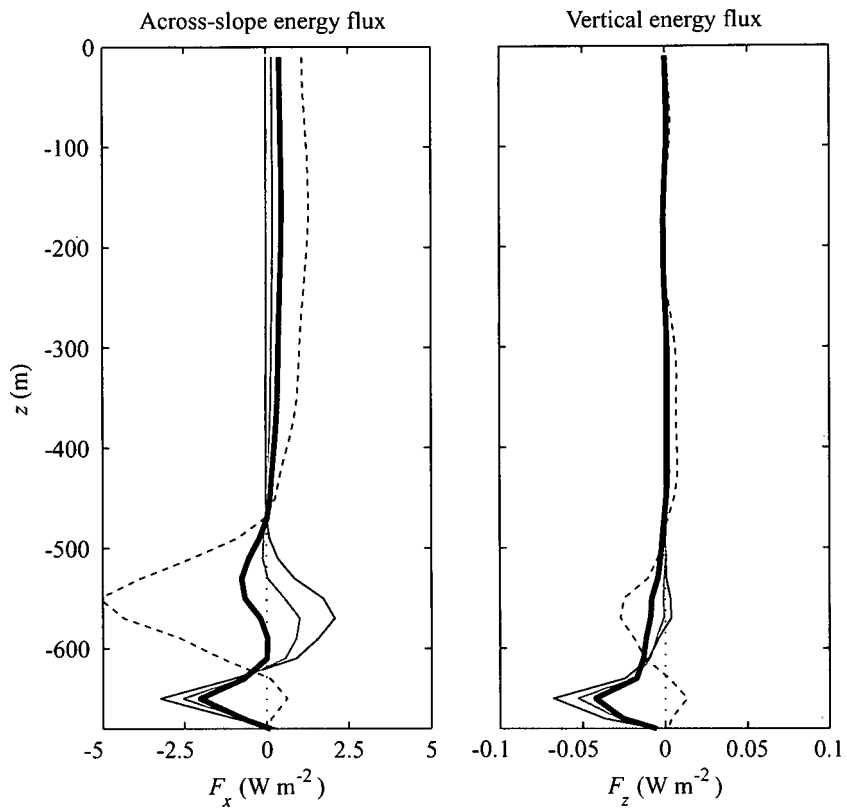

Figure 7.23: Across-slope and vertical internal wave energy fluxes at the 680 m isobath for *HighN*. The thick black lines are the true energy fluxes; the thin black lines are for the assumption $p' = 0$ at $z = 0$; the dashed black lines are for the assumption $p' = 0$ at $z = -H$; and the solid grey lines are for the assumption $\int_{-H}^{0} p'\, dz = 0$.

surface and the bottom. Again assumption (2) yields a very different energy flux profile with the wrong vertical structure.

The assumption that yields an internal wave energy flux profile closest to the true profile is (3), the baroclinic condition for pressure. However, the energy flux still deviates from the true profile in the pycnocline. This agreement can be improved upon by finding the typical depth where $p' = 0$ when using the modelled surface pressure perturbations and using this depth to constrain p'_{surf}. At the 680 m isobath $p' = 0$ between 550 and 570 m; this is used to make the fourth assumption about the pressure field in Chapter 5 ($p' = 0$ at $z = -560$ m) that yields an energy flux profile in very close agreement with the profile for assumption (3). This comparison suggests that, where the topographic slope is small, the baroclinicity condition for pressure is a good a priori assumption about the pressure field and yields an energy flux profile close to the model 'truth'.

7.5.5 Conclusions

Internal waves approaching a continental shelf slope are successfully simulated for different frequencies, modes, and stratification profiles. The greatest reflection of internal waves occurs where the topography is supercritical to the internal wave characteristic over an extensive region of the slope. However, the reflected energy flux profile does not necessarily match the vertical projection of α. For the run with uniform stratification and a linear slope supercritical to the forced M_2 internal tide, 115.1 W m^{-1} of the incident internal wave energy flux, 322.8 W m^{-1}, is reflected (36%). For the run with strong non-uniform stratification and mode-1 M_2 frequency forcing, the best approximation of the internal tide on the West Shetland slope, the slope is supercritical between 400 m and 800 m, and 643.2 W m^{-1} of the incident 942.2 W m^{-1} is reflected (68%). No internal wave reflection occurs for the high-frequency run, the best approximation of the non-linear internal waves on the West Shetland slope, because the slope is subcritical at all depths.

For all runs the energy flux at the shelf break is small compared to energy flux at the base of the slope. This convergence of internal wave energy implies large dissipation rates in the area above the slope. The energy convergence and implied dissipation rate on the linear slope is larger for the critical and supercritical runs than the subcritical run, while for the weak stratification runs the maximum energy convergence occurs at the depth of the pycnocline. For the run closest to the observed internal tide, the bulk dissipation rate in the area over the slope from the convergence of internal wave energy is 10^{-8} W kg^{-1}, comparable to measured

values of TKE dissipation rate on the West Shetland slope, but over an order of magnitude larger than the average rate of kinetic energy dissipation by viscosity because a steady state has not been reached. For this run and the run closest the observed non-linear internal waves, kinetic energy dissipation is enhanced in the pycnocline and on the slope. High-frequency internal wave energy is arrested where the slope intersects the pycnocline because the horizontal group velocity becomes too small to make significant progress on to the shelf and so the energy must be dissipated locally.

The final conclusion relates back to the internal tide energy flux calculation in Chapter 5. The a priori assumption about the pressure field that yields an energy flux profile at the 680 m isobath closest to the true profile (using the model surface pressure perturbations) is the baroclinicity condition for pressure. The model also predicts the best approximation of the surface pressure perturbation at the repeat station on the West Shetland slope is gained by assuming the pressure perturbation goes to zero at 560 m. The energy flux profile for this assumption is in very close agreement with the profile for the assumption of the baroclinicity condition for pressure.

Chapter 8

Summary and synthesis

8.1 Summary

In this chapter the key results from the six previous chapters are summarised and combined in a synthesis of this work. In Chapter 1 six questions were posed: 'On what time-scales do changes in the large-scale water mass structure of the Faroe-Shetland Channel occur?'; 'Were the hydrographic conditions during the slope mixing experiment extreme compared to the variability observed in the historic dataset?'; 'How much turbulent mixing occurs on the West Shetland slope?'; 'How much energy is transported onto the slope by internal waves?'; 'Can internal wave energy fluxes account for the measured mixing?'; and 'What factors effect how much internal wave energy is reflected and how much is dissipated on the slope?'. These questions are answered in the following three sections.

8.1.1 Historic data

The temperature and salinity structure of the Faroe-Shetland Channel is found to change on day-to-week to decadal time-scales. Of particular interest to the main aim of this thesis is variability in the structure and position of the main pycnocline, as this is where internal waves are likely to be concentrated. On day-to-week time-scales, the position of the pycnocline can change dramatically; temperature changes of the order 5°C within a week are observed at fixed levels within the pycnocline, equivalent to vertical isotherm displacements of the order 200 m. This is problematic when using moored instruments to measure internal wave variability because the pycnocline may shoal or deepen while the instruments are deployed so that the waves are poorly sampled. This occurred for a few days during the middle of the slope mixing experiment, resulting in possible underestimation of internal wave variability and energy fluxes.

The depth and thickness of the pycnocline varies seasonally, deepening by 80 m in autumn and thickening by nearly 50 m in spring. On decadal time-scales however, the pycnocline is thinning by 1.2 m per year and deepening by 1.8 m per year. The thickness of the pycnocline is measured as the vertical distance between isotherms so the thinning trend implies increasing buoyancy frequencies (in the absence of density compensating salinity changes) and so levelling of internal wave characteristics. Conversely, the ratio of the topographic slope to the characteristic slope where the pycnocline intersects the West Shetland slope may decrease as the pycnocline deepens because the slope gradient typically decreases with depth. However, the buoyancy frequency is high enough that the pycnocline would have to reach the bottom of the channel, or alternatively the shelf break, before the slope becomes completely subcritical to the semi-diurnal internal tide. The pycnocline stratification is weakened in model simulations (*LowN* runs), so that changing the depth changes the local topography from subcritical to supercritical. Interestingly, for these model runs the reflective behaviour of the internal tide is insensitive to the depth of the pycnocline.

The hydrographic conditions during the slope mixing experiment were not unusual when compared to the variability observed in the historic dataset. The mean depth of the main pycnocline over the West Shetland slope was 599 m, deeper than the mean from the historic data (432 m) but within three standard deviations. The mean pycnocline thickness was 83 m, thinner than the mean from the the historic data (132 m) but within two standard deviations.

8.1.2 Slope mixing experiment

During the slope mixing experiment a semi-diurnal internal tide and near-bed, non-linear internal waves were observed on the West Shetland slope. From indirect estimates of turbulent mixing, diapycnal eddy diffusivity on the slope is an order of magnitude larger than typical values for the interior of the open ocean.

The internal tide has an amplitude of the order 10 m and is associated with an across-slope energy flux of 155 W m^{-1} (Fig. 8.1 upper panels). The energy flux is maximum in the main pycnocline, with around 100 W m^{-1} integrated between 550 m and 650 m, but small compared to the across-slope energy flux of the barotropic tide (133 kW m^{-1}). The non-linear internal waves are higher frequency (typical wave periods are between 15 and 30 minutes) and bottom trapped by the main pycnocline maintained close to the seabed. These waves have amplitudes of up to 50 m but only occur intermittently in time, in the form of solitary waves, cnoidal wave trains, and solibores (Fig. 8.2 upper panel). The

wave trains occur at roughly semi-diurnal intervals but the phase relation with the local barotropic tide is variable, suggesting they are generated by the tide at a remote location. The mean velocity of the leading waves is 0.27 m s^{-1} at an angle of 132° up the shelf slope and they are associated with energy fluxes of up to 200 W m^{-2} (Fig. 8.2 lower panel). When the mixing estimates were made the energy flux was small but relatively uniform, between 10 and 15 W m^{-2}.

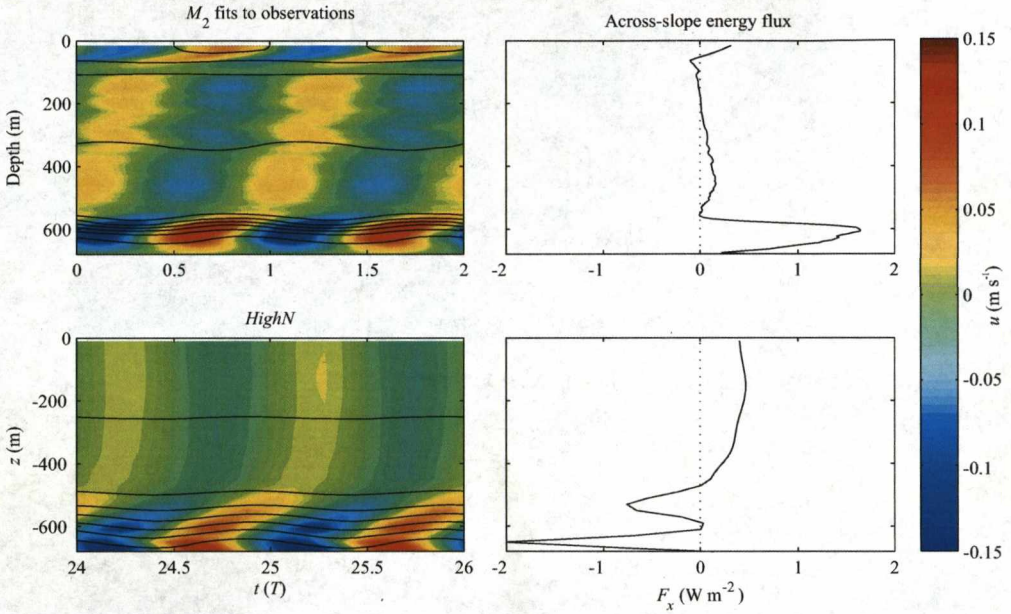

Figure 8.1: Across-slope baroclinic velocity and non-dimensional density (contoured every 2×10^{-4}) time series from M_2 fits to observations at the repeat station and from the numerical model run *HighN* at the 680 m isobath. Also shown are the across-slope internal tide energy fluxes.

The rate of TKE dissipation on the slope is estimated from Thorpe scale analysis of density overturns and using a finescale parameterisation of vertical shear and strain. The dissipation rates inferred from the two independent methods are within the bounds of uncertainty, of the order 5×10^{-8} W kg^{-1} in the main pycnocline; 5×10^{-9} W kg^{-1} in the seasonal thermocline; and 10^{-9} W kg^{-1} in the buoyancy minimum between the two regions of stratification (Fig. 8.3). The former is equivalent to a diapycnal eddy diffusivity of 2×10^{-4} m^2 s^{-1}, an order of magnitude larger than background levels.

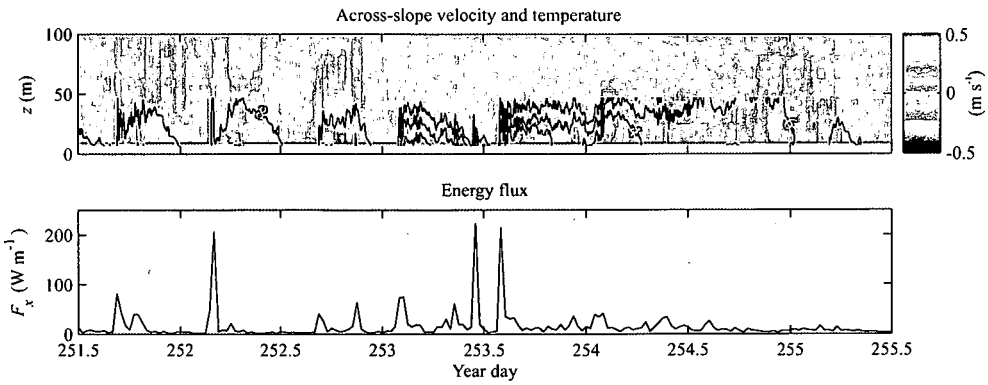

Figure 8.2: Across-slope velocity and temperature (contoured every 2°C) from the 'West' moored ADCP and thermistor mooring. Also shown is the the non-linear internal wave energy flux from the 'West' mooring pair.

The high TKE dissipation rate in the pycnocline can be sustained by the energy fluxes associated with the internal tide and non-linear internal waves if it is assumed that the whole up-slope energy flux in the pycnocline is dissipated in the region between the location of the energy flux estimate and the shelf slope. Bulk TKE dissipation rates from this assumption are 2×10^{-7} W kg^{-1} for the internal tide (a factor of four larger than the dissipation rate inferred from the Thorpe scale analysis and finescale parameterisation in the pycnocline) and of the order 5×10^{-8} W kg^{-1} for the non-linear internal waves.

The lower and upper reaches of the shelf slope are subcritical to the semi-diurnal internal tide because the near-bottom buoyancy frequency is close to zero. Near-bed stratification is maintained where the pycnocline intersects the slope and the topography becomes supercritical, coinciding with the depth at which the across-slope internal tide energy flux is largest. The calculated internal tide energy flux is the net energy flux of the incident and reflected waves so the fraction of incident energy that is reflected cannot be determined. However, a model simulation (*HighN*) suggests up to 68% of the incident energy is reflected. Some internal tide energy is expected to be dissipated in the bands of near-critical slope between the subcritical and supercritical regions; the same model simulation features enhanced kinetic energy dissipation on the slope at all depths.

The non-linear internal waves are bottom-trapped and so must dissipate or break in the local area because the near-bed buoyancy frequency further up the slope is less than the angular frequency of the waves. A model simulation of internal waves with an angular frequency slightly smaller than the buoyancy

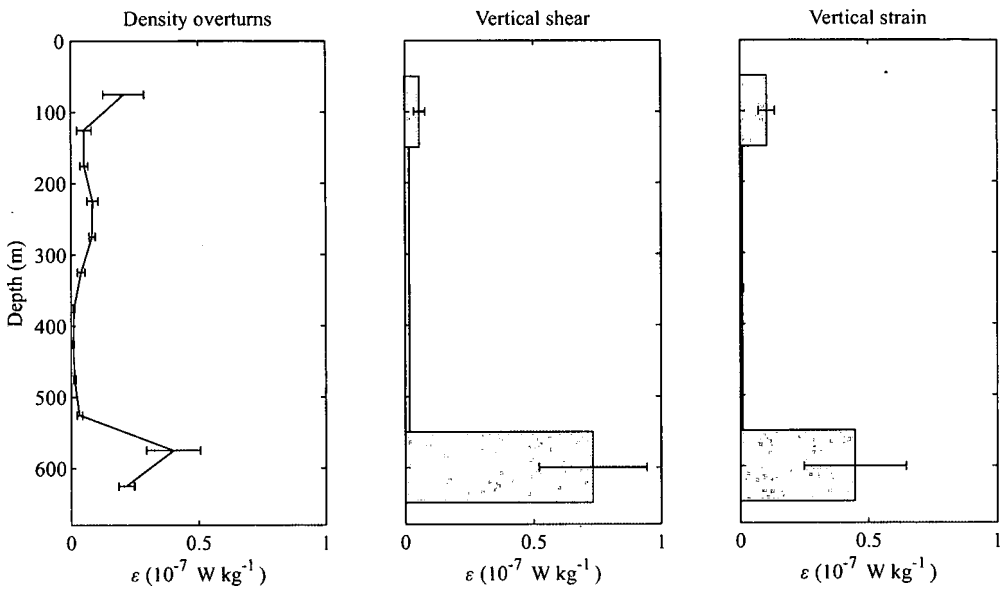

Figure 8.3: TKE dissipation rate from Thorpe scale analysis of density overturns and the finescale parameterisation of vertical shear and vertical strain. For Thorpe scaling the error bars are the standard error between 25 casts. For the finescale parameterisation the error bars are the standard error between five groups of casts.

frequency minimum (*HighNhf*) also features enhanced kinetic energy dissipation where the pycnocline intersects the slope. Although these internal waves can potentially exist on the shelf, up-slope of the intersection with the pycnocline, the horizontal group velocity is too small for the wave energy to make significant progress onto the shelf, so the energy is dissipated locally.

8.1.3 Numerical modelling of internal waves

Internal waves approaching a continental shelf slope are successfully simulated for different frequencies, modes, and stratification profiles. The semi-diurnal internal tide and higher-frequency, non-linear internal waves observed on the West Shetland slope are best simulated by runs *HighN* and *HighNhf* respectively (Fig. 8.4).

The fraction of internal wave energy that is reflected back into deep water is assessed by comparing the across-slope energy fluxes near the base of the slope for model runs with and without topography. The greatest reflection of internal waves occurs where the topography is supercritical to the internal wave charac-

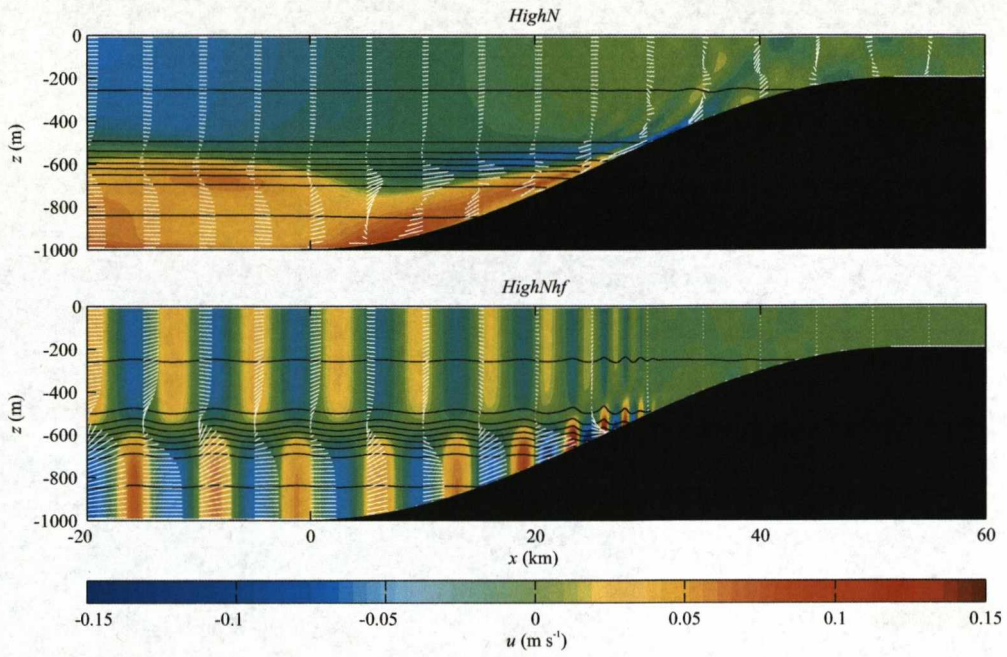

Figure 8.4: Across-slope baroclinic velocity and non-dimensional density (contoured every 2×10^{-4}) from the numerical model runs *HighN* and *HighNhf*. The white lines are across-slope and vertical internal wave energy flux vectors.

teristic over an extensive region of the slope. With uniform stratification and a linear shelf slope supercritical to the M_2 internal tide, 36% of the incident internal wave energy is reflected, compared with 2% and $< 1\%$ for critical and subcritical slopes respectively. With idealised stratification and shelf slope profiles, fit to potential temperature and salinity profiles from the Faroe-Shetland Channel and bathymetry data from the West Shetland slope (*HighN* runs), the slope is supercritical to the M_2 internal tide between 400 m and 800 m. 68% of the incident mode-1 internal wave energy is reflected, compared to 16% for mode-2 internal waves and $< 1\%$ for mode-3. However, the reflected energy flux profile does not necessarily match the vertical projection of the topographic slope to internal wave characteristic slope ratio and tends to be closely related to incident energy flux profile. This suggests that the internal waves maintain their mode structure upon reflection and so the reflective behaviour cannot be explained simply by critical slope theory. With an M_4 internal tide (*HighNm4*) or high-frequency internal waves (*HighNhf*) the slope is subcritical at all depths and little internal wave reflection occurs.

The fraction of internal wave energy that is dissipated on the shelf slope is assessed by comparing the across-slope energy flux at the base of the slope with the energy flux at the shelf break. With uniform stratification only 1% of the energy flux at the base of the slope reaches the shelf; $< 1\%$ for non-uniform stratification. This convergence of internal wave energy implies large dissipation rates in the area above the slope. Dissipation of kinetic energy by viscosity cannot account for this energy convergence because in most cases a steady state has not been reached. However, the spatial distribution of kinetic energy dissipation is promising for *HighN* and *HighNhf*; maximum values occur in the pycnocline and on the slope. With an M_4 internal tide (*HighNm4*) wave breaking on the slope occurs in the pycnocline.

The model is also used to re-assess the assumptions made about the pressure field when calculating the internal tide energy flux in Chapter 5. On the West Shetland slope, and perhaps on other gentle shelf slopes, the baroclinicity condition for pressure is a good a priori assumption and yields an energy flux profile close to the model 'truth'.

8.2 Synthesis

In this section, the propagation of internal waves in the Faroe Shetland Channel is described, from their generation at a remote location to their reflection or dissipation on the West Shetland slope. Three strands of evidence suggest the internal waves observed on the West Shetland slope are generated at a remote location and propagate into the region along the main pycnocline. Firstly, the non-linear internal waves are observed to propagate up the slope and have varied phase relations with the local barotropic tide. Secondly, the internal tide energy flux has a large up-slope component in the pycnocline. Finally, the velocity and density variability on the slope are consistent with model simulations of a mode-1 M_2 internal tide approaching the shelf slope (Fig. 8.1 lower panels).

This view is contrary to many studies of internal tides and turbulent mixing on continental shelf slopes, where the internal waves are assumed to be generated locally (e.g. Pingree and New 1991; Lien and Gregg 2001; Green et al. 2008). One notable exception is Nash et al. (2004) who suggest elevated near-bottom mixing at the base of the continental slope off Virginia arises from the supercritical reflection of a remotely generated, low-mode, M_2 internal tide. The location of the elevated mixing observed by Nash et al. is consistent with supercritical reflection

of downward propagating internal wave characteristics, similar to the modelled convergence of internal wave energy at the base of the supercritical linear slope.

A likely generation region of the internal tide in the Faroe-Shetland Channel is the Wyville Thomson Ridge (Sherwin, 1991). An internal tide generated at the ridge and propagating northeast through the channel may refract so that energy fluxes are directed up the shelf slopes on either side of the channel. The trains of high-frequency internal waves also appear to be tidally forced and may be a non-linear manifestation of the internal tide.

Once on the West Shetland slope the behaviour of the internal waves is determined by their frequency. Where the pycnocline intersects the shelf slope the topography is supercritical to the M_2 internal tide. The mode-1 horizontal energy flux at the base of the shelf slope is large at the surface and the bottom, decreasing to near-zero at mid-depths. However, as the internal tide progresses up the slope the energy flux minimum shoals to maintain mode-1 vertical structure in shallower water and the near-bed energy flux is amplified. At the location of the repeat station, slightly down-slope of the intersection with the pycnocline, the depth of the energy flux maximum coincides with the depth of the pycnocline and the region of supercritical slope. Approximately half the incident energy is reflected back into deeper water, but the internal tide maintains its mode structure upon reflection so that the reflected energy flux at the base of the slope is also large at the surface and the bottom. The rest of the energy is dissipated in the pycnocline and on the slope, causing turbulent mixing through shear instabilities and possibly internal wave breaking; little internal tide energy reaches the shelf break. For the M_4 internal tide, the slope is subcritical at all depths but internal wave breaking is likely.

The trains of high-frequency internal waves may develop from the internal tide at some remote location or on the shelf slope itself as the lower layer shoals and the wave velocity decreases. The near-bed energy flux is amplified as the internal waves progress up the slope, but all the energy must be dissipated before the intersection with the pycnocline because the near-bed buoyancy frequency further up the slope is too low to support them. The energy is likely dissipated by bottom stress and internal wave breaking, resulting in enhanced mixing on the slope. A schematic of the mixing process that occur on the West Shetland slope, including wind mixing and bottom mixing, is shown in Figure 8.5.

All internal wave energy must eventually be dissipated, either in shelf seas or the deep ocean, and in the right locations relatively small energy fluxes could make large contributions to global mixing. The transfer of energy from internal waves to

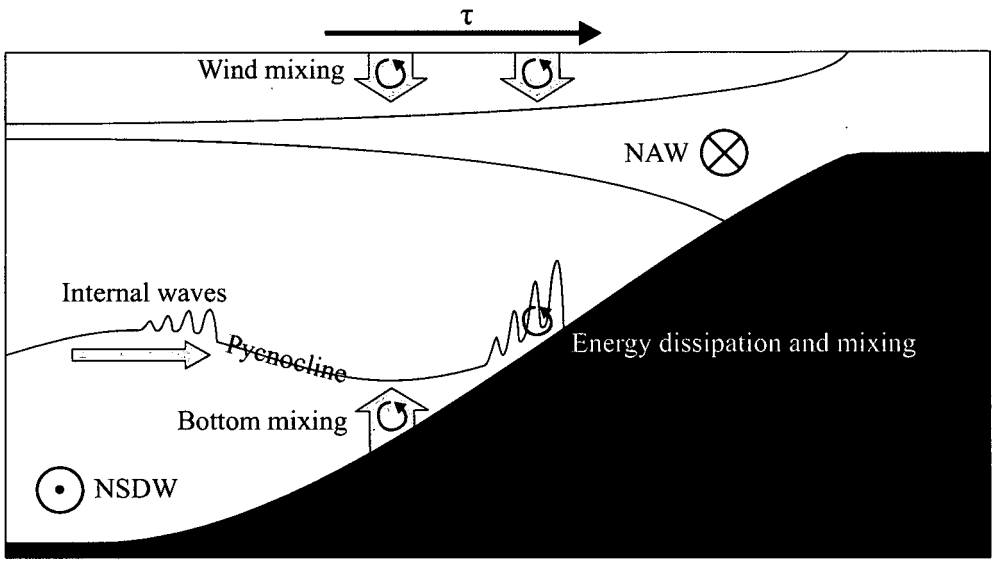

Figure 8.5: Schematic of mixing processes that occur on the West Shetland slope. Energy from surface forcing by the wind propagates downward and mixes the surface layer. Turbulence from bottom friction on barotropic tidal currents mixes the bottom boundary layer. Internal waves propagate along the main pycnocline and dissipate on the slope, causing turbulent mixing through shear instabilities and internal wave breaking. Near the surface NAW flows northeast along the shelf edge, while below the pycnocline NSDW flow southwest along the axis of the channel.

turbulent mixing is more efficient than from the barotropic tide or surface forcing by the wind. Moreover, internal wave energy tends to be dissipated in stratified regions where the most work on buoyancy needs to be done. In the global context the internal wave energy fluxes measured here are not large; in energetic regions energy fluxes of the order kW m^{-1} are not uncommon, for example the Hawaiian Ridge (Nash et al., 2006; Lee et al., 2006) and Monterey Submarine Canyon (Kunze et al., 2002). If enhanced mixing by internal wave breaking is typical of the main pycnocline along continental shelf slopes, this mechanism could make a significant contribution to mixing globally.

8.3 Further work

Occupation of the Fair Isle-Munken line by the Fisheries Research Services and the Faroese Marine Laboratory will likely continue owing to the importance of the region as a commercial fishery and continuing requirement to report on the state of territorial waters. Several features of the dataset identified here merit further analysis and will benefit from continued occupation. For example the thinning and deepening trend of the pycnocline; the decadal time-scale increase in the heat and salt content of the waters in the channel; and the inter-annual variability in the salinity of NAW. Another area worthy of further investigation is the geographical extent of the anomalously low salinity NSAIW observed in the Faroe-Shetland Channel during 1997. Comparison with temperature and salinity measurements from the Norwegian Sea and the Faroe-Bank Channel may allow the progress of the salinity anomaly to be tracked through the channels.

Most of the data from the slope mixing experiment is analysed here and a full comparison with the model simulations is in preparation. The data from a high-frequency ADCP on the NIOZ lander has been processed by Hans van Haren (NIOZ) and shows the structure of the near-bed, non-linear internal waves in greater detail than the ADCP data analysed here. Unfortunately no usable data were retrieved from STABLE and all the microstructure data from HOMER were lost during recovery.

The mooring array used in the slope mixing experiment has been deployed twice since September 2005. The first deployment was on the continental shelf slope in the Gulf of Cadiz (Portugal) in 2007, part of a European Geophysical Oceanography (GO) project combining seismic survey techniques (e.g. Holbrook et al. 2003) with traditional oceanographic measurements. The second deployment was off the coast of Svalbard (Arctic Ocean) in 2008 to measure mixing in

a dense water cascade down the shelf slope. Data from these two deployments are currently under analysis to investigate slope mixing processes in contrasting contexts.

Several modifications to the mooring array and sampling scheme would have allowed a more comprehensive analysis of internal waves and mixing processes on the West Shetland slope and are noted here for future reference. Firstly, direct turbulence measurements from a microstructure profiler are required to accurately estimate TKE dissipation and for comparison with Thorpe scale analysis and finescale parameterisations. Secondly, sacrifice of vertical resolution for more uniform sampling of the watercolumn aids the calculation of internal wave energy fluxes from mooring data by allowing the pressure-velocity work term to be determined. Thirdly, increasing the pressure resolution of near-bed CTD loggers may allow analysis of non-linear internal waves from pressure signals (e.g. Moum and Nash 2008). Finally, repeat stations at different locations across and along a shelf slope allow convergences of internal wave energy to be identified.

The numerical modelling investigation could be extended to three-dimensions, allowing geometric focusing of internal wave energy that may lead to localised regions of high amplitude waves (Bühler and Muller, 2007). The level of numerical dissipation in the model simulations of could be assessed by repeating the model runs with very low viscosities so that almost all the energy dissipation is by numerical discretisation.

Finally there is the continuing issue of the correct assumption to make about the pressure field when calculating internal wave energy fluxes. This is a problem over sloping topography because the vertical structure of velocity and pressure cannot be separated from horizontal position (Gerkema and van Haren, 2007). The baroclinicity condition for pressure is shown here to be a good a priori assumption over gently sloping topography, but over steeper topography assuming zero pressure perturbation at the bottom, as assumed by Gerkema and van Haren, or at the surface may yield a more accurate energy flux profile. A series of model runs with different topographic slope gradients and stratification profiles, to represent typical deep ocean and shelf sea conditions, could be used to determine under which circumstances each assumption should be made.

Appendix A

Historic data: Station locations and section occupations

Station	Latitude	Longitude
1	61°16′N	6°38′W
2	61°12′N	6°22′W
3	61°02′N	5°57′W
4	60°51′N	5°29′W
5	60°47′N	5°16′W
6	60°43′N	5°06′W
7	60°38′N	4°54′W
8	60°35′N	4°45′W
9	60°29′N	4°26′W
10	60°25′N	4°19′W
11	60°20′N	4°09′W
12	60°18′N	4°05′W
13	60°16′N	3°59′W
14	60°13′N	3°52′W
15	60°10′N	3°44′W
A	61°00′N	5°51′W
B	60°47′N	5°18′W
C	60°34′N	4°46′W
D	60°27′N	4°21′W
E	60°20′N	4°10′W

Table A.1: Location of the stations and moorings along the Fair Isle-Munken line. 1-15 are CTD stations, A-E are ADCP moorings

Cruise	Date	1	2	3	4	5	6	7	8	9	10	11	12	13	14	15
EX197308	20/08/1973		✓	✓	✓		✓		✓	✓	✓	✓		✓		✓
EX197308	23/08/1973		✓	✓	✓	✓	✓		✓	✓	✓	✓		✓		
EX197308	27/08/1973			✓	✓	✓	✓		✓	✓	✓	✓		✓		✓
EX197308	29/08/1973		✓	✓	✓	✓	✓		✓	✓	✓	✓		✓		✓
EX197308	02/09/1973			✓	✓		✓		✓	✓	✓	✓		✓		✓
EX197308	06/09/1973		✓	✓	✓	✓	✓		✓	✓	✓	✓		✓		✓
EX197308	09/09/1973		✓	✓	✓	✓	✓		✓	✓	✓	✓		✓		✓
EX197308	14/09/1973			✓	✓	✓	✓		✓	✓	✓	✓		✓		✓
SC197405	31/05/1974		✓	✓	✓	✓	✓		✓	✓	✓	✓		✓		✓
SC197405	04/06/1974		✓	✓	✓	✓	✓		✓	✓	✓	✓		✓		✓
SC197405	08/06/1974		✓	✓	✓	✓	✓		✓	✓	✓	✓		✓		✓
SC197407	11/07/1974		✓	✓	✓	✓	✓		✓	✓	✓	✓		✓		✓
EX197407	09/08/1974		✓	✓	✓	✓	✓		✓	✓	✓	✓		✓		
EX197504	23/05/1975		✓	✓	✓	✓	✓		✓	✓	✓	✓		✓		✓
EX197504	06/06/1975		✓	✓	✓	✓	✓		✓	✓	✓	✓		✓		✓
EX197512	18/12/1975		✓	✓	✓	✓	✓		✓	✓	✓	✓		✓		✓
EX197606	11/07/1976		✓	✓	✓	✓	✓		✓	✓	✓	✓		✓		✓
EX197606	26/07/1976			✓	✓	✓	✓		✓	✓	✓	✓		✓		✓
SC197701	16/07/1977		✓	✓	✓	✓	✓		✓	✓	✓	✓		✓		✓
SC197706	18/12/1977		✓	✓	✓	✓	✓		✓	✓	✓	✓		✓		✓

Table A.2: Stations sampled during each occupation of the Fair Isle-Munken line and the date of the occupation. Continued on the next five pages.

Cruise	Date	1	2	3	4	5	6	7	8	9	10	11	12	13	14	15
EX197806	26/05/1978										✓	✓		✓		✓
EX197806	10/06/1978		✓	✓	✓	✓	✓		✓							
SC197809	03/09/1978		✓	✓	✓	✓	✓		✓	✓	✓	✓		✓		✓
SC197907	06/07/1979			✓	✓	✓	✓		✓	✓	✓	✓		✓		✓
SC198012	21/11/1980		✓	✓	✓	✓	✓		✓	✓	✓	✓		✓		✓
SC198106	26/06/1981		✓	✓	✓	✓	✓		✓	✓	✓	✓		✓		✓
SC198111	17/11/1981		✓	✓	✓	✓	✓	✓	✓	✓	✓	✓				
EX198208	28/08/1982		✓	✓	✓	✓	✓	✓	✓	✓	✓	✓		✓		✓
SC198303	17/04/1983		✓	✓	✓	✓	✓	✓	✓	✓	✓	✓		✓		✓
EX198308	20/08/1983		✓	✓	✓	✓	✓	✓	✓	✓	✓	✓		✓		✓
SC198413	09/11/1984		✓	✓	✓	✓	✓	✓	✓	✓	✓	✓		✓		✓
SC198504	01/05/1985		✓	✓	✓	✓	✓		✓	✓	✓	✓		✓		✓
AB198610	12/03/1986				✓	✓	✓	✓	✓	✓	✓	✓		✓		✓
SC198604	26/04/1986		✓	✓	✓	✓	✓	✓	✓	✓	✓	✓		✓		✓
SC198709	23/09/1987		✓	✓	✓	✓	✓		✓	✓	✓	✓		✓		
SC198812	05/11/1988									✓	✓	✓		✓		✓
SC198910	30/09/1989		✓	✓	✓	✓	✓	✓	✓	✓	✓	✓		✓		✓
SC199010	26/09/1990		✓	✓	✓	✓	✓		✓	✓	✓	✓		✓		✓
SC199109	29/09/1991		✓	✓	✓	✓	✓	✓	✓	✓	✓	✓		✓		✓
SC199207	15/06/1992		✓	✓	✓	✓	✓	✓	✓	✓	✓	✓		✓		✓

Cruise	Date	1	2	3	4	5	6	7	8	9	10	11	12	13	14	15
SC199212	23/09/1992		✓	✓	✓	✓	✓	✓	✓	✓	✓	✓		✓		✓
SC199216	19/12/1992		✓	✓	✓	✓	✓	✓	✓	✓	✓	✓		✓		✓
SC199306	25/05/1993		✓	✓	✓	✓	✓	✓	✓	✓	✓	✓		✓		✓
SC199312	21/09/1993		✓	✓	✓	✓	✓	✓	✓	✓	✓	✓		✓		✓
SC199405	05/04/1994		✓	✓	✓	✓	✓	✓	✓	✓	✓	✓	✓	✓	✓	✓
GS199406	19/05/1994		✓	✓	✓	✓	✓	✓	✓	✓	✓	✓	✓	✓	✓	✓
SC199413	23/09/1994		✓	✓	✓	✓	✓	✓	✓	✓	✓	✓		✓		✓
SC199416	08/11/1994		✓	✓	✓	✓	✓	✓	✓	✓	✓	✓	✓	✓	✓	✓
SC199418	14/12/1994									✓	✓	✓	✓	✓	✓	✓
FA199508	19/02/1995	✓	✓	✓	✓	✓	✓	✓	✓	✓	✓	✓		✓		✓
SC199513	16/09/1995		✓	✓	✓	✓	✓	✓	✓	✓	✓	✓	✓	✓	✓	✓
FA199568	10/11/1995	✓	✓	✓	✓	✓	✓	✓	✓	✓	✓	✓		✓		✓
SC199516	28/11/1995								✓	✓	✓	✓	✓	✓	✓	✓
FA199608	19/02/1996	✓	✓	✓	✓	✓	✓	✓	✓	✓	✓	✓		✓		✓
FA199632	08/05/1996	✓			✓	✓	✓	✓	✓							
SC199610	03/06/1996		✓	✓	✓	✓	✓	✓	✓	✓	✓	✓	✓	✓	✓	✓
FA199644	14/06/1996	✓	✓	✓	✓	✓	✓	✓	✓	✓	✓	✓		✓		✓
FA199660	01/09/1996	✓	✓	✓	✓	✓	✓	✓	✓	✓	✓	✓		✓		✓
SC199617	19/10/1996		✓	✓	✓	✓	✓	✓	✓	✓	✓	✓	✓	✓	✓	✓
FA199688	08/11/1996	✓	✓	✓	✓	✓	✓	✓	✓	✓	✓	✓		✓		✓

Cruise	Date	1	2	3	4	5	6	7	8	9	10	11	12	13	14	15
FA199708	14/02/1997	✓	✓	✓	✓	✓	✓	✓	✓	✓	✓	✓		✓		✓
SC199704	26/03/1997		✓	✓	✓	✓	✓	✓	✓	✓	✓	✓	✓	✓	✓	✓
FA199740	23/05/1997	✓	✓	✓	✓	✓	✓	✓	✓	✓	✓	✓		✓		✓
FA199748	15/06/1997	✓	✓	✓	✓	✓	✓	✓	✓	✓	✓	✓		✓		✓
FA199764	31/08/1997	✓	✓	✓	✓	✓	✓	✓	✓	✓	✓	✓		✓		✓
SC199713	23/10/1997		✓	✓	✓	✓	✓	✓	✓	✓	✓	✓	✓	✓	✓	✓
FA199792	07/11/1997	✓	✓	✓	✓	✓	✓	✓	✓	✓	✓	✓		✓		✓
FA199808	14/02/1998	✓	✓	✓	✓	✓	✓	✓	✓	✓	✓	✓		✓		✓
SC199805	24/03/1998		✓	✓	✓	✓	✓	✓	✓	✓	✓	✓	✓	✓	✓	✓
FA199840	14/06/1998	✓	✓	✓	✓	✓	✓	✓	✓	✓	✓	✓		✓		✓
FA199864	13/09/1998	✓	✓	✓	✓	✓	✓	✓	✓	✓	✓	✓		✓		✓
SC199817	05/10/1998		✓	✓	✓	✓	✓	✓	✓	✓	✓	✓	✓	✓	✓	✓
FA199888	06/11/1998	✓	✓	✓	✓	✓	✓	✓	✓	✓	✓	✓		✓		✓
SC199820	04/12/1998		✓	✓	✓	✓	✓	✓	✓	✓	✓	✓	✓	✓	✓	✓
SC199907	03/05/1999		✓	✓	✓	✓	✓	✓	✓	✓	✓	✓	✓	✓	✓	✓
FA199940	11/06/1999	✓	✓	✓	✓	✓	✓	✓	✓	✓	✓	✓		✓		✓
FA199964	12/09/1999	✓	✓	✓	✓	✓	✓	✓	✓	✓	✓	✓		✓		✓
SC199915	16/09/1999		✓	✓	✓	✓	✓	✓	✓	✓	✓	✓	✓	✓	✓	✓
FA199988	06/11/1999	✓	✓	✓	✓	✓	✓	✓	✓	✓	✓	✓		✓		✓
SC199919	11/12/1999		✓	✓	✓	✓	✓	✓	✓	✓	✓	✓	✓	✓	✓	✓

Cruise	Date	1	2	3	4	5	6	7	8	9	10	11	12	13	14	15
FA200008	28/02/2000	✓	✓	✓	✓	✓	✓	✓	✓	✓	✓	✓		✓		✓
SC200007	09/05/2000		✓	✓	✓	✓	✓	✓	✓	✓	✓	✓	✓	✓	✓	✓
FA200048	08/07/2000	✓	✓	✓	✓	✓	✓	✓	✓	✓	✓	✓		✓		✓
FA200060	10/09/2000	✓	✓	✓	✓	✓	✓	✓	✓	✓	✓	✓		✓		✓
SC200016	09/10/2000		✓	✓	✓	✓	✓	✓	✓	✓	✓	✓	✓	✓	✓	✓
FA200084	04/11/2000	✓	✓	✓	✓	✓	✓	✓	✓	✓	✓	✓		✓		✓
SC200019	09/12/2000		✓	✓	✓	✓	✓	✓	✓	✓	✓	✓	✓	✓	✓	✓
FA200108	25/02/2001	✓	✓	✓	✓	✓	✓	✓	✓	✓	✓	✓		✓		✓
SC200108	08/05/2001		✓	✓	✓	✓	✓	✓	✓	✓	✓	✓	✓	✓	✓	✓
FA200140	18/06/2001	✓	✓	✓	✓	✓	✓	✓	✓	✓	✓	✓		✓		✓
FA200160	09/09/2001	✓	✓	✓	✓	✓	✓	✓	✓	✓	✓	✓		✓		✓
SC200115	12/10/2001		✓	✓	✓	✓	✓	✓	✓	✓	✓	✓	✓	✓	✓	✓
SC200125	17/10/2001							✓	✓	✓	✓	✓	✓	✓	✓	✓
SC200118	08/12/2001		✓	✓	✓	✓	✓	✓	✓	✓	✓	✓	✓	✓	✓	✓
FA200248	09/07/2002	✓	✓	✓	✓	✓	✓	✓	✓	✓	✓	✓		✓		✓
CZ200202	17/05/2002		✓	✓	✓	✓	✓	✓	✓	✓	✓	✓	✓	✓	✓	✓
FA200248	09/07/2002	✓	✓	✓	✓	✓	✓	✓	✓	✓	✓	✓		✓		
FA200264	09/09/2002	✓	✓	✓	✓	✓	✓	✓	✓	✓	✓	✓		✓		✓
SC200214	25/09/2002		✓	✓	✓	✓	✓	✓	✓	✓	✓	✓	✓	✓	✓	✓
SC200218	09/12/2002		✓	✓	✓	✓	✓	✓	✓	✓	✓	✓	✓	✓	✓	✓

Cruise	Date	1	2	3	4	5	6	7	8	9	10	11	12	13	14	15
FA200308	24/02/2003	✓	✓	✓	✓	✓	✓	✓	✓	✓	✓	✓		✓		✓
SC200307	01/05/2003		✓	✓	✓	✓	✓	✓	✓	✓	✓	✓	✓	✓	✓	✓
FA200334	02/06/2003	✓	✓	✓	✓	✓		✓	✓							
FA200336	16/06/2003	✓	✓	✓	✓	✓	✓	✓	✓	✓	✓	✓		✓		✓
FA200364	07/09/2003	✓	✓	✓	✓	✓	✓	✓	✓	✓	✓	✓		✓		✓
SC200314	18/09/2003		✓	✓	✓	✓	✓	✓	✓	✓	✓	✓	✓	✓	✓	✓
FA200388	03/11/2003	✓	✓	✓	✓	✓	✓	✓	✓	✓	✓			✓		✓
SC200318	10/12/2003			✓		✓		✓	✓	✓	✓	✓	✓	✓	✓	✓
FA200408	23/02/2004	✓	✓	✓	✓	✓	✓	✓	✓	✓	✓			✓		✓
SC200408	14/05/2004		✓	✓	✓	✓	✓	✓	✓	✓	✓	✓	✓	✓	✓	✓
FA200436	14/06/2004	✓	✓	✓	✓	✓	✓	✓	✓	✓	✓			✓		✓
FA200464	03/09/2004	✓	✓	✓	✓	✓	✓	✓	✓	✓	✓			✓		✓
SC200414	09/10/2004		✓	✓	✓	✓	✓	✓	✓	✓	✓	✓	✓	✓	✓	✓
SC200417	09/12/2004		✓	✓	✓	✓	✓	✓	✓	✓	✓	✓	✓	✓	✓	✓
FA200508	19/02/2005	✓	✓	✓	✓	✓	✓	✓	✓	✓	✓			✓		✓
SC200507	13/05/2005		✓	✓	✓	✓	✓	✓	✓	✓	✓	✓	✓	✓	✓	✓
FA200536	22/05/2005	✓	✓	✓	✓	✓	✓	✓	✓	✓	✓			✓		✓

Appendix B

Slope mixing experiment: Sections and moorings

	Location	Dates	No. of casts
Central section	60°07′N, 4°28′W to 60°54′N, 5°48′W	8-9th September	25
Southern section	60°30′N, 6°00′W to 59°50′N, 5°20′W	10-11th September	20
Northern section	60°32′N, 3°00′W to 61°00′N, 4°13′W	15-16th September	17
Repeat station	60°16′N, 4°42′W	11-12th September	25

Table B.1: Locations and dates of the three across-channel sections and repeat station. Also included is the number of casts in each dataset.

Mooring name and location	Dates	Depth (m)	Instrument	Height above bottom (m)
'West' ADCP 60°13′N, 4°42′W	7-21st September	559	RDI 150 kHz ADCP 200 m range 4 m vertical bins	1
'West' thermistor 60°13′N, 4°42′W	7-21st September	601	SBE MicroCAT Vemco Minilog	4 6, 10, 14, 18, 22, 26, 30, 34, 38, 42, 46, 50
'East' ADCP 60°14′N, 4°37′W	8-21st September	597	RDI 600 kHz ADCP 40 m range 2 m vertical bins	2
'East' thermistor 60°15′N, 4°37′W	8-21st September	597	SBE MicroCAT Vemco Minilog	4 5, 9, 13, 17, 21, 25, 29, 33, 37, 41, 45, 49, 53
'South' ADCP 60°13′N, 4°39′W	8-21st September	553	RDI 150 kHz ADCP 200 m range 4 m vertical bins	1
'South' thermistor 60°13′N, 4°38′W	8-21st September	556	Vemco Minilog	4, 8, 12, 16, 20, 24, 28, 32, 36, 40, 44, 48, 52
'North' ADCP 60°15′N, 4°31′W	7-30th September	653	RDI 75 kHz ADCP 250 m range 8 m vertical bins	6

Table B.2: Location, dates, depth, and instrumentation attached to the four ADCP and three thermistor moorings.

Appendix C

Numerical model: Domain size and resolution

Run	x_0 (km)	L (km)	Δx (m)	H (m)	Δz (m)	t_{end} (days)	Δt (sec)	Δt_{out} (sec)
UniNsub	394	600	500	1000	20	18.6	100	3600
UniNcrit	394	600	500	1000	20	18.6	100	3600
UniNsuper	394	600	500	1000	20	18.6	100	3600
LowN400	258	500	500	1000	20	18.6	100	3600
LowN600	258	500	500	1000	20	18.6	100	3600
LowN800	226	500	500	1000	20	18.6	100	3600
HighN	680	800	500	1000	20	18.6	100	3600
HighNm4	173	250	250	1000	20	9.8	100	1800
HighNhf	29	100	100	1000	20	1.8	100	400
HighNmode2	208	300	500	1000	20	18.6	100	3600
HighNmode3	134	300	500	1000	20	18.6	100	3600

Table C.1: Domain size and resolution for all model runs. x_0 is the distance of the base of the shelf slope from the Western boundary; L is the total length of the domain; Δx is the horizontal resolution; H is the total depth of the domain; Δz is the vertical resolution; t_{end} is the total length of the run; Δt is the time-step; and Δt_{out} is the time-step data is output.

Bibliography

Adcroft, A. and J. Marshall, 1997: Representation of topography by shaved cells in a height coordinate ocean model. *Monthly Weather Review*, **125**, 2293–2315.

Adcroft, A. J., C. N. Hill, and J. C. Marshall, 1997: A new treatment of the Coriolis term in C-grid models at both high and low resolutions. *Monthly Weather Review*, **127**, 1928–1936.

Alford, M. H., 2003a: Improved global maps and 54-year history of wind-work on ocean inertial motions. *Geophysical Research Letters*, **30**, 1424, doi:10.1029/2002GL016 614.

Alford, M. H., 2003b: Redistribution of energy available for ocean mixing by long-range propagation of internal waves. *Nature*, **423**, 159–162.

Armi, L. and H. Stommel, 1983: Four views of a portion of the North Atlantic subtropical gyre. *Journal of Physical Oceanography*, **13**, 828–857.

Baines, P. G., 1982: On internal tide generation models. *Deep-Sea Research*, **29**, 307–338.

Becker, G. and B. Hansen, 1988: Modified North Atlantic water. ICES CM 1988/C: 17, International Council for the Exploration of the Sea, Copenhagen, Denmark.

Berntsen, J., J. Xing, and A. Davies, 2008: Numerical studies of internal waves at a sill: sensitivity to horizontal grid size and subgrid scale closure. *Continental Shelf Research*, **28**, 1376–1393.

Blindheim, J., 1990: Arctic intermediate water in the Norwegian Sea. *Deep-Sea Research*, **37**, 1475–1489.

Blindheim, J., V. Borovkov, B. Hansen, S. A. Malmberg, W. R. Turrell, and S. Østerhus, 1996: Recent upper layer cooling and freshening in the Norwegian

Sea. ICES CM 1996/C: 7, International Council for the Exploration of the Sea, Copenhagen, Denmark.

Borenäs, K. and P. Lundberg, 2004: The Faroe-Bank Channel deep-water overflow. *Deep-Sea Research II*, **51**, 335–350.

Borenäs, K. M., I. L. Lake, and P. A. Lundberg, 2001: On the intermediate water masses of the Faroe-Bank Channel overflow. *Journal of Physical Oceanography*, **31**, 1904–1914.

Borenäs, K. M. and P. A. Lundberg, 1988: On the deep-water flow through the Faroe Bank Channel. *Journal of Geophysical Research*, **93**, 1281–1292.

Bühler, O. and C. J. Muller, 2007: Instability and focusing of internal tides in the deep ocean. *Journal of Fluid Mechanics*, **588**, 1–28.

Burchard, H. and H. Rennau, 2008: Comparative quantification of physically and numerically induced mixing in ocean models. *Ocean Modelling*, **20**, 293–311.

Cacchione, D. A., L. F. Pratson, and A. S. Ogston, 2002: The shaping of continental slopes by internal tides. *Science*, **296**, 724–727.

Cacchione, D. A. and C. Wunsch, 1974: Experimental study of internal waves over a slope. *Journal of Fluid Mechanics*, **66**, 223–239.

Cairns, J. L. and G. O. Williams, 1976: Internal wave observations from a midwater float: 2. *Journal of Geophysical Research*, **81**, 1943–1950.

Carter, G. S. and M. C. Gregg, 2002: Intense, variable mixing near head of Monterey Submarine Canyon. *Journal of Physical Oceanography*, **32**, 3145–3165.

Carter, G. S., M. C. Gregg, and M. A. Merrifield, 2006: Flow and mixing around a small seamount on Kaena Ridge, Hawaii. *Journal of Physical Oceanography*, **36**, 1036–1052.

De Silva, I. P. D., J. Imberger, and G. N. Ivey, 1997: Localised mixing due to a breaking internal wave ray at a sloping bed. *Journal of Fluid Mechanics*, **350**, 1–27.

Dickson, B., J. Meincke, I. Vassie, J. Jungclaus, and S. Østerhus, 1999: Possible predictability in the overflow from the Denmark Strait. *Nature*, **397**, 243–246.

Dickson, B., I. Yashayaev, J. Meincke, B. Turrell, S. Dye, and J. Holfort, 2002: Rapid freshening of the deep North Atlantic Ocean over the past four decades. *Nature*, **416**, 832–837.

Dickson, R. R. and J. Brown, 1994: The production of North Atlantic Deep Water: sources, rates, and pathways. *Journal of Geophysical Research*, **99**, 12 319–12 341.

Dickson, R. R., E. M. Gmitrowicz, and A. J. Watson, 1990: Deep water renewal in the northern North Atlantic. *Nature*, **344**, 848–850.

Dillon, T. M., 1982: Vertical overturns: a comparison of Thorpe and Ozmidov scales. *Journal of Geophysical Research*, **87**, 9601–9613.

Egbert, G. D. and R. D. Ray, 2000: Significant dissipation of tidal energy in the deep ocean inferred from satellite altimeter data. *Nature*, **405**, 775–778.

Egbert, G. D. and R. D. Ray, 2001: Estimates of M_2 tidal energy dissipation from TOPEX/Poseidon altimeter data. *Journal of Geophysical Research*, **106**, 22,475–22,502.

Emery, W. J. and R. E. Thomson, 2001: *Data Analysis Methods in Physical Oceanography*. 2d ed., Elsevier Science, Amsterdam.

Eriksen, C. C., 1982: Observations of internal wave reflection off sloping bottoms. *Journal of Geophysical Research*, **87**, 525–538.

Eriksen, C. C., 1985: Implications of ocean bottom reflection for internal wave spectra and mixing. *Journal of Physical Oceanography*, **15**, 1145–1156.

Eriksen, C. C., 1998: Internal wave reflection and mixing at Fieberling Guyot. *Journal of Geophysical Research*, **103**, 2977–2994.

Fer, I., R. Skogseth, and P. M. Haugan, 2004: Mixing of the Storfjorden overflow (Svalbard Archipelago) inferred from density overturns. *Journal of Geophysical Research*, **109**, C01 005, doi:10.1029/2003JC001 968.

Ferron, B., H. Mercier, K. Speer, and A. Gargett, 1998: Mixing in the Romanche Fracture Zone. *Journal of Physical Oceanography*, **28**, 1929–1945.

Fofonoff, N. P., 1969: Spectral characteristics of internal waves in the ocean. *Deep-Sea Research*, **16**, 59–71.

Foldvik, A., K. Aagaard, and T. Tørresen, 1988: On the velocity field of the East Greenland Current. *Deep-Sea Research*, **35**, 1335–1353.

Galbraith, P. S. and D. E. Kelley, 1996: Identifying overturns in CTD profiles. *Journal of Atmospheric and Oceanic Technology*, **13**, 688–702.

Garcia Lafuente, J., T. Sarhan, M. Vargas, J. Vargas, and F. Plaza, 1999: Tidal motions and tidally-induced fluxes through La Linea submarine canyon, western Alboran Sea. *Journal of Geophysical Research*, **104**, 3109–3119.

Gargett, A. E., P. J. Hendricks, T. B. Sanford, and T. R. Osborn, 1981: A composite spectrum of vertical shear in the upper ocean. *Journal of Physical Oceanography*, **11**, 1258–1271.

Garrett, C. and W. Munk, 1975: Space-time scales of internal waves: a progress report. *Journal of Geophysical Research*, **80**, 291–297.

Gerkema, T. and H. van Haren, 2007: Internal tides and energy fluxes over Great Meteor Seamount. *Ocean Science*, **3**, 441–449.

Govender, K., G. P. Mocke, and M. J. Alport, 2004: Dissipation of isotropic turbulence and length-scale measurements through the wave roller in laboratory spilling waves. *Journal of Geophysical Research*, **109**, C08 018, doi:10.1029/2003JC002 233.

Green, J. A., J. H. Simpson, S. Legg, and M. R. Palmer, 2008: Internal waves, baroclinic energy fluxes and mixing at the European shelf edge. *Continental Shelf Research*, **28**, 937–950.

Gregg, M. C., 1977: A comparison of finestructure spectra from the main thermocline. *Journal of Physical Oceanography*, **7**, 33–40.

Gregg, M. C., 1989: Scaling turbulent dissipation in the thermocline. *Journal of Geophysical Research*, **94**, 9686–9698.

Gregg, M. C. and E. Kunze, 1991: Shear and strain in Santa Monica Basin. *Journal of Geophysical Research*, **96**, 16,709–16,719.

Gregg, M. C., T. B. Sanford, and D. P. Winkel, 2003: Reduced mixing from the breaking of internal waves in equatorial waters. *Nature*, **422**, 513–513.

Hansen, B. and S. Østerhus, 2000: North Atlantic-Nordic Seas exchanges. *Progress in Oceanography*, **45**, 109–208.

Hansen, B., W. R. Turrell, and S. Østerhus, 2001: Decreasing overflow from the Nordic seas into the Atlantic Ocean through the Faroe Bank channel since 1950. *Nature*, **411**, 927–930.

Helland-Hansen, B., 1930: Physical oceanography and meteorology. *Report on the scientific results of the 'Michael Sar' North Atlantic deep-sea expedition, 1910.*

Henyey, F. S., J. Wright, and S. M. Flatte, 1986: Energy and action flow through the internal wave field: an eikonal approach. *Journal of Geophysical Research*, **91**, 8487–8495.

Hogg, N. G., 1983: Hydraulic control and flow separation in a multilayered fluid with applications to the Vema Channel. *Journal of Physical Oceanography*, **13**, 695–708.

Hogg, N. G., 1985: Multilayer hydraulic control with applications to the Alboran Sea circulation. *Journal of Physical Oceanography*, **15**, 454–466.

Holbrook, W. S. and L. Fer, 2005: Ocean internal wave spectra inferred from seismic reflection transects. *Geophysical Research Letters*, **32**, L15 604, doi:10.1029/2005GL023 733.

Holbrook, W. S., P. Paramo, S. Pearse, and R. W. Schmitt, 2003: Thermohaline fine structure in and oceanographic front from seismic reflection profiling. *Science*, **301**, 821–824.

Holloway, P. E. and M. A. Merrifield, 1999: Internal tide generation by seamounts, ridges, and islands. *Journal of Geophysical Research*, **104**, 25,937–25,951.

Hosegood, P., 2005: Observations of the imact of flow-topography interactions on mixing processes within a confined basin: the Faeroe-Shetland Channel. Ph.D. thesis, University of Utrecht.

Hosegood, P., J. Bonnin, and H. van Haren, 2004: Solibore-induced sediment resuspension in the Faeroe-Shetland Channel. *Geophysical Research Letters*, **31**, L09 301, doi:10.1029/2004GL019 544.

Hosegood, P. and H. van Haren, 2003: Ekman-induced turbulence over the continental slope in the Faeroe-Shetland Channel as inferred from spikes in current meter observations. *Deep-Sea Research I*, **50**, 657–680.

Hosegood, P. and H. van Haren, 2004: Near-bed solibores over the continental slope in the Faeroe-Shetland Channel. *Deep-Sea Research II*, **51**, 2943–2971.

Hosegood, P., H. Van Haren, and C. Veth, 2005: Mixing in the interior of the Faeroe-Shetland Channel. *Journal of Marine Research*, **63**, 529–561.

Hughes, S. L., W. R. Turrell, B. Hansen, and S. Østerhus, 2006a: Fluxes of Atlantic Water (volume, heat and salt) in the Faroe-Shetland Channel calculated from a decade of acoustic doppler current profiler data (1994-2005). Collaborative Report (01/06), Fisheries Research Services, 77 pp., Aberdeen, U. K.

Hughes, S. L., W. R. Turrell, B. Hansen, and S. Østerhus, 2006b: Long term measurments of currents in the Faroe Shetland Channel (1994-2002). Collaborative Report (01/05), Fisheries Research Services, 97 pp., Aberdeen, U. K.

Huthnance, J. M., 1995: Circulation, exchange and water masses at the ocean margin: the role of physical processes at the shelf edge. *Progress in Oceanography*, **35**, 353–431.

Huthnance, J. M., 2005: F. S. Poseidon cruise 328 slope mixing Torshavn to Aberdeen. Cruise report no. 48, Proudman Oceanographic Laboratory, 45 pp., Liverpool, U. K.

Ivey, G. N. and R. I. Nokes, 1989: Vertical mixing due to the breaking of critical internal waves on sloping boundaries. *Journal of Fluid Mechanics*, **204**, 479–500.

Ivey, G. N., K. B. Winters, and I. P. D. De Silva, 2000: Turbulent mixing in a sloping benthic boundary layer energised by internal waves. *Journal of Fluid Mechanics*, **418**, 59–76.

Johnson, G. C. and T. B. Sanford, 1992: Secondary circulation in the Faroe Bank Channel outflow. *Journal of Physical Oceanography*, **22**, 927–933.

Johnson, H. L. and C. Garrett, 2004: Effects of noise on Thorpe scales and run lengths. *Journal of Physical Oceanography*, **34**, 2359–2372.

Kawabe, M., 2008: Vertical and horizontal eddy diffusivities and oxygen dissipation rate in the subtropical Northwest Pacific. *Deep-Sea Research I*, **55**, 277–260.

Klymak, J. M. and J. N. Moum, 2003: Internal solitary waves of elevation advancing on a shoaling shelf. *Geophysical Research Letters*, **30**, 2045, doi:10.1029/2003GL017706.

Köhl, A., R. H. Käse, D. Stammer, and N. Serra, 2007: Causes of changes in the Denmark Strait overflow. *Journal of Physical Oceanography*, **37**, 1678–1696.

Kunze, E., E. Firing, J. M. Hummon, T. K. Chereskin, and A. M. Thurnherr, 2006: Global abyssal mixing inferred from lowered ADCP shear and CTD strain profiles. *Journal of Physical Oceanography*, **36**, 1553–1576.

Kunze, E., L. K. Rosenfeld, G. S. Carter, and G. M. C., 2002: Internal waves in Monterey Submarine Canyon. *Journal of Physical Oceanography*, **32**, 1890–1913.

Kunze, E. and T. B. Sanford, 1984: Observations of near-inertial waves in a front. *Journal of Physical Oceanography*, **14**, 566–581.

Ledwell, J. R., E. T. Montgomery, K. L. Polzin, L. C. St. Laurent, R. W. Schmitt, and J. M. Toole, 2000: Evidence for enhanced mixing over rough topography in the abyssal ocean. *Nature*, **403**, 179–182.

Ledwell, J. R., A. J. Watson, and C. S. Law, 1993: Evidence for slow mixing across the pycnocline from an open-ocean tracer-release experiment. *Nature*, **364**, 701–703.

Lee, C. M., E. Kunze, T. B. Sanford, J. D. Nash, M. A. Merrifield, and G. Holloway, 2006: Internal tides and turbulence along the 3000-m isobath of the Hawaiian Ridge. *Journal of Physical Oceanography*, **36**, 1165–1182.

Legg, S. and A. Adcroft, 2003: Internal wave breaking an concave and convex continental slopes. *Journal of Physical Oceanography*, **33**, 2224–2246.

Lien, R. C. and M. C. Gregg, 2001: Observations of turbulence in a tidal beam and across a coastal ridge. *Journal of Geophysical Research*, **106**, 4575–4591.

Lueck, R. G. and J. J. Picklo, 1990: Thermal inertia of conductivity cells: Observations with a Sea-Bird cell. *Journal of Atmospheric and Oceanic Technology*, **7**, 756–768.

Maas, L. R. M., D. Benielli, J. Sommeria, and F. A. Lam, 1997: Obsevation of an internal wave attractor in a confined stably stratified fluid. *Nature*, **388**, 557–561.

MacCready, P. and P. B. Rhines, 1993: Slippery bottom bounbary layers on a slope. *Journal of Physical Oceanography*, **23**, 5–22.

MacKinnon, J. A. and M. C. Gregg, 2003: Mixing on the late-summer New England shelf-solibores, shear and stratification. *Journal of Physical Oceanography*, **33**, 1476–1492.

Macrander, A., U. Send, H. Valdimarsson, S. Jónsson, and R. H. Käse, 2005: Interannual changes in the overflow from the Nordic Seas into the Atlantic Ocean through the Denmark Strait. *Geophysical Research Letters*, **32**, L06 606, doi:10.1029/2004GL021 463.

Marshall, J., A. Adcroft, C. Hill, L. Perelman, and C. Heisey, 1997a: A finite-volume, incompressible Navier Stokes model for studies of the ocean on parallel computers. *Journal of Geophysical Research*, **102**, 5753–5766.

Marshall, J., C. Hill, L. Perelman, and A. Adcroft, 1997b: Hydrostatic, quasi-hydrostatic and nonhydrostatic ocean modeling. *Journal of Geophysical Research*, **102**, 5733–5752.

Martin, J. H. A., 1993: Norwegian Sea intermediate water in the Faroe-Shetland Channel. *ICES Journal of Marine Science*, **50**, 195–201.

Mauritzen, C., J. Price, T. Sanford, and D. Torres, 2005: Circulation and mixing in the Faroese Channels. *Deep-Sea Research I*, **52**, 883–913.

Meincke, J., 1978: On the distribution of low salinity intermediate water around the Faroes. *Deutsche Hydrographische Zeitschrift*, **31**, 50–64.

Mied, R., C. Shen, C. Trump, and G. Lindemann, 1986: Internal-inertial waves in a Sargasso Sea front. *Journal of Physical Oceanography*, **16**, 1751–1762.

Morison, J., R. Anderson, N. Larson, E. D'Asaro, and T. Boyd, 1994: The correction for thermal-lag effects in Sea-Bird CTD data. *Journal of Atmospheric and Oceanic Technology*, **11**, 1151–1164.

Moum, J. N., D. R. Caldwell, J. D. Nash, and G. G. D., 2002: Observations of boundary mixing over the continental slope. *Journal of Physical Oceanography*, **32**, 2113–2130.

Moum, J. N., J. M. Klymak, J. D. Nash, A. Perlin, and W. D. Smyth, 2007: Energy transport by nonlinear internal waves. *Journal of Physical Oceanography*, **37**, 1968–1988.

Moum, J. N. and J. D. Nash, 2008: Seafloor pressure measurements of nonlinear internal waves. *Journal of Physical Oceanography*, **38**, 481–491.

Munk, W., 1966: Abyssal recipies. *Deep-Sea Research*, **13**, 707–730.

Munk, W., 1981: Internal waves and small-scale processes. *Evolution of Physical Oceanography, Scientific Surveys in Honour of Henry Stommel*, B. A. Warren and C. Wunsch, Eds., M.I.T. Press, Cambridge, Mass., 264–291.

Munk, W. and C. Wunsch, 1998: Abyssal recipies II: energetics of tidal and wind mixing. *Deep-Sea Research I*, **45**, 1977–2010.

Mysak, L. A. and F. Schott, 1977: Evidence for baroclinic instability of the Norwegian current. *Journal of Geophysical Research*, **82**, 2087–2095.

Nash, J. D., M. H. Alford, and E. Kunze, 2005: Estimating internal wave energy fluxes in the ocean. *Journal of Atmospheric and Oceanic Technology*, **22**, 1551–1570.

Nash, J. D., M. H. Alford, E. Kunze, K. Martini, and S. Kelly, 2007: Hotspots of deep ocean mixing on the Oregon continental slope. *Geophysical Research Letters*, **34**, L01 605, doi:10.1029/2006GL028 170.

Nash, J. D., E. Kunze, C. M. Lee, and T. B. Sanford, 2006: Structure of the baroclinic tide generated at Kaena Ridge, Hawaii. *Journal of Physical Oceanography*, **36**, 1123–1135.

Nash, J. D., E. Kunze, J. M. Toole, and R. W. Schmitt, 2004: Internal tide reflection and turbulent mixing on the continental slope. *Journal of Physical Oceanography*, **34**, 1117–1134.

Naveira Garabato, A. C., K. I. C. Oliver, A. J. Watson, and M. J. Messias, 2004a: Turbulent diapycnal mixing in the Nordic seas. *Journal of Geophysical Research*, **109**, C12 010, doi:10.1029/2004JC002 411.

Naveira Garabato, A. C., K. L. Polzin, B. A. King, K. J. Heywood, and M. Visbeck, 2004b: Widespread intense turbulent mixing in the Southern Ocean. *Science*, **303**, 210–213.

New, A. L., 1988: Internal tidal mixing in the Bay of Biscay. *Deep-Sea Research*, **35**, 691–709.

New, A. L. and R. D. Pingree, 1990: Evidence for internal tidal mixing near the shelf break in the Bay of Biscay. *Deep-Sea Research*, **37**, 1783–1803.

Oakey, N. S., 1982: Determination of the rate of dissipation of turbulent energy from simultaneous temperature and velocity shear microstructure measurements. *Journal of Physical Oceanography*, **12**, 256–271.

Osborn, T. R., 1980: Estimates of the local rate of vertical diffusion from dissipation measurements. *Journal of Physical Oceanography*, **10**, 83–89.

Østerhus, S., W. R. Turrell, S. Jónsson, and B. Hansen, 2005: Measured volume, heat, and salt fluxes from the Atlantic to the Arctic Mediterranean. *Geophysical Research Letters*, **32**, L07 603, doi:10.1029/2004GL022 188.

Ozmidov, R. V., 1965: On the turbulent exchange in a stably stratified ocean. *Atmospheric and Oceanic Physics*, **8**, 853–860.

Park, Y., J. Fuda, I. Durand, and A. C. Naveira Garabato, 2008: Internal tides and vertical mixing over the Kerguelen Plateau. *Deep Sea Research II*, **55**, 582–593.

Phillips, O. M., 1977: *The Dynamics of the Upper Ocean.* 2d ed., Cambridge University Press, Cambridge.

Pingree, R. D. and A. L. New, 1991: Abyssal penetration and bottom reflection of internal tide energy in the Bay of Biscay. *Journal of Physical Oceanography*, **21**, 28–39.

Polzin, K. L., E. Kunze, J. Hummon, and E. Firing, 2002: The finescale response of lowered ADCP velocity profiles. *Journal of Atmospheric and Oceanic Technology*, **19**, 205–224.

Polzin, K. L., N. S. Oakey, J. M. Toole, and R. W. Schmitt, 1996: Fine structure and microstructure characteristics across the northwest Atlantic Subtropical Front. *Journal of Geophysical Research*, **101**, 14,111–14,121.

Polzin, K. L., J. M. Toole, J. R. Ledwell, and R. W. Schmitt, 1997: Spatial variability of turbulent mixing in the abyssal ocean. *Science*, **276**, 93–96.

Polzin, K. L., J. M. Toole, and R. W. Schmitt, 1995: Finescale parameterizations of turbulent dissipation. *Journal of Physical Oceanography*, **25**, 306–328.

Prinsenberg, S. J. and M. Rattray, 1975: Effects of continental slope and variable Brunt-Väisälä frequecy on the coastal generation of internal tides. *Deep-Sea Research*, **22**, 251–263.

Ray, R. D. and G. T. Mitchum, 1997: Surface manifestations of internal tides in the deep ocean: observations from altimetry and island gauges. *Progress in Oceanography*, **40**, 135–162.

Rudnick, D. L., et al., 2003: From tides to mixing along the Hawaiian Ridge. *Science*, **301**, 355–357.

Sandstrom, H. and N. S. Oakey, 1995: Dissipation in internal tides and solitary waves. *Journal of Physical Oceanography*, **25**, 604–614.

Saunders, P. M., 1981: Practical conversion of pressure to depth. *Journal of Physical Oceanography*, **11**, 573–574.

Saunders, P. M., 1990: Cold outflow from the Faroe Bank Channel. *Journal of Physical Oceanography*, **20**, 29–43.

Schmitt, R. W., J. M. Toole, R. L. Koehler, E. C. Mellinger, and K. W. Doherty, 1988: The development of a fine- and microstructure profiler. *Journal of Atmospheric and Oceanic Technology*, **5**, 484–500.

Sherwin, T. J., 1988: Analysis of an internal tide observed on the Malin Shelf, north of Ireland. *Journal of Physical Oceanography*, **18**, 1035–1050.

Sherwin, T. J., 1991: Evidence of a deep internal tide in the Faeroe-Shetland channel. *Tidal Hydrodynamics*, B. B. Parker, Ed., John Wiley & Sons, New York, 469–488.

Sherwin, T. J. and W. R. Turrell, 2005: Mixing and advection of a cold water cascade over the Wyville Thomson Ridge. *Deep-Sea Research I*, **52**, 1392–1413.

Sherwin, T. J., W. R. Turrell, D. R. G. Jeans, and S. Dye, 1999: Eddies and a mesoscale deflection of the slope current in the Faroe-Shetland Channel. *Deep-Sea Research I*, **46**, 415–438.

Sherwin, T. J., M. O. Williams, W. R. Turrell, S. L. Hughes, and P. I. Miller, 2006: A description and analysis of mesoscale variability in the Färoe-Shetland Channel. *Journal of Geophysical Research*, **111**, C03 003, doi:10.1029/2005JC002 867.

Simpson, J. H. and J. Hunter, 1974: Fronts in the Irish Sea. *Nature*, **250**, 404–406.

Skagseth, Ø. and K. A. Orvik, 2002: Identifying fluctuations in the Norwegian Atlantic Slope Current by means of empirical orthogonal functions. *Continental Shelf Research*, **22**, 547–563.

Smith, W. H. F. and D. T. Sandwell, 1997: Global seafloor topography from satellite altimetry and ship depth soundings. *Science*, **277**, 1957–1962.

Stansfield, K., C. Garrett, and R. Dewey, 2001: The probability distribution of the Thorpe displacement within overturns in Juan de Fuca Strait. *Journal of Physical Oceanography*, **31**, 3421–3434.

Thomson, R. E. and W. S. Huggett, 1981: Wind-driven inertial oscillations of large spatial coherence. *Atmosphere-Ocean*, **19**, 281–306.

Thorpe, S. A., 1977: Turbulence and mixing in a Scottish Loch. *Philosophical Transactions of the Royal Society of London A*, **286**, 125–181.

Timmermans, M. L., C. Garrett, and E. Carmack, 2003: The thermohaline structure and evolution of the deep waters in the Canadian Basin, Arctic Ocean. *Deep-Sea Research I*, **50**, 1305–1321.

Toole, J. M., K. L. Polzin, and R. W. Schmitt, 1994: New estimates of diapycnal mixing in the abyssal ocean. *Science*, **264**, 1120–1123.

Toole, J. M., R. W. Schmitt, K. L. Polzin, and E. Kunze, 1997: Near-boundary mixing above the flanks of a midlatitude seamount. *Journal of Geophysical Research*, **102**, 947–959.

Turner, J. S., 1973: *Buoyancy effects in fluids*. Cambridge University Press, London.

Turrell, W. R., G. Slesser, R. D. Adams, R. Payne, and P. A. Gillibrand, 1999: Decadal variability in the composition of Faroe Shetland Channel bottom water. *Deep-Sea Research I*, **46**, 1–25.

van Aken, H. M., 1988: Transports of water masses through the Faroese Channels determined by an inverse method. *Deep-Sea Research*, **35**, 595–617.

van Aken, H. M. and D. Eisma, 1987: The circulation between Iceland and Scotland derived from water mass analysis. *Netherlands Journal of Sea Research*, **21**, 1–15.

Webb, D. J. and N. Suginohara, 2001: Vertical mixing in the ocean. *Nature*, **409**, 37.

Wijesekara, H. W., T. M. Dillon, and L. Padman, 1993: Some statistical and dynamical properties of trubulence in the oceanic pycnocline. *Journal of Geophysical Research*, **98**, 22,665–22,679.

Wunsch, C., 1969: Progressive internal waves on slopes. *Journal of Fluid Mechanics*, **35**, 131–144.

Wunsch, C., 1998: The work done by the wind on oceanic general circulation. *Journal of Physical Oceanography*, **28**, 2332–2340.